ADVANCED ELECTRODE MATERIALS AND FABRICATION OF SUPERCAPACITORS

ADVANCED ELECTRODE MATERIALS AND FABRICATION OF SUPERCAPACITORS

By Wenyu Liang, B.ENG

A Thesis Submitted to the School of Graduate Studies in Partial

Fulfillment of the Requirements for the Degree Doctor of Philosophy

McMaster University DOCTOR OF PHILOSOPHY (2021) Hamilton,

Ontario (Materials Science and Engineering)

TITLE: Advanced Electrode Materials and Fabrication of

Supercapacitors

AUTHOR: Wenyu Liang, B.Eng. (University of Science and

Technology Beijing, China)

SUPERVISOR: Dr. Igor Zhitomirsky, Distinguished Engineering

Professor, Ph.D., P.Eng.

NUMBER OF PAGES:XXXIII, 208

Lay Abstract

To reduce the consumption of fossil fuel and meet the surging demand of electric energy, intensive attention has been drawn to new energy storage device, such as capacitors, batteries and supercapacitors. Owing to their higher energy density compared with conventional capacitors and higher power density compared with batteries, supercapacitors are attracting tremendous research interest. The advantages of supercapacitors are fast charge-discharge rate, high power and energy density and excellent cyclic stability.

The objective of this work was to fabricate high-performance supercapacitor devices based on the development of advanced electrode materials. MXene and Fe-based composite materials were synthesized by conceptually new colloidal approach and some efficient dispersants were developed during the process. The enlarged voltage window and superior performance were recorded for asymmetric supercapacitors. The results presented in this work showed much more promising performance compared with that reported in the literature and paved the way for future research.

Abstract

Supercapacitors (SCs) have generated significant interest due to their advantages including lightweight, rapid charge-discharge, good rate capability and high cyclic stability. Electrodes are one of the most important factors influencing the performance of SCs. MXene is a promising candidate for supercapacitor electrodes, which is a relatively new material with formula $M_{n+1}X_nT_x$, where M is a transitional metal, X stands for C or N, and T_x is surface terminations. Due to its multi-layered structure, high surface area and rich redox chemistry, good electrochemical performance can be expected. To further enhance the conductivity of the MXene electrodes, multi-walled carbon nanotubes (MCNT) were applied as the conducting additive. The as-fabricated composite electrodes showed reduced resistance and enhanced electrochemical performance. Advanced co-dispersants such as cationic celestine blue (CCB) and anionic catechol violet (ACV) were employed to improve the dispersion of components. CCB and ACV can adsorb strongly on the MXene and MCNT surface to form a homogenous suspension and thus improve the mixing between them. Another advanced dispersant 3,4,5-trihydroxybenzamide (THB) also showed adsorption on both MXene and MCNT particles, favored their dispersive mixing and improved electrochemical performance.

Iron oxides are promising materials for negative electrodes for supercapacitors. The

attempt to combine highly capacitive Fe_3O_4 with MXene-MCNT composites proved the synergistic effect of individual components. Investigation of Zn-doped FeOOH as high active mass loading anode with MCNT as conducting additive allowed for enhanced performance. Zn-Fe double hydroxide materials are promising for the fabrication of advanced supercapacitor electrodes. A safe and neutral Na_2SO_4 electrolyte was was beneficial for the development of asymmetric devices with enlarged voltage window. For cathodes working in an overlapping window with Zn-FeOOH anode, polypyrrole coated carbon nanotube electrode was fabricated with a comparable capacitance. The advanced dopant eriochrome cyanine R (ECR) allowed for the uniform thickness of PPy coating on MCNT and enhanced charge transfer between PPy and MCNT was achieved. Enhanced capacitive properties of cathodes and anodes at high active mass loading working in complimentary voltage windows allowed for fabrication of high-performance supercapacitor, which was a promising device for practical applications.

Acknowledgement

My deepest gratitude is first to my supervisor, Dr. Igor Zhitomirsky for his constant

encouragement and guidance. Without his help I will never enjoy my Ph.D life so much.

His patience, hardworking and kindness has always inspired me to greater efforts.

I would like to thank my committee members Dr.Kitai and Dr. de Lannoy for their

valuable questions during the committee meetings every year. They made me realized

of my progress but also weakness and encouraged me with foresight of research.

There are many staffs and technicians who gave me assistance whenever needed and I

would like to thank Dr.Britten, Victoria Jarvis, Jhoynner Martinez, Chris Butcher,

Xiaogang Li, Ed McCaffery, Paul Dube and Mary-Anne Bechamp for their help.

It was my great pleasure to be part of Dr.Zhitomirsky's group. I really enjoyed past

several years working and studying with my colleagues: Ryan Poon, Jordan Milne, Ri

Chen, Amanda Clifford, Aseeb Syed, Zhengzheng Wang, Krishna Jangid, Sadman

Sakib, Mohamed Nawwar, Qinfu Zhao, Xinqian Liu, WenjuanYang, Coulton Boucher

and Chengwei Zhang. Thanks for their help and encouragement for my research,

study and daily life.

Last my thanks will go to my beloved family, my dad and mom, for their continuous

support, great confidence, and unconditional love all through past years. It is my

honor to be your children. And my love, Tai Kang, I am so glad to have you be my

side so that I own the courage to overcome any difficulty. Thank you for your endless

love, faith and support on both my academic and personal life.

Declaration of Academic Achievements

This dissertation was used to fulfill the requirements of the degree Doctor of Philosophy. The major research project was conducted from September 2018 to October 2021. The results of this dissertation were published or submitted in 8 papers in peer-reviewed journals, which were listed below:

1. **Liang W**, Zhitomirsky I. MXene–carbon nanotube composite electrodes for high active mass asymmetric supercapacitors. Journal of Materials Chemistry A. 2021;9(16):10335-44.

2. **Liang W**, Zhitomirsky I. Composite $Ti_3C_2T_x$-carbon nanotube electrodes with high active mass for supercapacitors. Open Ceramics. 2021 Sep 1;7:100158.

3. **Liang W**, Zhitomirsky I. Composite Fe_3O_4-MXene-Carbon Nanotube Electrodes for Supercapacitors Prepared Using the New Colloidal Method. Materials. 2021 Jan;14(11):2930.

4. **Liang W**, Zhitomirsky I. Zn-Fe double hydroxide-carbon nanotube anodes for asymmetric supercapacitors. Frontiers in Materials. 2020 May 14;7:137.

5. **Liang W**$^=$, Poon R$^=$, Zhitomirsky I. Zn-doped FeOOH-polypyrrole electrodes for supercapacitors. Materials Letters. 2019 Nov 15;255:126542. (=: Authors contribute equally to this publication)

6. Poon R$^=$, **Liang W**$^=$, Zhitomirsky I. Mn_3O_4 and (ZnFe) OOH Composites for

Supercapacitors with High Active Mass. Metallurgical and Materials Transactions A. 2020 Feb;51(2):855-62. (=: Authors contribute equally to this publication)

7. **Liang W**, Zhitomirsky I. MXene-polypyrrole electrodes for asymmetric supercapacitors. Electrochimica Acta. 2022 Jan 4:139843..

8. **Liang W,** Yang L, Sakib S and Zhitomirsky I. Capacitive properties of magnetic $CuFe_2O_4$ nanoparticles for electrical energy storage, Journal of Electrochemical Society, Under review.

In addition to the work presented above, I have also contributed to 2 papers that are published in peer-reviewed journals and are not covered in this dissertation.

9. Li X, Zhu J, **Liang W,** Zhitomirsky I. MXene ($Ti_3C_2T_x$) anodes for asymmetric supercapacitors with high active mass loading. Materials Chemistry and Physics. 2021 May 22:124748.

10. Baker K, Sikkema R, **Liang W**, Zhitomirsky I. Multifunctional Properties of Commercial Bile Salts for Advanced Materials Engineering. Advanced Engineering Materials. 2021 May;23(5):2001261.

Table of Contents

List of Figures

List of Tables

List of Abbreviations and Symbols

A ,mA(unit)	Ampere, milliamper
AC	Activated carbon
ACV/PCV	Anionic catechol violet/Pyrocatechol violet
AML	Active mass loading
C, μC (unit)	Coulomb, microcoulomb
C	Capacitance
C^+	Cationic species in electrolyte
C*	Complex differential capacitance
Cm	Gravimetric capacitance
Cs	Areal capacitance
Cs'	Real component of complex capacitance
Cs''	Imaginary component of complex capacitance
CCB/CB	(Cationic) Celestine blue
CNT	Carbon nanotube
CPC	Cetylpyridinium chloride
CV	Cyclic voltammetry or cyclic

	voltammogram
DI	Deionized
DLS	Dynamic light scattering
DLVO	Derjaguin-Landau-Verwey-Overbeek
e^-	Electron
ε_0	Permittivity of vacuum
E	Electrode potential
E^0	Standard electrode potential
EDLC	Electrochemical double layer capacitor
EIS	Electrochemical impedance spectroscopy
f	Frequency
F	Faraday constant
F, mF, μF (unit)	Farad, millifarad, microfarad
FTIR	Fourier-transform infrared spectroscopy
g, mg, μg (unit)	Gram, milligram, microgram
h (unit)	Hour
Hz, mHz, kHz (unit)	Hertz, milliHertz, kiloHertz
I	Current
K (unit)	Temperature in Kelvin
k	Boltzmann constant

L, mL (unit)	Liter, milliliter
m, cm, μm, nm (unit)	Meter, centimeter, micrometer, nanometer
M	Molar concentration
MCNT/MWCNT	Multiwalled carbon nanotube
SC	Supercapacitor
P	Maximum power
PEMA	poly (ethyl methacrylate)
PPy	Polypyrrole
PTFE	Polytetrafluoroethylene
PVB/PVBAA	Poly(vinyl butyral-co-vinyl alcohol-co-vinyl acetate)
Q	Charge stored
R	Resistance
s (unit)	Second
SCE	Saturated calomel electrode
SEM	Scanning electron microscopy
T	Temperature
TEM	Transmission electron microscopy
THB	3,4,5-trihydroxybenzamide
TL	Tolonium chloride

V	Voltage
V_{max}	Maximum voltage
V_{min}	Minimum voltage
W (unit)	Watt
wt%	Weight percentage
XRD	X-ray diffraction
Z^*	Total impedance
Z'	Real component of impedance
Z''	Imaginary component of impedance
Rm	Ratio of active material mass to current collector mass
°C (unit)	Temperature in Celsius

Chapter 1 Introduction

With the rapid development of science and technology, energy is of great importance to the sustainability of human societies. Due to the consumption of fossil fuels and their resulted pollution, there is an urgent need for sustainable and clean energy sources, such as solar, wind and tidal energy. However, without the sustainability, these kinds of energy cannot meet the demand of high-tech products[1]. To address these issues, energy storage and conversion technologies are of great importance. Supercapacitors (SCs), also known as ultracapacitors or electrochemical supercapacitors, have attracted significant attention due to their unique characteristics, such as high power density, short charging time, good cycling capability and low cost[2, 3].

Based on the mechanism of charge storage as well as the categories of active materials, there are three categories of SCs: electrochemical double layer capacitors (EDLCs), pseudocapacitors and hybrid supercapacitors. The first generation among these SCs is EDLCs which are fabricated using carbon-based active materials, especially carbon nanotubes (CNTs), activated carbon (AC) and carbon black, which have high specific surface area (SSA) for accommodation of more ions adsorption/desorption on their surface during charge and discharge. Pseudocapacitors are the second kind of SCs currently compounded by the transitional metal oxides such as MnO_2, RuO_2, NiO or conductive polymers with high specific capacitance and large energy storage capacity.

With the aim of increasing the energy density and power density of SCs, hybrid supercapacitors are fabricated as the combination of two different electrode materials with the overwhelming advantages of high power density, fast charging/discharging rate, sustainable cycling life (millions of cycles), and excellent cycle stability [4, 5].

MXenes are relatively new materials discovered in 2011[6], which are transition metal carbides, nitrides or carbonitrides. Among numerous MXene types, $Ti_3C_2T_x$ is the most studied material and has been investigated for applications in energy storage devices such as batteries[7] and SCs[8] for its high surface area, rich redox chemistry and good conductivity[9]. Of particular interest are the various composites, such as polymer-containing $Ti_3C_2T_x$/PVA[10], $Ti_3C_2T_x$/PPy[11], $Ti_3C_2T_x$/PANI[12], and metal oxide composites such as $Ti_3C_2T_x$/MnO_2[13], $Ti_3C_2T_x$/ZnO[14], $Ti_3C_2T_x$/Fe_3O_4[15], and carbon-based composites $Ti_3C_2T_x$/CNT[9], $Ti_3C_2T_x$/graphene[16], $Ti_3C_2T_x$/C[17]. However, the investigations of $Ti_3C_2T_x$-based materials for application in supercapacitor electrodes are limited to low active mass loadings, especially between 1-8 mg cm^{-2}[9]. It should be noted that for practical applications, the loading of active material is required to be higher than 20 mg cm^{-2}[18]. What's more, the critical influence of electrolyte and binder materials have not drawn adequate attention.

Iron-based materials are promising compounds for SC electrodes, including Fe_2O_3, Fe_3O_4, FeOOH, FeO_x, $CoFe_2O_4$ and $MnFe_2O_4$[19]. Like other oxide materials, high theoretical specific capacitance, low cost, natural abundance and non-toxicity are the

main advantages of Fe-containing electrode materials[20-22]. However, the poor electrochemical stability limited the performance to a great extent[19].

In this investigation, we focus on fabrication of advanced composite materials as negative electrodes for asymmetric supercapacitors. We developed conceptually new approaches of applying multifunctional molecule as a charge transfer mediator as well as a dispersing agent to improve mixing between components. In addition, we reported new advanced processing techniques for synthesis of non-agglomeration particles. The $Ti_3C_2T_x$ MXene, Fe-based composites as well as multifunctional $CuFe_2O_4$ composites were fabricated as negative electrodes at high active mass loading, and tested under enlarged potential range, which gave excellent electrochemical performance and were beneficial for the next generation of electrochemical energy storage devices.

Chapter 2 Literature review

2.1 The development and performance of supercapacitors

Electrochemical supercapacitors have experienced great development in recent years. As a remarkable patent of Becker, capacitors were firstly described based on high surface area carbon[23]. With the increasing population of hybrid electric vehicles in 1990s, ECs began to draw more attention. The studies on ECs' fabrication as well as electrochemical performance have attracted significant interest. There are alternative applications of ECs showing considerable market potentials, such as fast acceleration of vehicles, the ability to substitute conventional batteries and fuel cells, etc.

The excellent and overwhelming performance of ECs makes them an attractive energy storage option. The charge/discharge efficiency is extremely high, which can be finished in few minutes. In addition, the process is completely reversible so ECs can withstand a large number of charge/discharge cycles. Besides, ECs are more welcomed by the market since they are made of environmentally friendly raw materials. With high power density and high energy density, ECs have a wide range of applications in the future.

To explain the fundamental of ECs, a brief review of capacitors should be summarized as they are similar in terms of general operating mechanisms.

Figure 2.1 shows a simple electrostatic capacitor which consists of two conductive

plates with a dielectric separator in between. When an external power source (such as battery) is applied, electrons on the one of the electrodes of capacitor will travel to the positive terminal of the battery and leaves the electrode positively charged. Simultaneously, electrons on the negative terminal of battery will accumulate on the other electrode of the capacitor, making it negatively charged. The charging process will not stop until the potential difference between two plates of capacitor is equal to applied voltage. The two plates are now charged positively and negatively, respectively. The total amount of charge stored is given by equation 2-1,

$$Q=CV \qquad \text{(Eq. 2-1)}$$

Where Q is the total charge stored, V is voltage between two plates of capacitor and C stands for the capacitance of the capacitor. According to the equation 2-2, the specific capacitance is determined by the surface area A, vacuum permittivity ε_0, dielectric constant ε_r and thickness of the double-layer d.

$$C = \varepsilon_0 \varepsilon_r \frac{A}{d} \qquad \text{(Eq. 2-2)}$$
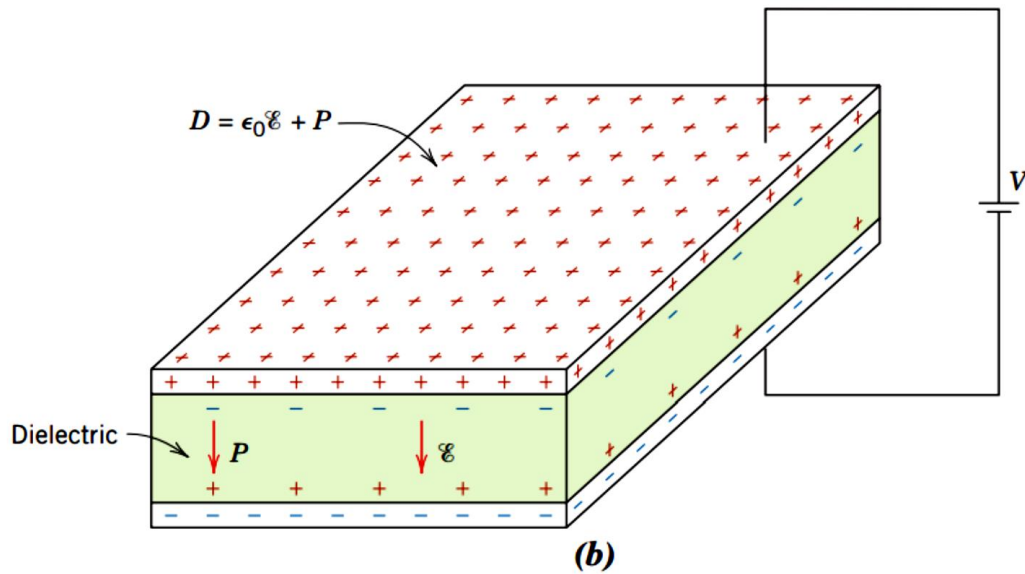
Figure 2.1 Diagram of a simple electrostatic capacitor [24]

The total charge stored is proportional to the voltage applied, and the total energy stored

in a capacitor is described by the following equation:

$$E = \frac{1}{2} C V^2 \qquad \text{(Eq. 2-3)}$$

And the power density can be written as:

$$P = \frac{V^2}{R_{ESR}} \qquad \text{(Eq. 2-4)}$$

where R_{ESR} is the equivalent series resistance. From these equations, it is obvious that

to achieve both high power and energy density, the operating voltage should be

increased. In addition, by increasing the capacitance the energy density will also be

increased.

2.2 Categories of supercapacitors

Based on the charge storage mechanism, ECs can be generally divided into three

groups: (i) electric double-layer supercapacitors (EDLC), (ii) Faradaic supercapacitors

(FS) or pseudocapacitors, and (iii) hybrid supercapacitors.

2.2.1 Electric double-layer supercapacitors

Figure 2.2 shows the schematic structure of an electric double layer capacitor

(EDLC), which includes two high surface area porous electrodes with a separator in

the middle. The separator is immersed in a special electrolyte. When the voltage is

applied to the capacitor, without any Faradic process, the charge is accumulated at the

interface between electrode and electrolyte. Finally, the accumulated charge forms an

electric double-layer, and the thickness of each layer is in the order of a few

angstroms (0.3-0.8 nm).
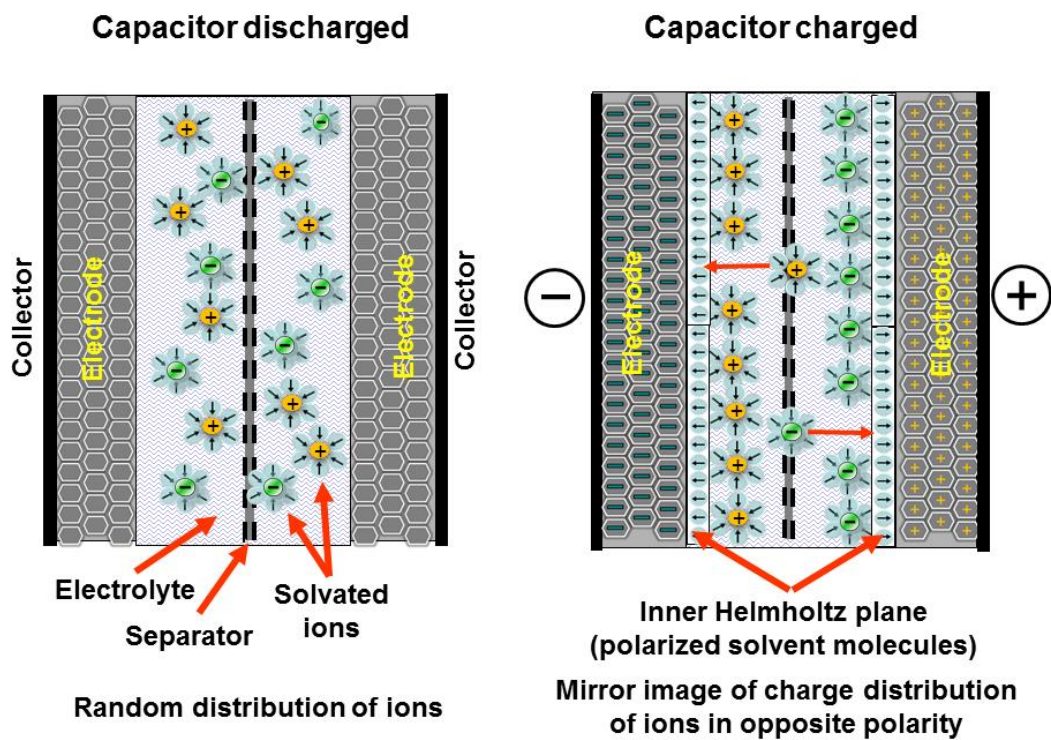
Figure 2.2 Schematic structure and principles of a single cell EDLCs [25]

In the charging process, the electrons travelling from the negative electrode will go

back to the positive electrode through an external load. In the electrolyte, the cations

go towards the negative electrode and the anions go to the positive one. These

processes can be showed in the electrochemical way as follows.
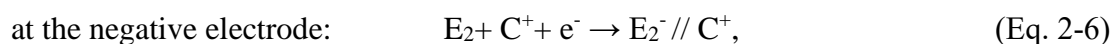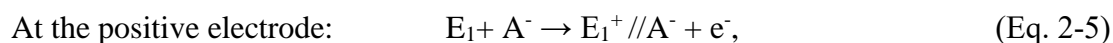
At the positive electrode: $E_1 + A^- \rightarrow E_1^+ // A^- + e^-$,   (Eq. 2-5)

at the negative electrode: $E_2 + C^+ + e^- \rightarrow E_2^- // C^+$,   (Eq. 2-6)

where E_1 and E_2 are the positive and negative electrodes, respectively. A^- is the anion

and C^+ is the cation. // represents the interface of the electrode and the electrolyte. The

discharge process can be represented by reverse of the above equations.

Based on equation 2-2, to achieve the high capacitance of the EDLC, high surface

area, high permittivity and a small distance between two electrodes are required. In

commercial applications, porous carbon materials are typically used as the electrode

materials for their large surface areas.

As a result, the capacitance and energy density of EDLCs are much higher than that of

conventional capacitor where the capacitance is just in the order of pF or μF typically.

Besides, without any redox reaction, EDLCs enjoy a much higher power density than

pseudocapacitors which involve redox reactions.

2.2.2 Pseudocapacitors

Significantly different from mechanism of electrochemical double-layer capacitors

(EDLCs) which mainly based on the electrostatic charge storage, there is always a

redox reaction during the charge/discharge process for pseudocapacitors. When an

external potential is applied, a fast and reversible redox reaction happen on the

electrode, which allows the charges to pass through the interface between the

electrode and electrolyte. The mechanisms of charge/discharge of a pseudocapacitor

are similar to that of a battery. During a charge process, the reactions at both two

electrodes can be expressed as follows:
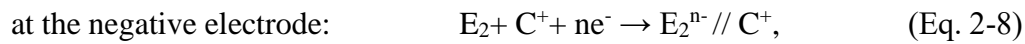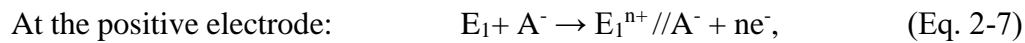
At the positive electrode: $E_1 + A^- \rightarrow E_1^{n+} // A^- + ne^-,$ (Eq. 2-7)

at the negative electrode: $E_2 + C^+ + ne^- \rightarrow E_2^{n-} // C^+,$ (Eq. 2-8)

where E_1 and E_2 are the positive and negative electrodes, respectively. A^- is the anion

and C^+ is the cation. // describes the interface of the electrode and the electrolyte. ne^-

represents the electrosorption valence which relates to the oxidation and reduction

reaction at the electrode. The discharge process can be represented by reverse of the

above equations.

ECs technology makes it possible to obtain high values of specific capacitance in

double-layer capacitors and pseudocapacitors. Double-layer capacitors could offer

outstanding charge storage because of high active area of electrodes and charge

separation at atomic dimension, while pseudocapacitors could realize high capacitance

due to the redox reaction taken places when applied an external potential. Comparison

of these two capacitors is shown in Table 2.1.

Table 2.1 Comparison of EDLCs and pseudocapacitors[26]

Characteristics	EDLCs	pseudocapacitors
Faradaic process	N/A	Yes
Capacitance	20–50 $\mu F\ cm^{-2}$	2000 $\mu F\ cm^{-2}$ for single-electron transferred process; 200–500 $mF\ cm^{-2}$ for multi-electrons transferred
Reversibility	Highly reversible	Quite reversible but has intrinsic electrode kinetic rate limitation
Advantage	High power density	High energy density

2.2.3 Hybrid (Asymmetric) supercapacitors

Hybrid supercapacitors are made by one electric double electrode with another

pseudocapacitive electrode, which overcome the shortcomings both of EDLCs and

pseudocapacitors. As is shown in Figure 2.3, hybrid supercapacitors with high

specific energy and high specific power fill the gap between symmetric

supercapacitors and Li-ion batteries.
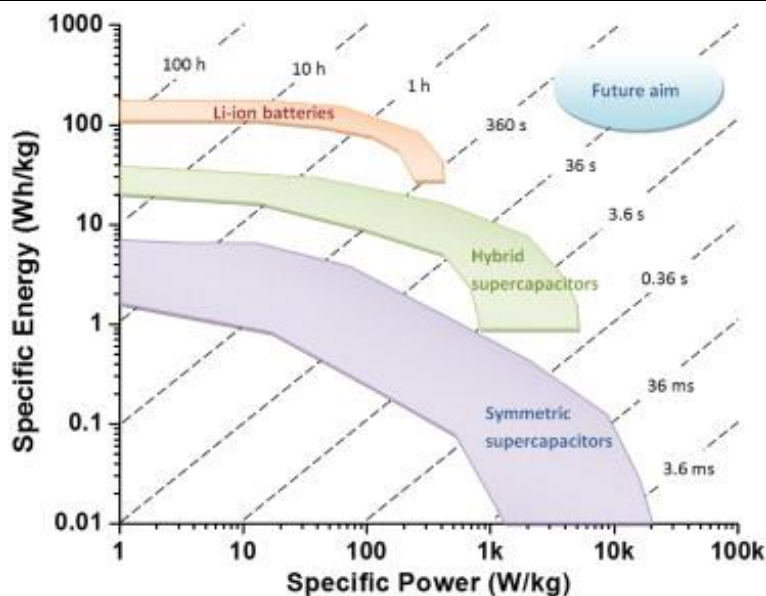
Figure 2.3 Ragone plot of three major electrochemical energy storage devices. Time constants are shown in dashed line, by dividing the specific energy with specific power[27]

2.3 Materials for electrodes of supercapacitors

The materials' structure and morphology have considerable influence on

electrochemical properties of supercapacitor electrodes. For EDLCs and

pseudocapacitors, carbon-based materials and transition metal oxides as well as

conductive polymer are widely used. As a combination of two different electrodes,

hybrid supercapacitors use composite electrodes materials.

2.3.1 Carbon-based materials for electrode of EDLCs
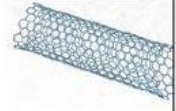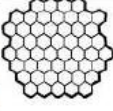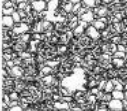
Since the mechanism of EDLCs is based on the accumulation of charges at the

interface between electrode and electrolyte, high specific surface area, low

electrochemical activity and high porosity are necessary. So carbon materials, like

carbon nanotube(CNT)[27, 28], graphene[29, 30], carbon aerogels[31, 32], activated

11

carbon[33] and other carbon-based materials, are widely used as the electrode

materials of EDLCs.

As shown in table 2.2, activated carbon has very high specific capacitance but low

conductivity, while CNT and graphene have low capacitance with high conductivity.

As a result, CNT and graphene are always used as additives to enhance the

conductivity of EDLCs electrodes.

Table 2.2 Onion-like carbon, carbon nanotubes, graphene, activated carbons, and
carbide-derived carbons used in EDLCs[34]

Material	Carbon onions	Carbon nanotubes	Graphene	Activated carbon	Carbide derived carbon	Templated carbon
Dimensionality	0-D	1-D	2-D	3-D	3-D	3-D
Conductivity	High	High	High	Low	Moderate	Low
Volumetric Capacitance	Low	Low	Moderate	High	High	Low
Cost	High	High	Moderate	Low	Moderate	High
Structure						

2.3.2 Redox-based materials

Compared to EDLCs, pseudocapacitors have a relatively higher capacitance. Based on

redox reaction, the charges can accumulate both in an electrostatic way and also in a

faradaic reaction way[35].

2.3.2.1 Conducting polymers

Conducting polymers offer benefits of easy fabrication and high conductivity, so they

attract much attention. The advanced conducting polymers are (i)polypyrrole (PPy),

(ii)polyaniline (PANI), (iii)polythiophene (PTh) and (iv)poly(3,4-

ethylenedioxythiophene) (PEDOT). Figure 2.4 shows their different molecular

structures.

In the charge/discharge process, the charges are accumulated by the redox reaction

taking place in the bulk volume of the film, instead of just on the surface as the case

of carbon. Therefore, the specific capacitance of ECs made by this kind of materials is

relatively high. However, there is a limitation of conductive polymers that they can

only be used within a rigid potential window, which limits their applications.

(A)   (B)   (C)   (D)
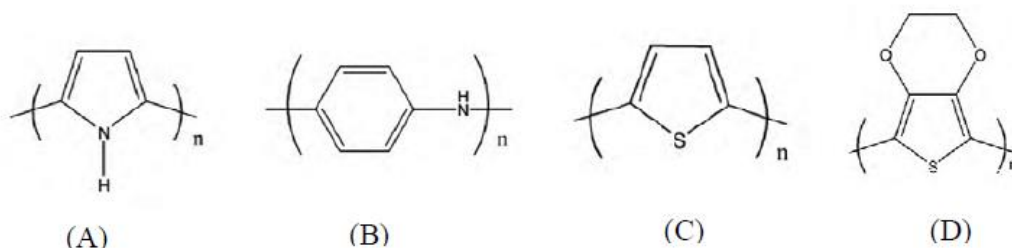
Figure 2.4 Various conducting polymer structures. A) polypyrrole (PPy), B) polyaniline
(PANI), C) polythiophene (PTh) and D) poly(3,4-ethylenedioxythiophene)(PEDOT).

2.3.2.2 Transition metal oxide materials

The table 2.3 shows the common metal oxide materials for pseudocapacitor

electrodes. It is obvious that RuO_2 has a high conductivity as well as a high

capacitance. However, applications of this material are limited by its high cost.

Therefore, it cannot be widely applied to industry. Therefore, other materials, such as

MnO_2, NiO and V_2O_5, attract more attention in recent years.

Table 2.3 Properties of different metal oxides[37]

Metal oxide	Potential range (V)	Conductivity (S/cm)	Theoretical capacitance (F/g)
MnO_2	0.9	10^{-5}-10^{-6}	1380
NiO	0.5	0.01-0.32	2584
Co_3O_4	0.45	10^{-4}-10^{-2}	3560
V_2O_5	1	10^{-4}-10^{-2}	2120
RuO_2	1.23	1-10^3	2200

2.3.3 Composite electrodes and hybrid configurations

As mentioned above, carbon-based materials offer great advantages. However, their

low capacitance is a serious limitation in many applications. On the other hand, with

low conductivity of transition metal oxides and low mechanical stability of polymer,

pseudocapacitors also have limitations.

As a result, the combination of those materials as composites is widely applied in

electrodes, leading to high power density, good mechanical properties, and long cycle

life.

2.4 Electrolyte Materials

An electrolyte is one of the most important components for ECs as well. The electric

conductance of the electrolyte exerts a strong influence on the equivalent series

resistance of the device, and thus its power output characteristics. On the other hand,

the extent of ionization and dielectric properties of the electrolyte influence the

specific capacitance of the electrode. The selection of a practical electrolyte requires

a high ionic concentration, wide voltage window, high electrochemical stability, high

purity, low cost and low toxicity.

There are two critical factors related to the conductance of the electrolyte: the

concentration of free charge carriers and the ionic mobility, which are mainly

dependent on the solubility of the salt in the solvent and the degree of dissociation of

dissolved salts. For ion pairs in an electrolyte solution, there are mainly three types:

the first type is the hydration shell contact, which provides high fraction of salts as

free charge carriers of electric current; the second kind is shared hydration shells,

resulting in the reduction of the distance between the solvated ions; when the solvent

is poor solvating, the cations and anions just contact with each other, which is the

third type of ion pairs. Figure 2.5 shows three stages of ion pairing illustrated above.
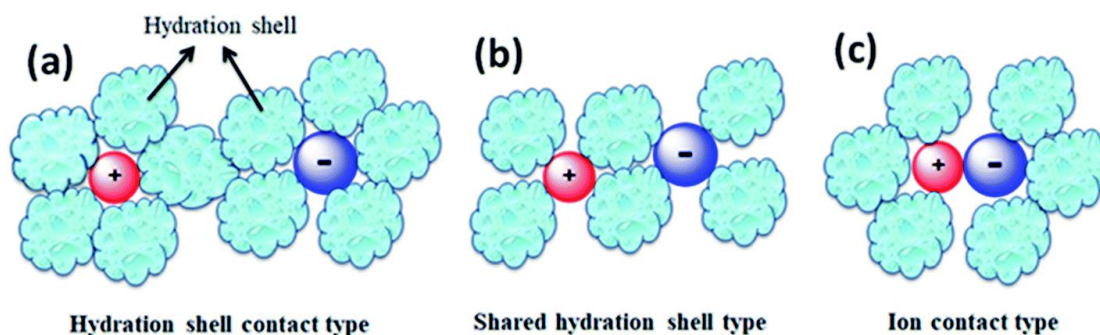
Figure 2.5 Types of ion pairs in an electrolyte solution: (a) solvated-ion pairs, (b) solvent shared ion pairs, and (c) contact ion pairs[37]

Conventional liquid electrolytes used in ECs can be classified by their materials into

three types: (1) aqueous electrolytes, (2) organic electrolytes and (3) ionic liquids.

2.4.1 Aqueous electrolytes

Dependent on the salt used, aqueous electrolytes can be acidic, basic or neutral. The

common aqueous electrolytes used in supercapacitors are H_2SO_4, KOH, KCl and

Na_2SO_4, etc. Compared to organic electrolytes, aqueous electrolytes have the

advantages of higher ionic concentrations and low resistance. Due to their high

conductivity, SCs fabricated using aqueous electrolytes can provide a high power

density than organic ones. Meanwhile, the preparation of aqueous electrolyte is much

easier and requires no special equipment or tight purity control compared to that of the

organic one. However, the small voltage window of the aqueous electrolyte needs to be

noticed and many efforts have been made to improve it. From the literatures, up to 2.2

V voltage window has been achieved[38].

2.4.2 Organic electrolytes

As mentioned above, organic electrolytes have the strength of larger operating voltage

window compared to the aqueous ones, which could lead to a higher energy density.

On the other hand, there are also some drawbacks such as the high electric resistance,

low power and capacitances as well as complex production conditions. In addition,

they are very sensitive to the contamination, especially from moisture. Organic

electrolytes could operate at potentials up to 3.6 V and are the most widely used in

commercially available ECs[39].

2.4.3 Ionic electrolytes

As the electrolyte often used at high temperatures, ionic liquids have a high ionic conductivity, low vapor pressure, non-flammability, wide electrochemical window and high thermal stability. To achieve the good performance of energy storage, it requires a good chemical stability as well as a high ionic conductivity. Figure 2.6 shows some typical organic electrolytes and ionic liquids with enlarged voltage windows.
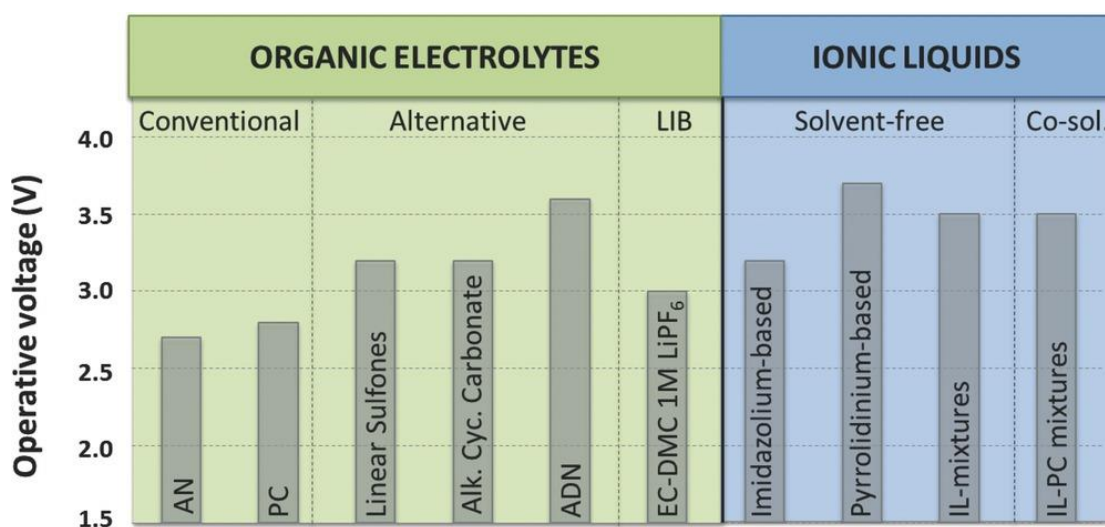
Figure 2.6 Comparison of the SCs operating voltage window achievable with organic and ionic electrolytes. AN (acetonitrile), PC (propylene carbonate), ADN (adiponitrile), Alkylat. Cyc. Carb. (alkylated cyclic carbonate), EC (ethylene carbonate), DMC (dimethyl carbonate), LiPF$_6$ (lithium hexafluorophosphate), IL (ionic liquids)[39].

2.5 References

1. Higgins, D., et al., *The application of graphene and its composites in oxygen reduction electrocatalysis: a perspective and review of recent progress.* Energy & Environmental Science, 2016. 9(2): p. 357-390.

2. Bao, L., J. Zang, and X. Li, *Flexible Zn2SnO4/MnO2 core/shell nanocable–carbon microfiber hybrid composites for high-performance supercapacitor electrodes.* Nano letters, 2011. 11(3): p. 1215-1220.

3. An, K.H., et al., *Electrochemical properties of high-power supercapacitors using single-walled carbon nanotube electrodes.* Advanced functional materials, 2001. 11(5): p. 387-392.

4. Simon, P. and Y. Gogotsi, *Materials for electrochemical capacitors.* Nature materials, 2008. 7(11): p. 845-854.

5. Ma, S.-B., et al., *A novel concept of hybrid capacitor based on manganese oxide materials.* Electrochemistry Communications, 2007. 9(12): p. 2807-2811.

6. Naguib, M., et al., *Two-dimensional nanocrystals produced by exfoliation of Ti3AlC2.* Advanced materials, 2011. 23(37): p. 4248-4253.

7. Tang, Q., Z. Zhou, and P. Shen, *Are MXenes promising anode materials for Li ion batteries? Computational studies on electronic properties and Li storage capability of Ti3C2 and Ti3C2X2 (X= F, OH) monolayer.* Journal of the American Chemical Society, 2012. 134(40): p. 16909-16916.

8. Zhao, M.Q., et al., *Flexible MXene/carbon nanotube composite paper with high volumetric capacitance.* Advanced materials, 2015. 27(2): p. 339-345.

9. Liang, W. and I. Zhitomirsky, *MXene–carbon nanotube composite electrodes for high active mass asymmetric supercapacitors.* Journal of Materials Chemistry A, 2021. 9(16): p. 10335-10344.

10. Ling, Z., et al., *Flexible and conductive MXene films and nanocomposites with high capacitance.* Proceedings of the National Academy of Sciences, 2014. 111(47): p. 16676-16681.

11. Le, T.A., et al., *Intertwined titanium carbide MXene within a 3 D Tangled polypyrrole nanowires matrix for enhanced supercapacitor performances.* Chemistry–A European Journal, 2019. 25(4): p. 1037-1043.

12. Lu, X., et al., *Hierarchical architecture of PANI@ TiO2/Ti3C2Tx ternary composite electrode for enhanced electrochemical performance.* Electrochimica Acta, 2017. 228: p. 282-289.

13. Jiang, H., et al., *A novel MnO2/Ti3C2Tx MXene nanocomposite as high performance electrode materials for flexible supercapacitors.* Electrochimica Acta, 2018. 290: p. 695-703.

14.   Hou, C. and H. Yu, *Zno/Ti3C2Tx monolayer electron transport layers with enhanced conductivity for highly efficient inverted polymer solar cells.* Chemical Engineering Journal, 2021. 407: p. 127192.

15.   Liang, W. and I. Zhitomirsky, *Composite Fe3O4-MXene-Carbon Nanotube Electrodes for Supercapacitors Prepared Using the New Colloidal Method.* Materials, 2021. 14(11): p. 2930.

16.   Aïssa, B., et al., *Transport properties of a highly conductive 2D Ti3C2Tx MXene/graphene composite.* Applied Physics Letters, 2016. 109(4): p. 043109.

17.   Shen, L., et al., *Carbon-intercalated Ti 3 C 2 T x MXene for high-performance electrochemical energy storage.* Journal of Materials Chemistry A, 2018. 6(46): p. 23513-23520.

18.   Chen, R., et al., *The Development of Pseudocapacitor Electrodes and Devices with High Active Mass Loading.* Advanced Energy Materials, 2020. 10(20): p. 1903848.

19.   Zeng, Y., et al., *Iron-based supercapacitor electrodes: advances and challenges.* Advanced Energy Materials, 2016. 6(24): p. 1601053.

20.   Chen, W., et al., *Hierarchical NiCo2O4@ Co-Fe LDH core-shell nanowire arrays for high-performance supercapacitor.* Applied Surface Science, 2018. 451: p. 280-288.

21.   Binitha, G., et al., *Electrospun α-Fe₂O₃ nanostructures for supercapacitor applications.* Journal of Materials Chemistry A, 2013. 1(38): p. 11698-11704.

22.   Wang, L., et al., *Preparation of Fe₃O₄ with high specific surface area and improved capacitance as a supercapacitor.* Nanoscale, 2013. 5(9): p. 3793-3799.

23.   Becker, H.I., *Low voltage electrolytic capacitor.* 1957, Google Patents.

24.   Callister Jr, W.D. and D.G. Rethwisch, *Fundamentals of materials science and engineering: an integrated approach.* 2012: John Wiley & Sons.

25.   Kötz, R. and M. Carlen, *Principles and applications of electrochemical capacitors.* Electrochimica acta, 2000. 45(15): p. 2483-2498.

26.   Zhang, Y., Feng, H., et al., *Progress of electrochemical capacitor electrode materials: A review.* International journal of hydrogen energy, 2009, *34*(11), p.4889-4899.

27.   Li, X. and B. Wei, *Supercapacitors based on nanostructured carbon.* Nano Energy, 2013. 2(2): p. 159-173.

28.   Honda, Y., et al., *Aligned MWCNT sheet electrodes prepared by transfer methodology providing high-power capacitor performance.* Electrochemical and Solid-State Letters, 2007. 10(4): p. A106-A110.

29.   Brownson, D.A., D.K. Kampouris, and C.E. Banks, *An overview of graphene in energy production and storage applications.* Journal of Power Sources, 2011. 196(11): p. 4873-4885.

30.   Miller, J.R., R. Outlaw, and B. Holloway, *Graphene double-layer capacitor with ac line-filtering performance.* Science, 2010. 329(5999): p. 1637-1639.

31.   Fang, B. and L. Binder, *Enhanced surface hydrophobisation for improved performance of carbon aerogel electrochemical capacitor.* Electrochimica acta, 2007. 52(24): p. 6916-6921.

32.   Liu, X.-M., et al., *Impedance of carbon aerogel/activated carbon composites as electrodes of electrochemical capacitors in aprotic electrolyte.* New Carbon Materials, 2007. 22(2): p. 153-158.

33.   Wang, H., et al., *From symmetric AC/AC to asymmetric AC/graphite, a progress in electrochemical capacitors.* Journal of power sources, 2007. 169(2): p. 375-380.

34.   Endo, M., et al., *Capacitance and pore-size distribution in aqueous and nonaqueous electrolytes using various activated carbon electrodes.* Journal of the Electrochemical Society, 2001. 148(8): p. A910-A914.

35.   Zhao, D.-D., et al., *Preparation of hexagonal nanoporous nickel hydroxide film and its application for electrochemical capacitor.* Electrochemistry communications, 2007. 9(5): p. 869-874.

36.   Zhi, M., et al., *Nanostructured carbon–metal oxide composite electrodes for supercapacitors: a review.* Nanoscale, 2013. 5(1): p. 72-88.

37.   Pal, B., et al., *Electrolyte selection for supercapacitive devices: A critical review.* Nanoscale Advances, 2019. 1(10): p. 3807-3835.

38.   Zhang, M., Y. Li, and Z. Shen, *"Water-in-salt" electrolyte enhanced high voltage aqueous supercapacitor with all-pseudocapacitive metal-oxide electrodes.* Journal of Power Sources, 2019. 414: p. 479-485.

39.   Béguin, F., et al., *Carbons and electrolytes for advanced supercapacitors.* Advanced materials, 2014. 26(14): p. 2219-2251.

Chapter 3 Objectives

As mentioned above, our main goal is to fabricate advanced composite electrodes and supercapacitor devices with high active mass loadings, high ratio of the active material mass to the current collector mass, high capacitance, good capacitance retention at high charge-discharge rates and low impedance.

Due to the relatively slow progress of anodes, we focused on the development of composite materials for negative electrodes based on different active materials, for example, MXene-based composites (Chapter 4, 5, 6 and 10), Fe-based composites (Chapter 7, 8 and 9) and new multifunctional materials (Chapter 11).

This was achieved by:

1) Development of efficient dispersants, new strategies and advanced colloidal techniques for improved dispersion of composites with individual components;

2) Fabrication of high electrochemical performance for composite electrodes with high mass loading as well as a high ratio of the active material mass to the current collector mass;

3) Investigation and optimization of individual levels of content in the composites by testing electrochemical performance of each electrode;

4) Fabrication advanced supercapacitor device with enhanced performance.

Chapter 4 MXene–carbon nanotube composite electrodes for high active mass asymmetric supercapacitors

W Liang* and I. Zhitomirsky*[α]

*Department of Materials Science and Engineering, McMaster University,

Hamilton, Ontario, L8S 4L7, Canada

[α]Corresponding Author: zhitom@mcmaster.ca; 905-525-9140 ext. 23914

4.1 Abstract

This article describes for the first time the fabrication of an asymmetric device, which is based on negative $Ti_3C_2T_x$ (MXene)–multiwalled carbon nanotube (MCNT) electrodes and positive polypyrrole (PPy) coated MCNT electrodes. The approach involves the feasibility studies of new strategies for achieving enhanced electrochemical performance of high active mass (AM) MXene electrodes. Good material performance at high AM of 35 mg cm^{-2} is linked to the application of multifunctional chelating dispersants for co-dispersion of $Ti_3C_2T_x$ and MCNT and advanced water insoluble hydrophilic binders. The experimental results reveal the effect of the chemical structure of the dispersants and binders on electrode performance. Another important finding is the ability of achieving high capacitance of PPy-coated MCNT positive electrodes in a complementary potential range. The analysis of cyclic voltammetry data in Na_2SO_4 electrolyte for $Ti_3C_2T_x$–MCNT electrodes shows areal capacitance of 1.93 F cm^{-2} which is substantially higher than literature results for pure $Ti_3C_2T_x$ and $Ti_3C_2T_x$ composites. Moreover, high capacitance is obtained at much lower electrical resistance. Especially important is the possibility of achieving higher capacitance equal to 0.94 F cm^{-2} for the asymmetric supercapacitor in 0–1.6 V window, compared to literature data for symmetric supercapacitors with significantly lower capacitances in smaller voltage windows.

4.2 Introduction

Various MXenes, such as carbides, carbonitrides and nitrides are under investigation

for applications in supercapacitors.[1–3] It has been widely reported that $Ti_3C_2T_x$ is a

promising MXene-type material[4,5] for supercapacitors and devices for capacitive

water deionization. $Ti_3C_2T_x$ offers benefits of high surface area, good electrical

conductivity and high capacitance.[5] The capacitive properties of $Ti_3C_2T_x$ are governed

by its unique microstructure as well as by the nature of surface functional groups of

this material, which contribute to its pseudocapacitive behavior.[6]

Many studies analyzed $Ti_3C_2T_x$ composites with TiO_2,[7]

$NiCo_2S_4$,[8] $Cu_{0.5}Co_{0.5}Se_2$,[9] Co_3O_4,[10] Mn_3O_4,[11] CuS,[12] MnO_2,[13] ZnO,[14] polypyrrole,[15,16]

polyaniline[17] and other capacitive materials.[18–21] The total capacitance of the

electrodes included contributions of different charging mechanisms of the individual

materials.[19] It was found that the synergy of different mechanisms can result in a

higher capacitance of the composite materials, compared to the capacitances of the

individual components.[22,23] Enhanced electrochemical performance has also been

achieved in nitrogen-doped $Ti_3C_2T_x$ due to the improved conductivity and redox-

active behavior of the nitrogen-containing functional groups.[24–26] $Ti_3C_2T_x$ materials

were combined with carbon black,[27] acetylene black,[28] and graphene[29] for the

fabrication of composites with enhanced electrical conductivity. Many studies

reported good cycling stability of the $Ti_3C_2T_x$-based composites.[30–35] Investigations

focused on the development of $Ti_3C_2T_x$-based composite electrodes[6,7,18,26,30,36–42] with

AM of 1–8 mg cm^{-2} and relatively high gravimetric capacitances (C_m, F g^{-1}) have

been reported. The areal capacitances (C_S, F cm^{-2}) of the electrodes were

typically[43,44] 0.2–1 F cm^{-2}.

Capacitive behavior of $Ti_3C_2T_x$ based electrodes was analyzed in different

electrolytes, such as KOH,[7,45] H_2SO_4,[15,16,41] HCl,[17] KCl,[46] Li_2SO_4,[47] Na_2SO_4,[47] and

K_2SO_4[47] and other electrolytes.[48,49] The electrodes were applied for the design of

symmetric supercapacitors with a voltage window[16,26,50,51] of 0.4–1.2 V. Larger

voltage windows can be achieved in asymmetric aqueous devices, containing two

different electrodes operating in different potential ranges in the same electrolyte. The

individual electrodes of the asymmetric supercapacitors must contain different charge

storage materials with different charging mechanisms in complementary potential

ranges. The enlarged voltage window of supercapacitor devices offers benefits of

higher energy density and higher power density.

Recent studies[52] highlighted the need in the development of supercapacitor electrodes

with high AM loadings and low ratio of current collector mass to the AM mass.

Further advances in the development of $Ti_3C_2T_x$-based supercapacitors can be

achieved by the fabrication of efficient electrodes with high AM for operation in

aqueous Na_2SO_4, which is a promising electrolyte for the design of aqueous

asymmetric supercapacitors with larger voltage windows. However, many

investigations of $Ti_3C_2T_x$-based materials in Na_2SO_4 electrolyte were based on the use

of electrodes with relatively low AM[47,53,54] in the range of 1–3 mg cm^{-2}. The

high C_m achieved at low AM loading indicates that good utilization of active material

at higher AM loading can potentially result in high C_S. However, it is challenging[52] to

achieve high C_S owing to the electrolyte diffusion limitations and reduced electrical

conductivity at high AM. The increase in AM to the level of 20 mg cm^{-2} allowed the

design of electrodes[55] with C_S of 1.087 F cm^{-2} for the galvanostatic charging at 1 mA

cm^{-2} and 0.783 F cm^{-2} at potential sweep conditions of 1 mV s^{-1}. Such

electrodes[55] facilitated the design of advanced symmetric $Ti_3C_2T_x$ supercapacitors.

The goal of this work was the manufacturing of composite $Ti_3C_2T_x$–MCNT electrodes

for applications in asymmetric supercapacitors. We prepared electrodes with high AM

of 35 mg cm^{-2} for operation in aqueous Na_2SO_4 electrolyte. This article reports

advanced colloidal fabrication strategies, which allowed for a high C_S of 1.93 F

cm^{-2} for $Ti_3C_2T_x$–MCNT electrodes. It was demonstrated that the use of chelating co-

dispersants for $Ti_3C_2T_x$ and MCNT was a key factor for the fabrication of advanced

electrodes. It is important to note, that polymer binders have relatively low density,

compared to that of inorganic materials. Therefore, a small mass content of a binder

added to the composite material results in a large volume content of the binder, which

limits ion access to the active material, especially in the case of high AM. Therefore,

special attention was focused on the binder selection and optimization of binder

content in the composite electrodes. Good electrochemical capacitive behavior of the

electrodes was linked to the beneficial effects of selected binders and dispersants. The

analysis of capacitive properties of the electrodes prepared using different dispersants

and binders gives an insight into the effect of the structure and properties of the

dispersant and binder materials on the electrode performance. With a desire to

increase the voltage window, we combined negative $Ti_3C_2T_x$–MCNT electrodes with

positive polypyrrole (PPy) coated MCNT electrodes in aqueous Na_2SO_4 for the

preparation of asymmetric supercapacitors. Good capacitive performance of the

individual electrodes in complementary voltage windows in aqueous Na_2SO_4 allowed

good device performance in the 0–1.6 V voltage window and C_S of 0.94 F cm^{-2} for

the device was obtained.

4.3 Experimental procedures

Anionic catechol violet (ACV) and cationic celestine blue (CCB) dispersants,

Na_2SO_4, poly (ethyl methacrylate) (PEMA, 515 kDa) and a co-polymer of vinyl

butyral, vinyl acetate and vinyl alcohol (PVBAA, 65 kDa) were purchased from

MilliporeSigma. The diameter and length of MCNT (Bayer Corp.) were 13 nm and 1–

2 μm, respectively. $Ti_3C_2T_x$ was supplied by Laizhou Kai Kai Ceramic Materials Co.,

Ltd., China.

Commercial Ni foam current collectors (95% porosity, Vale) were impregnated using slurries of pure $Ti_3C_2T_x$ or $Ti_3C_2T_x$–MCNT in isopropanol–water (85% isopropanol) or ethanol, containing PEMA or PVBAA binders. The use of highly porous Ni foam offered many benefits, such as light weight and possibility of formation of 3D porous conductive electrodes with high active mass loading and reduced content of non-conductive polymer binders. Electrodes were prepared with different MCNT : $Ti_3C_2T_x$ mass ratios, such as 1 : 9, 2 : 8, 3 : 7. The binder mass was 3% of the $Ti_3C_2T_x$ and MCNT total mass. The total AM of impregnated material was 35 mg cm^{-2}. ACV and CCB were used as co-dispersants for $Ti_3C_2T_x$ and MCNT. PPy coated MCNT were prepared as described in a previous investigation[56] and used for the fabrication of electrodes with AM = 35 mg cm^{-2}. $Ti_3C_2T_x$–MCNT anodes and PPy-coated MCNT cathodes were combined for the design of asymmetric supercapacitor cells. The mass of the individual electrodes was 35 mg cm^{-2}. The electrodes were separated by a porous polymer membrane. Pouch electrochemical cells were prepared, which contained 0.5 M Na_2SO_4 electrolyte.

Electrochemical impedance spectroscopy (EIS) and cyclic voltammetry (CV) investigations were conducted using a potentiostat (AMETEK 2273). Galvanostatic charge discharge (GCD) was performed by Biologic AMP 300. The capacitive behavior of the electrodes was tested in an aqueous 0.5 M Na_2SO_4 solution. High surface area Pt gauze was utilized as a counter electrode, and a saturated calomel

electrode (SCE) was used as a reference. The area of the working electrode was 1

cm^2. Capacitances C_S and C_m were obtained from the CV or GCD data, and

complex Cs* components (Cs' and Cs'') were calculated from the EIS testing results

obtained at AC signal of 5 mV, as it was described in a previous

investigation.[52] JEOL JSM-7000F microscope was used for SEM investigations.

4.4 Results and discussion

Fig. 4.1 presents SEM images for a commercial $Ti_3C_2T_x$ material used in this

investigation. The SEM image shows an open-layered structure, which facilitates ion

access to the AM for redox reactions. The structure contains chemically bonded layers.
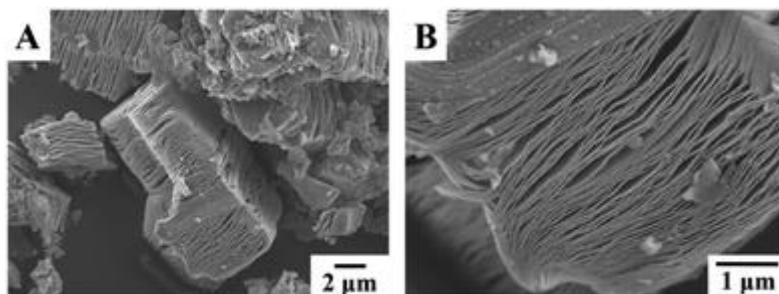
Fig. 4.1 SEM images at different magnification for as-received $Ti_3C_2T_x$.

In this investigation, commercial Ni foams were used as current collectors. Slurries of

$Ti_3C_2T_x$ and MCNT were prepared for impregnation of the current collectors. MCNT

created additional conductive network inside the Ni foam. The development of a

slurry of well dispersed particles for the impregnation of the foam is one of the critical

steps in the fabrication of advanced high AM electrodes. An important challenge in

the slurry development is mixing and co-dispersion of $Ti_3C_2T_x$ and MCNT. It was

found that two polyaromatic dispersants, containing catechol groups provided

efficient dispersion of $Ti_3C_2T_x$ and MCNT.

Fig. 4.2A and B shows chemical structures of cationic celestine blue (CCB) and

anionic catechol violet (ACV) dispersants used in this study. The polyaromatic

structures of the dispersants were beneficial for their adsorption on MCNT by the π–π

interaction mechanism.[57,58] It was suggested that catechol ligands of the molecules

facilitated their adsorption on $Ti_3C_2T_x$. It is known[59] that various catechol molecules

show strong adsorption on TiO_2 and other materials and allow for their efficient

dispersion. The adsorption mechanisms involved bridging or chelating bonding of the

catechol groups to the Ti atoms. Therefore, similar mechanisms can be proposed for

the dispersants bonding to the $Ti_3C_2T_x$ surface (Fig. 4.2C and D). Electric charges of

CCB and ACV facilitated electrostatic dispersion of $Ti_3C_2T_x$ and MCNT. The ability

to co-disperse $Ti_3C_2T_x$ and MCNT using CCB or ACV was beneficial for the

fabrication of the composites.
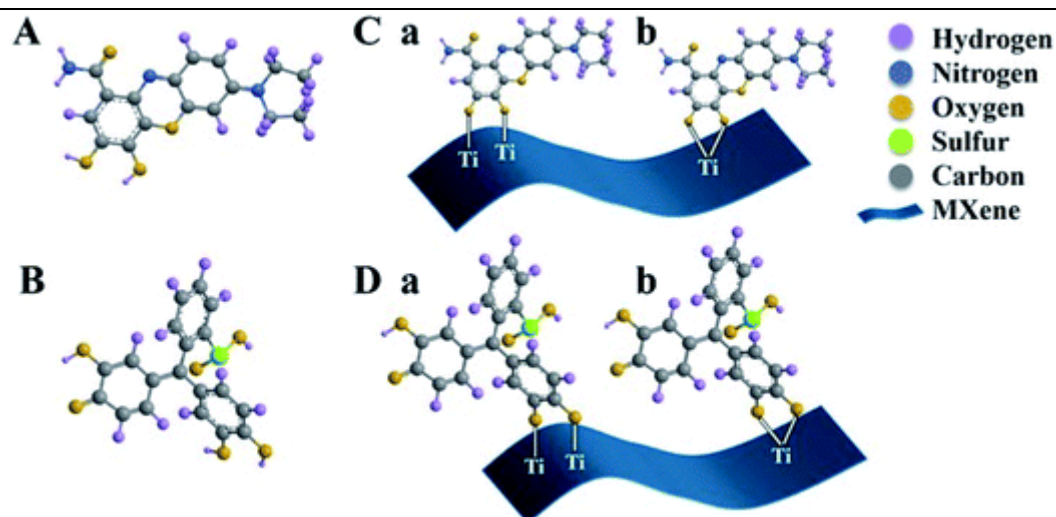
Fig. 4.2 (A and B) Structures of (A) CCB and (B) ACV; (C and D) adsorption of (C) CCB and (D) ACV on $Ti_3C_2T_x$: (a) bidentate bridging and (b) chelating bonding of Ti atoms on the material surface.

Binder is an important component of the supercapacitor electrodes. However, insufficient attention has been paid in the literature to the selection of binder materials. In previous investigations[27,28] polytetrafluoroethylene (PTFE) powder was used as a binder. The composite powders, containing $Ti_3C_2T_x$, conductive additives and PTFE were pressed in order to achieve binding. The PTFE mass content[27,28,60] in the composite electrodes was 5–10%. In other investigations[12,36,45,46,48] polyvinylidene fluoride (PVDF) polymer was used as a binder for the preparation of $Ti_3C_2T_x$-based electrodes with a PVDF mass content of 5–15%. The large volume content of a polymer results in poor ionic and electronic conductivities of the composite. Moreover, hydrophobic binders, such as PTFE, limit diffusion of aqueous electrolytes in pores of a bulk electrode. Therefore, the selection of a binder material and optimization of its content is important for the development of supercapacitors with high AM. It is in this regard that even in

some technologies, such as tape casting, where relatively large binder content is required for the fabrication of green tapes, the critical limit for the binder content is below 5 mass%. It is obvious that the binder content in the composite electrode material must be minimized. Therefore, it is important to avoid the use of binders, such as PTFE, in a solid form. A polymer binder must be dissolved in a non-toxic solvent to improve binder contact with particle surface. Another important factor is binder–particle interactions, which facilitate binder adsorption on functional inorganic materials. In this investigation, we used PEMA and PVBAA binders for the fabrication of supercapacitor electrodes. PEMA is a promising binder material due to its good mechanical properties, chemical stability and adsorption on inorganic particles.[61] The chemical structure of PEMA includes hydrophilic carbonyl groups, which play an important role in its adsorption on inorganic surfaces. PEMA is soluble in toxic solvents such as toluene and tetrahydrofuran, but it is insoluble in water and isopropanol. However, we found that PEMA is well soluble in a water–isopropanol mixture (85% isopropanol). Therefore, the use of toxic solvents can be avoided. The use of high molecular mass binders is critically important for practical applications. Organic polymers with molecular mass below 10–20 kDa show poor binding properties. In this investigation we used advanced PEMA binder with molecular mass of 515 kDa in a mixed isopropanol–water solvent (85% isopropanol). PVBAA is regarded as a water insoluble polymer. Therefore, ethanol slurries, containing dissolved PVBAA (65 kDa) were used. The chemical

structure of PVBAA contains hydrophilic vinyl alcohol monomers, which facilitate its adsorption on inorganic particles.

The hydrophilic carbonyl groups of PEMA and hydrophilic vinyl alcohol monomers of PVBAA make such polymers more hydrophilic, compared to PTFE and other polymer binders. It was suggested that such properties of PEMA and PVBAA offer benefits for their application in supercapacitors, based on aqueous electrolytes.

Fig. 4.3 shows CVs for pure $Ti_3C_2T_x$ and composite $Ti_3C_2T_x$–MCNT electrodes, containing different amounts of MCNT and PEMA as a binder. The electrodes showed rectangular CVs in the −0.3 to −1.1 V potential range.
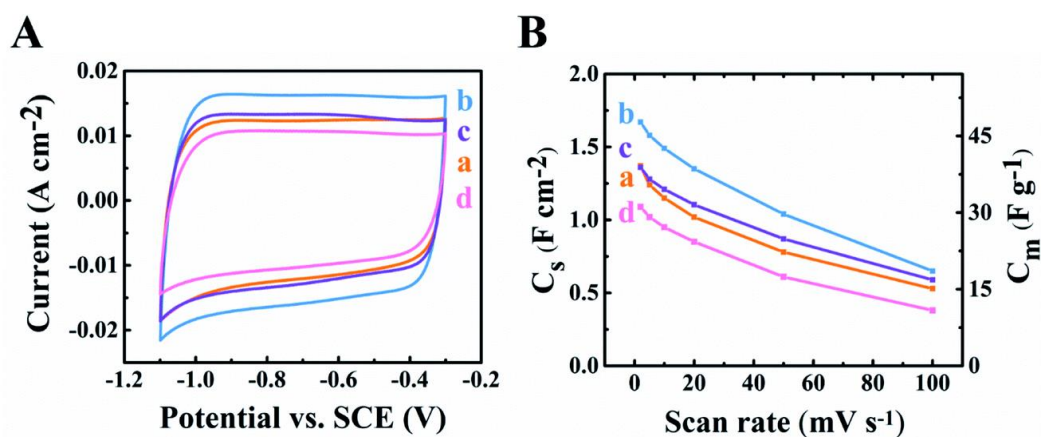
Fig. 4.3 (A) CVs at 10 mV s−1 and (B) capacitance dependences on a sweep rate for (a) $Ti_3C_2T_x$ (b) 90% $Ti_3C_2T_x$–10% MCNT, (c) 80% $Ti_3C_2T_x$–20% MCNT and (d) 70% $Ti_3C_2T_x$–30% MCNT electrodes with PEMA binder.

The electrodes showed capacitances of 1.37, 1.67, 1.36 and 1.08 F cm^{-2} for $Ti_3C_2T_x$, 90% $Ti_3C_2T_x$–10% MCNT, 80% $Ti_3C_2T_x$–20% MCNT and 70% $Ti_3C_2T_x$–30% MCNT electrodes, respectively, at 2 mV s^{-1}. The 90% $Ti_3C_2T_x$–10% MCNT electrodes showed

the highest capacitance. Moreover, the analysis of EIS data (Fig. 4.4A) indicated that

90% Ti$_3$C$_2$T$_x$–10% MCNT electrodes showed the lowest resistance $R = Z'$ and the

highest Cs' (Fig. 4.4B) at low frequencies. It was found that Cs, obtained from CVs

decreased with increasing sweep rate (Fig. 4.3B), whereas the Cs', obtained from EIS,

decreased with frequency (Fig. 4.4B) due to electrolyte diffusion limitations. The

imaginary components of AC capacitance Cs'' showed relaxation maxima (Fig. 4.4C).
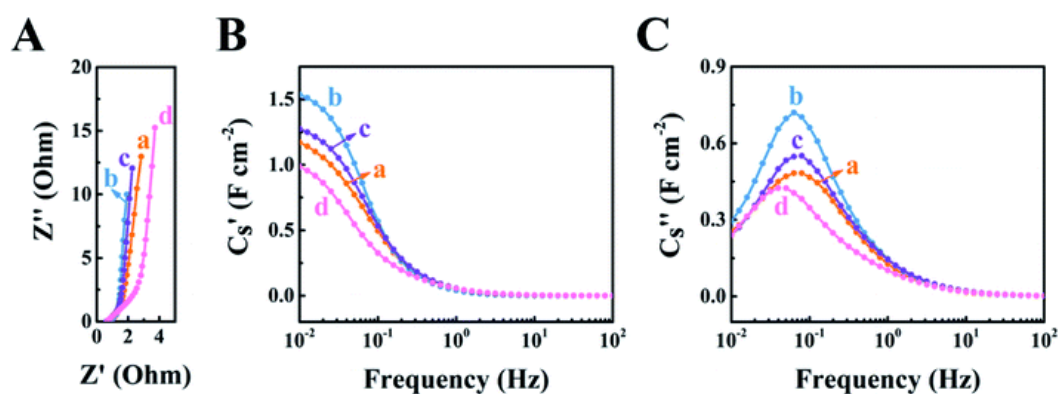
Fig. 4.4 (A) Impedance presentation in a Nyquist graph, (B and C) components of C*=Cs'-iCs'' as functions of frequency for (a) Ti$_3$C$_2$T$_x$, (b) 90% Ti$_3$C$_2$T$_x$–10% MCNT, (c) 80% Ti$_3$C$_2$T$_x$–20% MCNT and (d) 70% Ti$_3$C$_2$T$_x$–30% MCNT electrodes with PEMA binder.

The analysis of GCD behavior (Fig. 4.5A–D) of the electrodes with PEMA binder

showed nearly linear GCD curves at 3–35 mA cm^{-2}. The longest charge–discharge

times were observed for 90% Ti$_3$C$_2$T$_x$–10% MCNT due to higher capacitance of this

composite electrode. Fig. 4.5E shows capacitances, obtained from the GCD data. The

highest GCD capacitances were obtained for 90% Ti$_3$C$_2$T$_x$–10% MCNT

electrodes, Cs decreased from 1.92 to 1.31 F cm^{-2} with current density increase. The

experimental data indicated beneficial effect of MCNT and the content of MCNT was

optimized at a level of 10%. The obtained C_S were higher than C_S reported in literature

for pure $Ti_3C_2T_x$ and composite electrodes, described in Introduction.
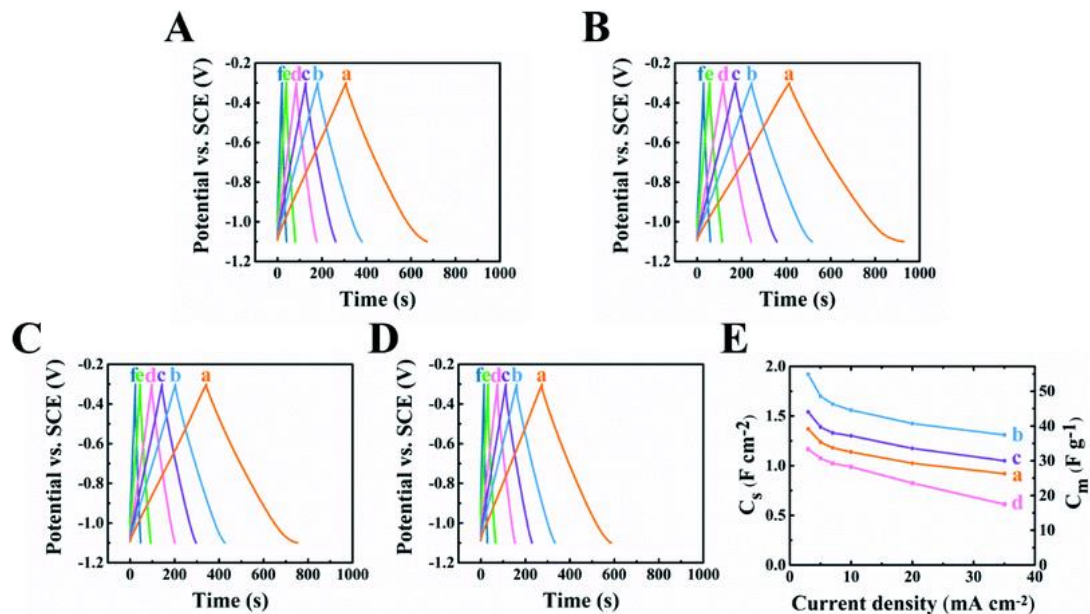
Fig. 4.5 (A–D) GCD data for (A) $Ti_3C_2T_x$, (B) 90% $Ti_3C_2T_x$–10% MCNT, (C) 80% $Ti_3C_2T_x$–20% MCNT, and (D) 70% $Ti_3C_2T_x$–30% MCNT electrodes with PEMA binder at (a) 3, (b) 5, (c) 7, (d) 10, (e) 20, and (f) 35 mA cm^{-2}, (E) capacitances versus current density, obtained from GCD for (a) $Ti_3C_2T_x$, (b) 90% $Ti_3C_2T_x$–10% MCNT, (c) 80% $Ti_3C_2T_x$–20% MCNT, and (d) 70% $Ti_3C_2T_x$–30% MCNT electrodes

CCB and ACV dispersants addressed the need for improved co-dispersion and mixing

of $Ti_3C_2T_x$ and MCNT. Both dispersants showed good dispersion of $Ti_3C_2T_x$ and

MCNT. Fig. 4.6A shows CV for 90% $Ti_3C_2T_x$–10% MCNT electrodes prepared using

ACV or CCB dispersants and PEMA or PVBAA binders.
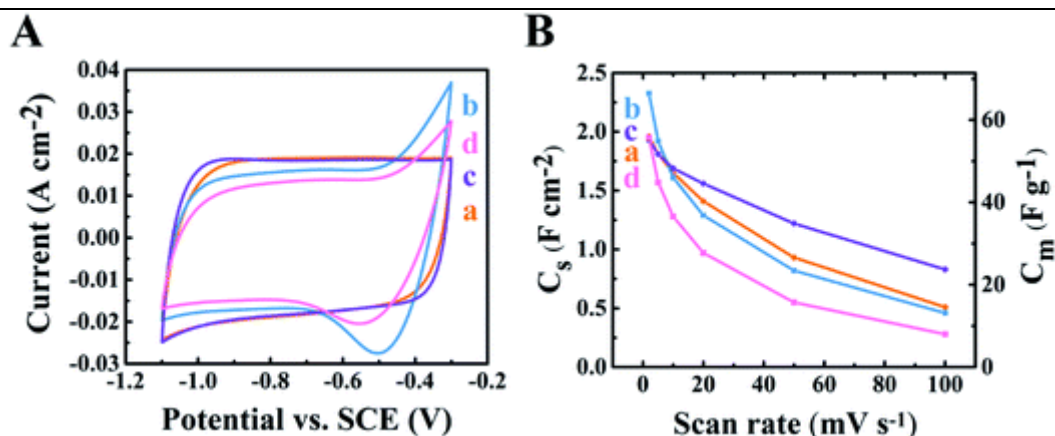
Fig. 4.6 (A) CVs at 10 mV s^{-1} and (B) capacitances at different sweep rates for 90% Ti$_3$C$_2$T$_x$–10% MCNT electrodes prepared using (a) ACV dispersant and PEMA binder, (b) CCB dispersant and PEMA binder, (c) ACV dispersant and PVBAA binder, and (d) CCB dispersant and PVBAA binder.

The electrodes, prepared using ACV dispersant showed nearly ideal rectangular shape CVs, whereas electrodes prepared using CCB showed redox peaks at potentials of −0.3 to −0.6 V (Fig. 4.6). The redox peaks can be attributed to the redox reactions[62] of the adsorbed CCB dispersant. The box-shape CVs obtained using ACV indicate good pseudocapacitive behavior. It should be noted that redox activity of ACV is related to oxidation of phenolic OH groups in the positive potential range. Therefore, the electrodes prepared using ACV did not show redox peaks in the negative potential range of −1.1 to −0.3 V. Such electrodes, containing PEMA and PVBAA binders showed capacitances of 1.96 and 1.93 F cm^{-2}, respectively, which were obtained at 2 mV s^{-1}. The composite electrodes have improved C$_S$, compared to the electrodes obtained without ACV or CCB (Fig. 4.3). The highest capacitances at different sweep rates were obtained using a PVBAA binder. The results of EIS studies (Fig. 4.7) showed that electrodes prepared using ACV dispersant have lower electrical resistance, represented

by the real part of the complex impedance. The electrodes prepared using ACV

dispersant and PVBAA binder showed the lowest resistance, highest real part of

capacitance and the highest relaxation frequency, related to the Cs'' maximum. The

highest relaxation frequency indicates improved capacitive behavior in agreement with

CV data at high sweep rates for this electrode.
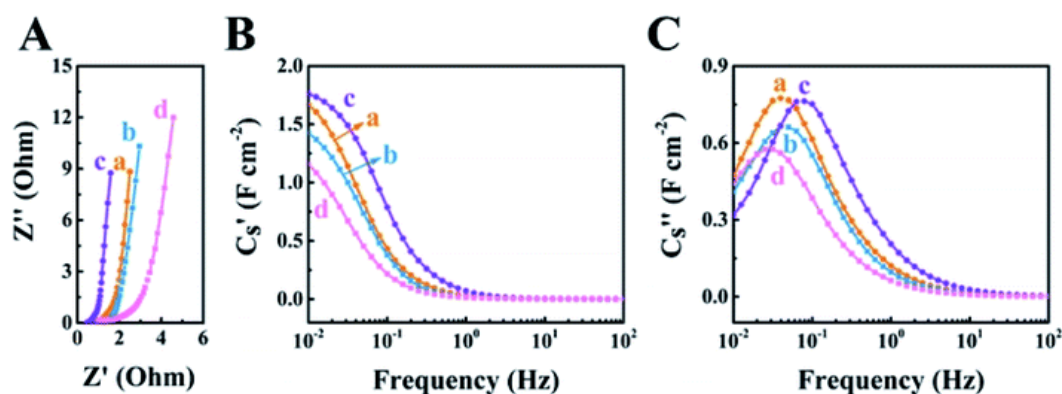
Fig. 4.7 (A) Nyquist EIS graph, (B) Cs' and (C) Cs'' as functions of AC frequency for
90% $Ti_3C_2T_x$–10% MCNT electrodes prepared using (a) ACV dispersant and PEMA
binder, (b) CCB dispersant and PEMA binder, (c) ACV dispersant and PVBAA binder,
and (d) CCB dispersant and PVBAA binder.

Fig. 4.8 shows GCD data for the 90% $Ti_3C_2T_x$–10% MCNT electrodes, prepared using

ACV or CCB dispersants and PEMA or PVBAA binders. The electrodes prepared using

ACV dispersant showed nearly linear charge–discharge behavior. The shapes of the

curves were essentially non-linear for electrodes prepared using CCB. Best

performance was achieved using ACV dispersant and PVBAA binder. The capacitance

of such electrodes decreased from 2.56 to 2.23 F cm^{-2} with GCD current density

increase.

37
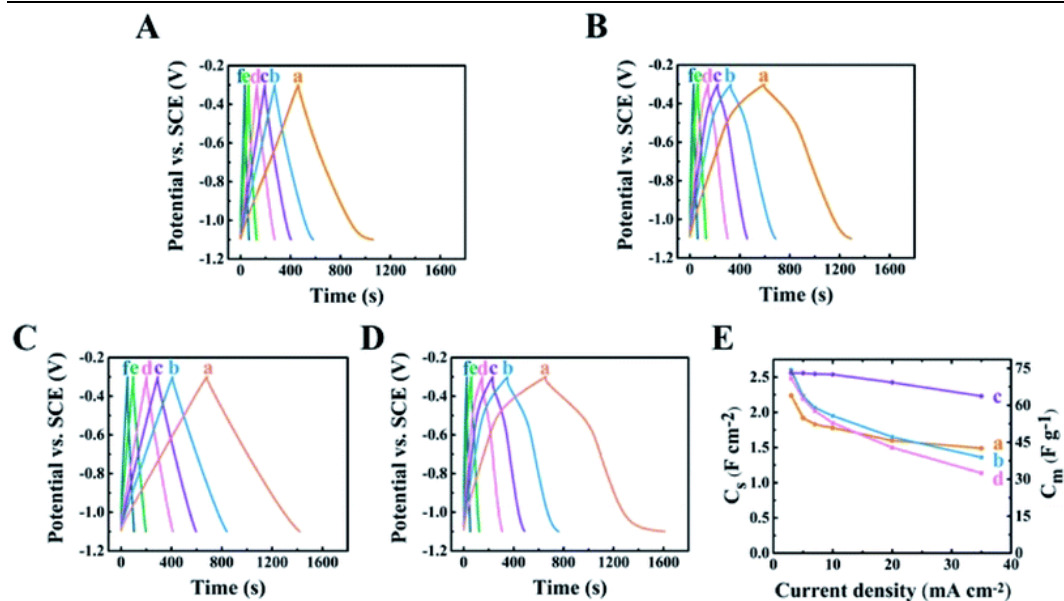
Fig. 4.8 (A–D) GCD data for 90% $Ti_3C_2T_x$–10% MCNT electrodes prepared using (A) ACV dispersant and PEMA binder, (B) CCB dispersant and PEMA binder, (C) ACV dispersant and PVBAA binder, and (D) CCB dispersant and PVBAA binder at (a) 3, (b) 5, (c) 7, (d) 10, (e) 20, and (f) 35 mA cm^{-2} and (E) capacitances calculated from the GCD data for electrodes formed using (a) ACV dispersant and PEMA binder, (b) CCB dispersant and PEMA binder, (c) ACV dispersant and PVBAA binder, and (d) CCB dispersant and PVBAA binder.

Testing results indicated that 90% $Ti_3C_2T_x$–10% MCNT electrodes prepared using ACV dispersant and PVBAA binder showed best performance at potentials of −1.1 to −0.3 V. Such electrodes were used as anodes for asymmetric cells.

The development of asymmetric cells requires the use of electrodes, which exhibit comparable C_S in the same electrolyte in complementary potential windows. Recent review[52] of high active mass supercapacitor electrodes with high C_S indicates that various materials, such as MnO_2, Mn_3O_4, V_2O_3 and PPy composites can be used for positive electrodes in the Na_2SO_4 electrolyte. It was found[52] that MnO_2, Mn_3O_4 and V_2O_3 based electrodes show good performance in potential range 0–0.9 V versus SCE.

However the performance of such electrodes in the negative potential range is poor due to their low capacitance, high impedance and poor cyclic stability. Therefore, PPy coated MCNT were used as positive electrodes in a complementary voltage window. In a previous investigation,[56] PPy-MCNT composites were analyzed at potentials of −0.5 to +0.4 V. In this research, the PPy-MCNT electrodes were analyzed in a potential window of −0.3 to +0.6 V vs. SCE. CV and GCD data showed nearly box shape current–potential and nearly triangular shape potential–current dependences, respectively (Fig. 4.9). The C_S values of 2.92 and 2.56 F cm^{-2}, were obtained at 2 mV s^{-1} from the CV data, and at 3 mA cm^{-2} from the GCD data, respectively.
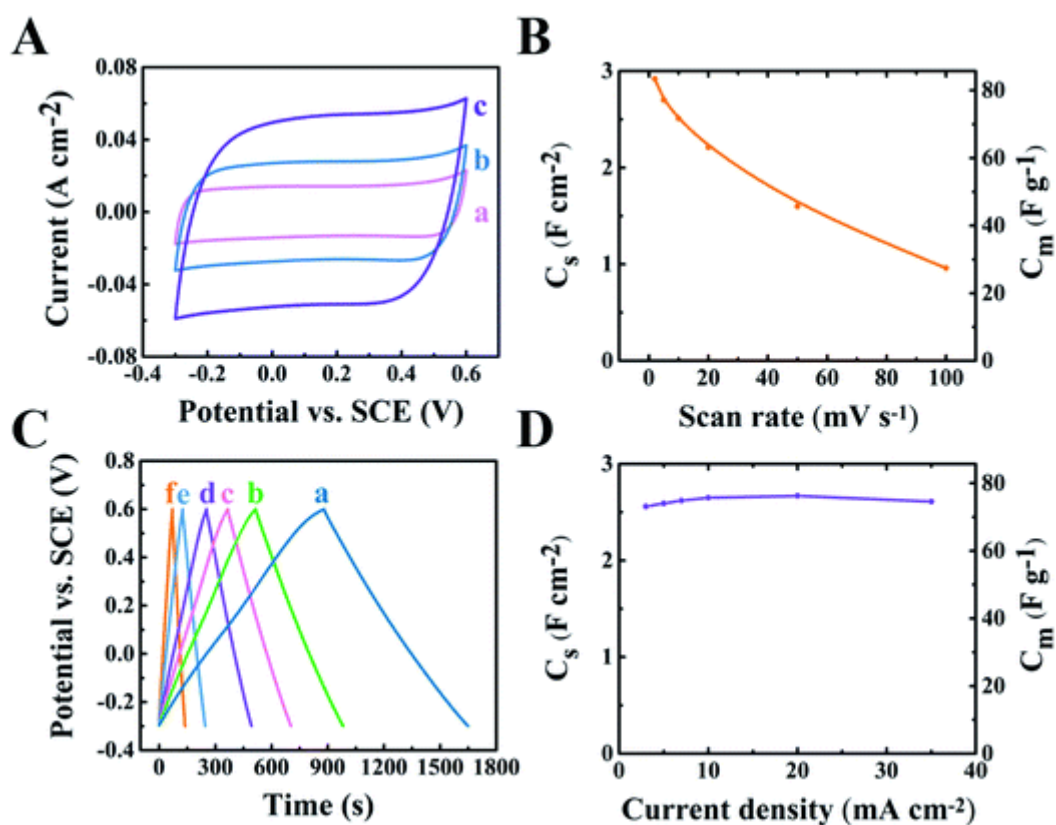
Fig. 4.9 (A) CVs at (a) 5, (b) 10, (c) 20 mV s^{-1}, (B) capacitances obtained from CVs, (C) GCD data at (a) 3, (b) 5, (c) 7, (d) 10, (e) 20, and (f) 35 mA cm^{-2} and (D) capacitances obtained from GCD for PPy coated MCNT electrodes.

The PPy coated MCNT electrodes showed relatively low electrical resistance, which is represented by a real part of the complex impedance in the Nyquist plot (Fig. 4.10A). The calculated Cs' at a frequency of 10 mHz was 2.17 F cm^{-2}. Observed Cs' reduction with frequency correlated with the relaxation maximum of Cs'' (Fig. 4.10B and C).
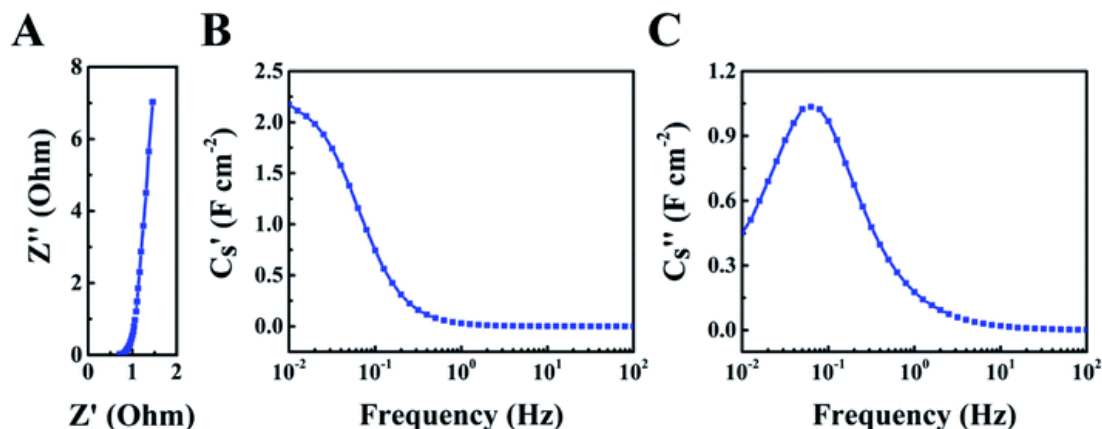
Fig. 4.10 (A) Nyquist EIS graph, (B) Cs' and (C) Cs'' as functions of AC frequency for PPy coated MCNT electrodes.

Good capacitive behavior of 90% Ti$_3$C$_2$T$_x$–10% MCNT electrodes in a potential window of −1.1 to −0.3 V and PPy-MCNT electrodes in a potential window −0.3 to +0.6 V indicates that such electrodes can be used as anodes and cathodes, respectively, for the development of asymmetric supercapacitors with enlarged voltage range. The box shape CVs of the individual electrodes were key factors for obtaining box shape CVs for the asymmetric device for voltages of 0–1.6 V (Fig. 4.11A). The CVs obtained for voltages of 0–1.8 V (Fig. 4.11B) were tilted. However, the asymmetric device showed comparable capacitances for both voltage windows (Fig. 4.11C). GCD data (Fig. 4.11D) represented triangular-shape curves for voltages of 0–1.6 V. However, the discharge curves for voltages of 0–1.8 V showed voltage reduction at the beginning of

the discharge (Fig. 4.11E) and the GCD curves were asymmetrical. The electrodes

showed comparable capacitances for voltages of 0–1.6 and 0–1.8 V (Fig. 4.11F). The

analysis of CV and GCD data indicated that device showed better performance at

voltages of 0–1.6 V.
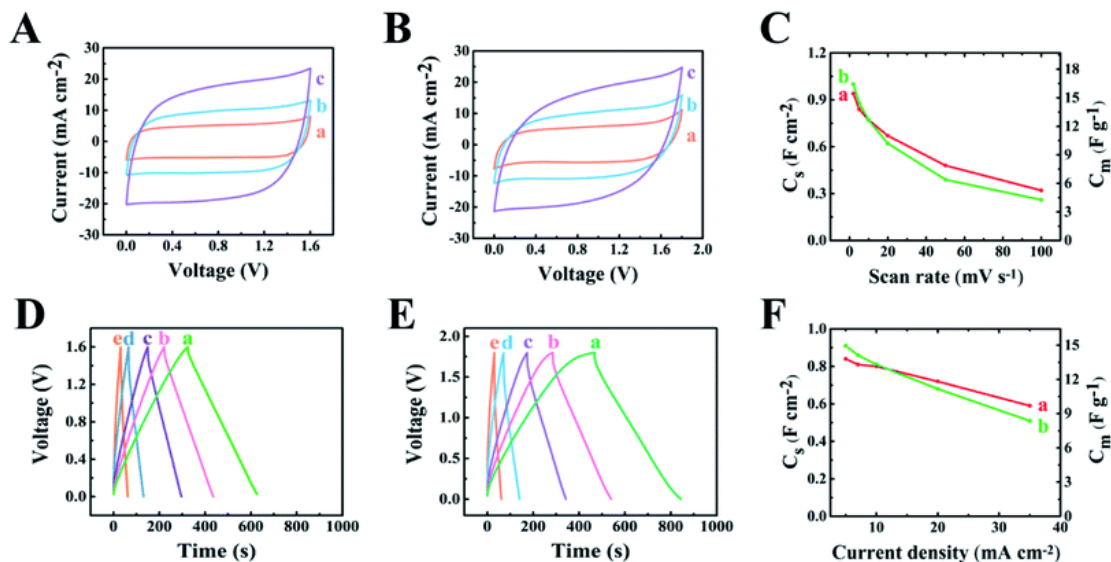
Fig. 4.11 (A and B) CVs in windows of (A) 0–1.6 V and (B) 0–1.8 V at (a) 5, (b) 10, and (c) 20 mV s^{-1}, (C) capacitances obtained from the CVs in windows (a) 0–1.6 V and (b) 0–1.8 V, (D and E) GCD data in windows of (D) 0–1.6 V and (E) 0–1.8 V at current densities of (a) 5, (b) 7, (c) 10, (d) 20, and (e) 35 mA cm^{-2}, (F) capacitances obtained from the GCD in windows (a) 0–1.6 V and (b) 0–1.8 V.

The capacitances C$_S$, obtained from the CVs at 2 mV s^{-1} and GCD at 5 mA cm^{-2} for

voltages of 0–1.6 V were 0.94 and 0.84 F cm^{-2}, respectively. The total resistance of

the device included contributions of both electrodes, and electrolyte in pores of a

membrane (Fig. 4.12A). The Cs' value of 0.71 F cm^{-2} was obtained at 10 mHz (Fig.

4.12B). The Cs'' maximum shifted to lower frequency, compared to individual

electrodes due to larger electrical resistance of the device (Fig. 4.12C).
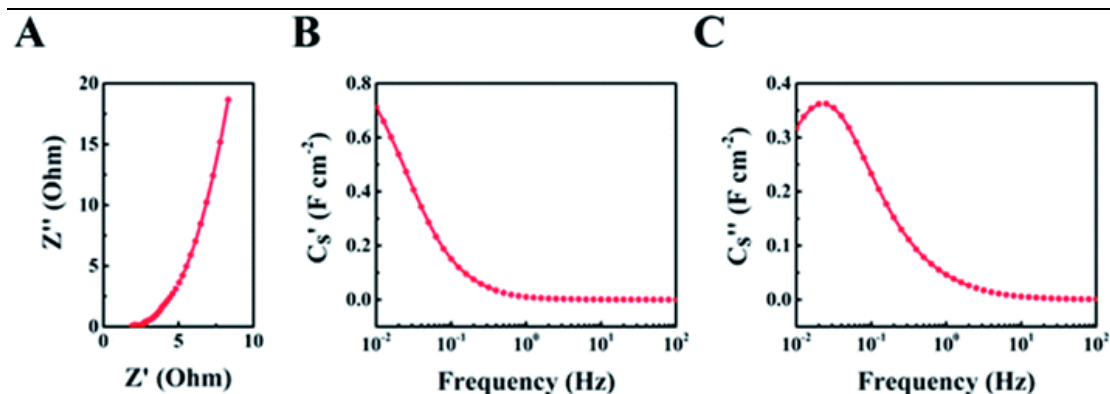
Fig. 4.12 (A) Nyquist EIS graph, (B) Cs' and (C) Cs'' as functions of AC frequency for an asymmetric cell.

Cycling of the cells in the windows of 0–1.6 V and 0–1.8 V showed capacitance retentions of 94 and 72%, respectively (Fig. 4.13). Therefore, the analysis of cyclic behavior (Fig. 4.13) coupled with the analysis of CV and GCD data (Fig. 4.11) indicated that for the improved device performance, the operation voltage window must be limited to 1.6 V. The cyclic behavior of cells depends on different factors, such as cyclic behavior of individual electrodes, stability of membrane and electrolyte. For practical applications such factors must be investigated, and long-term cyclic stability of the devices must be tested at least for 750 000 cycles at periodic cycling and voltage hold conditions.
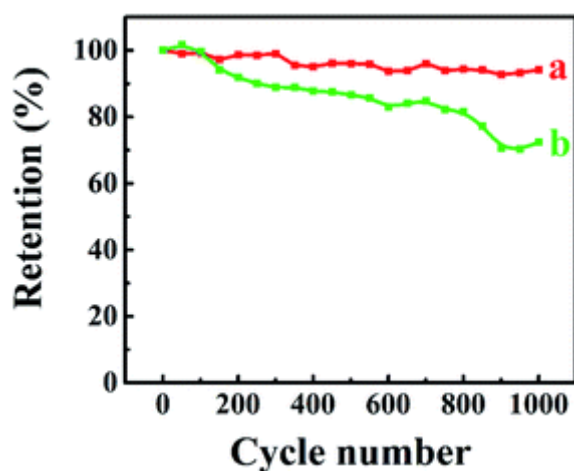
Fig. 4.13 Capacitance retention for an asymmetric cell obtained from CVs in voltage windows (a) 0–1.6 V and (b) 0–1.8 V.

The C_S values obtained by different methods for electrodes and devices depend on scan rate, current density and applied potential or voltage. However, the C_S values for 90% $Ti_3C_2T_x$–10% MCNT electrodes in Na_2SO_4 electrolyte are substantially higher, than the previously reported data for pure $Ti_3C_2T_x$ and composite electrodes, described in the Introduction. The record-high capacitances reported in the previous investigations[55] were 1087 mF cm^{-2} for a sweep rate of 1 mA cm^{-2} (783 mF cm^{-2} for the GCD testing at 1 mV s^{-1}) for $Ti_3C_2T_x$-based electrodes in the Na_2SO_4 electrolyte and 242 mF cm^{-2} at 1 mV s^{-1} for a symmetric cell for voltages of 0–0.9 V. In our investigation, significantly higher capacitance was achieved for $Ti_3C_2T_x$-based electrodes. Moreover, significantly higher capacitance was achieved for an asymmetric device in a larger voltage range of 0–1.6 V.

4.5 Conclusions

This investigation showed the feasibility of asymmetric device fabrication using $Ti_3C_2T_x$–MCNT negative electrodes and PPy-coated MCNT positive electrodes. With a desire to increase the areal capacitance of the negative electrodes, advanced chelating dispersants, such as ACV and CCB and advanced hydrophilic water-insoluble binders, such as PEMA and PVBAA, were utilized for the manufacturing of electrodes with high AM of 35 mg cm^{-2}. $Ti_3C_2T_x$–MCNT composites showed enhanced capacitive

performance, compared to pure $Ti_3C_2T_x$. The MCNT content in the composites was optimized at the level of 10%. ACV and CCB adsorbed on $Ti_3C_2T_x$ and MCNT by different mechanisms and allowed for their co-dispersion. Best electrochemical performance was achieved using ACV dispersant and PVBAA binder. The capacitance C_S of 1.93 F cm^{-2} was obtained from the CVs at 2 mV s^{-1}. The obtained C_S was substantially higher than reported literature results for pure $Ti_3C_2T_x$ and composites. The ability to achieve high C_S in Na_2SO_4 electrolyte opened the way for the manufacturing of asymmetric devices, which offered the benefits of higher voltage range, compared to symmetric $Ti_3C_2T_x$ based devices, reported in the literature. The investigation of PPy-coated MCNT electrodes showed that such electrodes exhibit excellent capacitive response for potentials of −0.3 to +0.6 V vs. SCE, which complements potential window of $Ti_3C_2T_x$–MCNT electrodes. The developed asymmetric device exhibited significantly higher C_S = 0.94 F cm^{-2} for a larger voltage range of 0–1.6 V compared to the previously reported results for $Ti_3C_2T_x$-based devices.

4.6 Acknowledgements

4.7 References

1. B. Anasori , M. R. Lukatskaya and Y. Gogotsi , Nat. Rev. Mater., 2017, 2 , 1 —17.
2. Y. Gogotsi and B. Anasori , ACS Nano, 2019, 13 , 8491 —8494.
3. S. Xu , G. Wei , J. Li , W. Han and Y. Gogotsi , J. Mater. Chem. A, 2017, 5 , 17442 —17451.
4. M. Alhabeb , K. Maleski , B. Anasori , P. Lelyukh , L. Clark , S. Sin and Y. Gogotsi , Chem. Mater., 2017, 29 , 7633 —7644.
5. A. Amiri , Y. Chen , C. B. Teng and M. Naraghi , Energy Storage Mater., 2020, 25 , 731 —739.
6. M. Hu , T. Hu , Z. Li , Y. Yang , R. Cheng , J. Yang , C. Cui and X. Wang , ACS Nano, 2018, 12 , 3578 —3586.
7. M. Cao , F. Wang , L. Wang , W. Wu , W. Lv and J. Zhu , J. Electrochem. Soc., 2017, 164 , A3933.
8. H. Li , X. Chen , E. Zalnezhad , K. Hui , K. Hui and M. J. Ko , J. Ind. Eng. Chem., 2020, 82 , 309 —316.
9. Y. A. Dakka , J. Balamurugan , R. Balaji , N. H. Kim and J. H. Lee , Chem. Eng. J., 2020, 385 , 123455.
10. R. Liu , A. Zhang , J. Tang , J. Tian , W. Huang , J. Cai , C. Barrow , W. Yang and J. Liu , Chem.–Eur. J., 2019, 25 , 5547 —5554.
11. K. O. Oyedotun , D. Y. Momodu , M. Naguib , A. A. Mirghni , T. M. Masikhwa , A. A. Khaleed , M. Kebede and N. Manyala , Electrochim. Acta, 2019, 301 , 487 —499.
12. Z. Pan , F. Cao , X. Hu and X. Ji , J. Mater. Chem. A, 2019, 7 , 8984 — 8992.
13. R. B. Rakhi , B. Ahmed , D. Anjum and H. N. Alshareef , ACS Appl. Mater. Interfaces, 2016, 8 , 18806 —18814.
14. F. Wang , M. Cao , Y. Qin , J. Zhu , L. Wang and Y. Tang , RSC Adv., 2016, 6 , 88934 —88942.
15. J. Cao , Y. Han , X. Zheng and Q. Wang , J. Appl. Polym. Sci., 2019, 136 , 47003.
16. X. Jian , M. He , L. Chen , M.-m. Zhang , R. Li , L.-j. Gao , F. Fu and Z.-h. Liang , Electrochim. Acta, 2019, 318 , 820 —827.
17. X. Lu , J. Zhu , W. Wu and B. Zhang , Electrochim. Acta, 2017, 228 , 282 —289.
18. R. Ramachandran , K. Rajavel , W. Xuan , D. Lin and F. Wang , Ceram. Int., 2018, 44 , 14425 —14431.

19. Y. Wang , H. Dou , J. Wang , B. Ding , Y. Xu , Z. Chang and X. Hao , J. Power Sources, 2016, 327 , 221 —228.

20. Q. X. Xia , N. M. Shinde , J. M. Yun , T. Zhang , R. S. Mane , S. Mathur and K. H. Kim , Electrochim. Acta, 2018, 271 , 351 —360.

21. X. Zhang , Y. Liu , S. Dong , Z. Ye and Y. Wei , J. Alloys Compd., 2018, 744 , 507 —515.

22. Y. Ren , J. Zhu , L. Wang , H. Liu , Y. Liu , W. Wu and F. Wang , Mater. Lett., 2018, 214 , 84 —87.

23. Y. Tang , J. Zhu , C. Yang and F. Wang , J. Alloys Compd., 2016, 685 , 194 —201.

24. Y. Tang , J. Zhu , W. Wu , C. Yang , W. Lv and F. Wang , J. Electrochem. Soc., 2017, 164 , A923.

25. Y. Tian , W. Que , Y. Luo , C. Yang , X. Yin and L. B. Kong , J. Mater. Chem. A, 2019, 7 , 5416 —5425.

26. Y. Wen , T. E. Rufford , X. Chen , N. Li , M. Lyu , L. Dai and L. Wang , Nano Energy, 2017, 38 , 368 —376.

27. Y. Gao , L. Wang , Z. Li , Y. Zhang , B. Xing , C. Zhang and A. Zhou , J. Adv. Ceram., 2015, 4 , 130 —134.

28. J. Guo , Y. Zhao , N. Jiang , A. Liu , L. Gao , Y. Li , H. Wang and T. Ma , Electrochim. Acta, 2018, 292 , 168 —179.

29. K. Wang , B. Zheng , M. Mackinder , N. Baule , H. Qiao , H. Jin , T. Schuelke and Q. H. Fan , Energy Storage Mater., 2019, 20 , 299 —306.

30. H. Wang , J. Zhang , Y. Wu , H. Huang and Q. Jiang , Electrochem. Commun., 2017, 81 , 48 —51.

31. W. Wu , D. Niu , J. Zhu , Y. Gao , D. Wei , C. Zhao , C. Wang , F. Wang , L. Wang and L. Yang , Ceram. Int., 2019, 45 , 16261 —16269.

32. C. Yang , W. Que , Y. Tang , Y. Tian and X. Yin , J. Electrochem. Soc., 2017, 164 , A1939.

33. W. Yuan , L. Cheng , B. Zhang and H. Wu , Ceram. Int., 2018, 44 , 17539 —17543.

34. C. Zhang , L. Wang , W. Lei , Y. Wu , C. Li , M. A. Khan , Y. Ouyang , X. Jiao , H. Ye and S. Mutahir , Mater. Lett., 2019, 234 , 21 —25.

35. Y. Zhang , Z. Yang , B. Zhang , J. Li , C. Lu , L. Kong and M. Liu , J. Alloys Compd., 2020, 155343.

36. X. He , T. Bi , X. Zheng , W. Zhu and J. Jiang , Electrochim. Acta, 2020, 332 , 135514.

37. T. A. Le , N. Q. Tran , Y. Hong and H. Lee , Chem. - Eur. J., 2019, 25 , 1037 —1043.

38. Z. Li , C. Ma , Y. Wen , Z. Wei , X. Xing , J. Chu , C. Yu , K. Wang and Z.-K. Wang , Nano Res., 2020, 13 , 196 —202.

39. Y. Li , Y. Deng , J. Zhang , Y. Han , W. Zhang , X. Yang , X. Zhang and W. Jiang , Nanoscale, 2019, 11 , 21981 —21989.

40. S.-Y. Lin and X. Zhang , J. Power Sources, 2015, 294 , 354 —359.

41. L. Shen , X. Zhou , X. Zhang , Y. Zhang , Y. Liu , W. Wang , W. Si and X. Dong , J. Mater. Chem. A, 2018, 6 , 23513 —23520.

42. C. Yang, W. Que , X. Yin , Y. Tian , Y. Yang and M. Que , Electrochim. Acta, 2017, 225 , 416 —424.

43. X. Wang, H. Li , H. Li , S. Lin , W. Ding , X. Zhu , Z. Sheng , H. Wang , X. Zhu and Y. Sun , Adv. Funct. Mater., 2020, 30 , 0190302.

44. W. Wu , D. Niu , J. Zhu , Y. Gao , D. Wei , X. Liu , F. Wang , L. Wang and L. Yang , J. Electroanal. Chem., 2019, 847 , 113203.

45. X. Li , J. Zhu , L. Wang , W. Wu and Y. Fang , Electrochim. Acta, 2017, 258 , 291 —301.

46. K. Kim , M. Okubo and A. Yamada , J. Electrochem. Soc., 2019, 166 , A3739.

47. J. Li , X. Yuan , C. Lin , Y. Yang , L. Xu , X. Du , J. Xie , J. Lin and J. Sun , Adv. Energy Mater., 2017, 7 , 1602725.

48. J. Luo , W. Zhang , H. Yuan , C. Jin , L. Zhang , H. Huang , C. Liang , Y. Xia , J. Zhang and Y. Gan , ACS Nano, 2017, 11 , 2459 —2469.

49. M. Shi , M. Narayanasamy , C. Yang , L. Zhao , J. Jiang , S. Angaiah and C. Yan , Electrochim. Acta, 2020, 334 , 135546.

50. H. Li , R. Chen , M. Ali , H. Lee and M. J. Ko , Adv. Funct. Mater., 2020, 2002739.

51. Z. Pan and X. Ji , J. Power Sources, 2019, 439 , 227068.

52. R. Chen , M. Yu , R. P. Sahu , I. K. Puri and I. Zhitomirsky , Adv. Energy Mater., 2020, 10 , 1903848.

53. W. Wu , D. Wei , J. Zhu , D. Niu , F. Wang , L. Wang , L. Yang , P. Yang and C. Wang , Ceram. Int., 2019, 45 , 7328 —7337.

54. B. Yang , Y. She , C. Zhang , S. Kang , J. Zhou and W. Hu , Nanomaterials, 2020, 10 , 345.

55. M. Guo , C. Liu , Z. Zhang , J. Zhou , Y. Tang and S. Luo , Adv. Funct. Mater., 2018, 28 , 1803196.

56. Y. Zhu , K. Shi and I. Zhitomirsky , J. Mater. Chem. A, 2014, 2 , 14666 —14673.

57. K. Shi and I. Zhitomirsky , J. Colloid Interface Sci., 2013, 407 , 474 —481.

58. M. S. Ata , R. Poon , A. M. Syed , J. Milne and I. Zhitomirsky , Carbon, 2018, 130 , 584 —598 .

59. M. Ata , Y. Liu and I. Zhitomirsky , RSC Adv., 2014, 4 , 22716 —22732.

60. Z. Li , Y. Liu , D. Guo , R. Jia , X. Zhai and L. Zhang , Mater. Res. Express, 2019, 6 , 065056.

61. S. Fares Nat. Sci., 2012, 4 , 499 —507.

62. M. Nawwar , R. Poon , R. P. Sahu , I. K. Puri and I. Zhitomirsky , Ceram. Int., 2020, 46 , 18851 —18858.

Chapter 5 Composite Ti$_3$C$_2$T$_x$-carbon nanotube electrodes with high active mass for supercapacitors

W Liang* and I. Zhitomirsky*[α]

*Department of Materials Science and Engineering, McMaster University,

Hamilton, Ontario, L8S 4L7, Canada

[α]Corresponding Author: zhitom@mcmaster.ca; 905-525-9140 ext. 23914

5.1 Abstract

Pure $Ti_3C_2T_x$ and $Ti_3C_2T_x$ -multiwalled carbon nanotube (MCNT) anodes with 35 mg

cm^{-2} active mass (AM) are prepared. The 90%$Ti_3C_2T_x$-10%MCNT electrode shows

the capacitance (C_S) of 1.78 F cm^{-2} for 2 mV s^{-1} cyclic voltammetry sweep and 1.95

F cm^{-2} for a constant current discharge at 3 $mAcm^{-2}$ in 0.5 M Na_2SO_4 aqueous

medium. The C_S of the $Ti_3C_2T_x$-10 MCNT anode significantly exceeds the literature

results for other $Ti_3C_2T_x$ anodes. The $Ti_3C_2T_x$-MCNT electrodes, showed low

resistance and good C_S retention at fast charging. Good electrode properties at high

AM are achieved due to the use of advanced catecholate-type dispersant. The 3,4,5-

trihydroxybenzamide (THB) dispersant showed adsorption on $Ti_3C_2T_x$ and MCNT,

favoured their dispersive mixing, and enhanced C_S of the composite. High C_S in

aqueous 0.5 M Na_2SO_4 medium is promising for application in

asymmetric supercapacitor cells operating in enlarged voltage range.

5.2 Introduction

$Ti_3C_2T_x$ belongs to the family of MXene-type ceramic materials, which are of great interest for electrodes of supercapacitors [1]. The interest in $Ti_3C_2T_x$ is attributed to its high capacitance and low electrical resistivity. Promising capacitive properties of $Ti_3C_2T_x$ result from its high surface area and redox active nature of surface functional groups.

High specific capacitance (C_m) normalized by AM was reported for composite electrodes [[2], [3], [4]] with relatively low AM, typically below 8 mg cm^{-2}. The C_S of such electrodes was below 1 F cm^{-2}. $Ti_3C_2T_x$ – based electrodes were utilized for the fabrication of symmetric supercapacitors, containing two similar $Ti_3C_2T_x$ – based electrodes, with maximum operation voltages of 0.4–1.2 V [5,6]. $Ti_3C_2T_x$– carbon nanotube films were developed for the fabrication of flexible devices [7]. The progress in applications of supercapacitor devices will depend on the ability to fabricate efficient electrodes and devices with high C_S, which can be achieved at high AM. Another practically important benefit of high AM electrodes is their low ratio of the mass of electrochemically inactive components to the AM. With a goal to increase the energy-power characteristics, there is a growing trend in devices that operate in enlarged voltage windows. Of particular importance are environmentally friendly neutral electrolytes, such as Na_2SO_4, which facilitate the design of asymmetric aqueous cells with voltage windows above 1.2 V.

$Ti_3C_2T_x$-based electrodes with AM of 1–3 mg cm^{-2} were analyzed in

Na_2SO_4 electrolyte [[8], [9], [10]] and relatively high C_m were obtained at such low

AM loadings. Therefore, the development of electrodes with higher AM can

potentially result in high C_S. However, it is challenging [11] to achieve high C_S owing

to the electrolyte diffusion limitations and large electrical resistance at high AM.

The goal of our work was the fabrication of $Ti_3C_2T_x$- MCNT anodes for

supercapacitors with high C_S in an aqueous Na_2SO_4 electrolyte. Enhanced anode

performance at AM of 35 mg cm^{-2} was achieved using THB as a co-dispersant for

$Ti_3C_2T_x$ and MCNT. The mechanisms of THB adsorption on $Ti_3C_2T_x$ and MCNT are

discussed.

THB and Na_2SO_4 (Millipore Sigma), MCNT (Bayer), $Ti_3C_2T_x$ (Laizhou Kai Kai

Ceramic Materials Co) and Ni foams (95% porosity, Vale) were used. As received

$Ti_3C_2T_x$ (Supplementary information, Figure S1) showed a relatively broad particle

size distribution, more than 90% particles had a diameter in the range of 0.5–10 μm.

The commercial PVB binder (Millipore Sigma, MW = 65,000) used in this

investigation, was a co-polymer of vinyl butyral, vinyl acetate and vinyl alcohol.

$Ti_3C_2T_x$ and MCNT were dispersed in ethanol, mixed with PVB (3 wt%) and obtained

mixtures were impregnated into Ni foams. The AM loadings were 35 mg cm^{-2} for

electrodes containing $Ti_3C_2T_x$ with 0, 10 and 20 wt% MCNT.

Electrochemical impedance spectroscopy (EIS) and cyclic voltammetry (CV)

investigations were conducted using a potentiostat (AMETEK 2273). Galvanostatic

charge discharge (GCD) was performed by Biologic AMP 300. The capacitive

behavior of the electrodes was tested in an aqueous 0.5 M Na_2SO_4. Pt gauze was

utilized as a counter electrode, and a saturated calomel electrode (SCE) served as a

reference. The working electrode area was 1 cm^2. Capacitances C_S and C_m were

derived from the CV or GCD data, and complex C_S* components (C_S' and C_S'') were

derived from the EIS testing results obtained at AC signal of 5 mV. Microstructure

analysis was performed with the aid of a microscope JEOL SEM (JSM-7000F).

5.3. Results and discussion

SEM images for as-received $Ti_3C_2T_x$ are shown in Fig. 5.1A and B. $Ti_3C_2T_x$ exhibits

an open-layered structure, which is beneficial for ion access to its surface. The particle

size was 3–10 μm. The relatively large particle size resulted in poor colloidal stability

of the particles. The commercial MCNT were supplied as an agglomerated material,

containing 0.5 mm agglomerates. The SEM images of such agglomerates were

presented in a previous investigation [12]. Therefore, efficient dispersion of MCNT is

necessary for the preparation of composites.
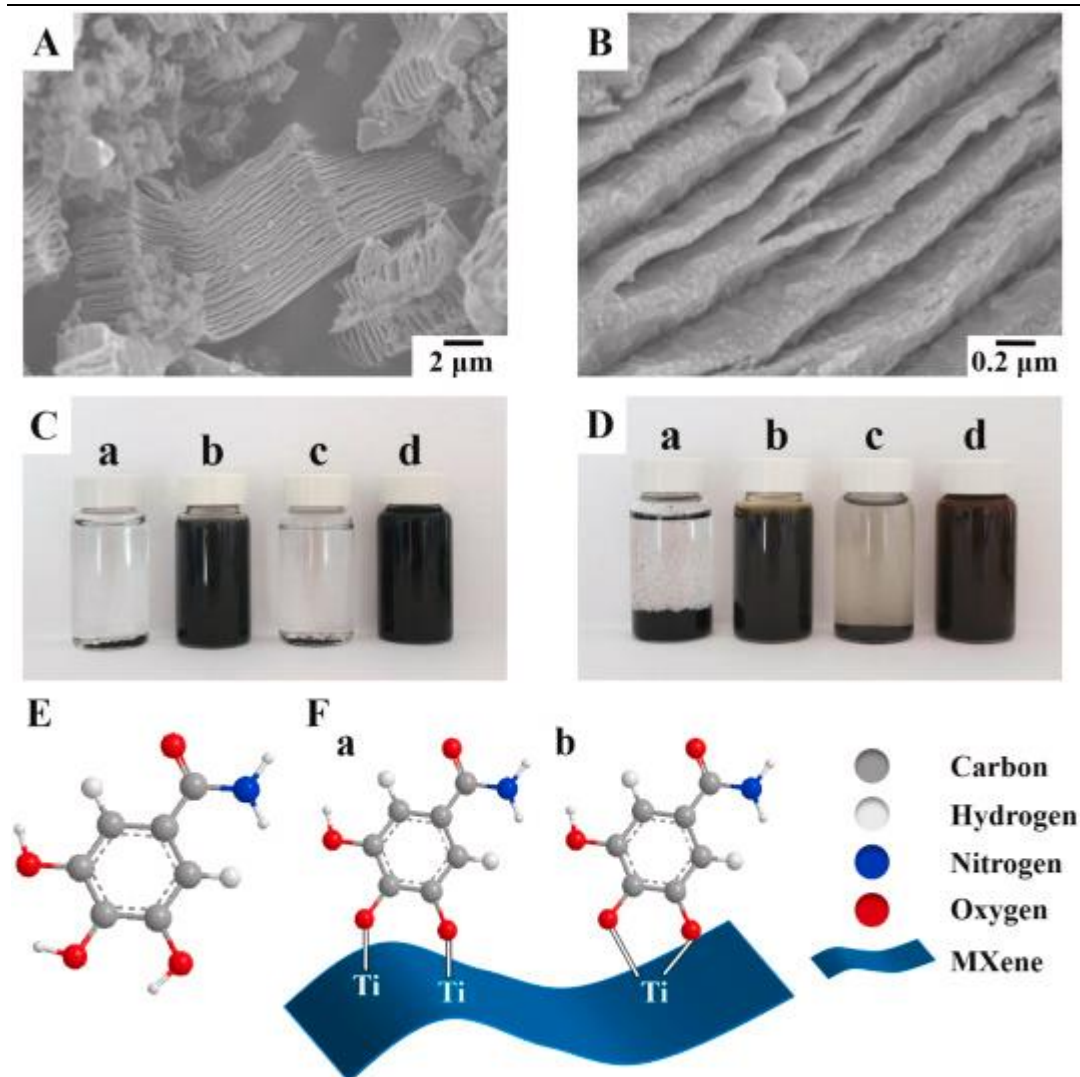
Fig. 5.1. (A,B) SEM images of as-received $Ti_3C_2T_x$ at different magnifications, (C,D) sedimentation test for (C)1 g L^{-1} MCNT and (D)1 g L^{-1} $Ti_3C_2T_x$: (a) without THB in water (b) with THB in water (c) without THB in ethanol and (d) with THB in ethanol, (E) THB structure, (F) THB adsorption on $Ti_3C_2T_x$ surface by (a) bidentate bridging and (b) bidentate chelating.

The use of THB as a dispersant facilitated the formation of stable $Ti_3C_2T_x$ and MCNT

suspensions in water and ethanol. Fig. 5.1C and D compares $Ti_3C_2T_x$ and MCNT

suspensions with and without THB, and it indicates that THB allows good dispersion

of both materials. The chemical structure of THB (Fig. 5.1E) favors the adsorption on

both materials. The aromatic THB molecules adsorbed on MCNT by the π-π

interaction mechanism [13]. It is known [14] that various catechol molecules show

strong adsorption on TiO_2 and other materials and allow for their efficient dispersion.

The adsorption mechanisms involved bridging or chelating bonding of the catechol

groups to the Ti atoms. Therefore, similar mechanisms can be proposed for the THB

bonding to the $Ti_3C_2T_x$ surface (Fig. 5.1F). It is important to note that $Ti_3C_2T_x$ can be

partially oxidized in air or in the suspension and contain surface O, OH or other

groups. Recent reviews [14,15] indicated that catecholate and gallate molecules are

strongly adsorbed on metals, alloys, oxides, hydroxides, carbonates, borates and other

materials and their catecholate-type bonding mechanisms, confirmed by various

techniques, can be described by the schematic, shown in Fig. 5.1F. The ability to co-

disperse $Ti_3C_2T_x$ and MCNT using THB was beneficial for their mixing, and

fabrication of composite electrodes by loading of nickel foam from a stable mixed

suspension. The use of a stable suspension of well-dispersed components was a key

factor for the preparation of high AM electrodes.

Another important factor for the successful design of advanced high AM electrodes,

was the use of PVB binder. The co-polymer binder, PVB, offers advantages

for ceramic processing, compared to individual polymer binders [16]. Vinyl alcohol

monomers of PVB facilitate adsorption of this binder on ceramic particles by

formation of hydrogen bonds with surface OH groups of the particles. Butyral

segments are well-solvated by organic solvents, such as ethanol, and directed towards

the bulk solution, providing steric stabilization [16]. Therefore, the binding and

dispersing properties of this polymer facilitated the fabrication of electrodes with low

binder content of 3%.

$Ti_3C_2T_x$ and composite electrodes, containing 10% MCNT ($Ti_3C_2T_x$/10MCNT) and

20% MCNT ($Ti_3C_2T_x$/20MCNT) were tested, and C_S data was acquired by different

methods. The electrodes showed nearly rectangular current versus potential

dependences in the CV test (Fig. 5.2A). The $Ti_3C_2T_x$/10MCNT electrodes showed

higher capacitance ($C_S = 1.78$ F cm^{-2}), compared with $Ti_3C_2T_x$/20MCNT ($C_S = 1.58$

F cm^{-2}) and pure $Ti_3C_2T_x$ ($C_S = 1.23$ F cm^{-2}) at a 2 mVs^{-1}. The analysis of

C_S retention (R_{100}) at 100 mV s^{-1} CV sweep showed additional evidence of superior

performance of $Ti_3C_2T_x$/10MCNT, which exhibited $R_{100} = 50.6\%$, whereas

$Ti_3C_2T_x$/20MCNT and pure $Ti_3C_2T_x$ exhibited R_{100} values of 48.7% and 23.6%,

respectively.
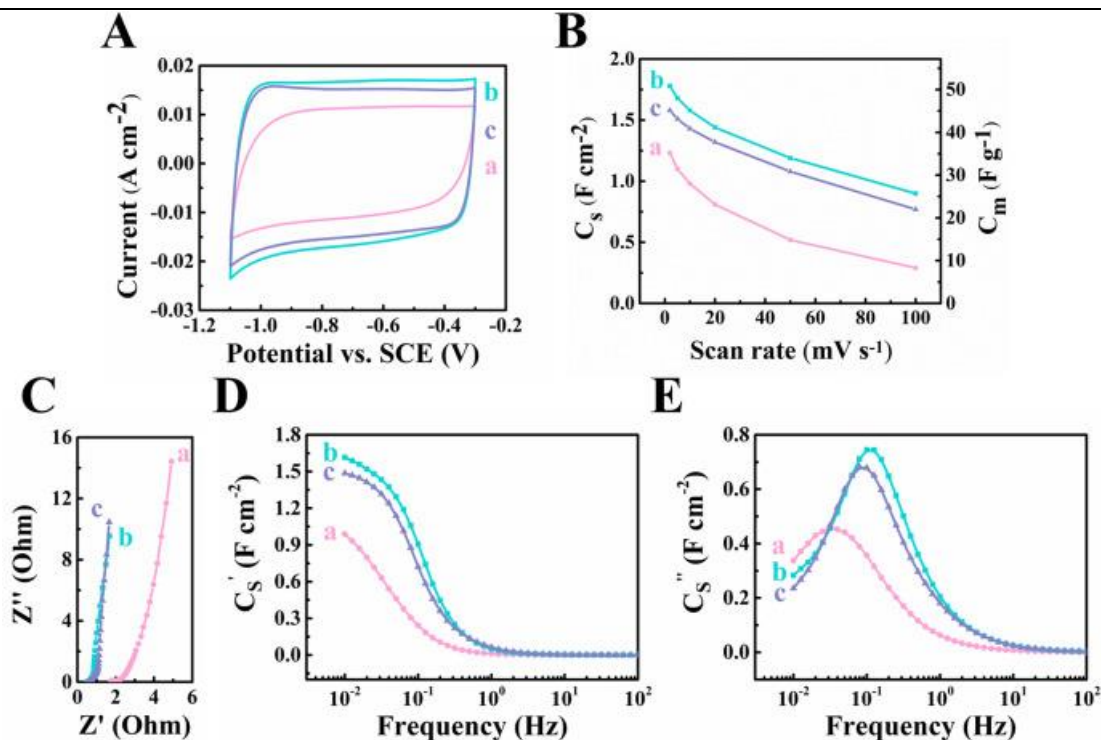
Fig. 5.2. (A) CV data, (B) capacitances derived from CVs, (C) Nyquist graph and (D,E) frequency response of C_S components for (a)$Ti_3C_2T_x$, (b)$Ti_3C_2T_x$/10MCNT, and (c)$Ti_3C_2T_x$/20MCNT.

EIS showed that the resistance (Z') decreased in the following order $Ti_3C_2T_x$ > $Ti_3C_2T_x$/20MCNT > $Ti_3C_2T_x$/10MCNT. The electrodes, containing MCNT, showed higher C_S', compared to pure $Ti_3C_2T_x$ with the highest capacitances recorded for $Ti_3C_2T_x$/10MCNT. The relaxation frequencies f_r for the $Ti_3C_2T_x$, $Ti_3C_2T_x$/20MCNT, and $Ti_3C_2T_x$/10MCNT electrodes, corresponding to C_S'' maxima (Fig. 5.2E), were found to be 0.033, 0.088 and 0.100 Hz. The highest f_r correlates with highest R_{100} for $Ti_3C_2T_x$/10MCNT and indicates improved capacitive response at low charge-discharge times.

GCD studies (Fig. 5.3A–C) showed nearly linear GCD curves at 3–35 mA cm^{-2}. The longest charge-discharge times were observed for $Ti_3C_2T_x$/10MCNT due to its higher

capacitance. The highest GCD capacitances (Fig. 5.3D) were obtained for

$Ti_3C_2T_x$/10MCNT electrodes, C_S decreased from 1.95 to 1.53 F cm^{-2} for GCD current

variation 3–35 mA cm^{-2} and showed the highest capacitance retention (78.5%) with

increasing current density, compared to pure $Ti_3C_2T_x$ and $Ti_3C_2T_x$/20MCNT. It is

hypothesized that the addition of MCNT to $Ti_3C_2T_x$ resulted in enhanced

electronic conductivity of the electrode material and allowed for enhanced

capacitance of $Ti_3C_2T_x$/10MCNT, compared to pure $Ti_3C_2T_x$. Therefore, the use of

MCNT as a conductive additive allowed for better utilization of capacitive properties

of $Ti_3C_2T_x$ in the composite material. However, MCNT have low capacitance and the

higher MCNT content in the $Ti_3C_2T_x$/20MCNT resulted in lower capacitance of the
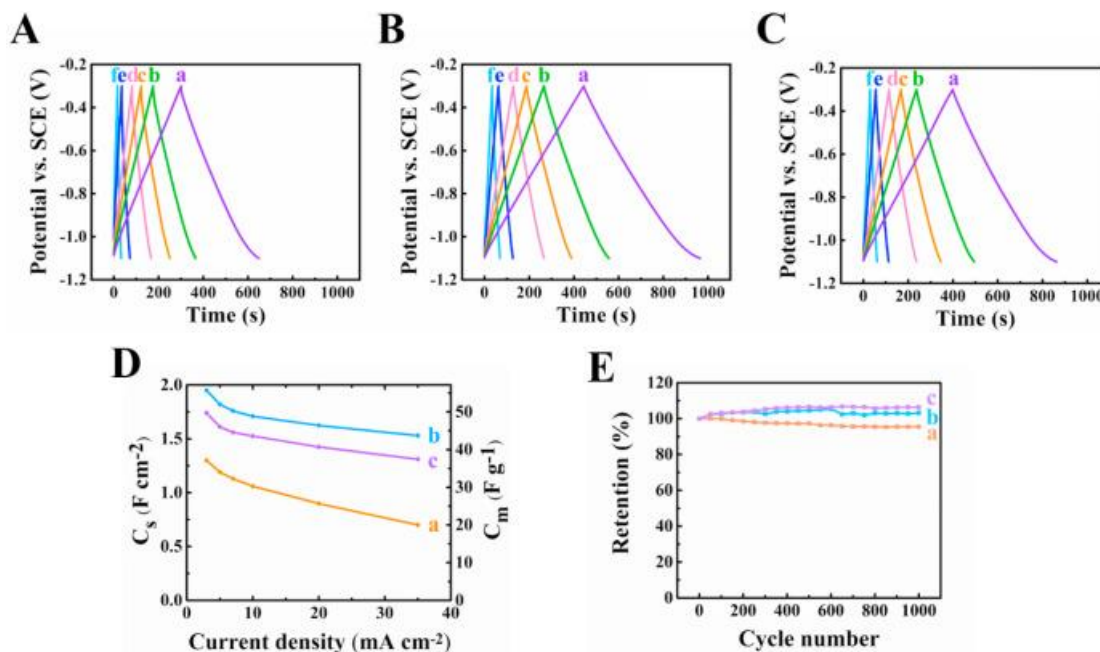
electrode.

Fig. 5.3. (A–C) GCD data for (A)$Ti_3C_2T_x$, (B)$Ti_3C_2T_x$/10MCNT, and (C)$Ti_3C_2T_x$/20MCNT at (a–f)3,5,7,10,20, and 35 mA cm^{-2}, (D) capacitance as a function of GCD current, and (E) capacitance retention for (a) $Ti_3C_2T_x$,

(b)$Ti_3C_2T_x$/10MCNT, and (c)$Ti_3C_2T_x$/20MCNT.

Pure $Ti_3C_2T_x$ electrodes showed relatively small variations in capacitance during 1000

cycles and the capacitance retention (C_R) was found to be 96% after 1000 cycles.

$Ti_3C_2T_x$/10MCNT and $Ti_3C_2T_x$/20MCNT electrodes showed slight increase in C_R for

the first 150–200 cycles. The C_R values for 1000 cycles for $Ti_3C_2T_x$/10MCNT and

$Ti_3C_2T_x$/20MCNT were found to be 103 and 106%, respectively. The slight

C_R increase can result from changes in the wetting behavior of the electrodes during

initial cycling.

5.4. Conclusions

$Ti_3C_2T_x$-MCNT electrodes exhibited significantly higher capacitance, compared to

literature data for $Ti_3C_2T_x$ based electrodes. The highest capacitance was achieved for

$Ti_3C_2T_x$/10MCNT electrodes, which showed $C_S = 1.95$ F cm^{-2} in 0.5 M

Na_2SO_4 electrolytes. The analysis of capacitances at different sweep rates,

frequencies, and discharge currents showed high capacitance retention at fast charge-

discharge. Moreover, the electrodes showed low resistance. Good material utilization

at high AM was achieved due to the use of THB dispersant and PVB binder. THB

adsorbed on $Ti_3C_2T_x$ and MCNT, allowed for their enhanced dispersive mixing,

which, in turn allowed for enhanced capacitance. The ability to achieve high

capacitance in the environmentally friendly Na_2SO_4 medium is promising for the

construction of advanced asymmetric cell with expanded voltage operation range.

5.5 Acknowledgement

5.6 Supplementary Materials
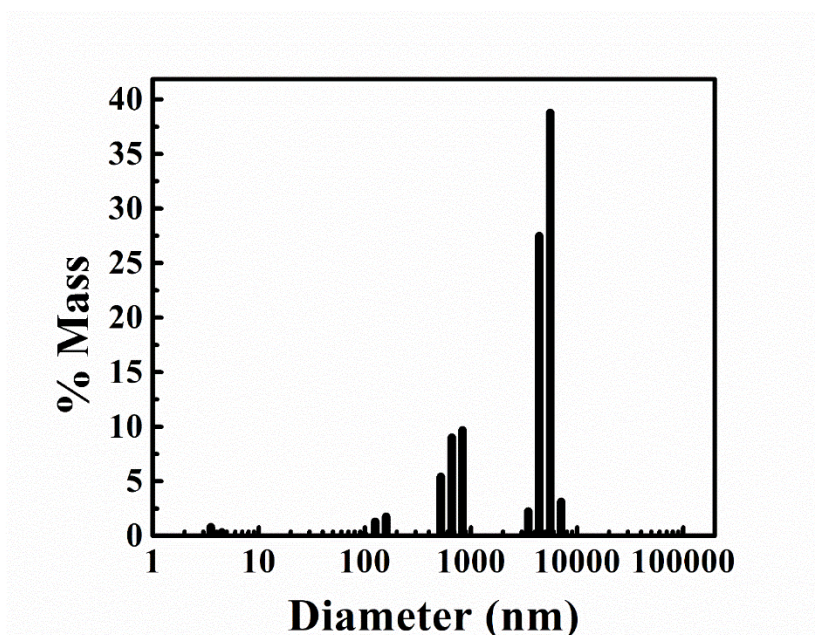
Figure 5.4. Particle size distribution for as received $Ti_3C_2T_x$ measured using dynamic light scattering (DLS, DelsaMax Pro: Beckman Coulter)

5.7 References

[1] Y. Gogotsi, B. Anasori, The rise of MXenes, ACS Nano 13 (2019) 8491–8494.

[2] X. He, T. Bi, X. Zheng, W. Zhu, J. Jiang, Nickel cobalt sulfide nanoparticles grown on titanium carbide MXenes for high-performance supercapacitor, Electrochim. Acta 332 (2020) 135514.

[3] Y. Li, Y. Deng, J. Zhang, Y. Han, W. Zhang, X. Yang, X. Zhang, W. Jiang, Tunable energy storage capacity of two-dimensional $Ti_3C_2T_x$ modified by a facile twostep pillaring strategy for high performance supercapacitor electrodes, Nanoscale 11 (45) (2019) 21981–21989.

[4] L. Shen, X. Zhou, X. Zhang, Y. Zhang, Y. Liu, W. Wang, W. Si, X. Dong, Carbonintercalated Ti_3C_2Tx MXene for high-performance electrochemical energy storage, J. Mater. Chem. 6 (46) (2018) 23513–23520.

[5] H. Li, R. Chen, M. Ali, H. Lee, M.J. Ko, In situ grown MWCNTs/MXenes nanocomposites on carbon cloth for high-performance flexible supercapacitors, Adv. Funct. Mater. (2020) 2002739.

[6] Z. Pan, X. Ji, Facile synthesis of nitrogen and oxygen co-doped C@ Ti3C2 MXene for high performance symmetric supercapacitors, J. Power Sources 439 (2019) 227068.

[7] H. Chen, L. Yu, Z. Lin, Q. Zhu, P. Zhang, N. Qiao, B. Xu, Carbon nanotubes enhance flexible MXene films for high-rate supercapacitors, J. Mater. Sci. 55 (3) (2020) 1148–1156.

[8] J. Li, X. Yuan, C. Lin, Y. Yang, L. Xu, X. Du, J. Xie, J. Lin, J. Sun, Achieving high pseudocapacitance of 2D titanium carbide (MXene) by cation intercalation and surface modification, Advanced Energy Materials 7 (15) (2017) 1602725.

[9] W. Wu, D. Wei, J. Zhu, D. Niu, F. Wang, L. Wang, L. Yang, P. Yang, C. Wang, Enhanced electrochemical performances of organ-like Ti_3C_2 MXenes/polypyrrole composites as supercapacitors electrode materials, Ceram. Int. 45 (6) (2019) 7328–7337.

[10] B. Yang, Y. She, C. Zhang, S. Kang, J. Zhou, W. Hu, Nitrogen doped intercalation $TiO_2/TiN/Ti_3C_2T_x$ nanocomposite electrodes with enhanced pseudocapacitance, Nanomaterials 10 (2) (2020) 345.

[11] R. Chen, M. Yu, R.P. Sahu, I.K. Puri, I. Zhitomirsky, The development of pseudocapacitor electrodes and devices with high active mass loading, Advanced Energy Materials 10 (20) (2020) 1903848.

[12] C. Wallar, R. Poon, I. Zhitomirsky, High areal capacitance of V_2O_3–carbon nanotube electrodes, J. Electrochem. Soc. 164 (14) (2017) A3620–A3627.

[13] K. Shi, I. Zhitomirsky, Electrophoretic nanotechnology of graphene–carbon nanotube and graphene–polypyrrole nanofiber composites for electrochemical supercapacitors, J. Colloid Interface Sci. 407 (2013) 474–481.

[14] M. Ata, Y. Liu, I. Zhitomirsky, A review of new methods of surface chemical modification, dispersion and electrophoretic deposition of metal oxide particles, RSC Adv. 4 (43) (2014) 22716–22732.

[15] R.M.E. Silva, R. Poon, J. Milne, A. Syed, I. Zhitomirsky, New developments in liquid-liquid extraction, surface modification and agglomerate-free processing of inorganic particles, Adv. Colloid Interface Sci. 261 (2018) 15–27.

[16] I. Zhitomirsky, A. Petric, Electrophoretic deposition of ceramic materials for fuel cell applications, J. Eur. Ceram. Soc. 20 (12) (2000) 2055–2061

Chapter 6 Composite Fe₃O₄-MXene-Carbon Nanotube Electrodes for Supercapacitors Prepared Using the New Colloidal Method

W Liang* and I. Zhitomirsky*[α]

*Department of Materials Science and Engineering, McMaster University,

Hamilton, Ontario, L8S 4L7, Canada

[α]Corresponding Author: zhitom@mcmaster.ca; 905-525-9140 ext. 23914

6.1 Abstract

MXenes, such as $Ti_3C_2T_x$, are promising materials for electrodes of supercapacitors

(SCs). Colloidal techniques have potential for the fabrication of advanced

$Ti_3C_2T_x$ composites with high areal capacitance (C_S). This paper reports the

fabrication of $Ti_3C_2T_X$-Fe_3O_4-multiwalled carbon nanotube (CNT) electrodes, which

show C_S of 5.52 F cm^{-2} in the negative potential range in 0.5 M Na_2SO_4 electrolyte.

Good capacitive performance is achieved at a mass loading of 35 mg cm^{-2} due to the

use of Celestine blue (CB) as a co-dispersant for individual materials. The

mechanisms of CB adsorption on $Ti_3C_2T_X$, Fe_3O_4, and CNTs and their electrostatic

co-dispersion are discussed. The comparison of the capacitive behavior of $Ti_3C_2T_X$-

Fe_3O_4-CNT electrodes with $Ti_3C_2T_X$-CNT and Fe_3O_4-CNT electrodes for the same

active mass, electrode thickness and CNT content reveals a synergistic effect of the

individual capacitive materials, which is observed due to the use of CB. The high

C_S of $Ti_3C_2T_X$-Fe_3O_4-CNT composites makes them promising materials for

application in negative electrodes of asymmetric SC devices.

6.2 Introduction

$Ti_3C_2T_x$ belongs to the family of MXene-type materials, which are of great

technological interest for applications in electrodes of SCs [1–3]. The interest in

$Ti_3C_2T_x$ is attributed to the high capacitance and low electrical resistivity of this

material. The promising capacitive properties of $Ti_3C_2T_x$ result from its high surface

area and the redox active nature of surface functional groups. Enhanced capacitive

properties were obtained for $Ti_3C_2T_x$ composites, containing different conductive

additives, such as graphene [4], acetylene black [5], and carbon black [6] and for

nitrogen-doped $Ti_3C_2T_x$ [7–9]. Moreover, advanced $Ti_3C_2T_x$ composites were

developed, containing other components, such as ZnO [10], MnO_2 [11], TiO_2 [12],

and Mn_3O_4 [13]. Investigations revealed the stable cycling behavior of $Ti_3C_2T_x$

composites [14–19].

High specific capacitance (Cm) normalized by active mass (AM) was reported for

composite electrodes [9,12,14,20–28] with relatively low AMs, typically below 8 mg

cm^{-2}. The C_S of such electrodes was below 1 F cm^{-2}. Capacitive properties of $Ti_3C_2T_x$

composites were tested in various electrolytes, such as HCl [29], H_2SO_4 [27,30,31],

KOH [12,32], KCl [33], K_2SO_4 [34], Na_2SO_4 [34], Li_2SO_4 [34], and other electrolytes

[35,36]. $Ti_3C_2T_x$ based electrodes were utilized for the fabrication of symmetric SCs,

containing two similar $Ti_3C_2T_x$-based electrodes, with maximum operation voltages in

the range of 0.4–1.2 V [9,31,37,38]. The progress in applications of SC devices will

depend on the ability to fabricate efficient electrodes and devices with high Cs, which

can be achieved at high AM loadings. Another important benefit of high AM

electrodes is their low ratio of the mass of electrochemically inactive components to

the AMs. With the goal to increase energy–power characteristics, there is a growing

trend in devices that operate in enlarged voltage windows. Of particular importance

are environmentally friendly neutral electrolytes, such as Na_2SO_4, which facilitate the

design of asymmetric aqueous cells with voltage windows above 1.2 V.

$Ti_3C_2T_x$ -based electrodes with AMs of 1–3 mg cm^{-2} were analyzed in Na_2SO_4

electrolyte [34,39,40] and relatively high Cm were obtained at such low AM loadings.

Therefore, the development of electrodes with higher AMs can potentially result in

high C_S. However, it is challenging [41] to achieve high C_S owing to the electrolyte

diffusion limitations and high electrical resistance at high AMs. The increase in AM

to the level of 20 mg cm^{-2} allowed the design of composites [42] with Cs of 1.087 F

cm^{-2} at the galvanostatic charging conditions of 1 mA cm^{-2} and 0.783 F cm^{-2} at

potential sweep conditions of 1 mV s^{-1}. Such electrodes [42] were utilized for

symmetric $Ti_3C_2T_x$ SC.

The objective of this study was to form Fe_3O_4-$Ti_3C_2T_x$-CNT electrodes for SCs. The

use of CB as a co-dispersant allowed the fabrication of electrodes, which showed

good electrochemical performance at AM of 35 mg cm^{-2}. CB allowed adsorption on

individual materials and their dispersion due its polyaromatic structure, containing a

chelating catechol ligand and electric charge. The experimental data of this

investigation showed that C_S of 5.52 F cm^{-2} can be achieved in the negative potential

range in 0.5M Na$_2$SO$_4$ electrolyte due to the use of advanced co-dispersant and a

synergistic effect of the individual components.

6.3 Experimental procedure

Celestine blue (CB), FeCl$_3$ 6H$_2$O, FeCl$_2$ 4H$_2$O, NH$_4$OH, Na$_2$SO$_4$, co-polymer of vinyl

butyral, vinyl acetate and vinyl alcohol (PVBAA, 65 kDa) were purchased from

Millipore Sigma, Burlington, MA, USA. The diameter and length of CNT

(multiwalled, Bayer Corp. Whippany, NJ, USA) were 13 nm and 1–2 μm,

respectively. Ti$_3$C$_2$T$_x$ was purchased from Laizhou Kai Kai Ceramic Materials Co.,

Ltd., Laizhou, China. Fe$_3$O$_4$ was prepared as described in by a chemical precipitation

method [43] from solutions of FeCl$_2$ and FeCl$_3$, containing dispersed CNT or co-

dispersed CNT and Ti$_3$C$_2$T$_x$. In contrast to the previous investigation [43], pristine

CNT were used. In this approach, CNT and Ti$_3$C$_2$T$_x$ were dispersed or co dispersed

using CB as a surfactant. For the fabrication of Fe$_3$O$_4$-CNT electrodes, the synthesis

of Fe$_3$O$_4$ was performed in the presence of CNT, dispersed using CB. For the

fabrication of Ti$_3$C$_2$T$_x$-CNT electrodes, Ti$_3$C$_2$T$_x$ was co-dispersed with CNT in water

using CB as a co-dispersant. Active materials (AM) for Ti$_3$C$_2$T$_x$-Fe$_3$O$_4$-CNT

electrodes were prepared by precipitating Fe3O4 in the presence of co-dispersed

$Ti_3C_2T_x$ and CNT. The amount of the CB dispersant in the suspension was 15% of the

total mass of $Ti_3C_2T_x$, Fe_3O_4 and CNT. After filtration, obtained AM were washed

with water and ethanol in order to remove non-adsorbed dispersant and dried in air. In

order to analyze the effect of CB, AM for $Ti_3C_2T_x$-(Fe_3O_4-CNT) electrodes were

prepared by fabrication of Fe_3O_4-CNT powder, as described above, and its mixing

with $Ti_3C_2T_x$. The $Ti_3C_2T_x$/ Fe_3O_4 mass ratio was 5:3 in the $Ti_3C_2T_x$-(Fe_3O_4-CNT)

and $Ti_3C_2T_x$- Fe_3O_4-CNT electrodes. The mass ratio of CNT to the mass of active

materials, such as Fe_3O_4 in Fe_3O_4-CNT, $Ti_3C_2T_x$ in $Ti_3C_2T_x$-CNT, Fe_3O_4 and $Ti_3C_2T_x$

(total) in $Ti_3C_2T_x$-(Fe_3O_4-CNT) and $Ti_3C_2T_x$- Fe_3O_4-CNT was 1:4.

Obtained powders were used for the fabrication of slurries in ethanol for the

impregnation of commercial Ni foam current collectors (95% porosity, Vale, Rio de

Janeiro, Brazil). The slurries contained dissolved PVBAA binder. The mass of the

binder was 3% of the total mass of the active material (AM). The total AM of

impregnated material after drying was 35 mg cm^{-2}, which included 3% PVBAA

binder. All of the impregnated Ni foams were pressed using a calendering machine in

order to obtain a final electrode thickness of 0.38 mm.

Electrochemical impedance spectroscopy (EIS) and cyclic voltammetry (CV) studies

were performed using a potentiostat (PARSTAT 2273, AMETEK, Berwyn, PA,

USA). Galvanostatic charge discharge (GCD) was conducted using a Biologic AMP

300 potentiostat. The capacitive behavior of the electrodes was tested in an aqueous

0.5 M Na_2SO_4 solution. Pt gauze was utilized as a counter electrode, and a saturated

calomel electrode (SCE) was used as a reference. The area of the working electrode

was 1 cm2. Capacitances Cs and Cm, normalized by the electrode area or mass of the

active material, respectively, were obtained from the CV or GCD data, and complex

Cs* components (Cs' and Cs") were calculated from the EIS testing results obtained

at a signal of 5 mV, as described in [41]. JSM-7000F microscope (JEOL, Peabody,

MA, USA) was used for SEM investigations.

6.4 Results and Discussion

Figure 6.1A,B shows SEM images of $Ti_3C_2T_x$ particles used in this investigation. The

particles exhibit an accordion-like structure, which is beneficial for electrolyte access

to the material. However, some small pores may not be accessible by the electrolyte.

It is in this regard that the investigations of other pseudocapacitive materials did not

show correlation between BET surface area and capacitance [44–47]. The SEM

images of $Ti_3C_2T_x$-Fe_3O_4-CNT composites (Figure 6.1C,D) show that $Ti_3C_2T_x$

particles were covered with Fe_3O_4 and CNT.
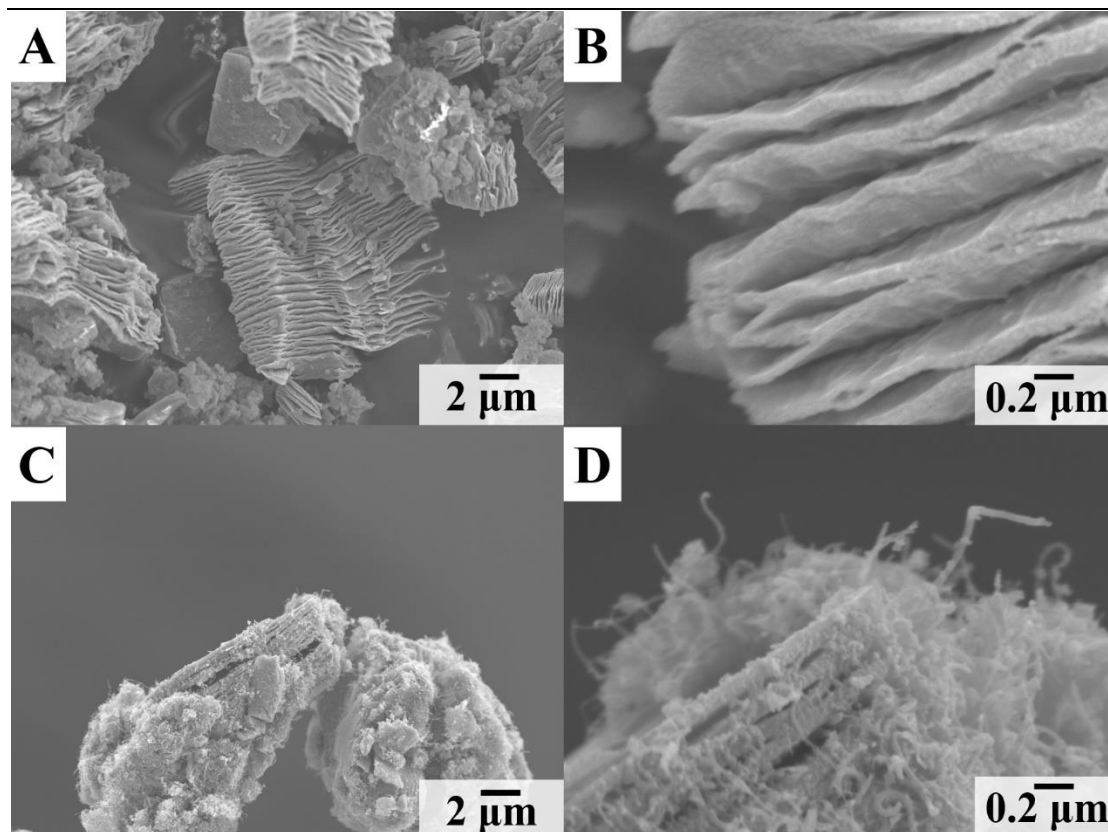
Figure 6.1. SEM images at different magnifications of (A,B) as-received Ti3C2Tx and (C,D) Ti$_3$C$_2$T$_x$-Fe$_3$O$_4$-CNT.

Ti$_3$C$_2$T$_x$ particles were used for the fabrication of composite Ti$_3$C$_2$T$_x$- Fe$_3$O$_4$-CNT electrodes. Pure Ti$_3$C$_2$T$_x$-CNT and Fe$_3$O$_4$-CNT electrodes were also fabricated and tested for comparison. The X-ray diffraction patterns of the composite Ti$_3$C$_2$T$_x$-CNT, Fe$_3$O$_4$-CNT, and Ti$_3$C$_2$T$_x$-Fe$_3$O$_4$-CNT materials presented in the Supplementary Information (Figure 6.9) show diffraction peaks of the individual components. All the electrodes contained 20% CNTs as conductive additives. In this investigation, CNTs were used as conductive additives for capacitive Fe$_3$O$_4$ [48–50] and Ti$_3$C$_2$T$_x$ [1–3] materials. Previous investigations highlighted the need for the fabrication of electrodes with high AMs and enhanced ratio of the AM to the mass of current collector and other

passive components [41]. Commonly used so far are activated carbon (AC) commercial supercapacitors with high AM [41,51] of about 10 mg cm^{-2}. Another important parameter is electrode thickness [52]. It has been demonstrated that significant uncertainty in supercapacitor metrics stems from reporting gravimetric capacitance of thick electrodes with low packing density [51]. In such electrodes, empty space is filled by an electrolyte, thereby increasing the weight of the device without adding capacitance. However, such electrodes show enhanced AM normalized capacitance due to enhanced access of the electrolyte to the active materials [51]. Investigations showed that electrodes must be of comparable thickness for the comparison of their performance [53]. It is important to note that AC has a relatively low density and typical thickness of AC electrodes with active mass of 10 mg·cm^{-2} is about 0.6 mm [54]. In our investigation, the thickness of all the investigated electrodes was 0.38 mm and AM loading was 35 mg·cm^{-2}. The higher AM of the fabricated electrodes, compared to that of AC electrodes, resulted from higher density of $Ti_3C_2T_x$ and Fe_3O_4 materials used in this investigation. The high AM loading was beneficial for increasing the ratio of AM - to the total mass, which includes not only AM, but also mass of current collectors, electrolyte and other components. The ability to achieve high capacitance using electrodes with high AM and low impedance is critical for the development of advanced electrodes.

In this investigation, CB was used as a dispersant for $Ti_3C_2T_x$, Fe_3O_4 and CNTs. CB has

generated significant interest as an advanced dispersant for the fabrication of composites for supercapacitors and other applications [55,56,57]. Sedimentation tests showed good colloidal stability of the $Ti_3C_2T_x$, Fe_3O_4 and CNT suspensions, prepared using CB. It is important to note that the chemical structure of CB contains a catechol ligand, which facilitates CB adsorption on inorganic materials by complexation of metal atoms on the material surface [58]. Such interactions of CB with Ti atoms on the $Ti_3C_2T_x$ surface or Fe atoms on the Fe_3O_4 surface facilitated CB adsorption. The polyaromatic structure of CB allowed for its adsorption on CNTs and the adsorption mechanism of CB involved π-π interactions with side walls of CNTs [59]. The adsorbed cationic CB allowed for electrostatic dispersion of $Ti_3C_2T_x$, Fe_3O_4 and CNT and facilitated their enhanced mixing. Co-dispersion of $Ti_3C_2T_x$ with CNTs and Fe_3O_4 with CNTs allowed for good performance of $Ti_3C_2T_x$-CNT and Fe_3O_4-CNT electrodes at high AM loadings.

Figure 6.2 shows capacitive performances of $Ti_3C_2T_x$-CNT and Fe_3O_4-CNT electrodes. Cyclic voltammetry (CV) studies showed nearly rectangular shape CVs for $Ti_3C_2T_x$-CNT electrodes and $C_S = 1.96$ F·cm^{-2} at 2 mV s^{-1}. The obtained C_S was significantly higher than literature data for $Ti_3C_2T_x$ based electrodes, discussed in the Introduction. The capacitance retention at 100 mV·s^{-1} was 23.5%. Relatively high capacitances were also achieved using Fe_3O_4-CNT electrodes. The highest $C_S = 4.42$ F·cm^{-2} was attained at 2 mV·s^{-1}. The use of CB as a co-dispersant allowed for higher capacitance of the

Fe_3O_4-CNT electrodes compared to the previous results [43] for the Fe_3O_4-CNT electrodes, containing functionalized CNTs. The capacitance retention at 100 mV s^{-1} was 14.9%. The capacitive properties of Fe_3O_4-CNT composites resulted from the double layer charging mechanism of Fe_3O_4 and CNTs and pseudocapacitive mechanism of Fe_3O_4, attributed to Fe^{2+}/Fe^{3+} redox couple [48,49,50].
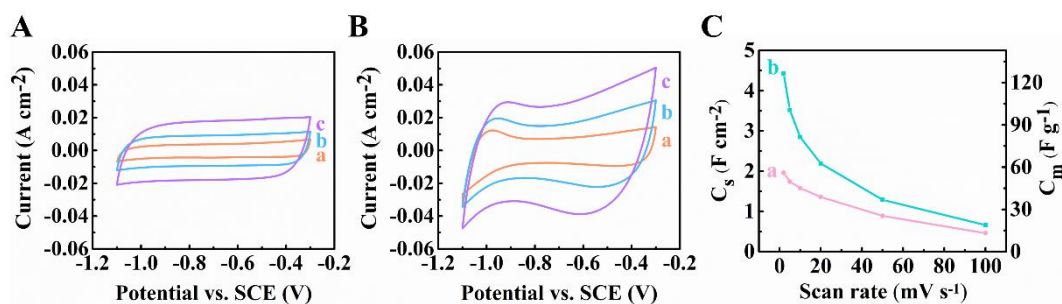
Figure 6.2. (A,B) Cyclic voltammetry data at (a) 2, (b) 5 and (c) 10 mV s^{-1}, (C) capacitances for ((A,C) (a)) $Ti_3C_2T_X$-CNT and ((B,C) (b)) Fe_3O_4-CNT electrodes.

Figure 6.3 shows EIS data for the $Ti_3C_2T_x$-CNT and Fe_3O_4-CNT electrodes. The Nyquist plot of complex impedance revealed lower resistance, R = Z', compared to the literature data [42]. The low electrical resistance is an important factor controlling capacitive performance of electrodes. The differential capacitance C_S' derived from the EIS data at 5 mV signal amplitude was inferior to the integral C_S calculated for potential span of 0.8 V. The discrepancy can be attributed to different parameters, such as charge–discharge time, electrode potential and limited accessibility of some redox sites at low voltages. The electrodes showed relatively high relaxation frequencies [60,61], corresponding to C_S'' maxima.
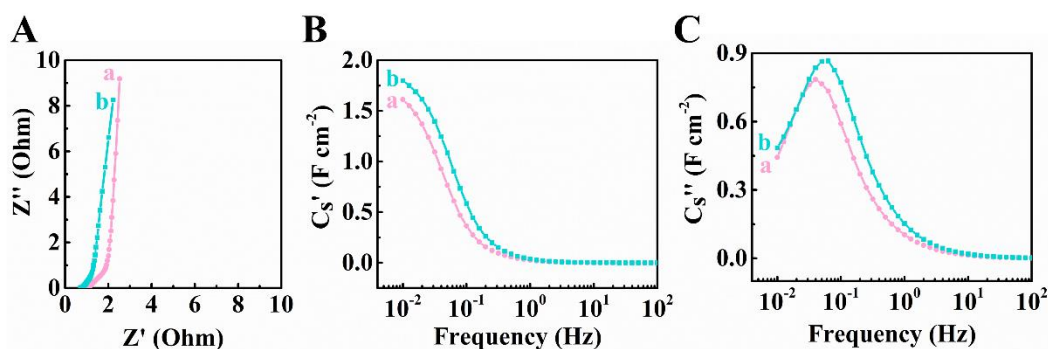
Figure 6.3. (A) Nyquist Z" vs. Z' graph for EIS data, (B) C_S' and (C) C_S", derived from the EIS data for (a) $Ti_3C_2T_X$-CNT and (b) Fe_3O_4-CNT electrodes.

Figure 6.4A,B shows charge-discharge behavior of the $Ti_3C_2T_X$-CNT and Fe_3O_4-CNT electrodes. The electrodes showed nearly triangular symmetric GCD profile. The capacitances were calculated from the GCD data and are presented in Figure 6.4C. C_S reduced from 2.05 to 1.40 F·cm^{-2} and from 3.41 to 2.5 F·cm^{-2}, for $Ti_3C_2T_X$-CNT and Fe_3O_4-CNT electrodes, respectively, in the current range 3–35 mA·cm^{-2}. The GCD data showed good capacitance retention with increasing current density.
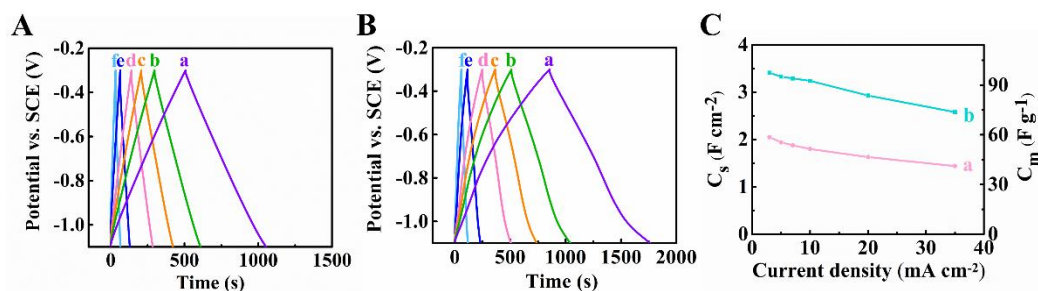
Figure 6.4. Galvanostatic charge–discharge curves of (A)$Ti_3C_2T_X$-CNT, (B) Fe_3O_4-CNT at (a) 3, (b) 5 (c) 7, (d) 10 (e) 20 and (f) 35 mA·cm^{-2}, (C) capacitances derived from GCD tests for (a) $Ti_3C_2T_X$-CNT and (b) Fe_3O_4-CNT electrodes.

This investigation revealed a synergistic effect of $Ti_3C_2T_X$, CNT and Fe_3O_4, which allowed for enhanced capacitance of the composite $Ti_3C_2T_X$-Fe_3O_4-CNT electrodes, compared to the capacitances of $Ti_3C_2T_X$-CNT and Fe_3O_4-CNT electrodes at the same

AM, electrode thickness and CNT content. The use of CB as a dispersant was critical to achieve enhanced capacitance. The effect of CB is evident from the comparison of testing results for two composites, prepared at different experimental conditions, as was described in the Materials and Methods section. $Ti_3C_2T_X$-(Fe_3O_4-CNT) electrodes were prepared by precipitation of Fe_3O_4 in the presence of CNTs dispersed with CB, followed by washing drying and mixing with $Ti_3C_2T_X$. In contrast $Ti_3C_2T_X$-Fe_3O_4-CNT electrodes were prepared by precipitation of Fe_3O_4 in the presence of co-dispersed $Ti_3C_2T_X$ and CNTs.

CV testing results showed significantly larger CV areas for $Ti_3C_2T_X$-Fe_3O_4-CNT, compared to $Ti_3C_2T_X$-(Fe_3O_4-CNT) electrodes (Figure 6.5A,B). This resulted in higher capacitance of the $Ti_3C_2T_X$-Fe_3O_4-CNT and indicated the influence of CB dispersant used for the preparation of the composites on the properties of the electrodes. The highest capacitances of 5.52 and 3.90 $F \cdot cm^{-2}$ were obtained for $Ti_3C_2T_X$-Fe_3O_4-CNT and $Ti_3C_2T_X$-(Fe_3O_4-CNT) electrodes, respectively, at 2 $mV \cdot s^{-1}$. In order to analyze the charge storage properties of the electrodes, a parameter b was calculated from the following equation [62,63].

$$i = av^b \tag{1}$$

where i is a current, v—scan rate and a is a parameter. Parameter b was found to be 0.68 for the $Ti_3C_2T_X$-Fe_3O_4-CNT electrodes (Figure 6.10). It is known that b = 1 for purely double-layer capacitive mechanism and b = 0.5 for battery-type materials. The

electrodes with $0.5 < b < 1$ combine capacitive and battery properties. According to

[62], the battery-type charge storage mechanism is dominant for electrodes with $0.5 <$

$b < 0.8$. Therefore, the $Ti_3C_2T_X$-Fe_3O_4-CNT electrodes show mixed double-layer

capacitive and battery-type properties with a dominant battery-type charge storage

mechanism.
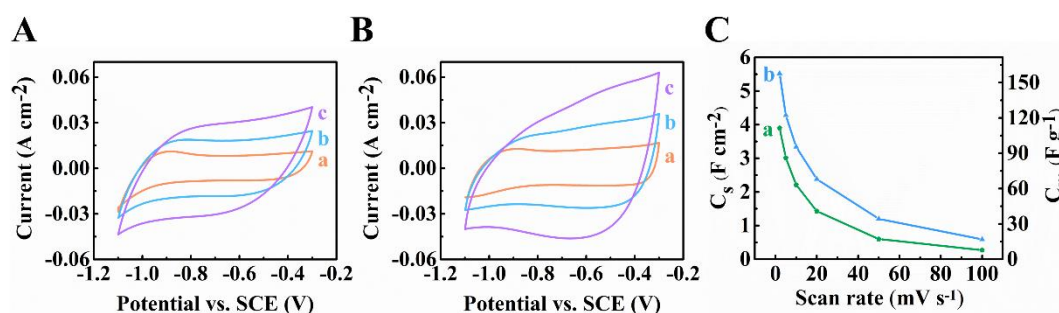
Figure 6.5. (A,B) Cyclic voltammetry data at (a) 2, (b) 5 and (c) 10 mV·s^{-1}, (C) capacitances for ((A,C) (a)) $Ti_3C_2T_X$-(Fe_3O_4-CNT) and ((B,C) (b)) $Ti_3C_2T_X$-Fe_3O_4-CNT electrodes.

EIS studies (Figure 6.6) revealed lower resistance, higher capacitance and higher

relaxation frequency of $Ti_3C_2T_X$-Fe_3O_4-CNT electrodes, compared to $Ti_3C_2T_X$-(Fe_3O_4-

CNT) electrodes. GCD data showed nearly triangular symmetric charge–discharge

curves, with longer charge and discharge times for $Ti_3C_2T_X$-Fe_3O_4-CNT electrodes,

compared to $Ti_3C_2T_X$-(Fe_3O_4-CNT) at the same current densities (Figure 6.7A,B). The

longer charge/discharge times indicated higher capacitances. The capacitances were

calculated from the GCD data and presented in Figure 6.7C at different current

densities. C_S reduced from 4.35 to 3.33 F·cm^{-2} and from 3.46 to 2.58 F·cm^{-2} for

Ti$_3$C$_2$T$_X$-Fe$_3$O$_4$-CNT and Ti$_3$C$_2$T$_X$-(Fe$_3$O$_4$-CNT) composites, respectively, with

current increase from 3 to 35 mA·cm^{-2}.
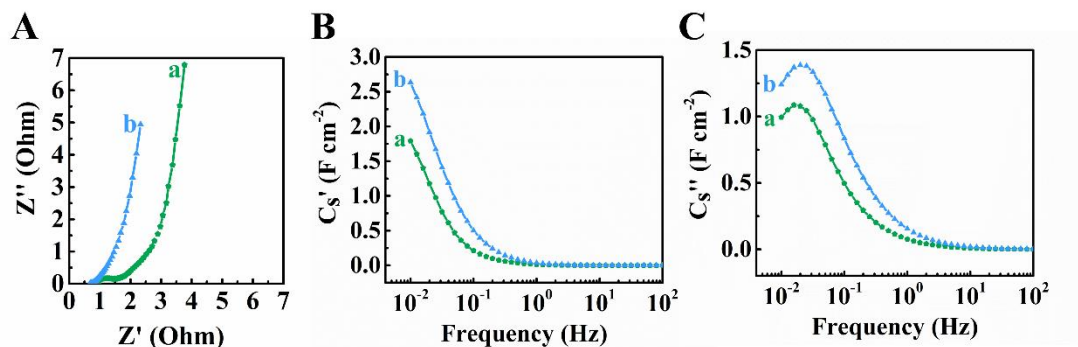
Figure 6.6. (A) Nyquist Z" vs. Z' graph for EIS data, ((B,C)), (B) C$_S$' and (C) C$_S$",
derived from the EIS data for (a) Ti$_3$C$_2$T$_X$-(Fe$_3$O$_4$-CNT) and (b) Ti$_3$C$_2$T$_X$-Fe$_3$O$_4$-CNT
electrodes.
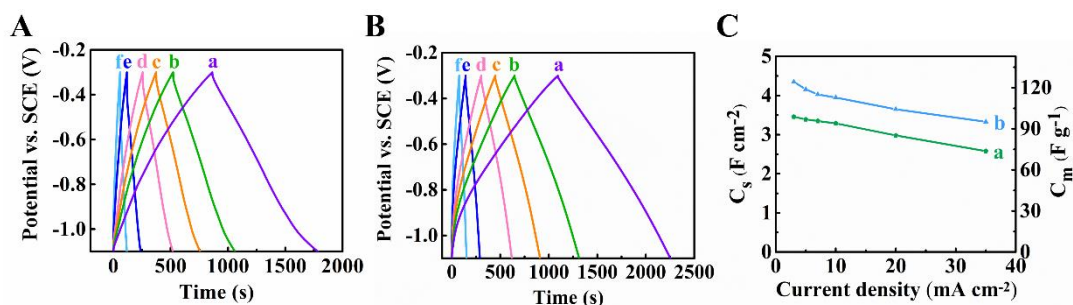
Figure 6.7. GCD curves for (A) Ti$_3$C$_2$T$_X$-Fe$_3$O$_4$-CNT), (B) Ti$_3$C$_2$T$_X$-Fe$_3$O$_4$-CNT at (a)
3, (b) 5 (c) 7, (d) 10 (e) 20 and (f) 35 mA·cm^{-2}, (C) capacitances versus current density,
calculated from GCD data for (a) Ti$_3$C$_2$T$_X$-(Fe$_3$O$_4$-CNT) and (b) Ti$_3$C$_2$T$_X$-Fe$_3$O$_4$-CNT.

The analysis of capacitances, measured using CV, EIS and GCD techniques showed

that the capacitances of the Ti$_3$C$_2$T$_X$-Fe$_3$O$_4$-CNT electrodes are higher than the

capacitances of the Ti$_3$C$_2$T$_x$-CNT and Fe$_3$O$_4$-CNT electrodes. Therefore, the

experimental results of this work showed a synergistic effect of the individual

capacitive materials. The comparison of the data for Ti$_3$C$_2$T$_X$-Fe$_3$O$_4$-CNT and

Ti$_3$C$_2$T$_X$-(Fe$_3$O$_4$-CNT) electrodes and literature data of the previous investigations for

$Ti_3C_2T_X$ [42] and Fe_3O_4 electrodes [43] showed the beneficial effect of co-dispersion of the individual components, which was achieved using CB as a dispersant. The ability to achieve high C_S of 5.52 F·cm^{-2} in the negative potential range in Na_2SO_4 is beneficial for the preparation of asymmetric SC. $Ti_3C_2T_X$-Fe_3O_4-CNT electrodes showed relatively high C_S, compared to other anode materials [41]. The comparison with C_S for other $Ti_3C_2T_X$-based electrodes in Na_2SO_4 electrolyte (Table 6.1) showed significant improvement in C_S. The capacitance of the negative electrodes is usually lower than that of positive electrodes. Advanced positive electrodes, based on MnO_2, Mn_3O_4, and $BiMn_2O_5$ have been developed with capacitance of about 5–8 F cm^{-2} in the positive potential range [41]. Therefore, the capacitance of $Ti_3C_2T_X$-Fe_3O_4-CNTs is comparable with capacitances of advanced positive electrodes. The $Ti_3C_2T_X$-Fe_3O_4-CNT electrodes showed a slight C_S increase for the first 400 cycles and remained nearly constant after this initial increase (Figure 6.8). A similar increase was observed in the literature for other materials and was attributed to microstructure changes during initial cycling [64,65]. In contrast, the capacitance of the $Ti_3C_2T_X$- CNT and Fe_3O_4-CNT electrodes decreased after cycling (Figure 6.8).
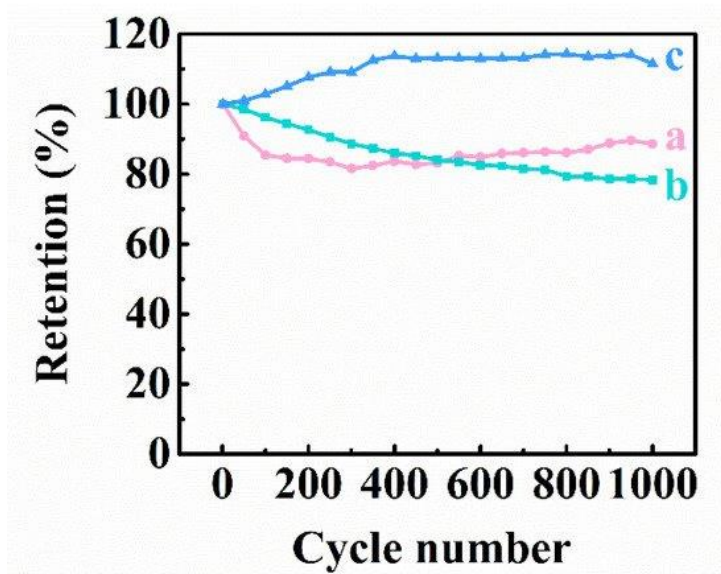
Figure 6.8. Capacitance retention for (a) $Ti_3C_2T_X$-CNT, (b) Fe_3O_4-CNT and (c) $Ti_3C_2T_X$-Fe_3O_4-CNT electrodes.

6.5 Conclusions

$Ti_3C_2T_X$-Fe_3O_4-CNT electrodes have been developed, which showed C_S of 5.52

$F \cdot cm^{-2}$ in the negative potential range in 0.5 M Na_2SO_4 electrolyte. Such electrodes

are promising for applications in asymmetric supercapacitor devices due to the high

capacitance, which is comparable with the capacitance of advanced positive

electrodes. The use of CB as an advanced co-dispersant allowed for the fabrication of

$Ti_3C_2T_X$-Fe_3O_4-CNT electrodes, which showed good capacitive performance at high

AM loadings. The comparison of capacitive behavior of $Ti_3C_2T_X$-Fe_3O_4-CNT

electrodes with $Ti_3C_2T_X$-CNT and Fe_3O_4-CNT electrodes with the same AM,

thickness and CNT content revealed a synergistic effect of the individual capacitive

materials.

6.6 Acknowledgements

SEM investigations were performed at the Canadian Centre for Electron Microscopy.

6.7 Supplementary Materials
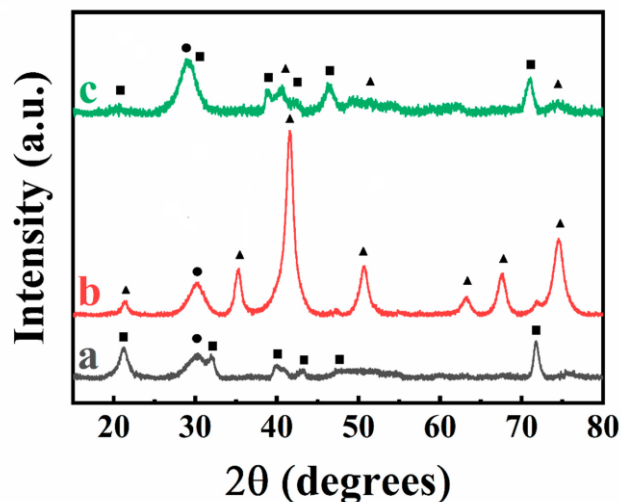
Figure 6.9. X-ray diffraction patterns of (a) $Ti_3C_2T_X$-CNT and (b) Fe_3O_4-CNT and (c) $Ti_3C_2T_X$-Fe_3O_4-CNT composites (■ - $Ti_3C_2T_X$, ● – CNT, ▲ – Fe_3O_4).
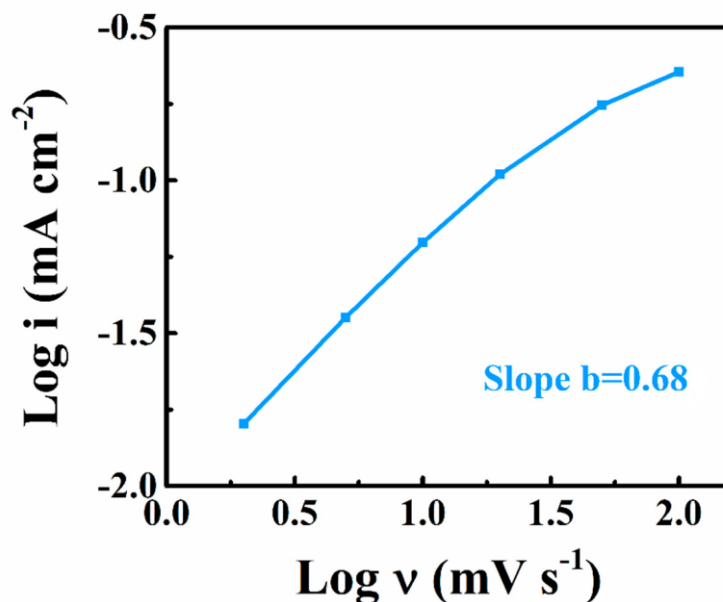
Figure 6.10. Current (i) versus scan rate (ν) dependence in a logarithmic scale used for the calculation of parameter b for $Ti_3C_2T_X$-Fe_3O_4-CNT electrodes from the equation

[66] $i = av^b$.

Table 6.1. Characteristics of $Ti_3C_2T_X$-based electrodes with high active mass in Na_2SO_4 electrolyte.

Material	Active Mass mg cm^{-2}	Potential Window	Areal Capacitance F cm^{-2}	Reference
$Ti_3C_2T_x$-acetylene black	20	0-0.9 V*	1.087	[67]
$Ti_3C_2T_x$-CNT	35	-1.1- -0.3 V vs SCE	1.93	[68]
$Ti_3C_2T_x$-CNT	40	-1.1- -0.3 V vs SCE	2.26	[69]
$Ti_3C_2T_x$-Fe_3O_4-CNT	35	-1.1- -0.3 V vs SCE	5.52	This work

*Measurements performed in two electrode configuration

6.8 References

1. Anasori, B.; Lukatskaya, M.R.; Gogotsi, Y. 2D metal carbides and nitrides (MXenes) for energy storage. *Nat. Rev. Mater.* **2017**, *2*, 16098.

2. Xu, S.; Wei, G.; Li, J.; Han, W.; Gogotsi, Y. Flexible MXene–graphene electrodes with high volumetric capacitance for integrated co-cathode energy conversion/storage devices. *J. Mater. Chem. A* **2017**, *5*, 17442–17451.

3. Gogotsi, Y.; Anasori, B. The Rise of MXenes. *ACS Nano* **2019**, *13*, 8491–8494.

4. Wang, K.; Zheng, B.; Mackinder, M.; Baule, N.; Qiao, H.; Jin, H.; Schuelke, T.; Fan, Q.H. Graphene wrapped MXene via plasma exfoliation for all-solid-state flexible supercapacitors. *Energy Storage Mater.* **2019**, *20*, 299–306.

5. Guo, J.; Zhao, Y.; Jiang, N.; Liu, A.; Gao, L.; Li, Y.; Wang, H.; Ma, T. One-pot synthesis of 2D $Ti_3C_2/Ni_2CO_3(OH)_2$ composite as electrode material with superior capacity and high stability for hybrid supercapacitor. *Electrochim. Acta* **2018**, *292*, 168–179.

6. Gao, Y.; Wang, L.; Li, Z.; Zhang, Y.; Xing, B.; Zhang, C.; Zhou, A. Electrochemical performance of Ti_3C_2 supercapacitors in KOH electrolyte. *J. Adv. Ceram.* **2015**, *4*, 130–134.

7. Tang, Y.; Zhu, J.; Wu, W.; Yang, C.; Lv, W.; Wang, F. Synthesis of Nitrogen-Doped Two-Dimensional Ti_3C_2 with Enhanced Electrochemical Performance. *J. Electrochem. Soc.* **2017**, *164*, A923–A929.

8. Tian, Y.; Que, W.; Luo, Y.; Yang, C.; Yin, X.; Kong, L.B. Surface nitrogen-modified 2D titanium carbide (MXene) with high energy density for aqueous supercapacitor applications. *J. Mater. Chem. A* **2019**, *7*, 5416–5425.

9. Wen, Y.; Rufford, T.E.; Chen, X.; Li, N.; Lyu, M.; Dai, L.; Wang, L. Nitrogen-doped $Ti_3C_2T_x$ MXene electrodes for high-performance supercapacitors. *Nano Energy* **2017**, *38*, 368–376.

10. Wang, F.; Cao, M.; Qin, Y.; Zhu, J.; Wang, L.; Tang, Y. ZnO nanoparticle-decorated two-dimensional titanium carbide with enhanced supercapacitive performance. *RSC Adv.* **2016**, *6*, 88934–88942.

11. Rakhi, R.B.; Ahmed, B.; Anjum, D.H.; Alshareef, H.N. Direct Chemical Synthesis of MnO_2 Nanowhiskers on Transition-Metal Carbide Surfaces for Supercapacitor Applications. *ACS Appl. Mater. Interfaces* **2016**, *8*, 18806–18814.

12. Cao, M.; Wang, F.; Wang, L.; Wu, W.; Lv, W.; Zhu, J. Room Temperature Oxidation of Ti_3C_2 MXene for Supercapacitor Electrodes. *J. Electrochem. Soc.* **2017**, *164*, A3933–A3942.

13. Oyedotun, K.O.; Momodu, D.Y.; Naguib, M.; Mirghni, A.A.; Masikhwa, T.M.; Khaleed, A.A.; Kebede, M.; Manyala, N. Electrochemical performance of two-

dimensional Ti_3C_2-Mn_3O_4 nanocomposites and carbonized iron cations for hybrid supercapacitor electrodes. *Electrochim. Acta* **2019**, *301*, 487–499.

14. Wang, H.; Zhang, J.; Wu, Y.; Huang, H.; Jiang, Q. Achieving high-rate capacitance of multi-layer titanium carbide (MXene) by liquid-phase exfoliation through Li-intercalation. *Electrochem. Commun.* **2017**, *81*, 48–51.

15. Wu, W.; Niu, D.; Zhu, J.; Gao, Y.; Wei, D.; Zhao, C.; Wang, C.; Wang, F.; Wang, L.; Yang, L. Hierarchical architecture of Ti_3C_2@PDA/NiCo$_2$S$_4$ composite electrode as high-performance supercapacitors. *Ceram. Int.* **2019**, *45*, 16261–16269.

16. Yang, C.; Que, W.; Tang, Y.; Tian, Y.; Yin, X. Nitrogen and Sulfur Co-Doped 2D Titanium Carbides for Enhanced Electrochemical Performance. *J. Electrochem. Soc.* **2017**, *164*, A1939–A1945.

17. Yuan, W.; Cheng, L.; Zhang, B.; Wu, H. 2D-Ti_3C_2 as hard, conductive substrates to enhance the electrochemical performance of MnO_2 for supercapacitor applications. *Ceram. Int.* **2018**, *44*, 17539–17543.

18. Zhang, C.; Wang, L.; Lei, W.; Wu, Y.; Li, C.; Khan, M.A.; Ouyang, Y.; Jiao, X.; Ye, H.; Mutahir, S.; et al. Achieving quick charge/discharge rate of $3.0\ V\ s^{-1}$ by 2D titanium carbide (MXene) via N-doped carbon intercalation. *Mater. Lett.* **2019**, *234*, 21–25.

19. Zhang, Y.; Yang, Z.; Zhang, B.; Li, J.; Lu, C.; Kong, L.; Liu, M. Self-assembly of secondary-formed multilayer La/e-Ti_3C_2 as high performance supercapacitive material with excellent cycle stability and high rate capability. *J. Alloys Compd.* **2020**, *835*, 155343.

20. He, X.; Bi, T.; Zheng, X.; Zhu, W.; Jiang, J. Nickel cobalt sulfide nanoparticles grown on titanium carbide MXenes for high-performance supercapacitor. *Electrochim. Acta* **2020**, *332*, 135514.

21. Hu, M.; Hu, T.; Li, Z.; Yang, Y.; Cheng, R.; Yang, J.; Cui, C.; Wang, X. Surface functional groups and interlayer water determine the electrochemical capacitance of Ti_3C_2 T x MXene. *ACS Nano* **2018**, *12*, 3578–3586.

22. Le, T.A.; Tran, N.Q.; Hong, Y.; Lee, H. Intertwined Titanium Carbide MXene within a 3D Tangled Polypyrrole Nanowires Matrix for Enhanced Supercapacitor Performances. *Chem. A Eur. J.* **2018**, *25*, 1037–1043.

23. Li, Z.; Ma, C.; Wen, Y.; Wei, Z.; Xing, X.; Chu, J.; Yu, C.; Wang, K.; Wang, Z.-K. Highly conductive dodecaborate/MXene composites for high performance supercapacitors. *Nano Res.* **2019**, *13*, 196–202.

24. Li, Y.; Deng, Y.; Zhang, J.; Han, Y.; Zhang, W.; Yang, X.; Zhang, X.; Jiang, W. Tunable energy storage capacity of two-dimensional $Ti_3C_2T_x$ modified by a facile two-step pillaring strategy for high performance supercapacitor electrodes. *Nanoscale* **2019**, *11*, 21981–21989.

25. Lin, S.-Y.; Zhang, X. Two-dimensional titanium carbide electrode with large

mass loading for supercapacitor. *J. Power Sources* **2015**, *294*, 354–359.

26. Ramachandran, R.; Rajavel, K.; Xuan, W.; Lin, D.; Wang, F. Influence of $Ti_3C_2T_x$ (MXene) intercalation pseudocapacitance on electrochemical performance of Co-MOF binder-free electrode. *Ceram. Int.* **2018**, *44*, 14425–14431.

27. Shen, L.; Zhou, X.; Zhang, X.; Zhang, Y.; Liu, Y.; Wang, W.; Si, W.; Dong, X. Carbon-intercalated $Ti_3C_2T_x$ MXene for high-performance electrochemical energy storage. *J. Mater. Chem. A* **2018**, *6*, 23513–23520.

28. Yang, C.; Que, W.; Yin, X.; Tian, Y.; Yang, Y.; Que, M. Improved capacitance of nitrogen-doped delaminated two-dimensional titanium carbide by urea-assisted synthesis. *Electrochim. Acta* **2017**, *225*, 416–424.

29. Lu, X.; Zhu, J.; Wu, W.; Zhang, B. Hierarchical architecture of PANI@ TiO_2/$Ti_3C_2T_x$ ternary composite electrode for enhanced electrochemical performance. *Electrochim. Acta* **2017**, *228*, 282–289.

30. Cao, J.; Han, Y.; Zheng, X.; Wang, Q. Preparation and electrochemical performance of modified $Ti_3C_2T_x$/polypyrrole composites. *J. Appl. Polym. Sci.* **2019**, *136*, 47003.

31. Jian, X.; He, M.; Chen, L.; Zhang, M.-M.; Li, R.; Gao, L.-J.; Fu, F.; Liang, Z.-H. Three-dimensional carambola-like MXene/polypyrrole composite produced by one-step co-electrodeposition method for electrochemical energy storage. *Electrochim. Acta* **2019**, *318*, 820–827.

32. Li, X.; Zhu, J.; Wang, L.; Wu, W.; Fang, Y. In–situ growth of carbon nanotubes on two–dimensional titanium carbide for enhanced electrochemical performance. *Electrochim. Acta* **2017**, *258*, 291–301.

33. Kim, K.; Okubo, M.; Yamada, A. Interfacial Dissociation of Contact-Ion-Pair on MXene Electrodes in Concentrated Aqueous Electrolytes. *J. Electrochem. Soc.* **2019**, *166*, A3739–A3744.

34. Li, J.; Yuan, X.; Lin, C.; Yang, Y.; Xu, L.; Du, X.; Xie, J.; Lin, J.; Sun, J. Achieving High Pseudocapacitance of 2D Titanium Carbide (MXene) by Cation Intercalation and Surface Modification. *Adv. Energy Mater.* **2017**, *7*, 1602725.

35. Luo, J.; Zhang, W.; Yuan, H.; Jin, C.; Zhang, L.; Huang, H.; Liang, C.; Xia, Y.; Zhang, J.; Gan, Y.; et al. Pillared Structure Design of MXene with Ultralarge Interlayer Spacing for High-Performance Lithium-Ion Capacitors. *ACS Nano* **2017**, *11*, 2459–2469.

36. Shi, M.; Narayanasamy, M.; Yang, C.; Zhao, L.; Jiang, J.; Angaiah, S.; Yan, C. 3D interpenetrating assembly of partially oxidized MXene confined Mn–Fe bimetallic oxide for superior energy storage in ionic liquid. *Electrochim. Acta* **2020**, *334*, 135546.

37. Li, H.; Chen, R.; Ali, M.; Lee, H.; Ko, M.J. In Situ Grown MWCNTs/MXenes Nanocomposites on Carbon Cloth for High-Performance Flexible

Supercapacitors. *Adv. Funct. Mater.* **2020**, *30*, 2002739.

38. Pan, Z.; Ji, X. Facile synthesis of nitrogen and oxygen co-doped C@Ti_3C_2 MXene for high performance symmetric supercapacitors. *J. Power Sources* **2019**, *439*, 227068.

39. Wu, W.; Wei, D.; Zhu, J.; Niu, D.; Wang, F.; Wang, L.; Yang, L.; Yang, P.; Wang, C. Enhanced electrochemical performances of organ-like Ti_3C_2 MXenes/polypyrrole composites as supercapacitors electrode materials. *Ceram. Int.* **2019**, *45*, 7328–7337.

40. Yang, B.; She, Y.; Zhang, C.; Kang, S.; Zhou, J.; Hu, W. Nitrogen Doped Intercalation TiO_2/TiN/$Ti_3C_2T_x$ Nanocomposite Electrodes with Enhanced Pseudocapacitance. *Nanomaterials* **2020**, *10*, 345.

41. Chen, R.; Yu, M.; Sahu, R.P.; Puri, I.; Zhitomirsky, I. The Development of Pseudocapacitor Electrodes and Devices with High Active Mass Loading. *Adv. Energy Mater.* **2020**, *10*, 1903848.

42. Guo, M.; Liu, C.; Zhang, Z.; Zhou, J.; Tang, Y.; Luo, S. Flexible $Ti_3C_2T_x$@Al electrodes with Ultrahigh Areal Capacitance: In Situ Regulation of Interlayer Conductivity and Spacing. *Adv. Funct. Mater.* **2018**, *28*, 1803196.

43. Nawwar, M.; Poon, R.; Chen, R.; Sahu, R.P.; Puri, I.K.; Zhitomirsky, I. High areal capacitance of Fe_3O_4-decorated carbon nanotubes for supercapacitor electrodes. *Carbon Energy* **2019**, *1*, 124–133.

44. Reddy, R.N.; Reddy, R.G. Sol—Gel MnO_2 as an electrode material for electrochemical capacitors. *J. Power Sources* **2003**, *124*, 330–337.

45. Jeong, Y.U.; Manthiram, A. Nanocrystalline Manganese Oxides for Electrochemical Capacitors with Neutral Electrolytes. *J. Electrochem. Soc.* **2002**, *149*, A1419–A1422.

46. Dong, W.; Rolison, D.R.; Dunna, B. Electrochemical Properties of High Surface Area Vanadium Oxide Aerogels. *Electrochem. Solid State Lett.* **1999**, *3*, 457–459.

47. Dong, W.; Sakamoto, J.S.; Dunn, B. Electrochemical properties of vanadium oxide aerogels. *Sci. Technol. Adv. Mater.* **2003**, *4*, 3–11.

48. Sinan, N.; Unur, E. Fe3O4/carbon nanocomposite: Investigation of capacitive & magnetic properties for supercapacitor applications. *Mater. Chem. Phys.* **2016**, *183*, 571–579.

49. Ghaly, H.A.; El-Deen, A.G.; Souaya, E.R.; Allam, N.K. Asymmetric supercapacitors based on 3D graphene-wrapped V_2O_5 nanospheres and Fe_3O_4@3D graphene electrodes with high power and energy densities. *Electrochim. Acta* **2019**, *310*, 58–69.

50. Nithya, V.D.; Arul, N.S. Progress and development of Fe_3O_4 electrodes for supercapacitors. *J. Mater. Chem. A* **2016**, *4*, 10767–10778.

51. Gogotsi, Y.; Simon, P. True Performance Metrics in Electrochemical Energy

Storage. *Science* **2011**, *334*, 917–918.

52. Li, J.; Zhitomirsky, I. Cathodic electrophoretic deposition of manganese dioxide films. *Colloids Surf. A Physicochem. Eng. Asp.* **2009**, *348*, 248–253.

53. Stoller, M.D.; Ruoff, R.S. Best practice methods for determining an electrode material's performance for ultracapacitors. *Energy Environ. Sci.* **2010**, *3*, 1294–1301.

54. Chen, J.; Fang, K.; Chen, Q.; Xu, J.; Wong, C.-P. Integrated paper electrodes derived from cotton stalks for high-performance flexible supercapacitors. *Nano Energy* **2018**, *53*, 337–344.

55. Liu, Y.; Zhitomirsky, I. Electrochemical supercapacitor based on multiferroic $BiMn_2O_5$. *J. Power Sources* **2015**, *284*, 377–382.

56. Liang, W.; Zhitomirsky, I. Zn-Fe Double Hydroxide-Carbon Nanotube Anodes for Asymmetric Supercapacitors. *Front. Mater.* **2020**, *7*, 137.

57. Liu, Y.; Ata, M.S.; Shi, K.; Zhu, G.-Z.; Botton, G.A.; Zhitomirsky, I. Surface modification and cathodic electrophoretic deposition of ceramic materials and composites using celestine blue dye. *RSC Adv.* **2014**, *4*, 29652–29659.

58. Ata, M.S.; Liu, Y.; Zhitomirsky, I. A review of new methods of surface chemical modification, dispersion and electrophoretic deposition of metal oxide particles. *RSC Adv.* **2014**, *4*, 22716–22732.

59. Ata, M.S.; Poon, R.; Syed, A.M.; Milne, J.; Zhitomirsky, I. New developments in non-covalent surface modification, dispersion and electrophoretic deposition of carbon nanotubes. *Carbon* **2018**, *130*, 584–598.

60. Zhu, Y.; Shi, K.; Zhitomirsky, I. Polypyrrole coated carbon nanotubes for supercapacitor devices with enhanced electrochemical performance. *J. Power Sources* **2014**, *268*, 233–239.

61. Shi, K.; Zhitomirsky, I. Fabrication of Polypyrrole-Coated Carbon Nanotubes Using Oxidant–Surfactant Nanocrystals for Supercapacitor Electrodes with High Mass Loading and Enhanced Performance. *ACS Appl. Mater. Interfaces* **2013**, *5*, 13161–13170.

62. Okhay, O.; Tkach, A. Graphene/Reduced Graphene Oxide-Carbon Nanotubes Composite Electrodes: From Capacitive to Battery-Type Behaviour. *Nanomaterials* **2021**, *11*, 1240.

63. Gogotsi, Y.; Penner, R.M. Energy Storage in Nanomaterials—Capacitive, Pseudocapacitive, or Battery-like? *ACS Nano* **2018**, *12*, 2081–2083.

64. Rorabeck, K.; Zhitomirsky, I. Application of Octanohydroxamic Acid for Salting out Liquid–Liquid Extraction of Materials for Energy Storage in Supercapacitors. *Molecules* **2021**, *26*, 296.

65. Rorabeck, K.; Zhitomirsky, I. Salting-out aided dispersive extraction of Mn_3O_4 nanoparticles and carbon nanotubes for application in supercapacitors. *Colloids Surf. A Physicochem. Eng. Asp.* **2021**, *618*, 126451.

66. Okhay, O.; Tkach, A.; Graphene/Reduced Graphene Oxide-Carbon Nanotubes Composite Electrodes: From Capacitive to Battery-Type Behaviour. Nanomaterials 2021, 11, 1240.

67. Guo, M.; Liu, C.; Zhang, Z.; Zhou, J.; Tang, Y.; Luo, S. Flexible $Ti_3C_2T_x$ @ Al electrodes with ultrahigh areal capacitance: in situ regulation of interlayer conductivity and spacing. Adv. Funct. Mater. 2018, 28, 1803196.

68. Liang, W.; Zhitomirsky, I.; MXene–carbon nanotube composite electrodes for high active mass asymmetric supercapacitors. J. Mater. Chem. A 2021, 9, 10335–10344.

69. Li, X.; Zhu, J.; Liang, W.; Zhitomirsky, I.; MXene ($Ti_3C_2T_x$) Anodes for Asymmetric Supercapacitors with High Active Mass Loading. Mater. Chem. Phys. 2021, in press.

Chapter 7 Zn-Fe Double Hydroxide-Carbon Nanotube Anodes for Asymmetric Supercapacitors

W Liang* and I. Zhitomirsky*[α]

*Department of Materials Science and Engineering, McMaster University,

Hamilton, Ontario, L8S 4L7, Canada

[α]Corresponding Author: zhitom@mcmaster.ca; 905-525-9140 ext. 23914

7.1 Abstract

Zn-Fe double hydroxide (Zn-Fe-DH)–multiwalled carbon nanotube (MWCNT) composite has been developed as a new material for energy storage in negative electrodes of asymmetric supercapacitors. A conceptually new approach is based on the use of celestine blue (CB) dye as a multifunctional additive. We discovered that CB acted as a co-dispersant for Zn-Fe-DH and MWCNT and facilitated their mixing. New strategy was based on the use of CB as charge transfer mediator, which facilitated charge-discharge reactions. The electrodes showed a capacitance of 5.2 F cm^{-2} in 0.5 M Na$_2$SO$_4$ electrolyte in a voltage window of -1.0 to -0.2 V vs. saturated calomel electrode and good cyclic stability. A new asymmetric device has been developed, containing Zn-Fe-DH-MWCNT negative electrodes and polypyrrole coated MWCNT positive electrodes. Good capacitive behavior of cathode and anode materials was achieved at high active mass of 40 mg cm^{-2} in partially overlapping potential windows. The device showed promising performance in a voltage window of 1.6 V. The capacitance of 2.2 F cm^{-2} was obtained at a scan rate of 2 mV s^{-1}.

7.2 Introduction

Transition metal-based materials have generated significant interest for applications in energy generation and storage devices (Cheong and Zhitomirsky, 2009; Zhai et al., 2018; Cesano et al., 2019; Chen et al., 2019; Dong et al., 2019). Various oxides, such as Fe_2O_3 (Nasibi et al., 2012), Mn_3O_4 (Dubal et al., 2009), MnO_2 (Su and Zhitomirsky, 2014), NiO (Chai et al., 2012), and Co_3O_4 (Xia et al., 2011) were investigated for electrodes of supercapacitors. Oxide materials showed high capacitance and good power-energy characteristics. However, due to poor electrolyte access to the active material and high electrical resistance, the specific capacitance decreases significantly with increasing active material mass. The active mass loadings for practical applications must be ≥ 10 mg cm^{-2} (Brisse et al., 2018).

There has been significant progress in the development of capacitive transition metal hydroxide materials. Enhanced electrochemical performance for active mass loadings of 10–28.6 mg cm^{-2} has been achieved (Chen et al., 2015; Xu et al., 2016). New techniques have been developed for the fabrication of different nanoparticles, such as nanoleafs (Xu et al., 2016), coin-like nanoplatelets (Li et al., 2011), flower-like particles (Zhang Y. et al., 2015), and nanorods (Lakshmi et al., 2014). Different $Ni(OH)_2$ phases have been investigated, such as α-$Ni(OH)_2$ (Xu et al., 2016) and β-$Ni(OH)_2$ (Li et al., 2011). New methods have been developed for the fabrication of $Ni(OH)_2$ coated carbon nanotubes (Wang et al., 2006b). Research efforts were focused on the synthesis of

90

nanoparticles with small particle size, high surface area, advanced design, and optimization of electrolyte composition (Xi et al., 2017). Significant interest has been generated in the development of flexible devices (Ma et al., 2016).

Various strategies have been developed for the fabrication of cobalt hydroxide and composite electrodes with active mass of 10–25 mg cm^{-2}. A hydrothermal method has been developed for the fabrication of CoOOH nanorods with a diameter of 5–10 nm (Raj et al., 2015). The nanorod nanostructure allowed for high capacitance and good cyclic stability (Raj et al., 2015). The development of advanced deposition and synthesis methods for α-Co(OH)$_2$ and β-Co(OH)$_2$ resulted in enhanced performance (Gao et al., 2013; Aghazadeh et al., 2014; Zhou et al., 2015).

There is substantial interest in investigating FeOOH and composite materials for negative electrodes. Electrochemical testing was performed in Li$_2$SO$_4$, and Na$_2$SO$_4$ electrolytes, which offer benefits for the fabrication of asymmetric devices with relatively large voltage windows (Jin et al., 2008). The columned β-FeOOH particles with diameters and lengths in the ranges of 40–50 and 200–300 nm, respectively, were prepared and used for the fabrication of electrodes (Jin et al., 2008) with mass loading of 10 mg cm^{-2}. The electrodes showed a capacitance of 116 F g^{-1} within the potential window −0.85 to −0.1 V. The high power density of 3,700 W kg^{-1} and energy density of 12 Wh kg^{-1} were achieved for an asymmetric device, containing FeOOH as a negative and MnO$_2$ as a positive electrode in a voltage window of 1.85 V.

The development of new colloidal techniques (Silva et al., 2018) facilitated the fabrication of FeOOH and composite electrodes with active mass of 36–39.6 mg cm^{-2}. New techniques for the fabrication of non-agglomerated particles (Chen et al., 2018) allowed for enhanced performance of FeOOH electrodes. Asymmetric devices (Chen et al., 2018) containing α–FeOOH-carbon nanotube negative electrodes and MnO$_2$-carbon nanotube positive electrodes showed good electrochemical performance.

It was discovered that enhanced capacitive properties can be achieved in double hydroxides in KOH electrolyte. The addition of Co to Ni(OH)$_2$ resulted in the changes of microstructure (Liu et al., 2013) and a drastic improvement in the capacitance. Nanostructured Co-Si and Co-Al and Ni-Al double hydroxides were prepared with mass loadings of 20–28 mg cm^{-2}, respectively (Wang et al., 2005, 2006a, 2010; Zhang et al., 2006; Hu et al., 2013) and tested in alkaline solutions. Good electrochemical performance was achieved in hybrid Ni-Co arrays formed on a copper foam. The Ni–Co hydroxide/Cu(OH)$_2$ nanoarray exhibited ultrahigh capacitance, excellent rate capacity and good cycling stability (Zhang et al., 2016).

Previous investigations showed that the development and testing of double hydroxide materials is a promising avenue for the fabrication of advanced supercapacitor electrodes. The objective of this investigation was the development of Zn-Fe double hydroxide (Zn-Fe-DH) for negative electrodes of supercapacitors. Following this work objective, we have developed electrodes with high active mass in order to meet

requirements (Brisse et al., 2018) of mass loadings ≥ 10 mg cm^{-2} for practical applications. The approach was based on the use of celestine blue dye as a multifunctional dispersant. We targeted the development of electrodes for operation in Na$_2$SO$_4$ electrolyte, which is beneficial for the development of asymmetric devices with enlarged voltage window. An asymmetric device has been fabricated and tested, containing Zn-Fe-DH negative electrodes and polypyrrole-MWCNT positive electrodes.

7.3 Experimental procedures

Iron chloride hexahydrate (FeCl$_3$·6H$_2$O), zinc chloride (ZnCl$_2$), celestine blue (CB), sodium sulfate (Na$_2$SO$_4$), eriochrome cyanine R (ECR), pyrrole (Py), ammonium persulfate [(NH$_4$)$_2$S$_2$O$_8$]] (APS), and poly(vinyl butyral-co-vinyl-alcohol-co-vinyl acetate) (PVB, average Mw = 50,000–80,000) were purchased from Sigma Aldrich Corp. Multi-walled carbon nanotubes (MWCNT, ID 4 nm, OD 13 nm, length 1~2 μm) were purchased from Bayer (Germany), and Ni foams with 95% porosity were provided by Vale Canada Limited.

Synthesis of Zn-Fe-DH was performed by a chemical precipitation method, described in the literature (Krehula et al., 2006) which presents data on characterization of this material. In a typical procedure, MWCNT were added to 50 mL of CB solution in a mass ratio 1:1 and obtained suspension was ultrasonicated for 0.5 h. ZnCl$_2$ and

FeCl$_3 \cdot$6H$_2$O in a molar ratio R = [39]/[39]+[Fe] of 0.1 were dissolved in DI water. The

pH of the solution was adjusted to 13.8 by dropwise addition of 4M NaOH for the

precipitation of Zn-Fe-DH. Then suspensions of CB dispersed MWCNTs and Zn-Fe-

DH were mixed and ultrasonicated for 45 min, followed by the filtration and drying

procedure at 60°C for 24 h. The composites were mixed with PVB (3% by mass) and

impregnated from a suspension in ethanol into the Ni foam current collectors. The

negative electrodes were fabricated with mass loadings of 40 mg cm^{-2}.

For the synthesis of polypyrrole-coated MWCNT (PPy-MWCNT), ECR and MWCNT

were mixed in 50 mL DI water in a mass ratio of 2:9, followed by ultrasonication for

30 min. The obtained MWCNT suspensions, containing ECR as a dispersant, were kept

in ice bath to maintain the temperature at 4°C, and 0.24 mL of Py solution was added.

Chemical polymerization of PPy was performed by addition of APS solution to the Py-

MWCNT mixture, containing ECR as a dopant for PPy polymerization and dispersant

for MWCNT. Obtained PPy-MWCNT contained PPy and MWCNT in a mass ratio 3:7.

The reaction was carried out for 5 h. PPy-MWCNT were filtrated and dried at 60°C for

24 h. PPy-MWCNT were mixed with PVB (3% by mass) in ethanol and impregnated

into the Ni foam current collectors. The positive electrodes were fabricated with mass

loadings of 40 mg cm^{-2}.

Cyclic voltammetry (CV) and impedance spectroscopy (EIS) were performed using a

potentiostat (PARSTAT 2273, Princeton Applied Research). The electrochemical

measurements were carried out in a three-electrode setup with 0.5 M Na_2SO_4 electrolyte.

Pt gauze and saturated calomel electrode (SCE) were used as counter and reference

electrodes, respectively, and the area of working electrode was 1 cm^2. CV studies were

performed at scan rates of 2–100 mV s^{-1}, and the gravimetric capacitance (C_m =

$Q/2\Delta Vm$) and areal capacitance (C_s = $Q/2\Delta VA$) were calculated by integrating the CV

curve area (Shi and Zhitomirsky, 2010) to obtain charge Q, and subsequently dividing

by the voltage window (ΔV) and mass (m) or area (A). EIS measurements were carried

out in the frequency range of 10 mHz–100 kHz with a sinusoidal signal of 10 mV. The

components of complex capacitance (Cs' and Cs'') were calculated from the EIS data

as $Cs' = Z''/\omega|Z|^2A$ and $Cs'' = Z'/\omega|Z|^2A$, where $\omega = 2\pi f$ and f is frequency.

Galvanostatic charge-discharge of the device was performed using a battery analyzer

(BST8-MA, MTI Corp.).

7.4 Results and discussion

Figure 7.1A shows chemical structure of CB, used in this investigation as a co-

dispersant for MWCNT and Zn-Fe-DH. The dispersant adsorption on inorganic

particles plays an important role in the particle dispersion (Wang et al., 2011). The

polyaromatic structure of CB was beneficial for its adsorption on MWCNT, which

involved π-π interactions (Ata et al., 2018). It should be noted that the chemical

structure of CB contains a catechol group. Various molecules from catechol family

showed strong adsorption on various inorganic materials (Ata et al., 2014). Similar to

other catecholates, the adsorption of CB on Zn-Fe-DH involved bridging or chelating

bonding (Figure 7.1B). Moreover, electrostatic interactions promoted CB adsorption on

Zn-Fe hydroxide. Electrophoretic deposition experiments showed that Zn-Fe-DH

particles, precipitated at pH = 13.8, were negatively charged. Therefore, the

electrostatic attraction of negatively charged Zn-Fe-DH and positively charged CB

facilitated CB adsorption on the Zn-Fe-DH particles. It was found that adsorbed

cationic CB provided electrostatic dispersion of MWCNT and Zn-Fe-DH particles.

Sedimentation tests revealed enhanced stability of MWCNT and Zn-Fe-DH

suspensions, containing CB. It was hypothesized that CB can potentially improve

mixing of MWCNT and Zn-Fe-DH because CB, adsorbed on the MWCNT, interacted

with Zn-Fe-DH particles by chemical bonding or electrostatic interactions.

A

B
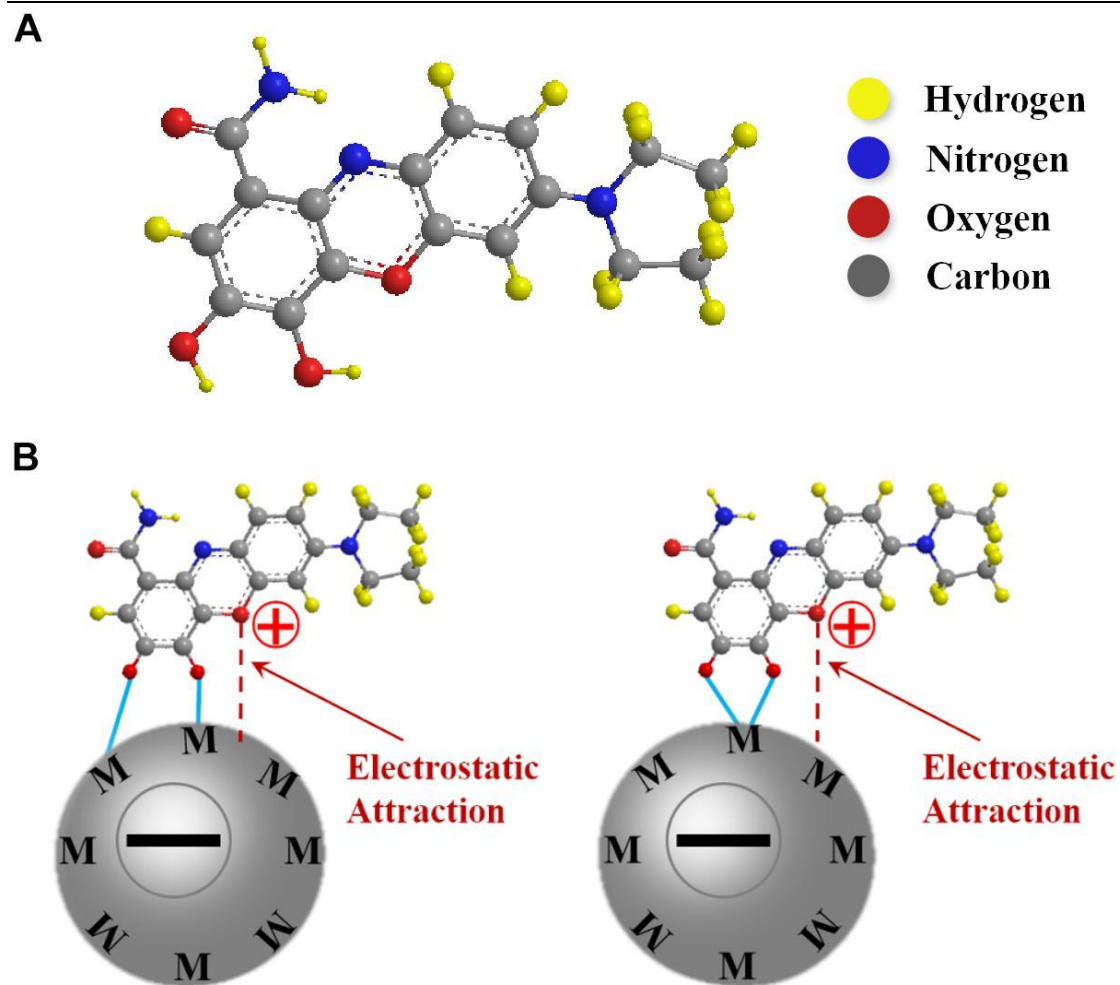
Figure 7.1. (A) Chemical structure of CB (B) adsorption mechanisms of CB on metal surface by (a) bridging and (b) chelation.

Figure 7.2 shows Zn-Fe-DH -MWCNT composite particles. The typical size of the particles was 0.5–3 μm (Figure 7.2A). The SEM image at higher magnification (Figure 7.2B) showed that MWCNT created a network inside the Zn-Fe-DH matrix. The conductive MWCNT matrix was beneficial for capacitive behavior.
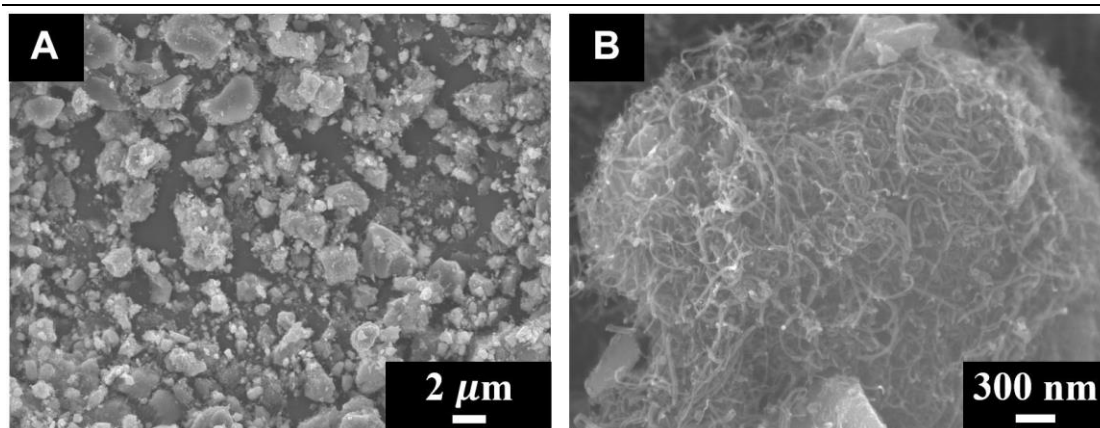
Figure 7.2. SEM for Zn-Fe-DH -MWCNT at (A,B) different magnifications.

The SEM data coupled with sedimentation tests confirm that CB provided dispersion

of Zn-Fe-DH and MWCNT, which was beneficial for their enhanced mixing. The SEM

images of as-received MWCNT were presented in a previous investigation (Wallar et

al., 2017). As-received MWCNT formed large agglomerates with a typical size of 500

μm. It is challenging to break down such agglomerates. However, such large

agglomerates were not observed in the low magnification image shown in Figure 7.2A.

Therefore, CB allowed efficient dispersion of MWCNT, which formed much smaller

composite particles, containing MWCNT in the Zn-Fe-DH matrix (Figure 7.2B). The

Zn-Fe-DH electrode showed a nearly rectangular CV (Figure 7.3). The capacitance of

5.2 F cm^{-2} was achieved at a scan rate of 2 mV s^{-1}. The high capacitance was achieved

at relatively low resistance R = Z' (Figure 7.4A). The frequency dependence of complex

capacitance showed a relaxation type dispersion (Figures 7.4B,C) with relaxation

frequency of about 50 mHz. EIS data indicated that the electrodes prepared using CB

showed reduced resistance and higher capacitance, compared to the electrodes prepared

without CB (Supplementary Figures 7.11A–C). The electrodes showed capacitance retention of 98% after 1,000 cycles (Figure 7.5). The capacitive behavior of the electrodes has also been studied by chronopotentiometry. Figure 7.6 shows typical charge-discharge curves at different current densities. The charge-discharge curves at different current densities in the range of 3–10 mA cm^{-2} were of nearly triangular shape in the voltage window of −1.0 to −0.2 V. Good electrochemical performance of the electrodes was achieved at active mass loading of 40 mg cm^{-2}, which is important for practical applications. It is important to note that low capacitance of negative electrodes is a limiting factor in the development of asymmetric supercapacitor devices. Another difficulty is related to poor cyclic stability of FeOOH electrodes (Shou et al., 2012). Therefore, the high capacitance of the Zn-Fe-DH-MWCNT composites and good cyclic stability are promising for the development of novel supercapacitor devices. It is suggested that more electrochemically negative Zn component allowed for the improved stability of FeOOH active material during cycling. We also suggested that CB facilitates charge transfer (CT) between Zn-Fe-DH and MWCNT and allows for better utilization of charge storage properties of Zn-Fe-DH. The enhanced CT resulted from the catecholate type bonding of CB to Zn-Fe-DH. Catechol-type molecules are widely used as CT mediators in different fields, such as electropolymerization on metal substrates (Tallman et al., 2002; Shi and Zhitomirsky, 2011; Chen and Zhitomirsky, 2013), photovoltaic devices (Wang et al., 2009; Varaganti and Ramakrishna,

2010; Verma et al., 2011) and advanced sensors (Sangeetha and Sriman Narayanan, 2014). In addition, a redox-type mode of the CT mediation can be considered. It is known that CB is an efficient redox-type CT mediator for electrocatalysis (Noorbakhsh et al., 2008), where it is used to transfer electrons between analytes and electrodes. CB shows redox properties in a negative potential range with high electron CT rate constant, excellent reversibility and chemical stability (Noorbakhsh et al., 2008). Therefore, high capacitance of the Zn-Fe-DH-MWCNT electrodes resulted from good dispersion and mixing of the individual components and enhanced CT achieved using CB as a multifunctional additive. It should be noted that direct contribution of CB to the total capacitance is very small due to low amount of CB used and small specific capacitance of this relatively large molecule. The Zn-Fe-DH-MWCNT showed enhanced performance in the negative potential range and outperformed many other candidate materials in the same potential window at high active mass loading in Na_2SO_4 electrolyte. Of particular importance is nearly ideal box shape CV and high areal capacitance. As pointed out above, many hydroxide materials show good capacitive behavior in alkaline electrolytes, such as KOH. The use of environmentally more friendly Na_2SO_4 electrolyte offers benefits for the development of asymmetric devices with enlarged voltage window. Therefore, the Zn-Fe-DH-MWCNT composites were used as negative electrodes for asymmetric supercapacitor devices.
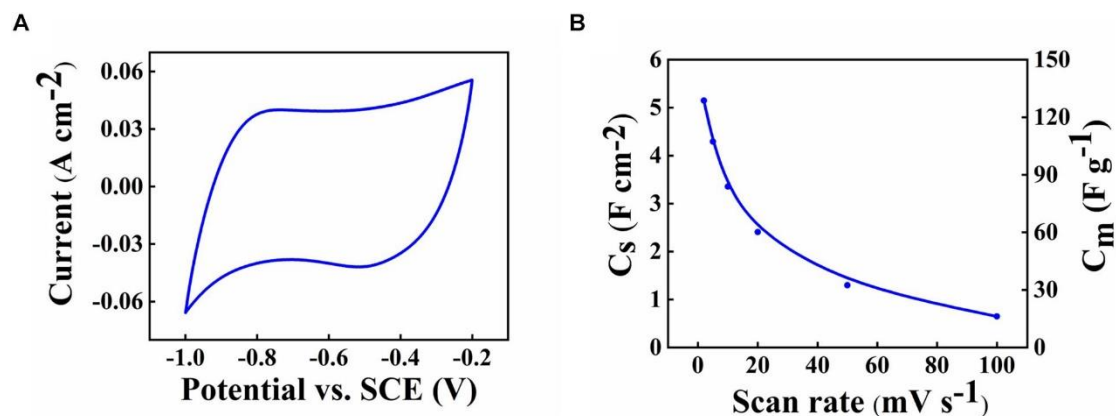
Figure 7.3. (A) CVs at scan rate of 10 mV s^{-1} and (B) C$_S$ and C$_m$ for Zn-Fe-DH - MWCNT.
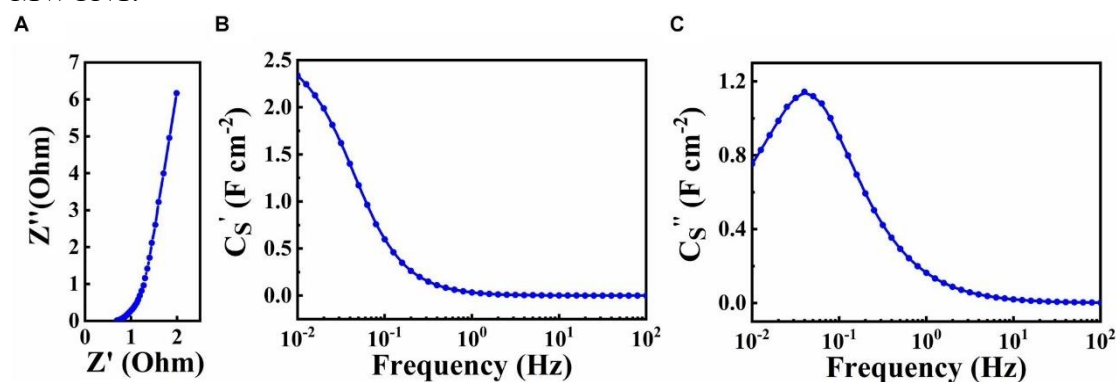
Figure 7.4. (A) Nyquist plot of complex impedance and frequency dependences of complex capacitance components (B) Cs′ and (C) Cs″ for Zn-Fe-DH -MWCNT.
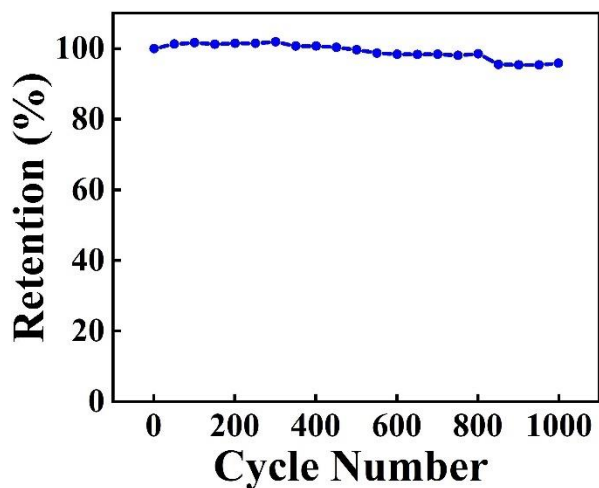
Figure 7.5. Capacitance retention vs. cycle number for Zn-Fe-DH -MWCNT.
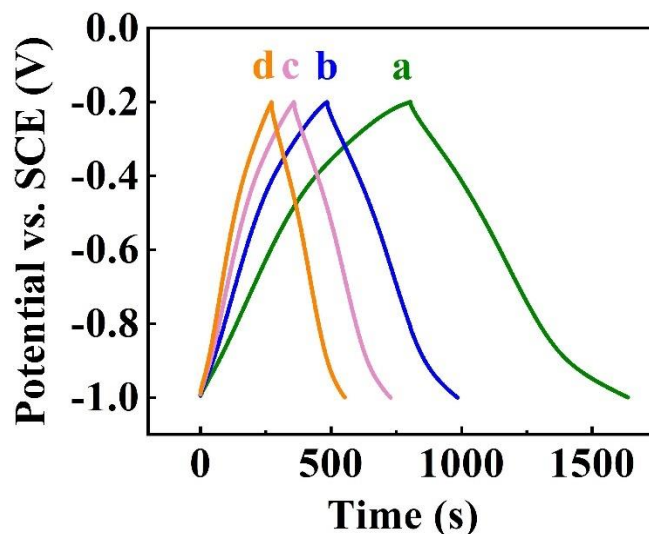
Figure 7.6. Galvanostatic charge-discharge curves at current densities of (a) 3, (b) 5, (c) 7, (d) 10 mA cm^{-2} for Zn-Fe-DH -MWCNT.

The fabrication of asymmetric devices with enlarged voltage window requires the development of positive and negative electrodes, operating in partially overlapping voltage windows in the same electrolyte (Zhang Z. et al., 2015; Attias et al., 2017). We found that PPy-MWCNT electrodes are promising as positive electrodes for asymmetric supercapacitor devices in a combination with negative Zn-Fe-DH - MWCNT electrodes. Figure 7.7 shows a microstructure of the PPy-MWCNT material, prepared by a chemical polymerization. The material consisted of PPy coated MWCNT. The ECR dispersant for MWCNT acted as an anionic dopant for PPy polymerization and allowed for the fabrication of uniformly coated MWCNT. Such microstructure allowed for enhanced charge transfer between MWCNT and PPy. The CV for the PPy-MWCNT electrode in the 0.5 M Na$_2$SO$_4$ electrolyte was of nearly rectangular shape (Figure 7.8) in a voltage window of −0.3 to +0.6 V, which partially

overlapped with a voltage window of Zn-Fe-DH -MWCNT negative electrodes. The

highest capacitance of 4.2 F cm^{-2} was achieved at a scan rate of 2 mV s^{-1}. The

capacitance decreased with increasing scan rate due to electrolyte diffusion limitation

in pores. Good electrochemical performance was achieved at a mass loading of 40 mg

cm^{-2}, which allowed for a relatively high ratio (0.5) of mass loading to current

collector mass.
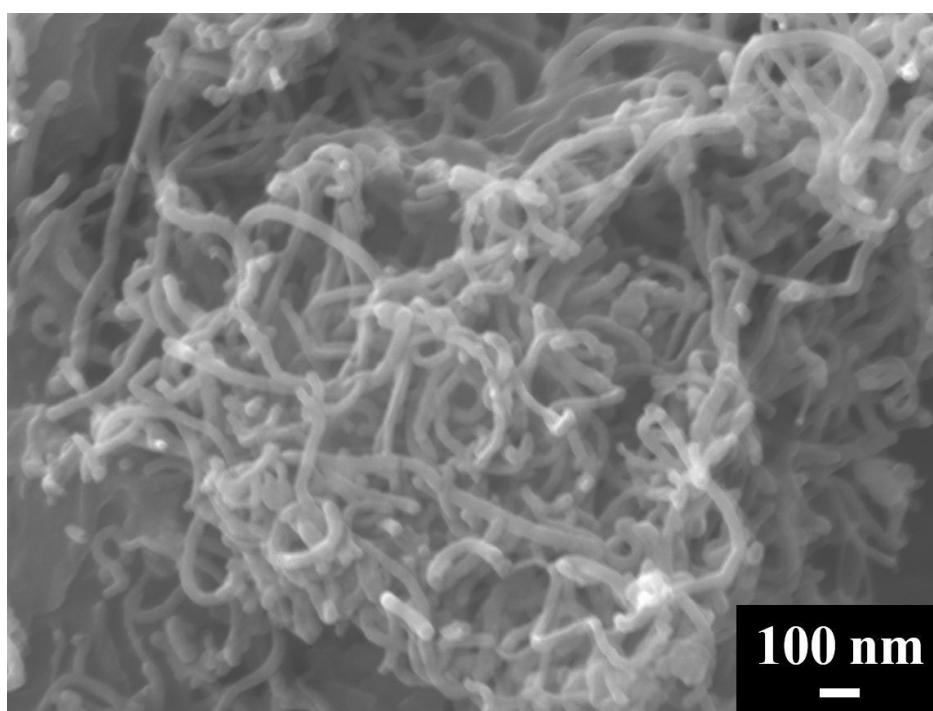
Figure 7.7. SEM image of PPy-MWCNT composite.
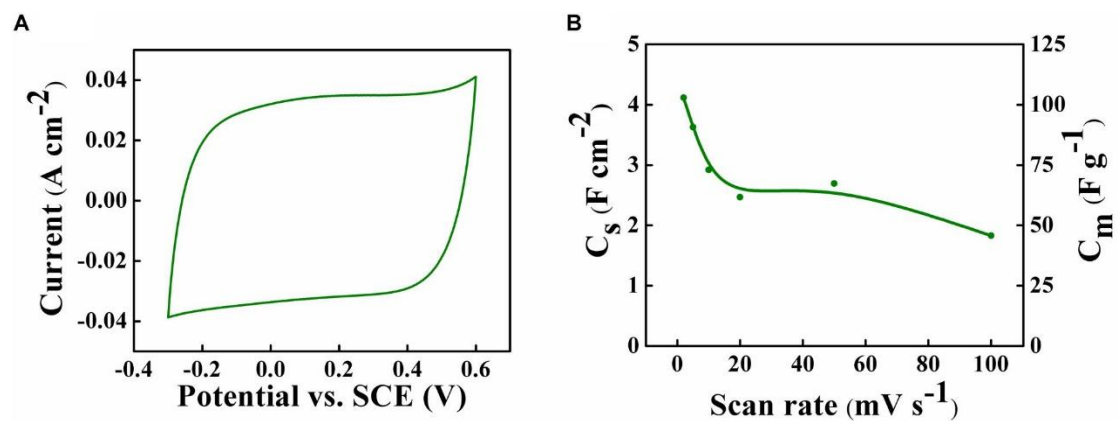
Figure 7.8. (A) CV at scan rate of 10 mV s^{-1} and (B) C_s and C_m vs. scan rate for PPy-MWCNT composite.

The Zn-Fe-DH -MWCNT negative electrodes and PPy-MWCNT positive electrodes were used for the fabrication of a novel asymmetric supercapacitor device. Such device showed a nearly rectangular CV in a voltage window of 1.6 V in 0.5 M Na$_2$SO$_4$ electrolyte (Figure 7.9). The areal capacitance, calculated from the CV data was found to be 2.2 F cm^{-2} at a scan rate of 2 mV s^{-1}. The device showed triangular shape charge-discharge curves at different current densities in a voltage window of 1.6 V (Figure 7.10).
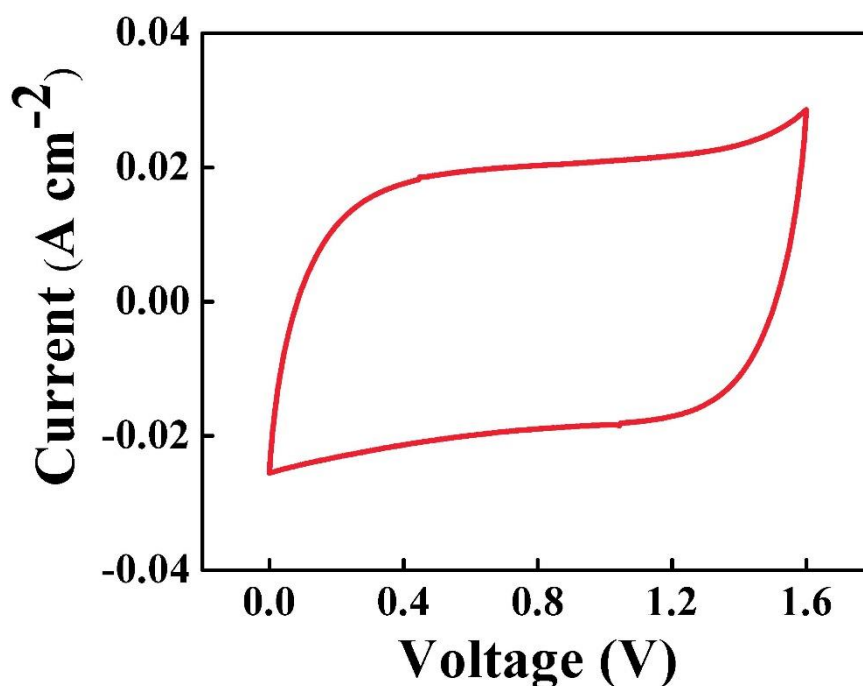
Figure 7.9. CV at scan rate of 10 mV s^{-1} of asymmetric supercapacitor cell containing Zn-Fe-DH -MWCNT negative electrode and PPy-MWCNT positive electrode.
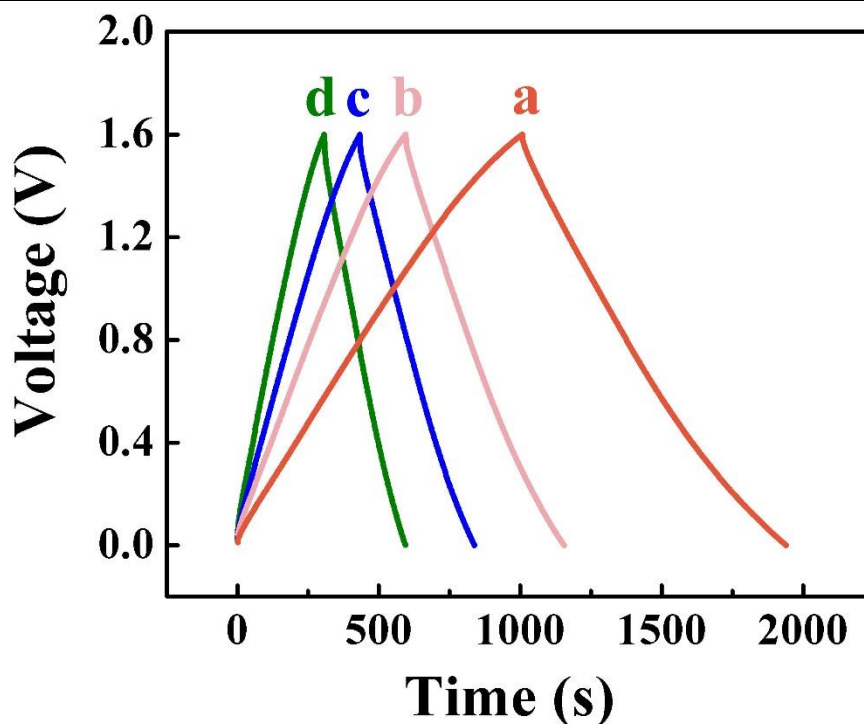
Figure 7.10. Galvanostatic charge-discharge curves at current densities of (a) 3, (b) 5, (c) 7, (d) 10 mA cm^{-2} for asymmetric supercapacitor cell.

7.5 Conclusion

Zn-Fe-DH-MWCNT composite has been developed as a new material for energy storage in negative electrodes of asymmetric supercapacitors. A conceptually new approach is based on the use of CB as a multifunctional additive. We discovered that CB acted as a co-dispersant for Zn-Fe-DH and MWCNT and facilitated their mixing. New strategy was based on the use of CB as charge transfer mediator, which facilitated charge-discharge reactions. The electrodes showed a capacitance of 5.2 F cm^{-2} in a voltage window of -1.0 to -0.2 V vs. SCE and good cyclic stability. A new asymmetric device has been developed, containing Zn-Fe-DH-MWCNT negative electrodes and

PPy-MWCNT positive electrodes. Good capacitive behavior of cathode and anode

materials was achieved at high active mass of 40 mg cm^{-2} in partially overlapping

potential windows. The device showed promising performance in a voltage window of

1.6 V. The capacitance of 2.2 F cm^{-2} was obtained at a scan rate of 2 mV s^{-1}.

7.6 Acknowledgements

7.7 Supplementary Material

Figure 7.11. (A) Nyquist plot of complex impedance and (B,C) frequency dependence of complex capacitances (B) Cs' and (C) Cs" for (a)ZnFe-CNT and (b) ZnFeCB-CNT.

7.8 References

1. Aghazadeh, M., Dalvand, S., and Hosseinifard, M. (2014). Facile electrochemical synthesis of uniform β-co (oh) 2 nanoplates for high performance supercapacitors. *Ceram. Intern.* 40, 3485–3493.

2. Ata, M., Liu, Y., and Zhitomirsky, I. (2014). A review of new methods of surface chemical modification, dispersion and electrophoretic deposition of metal oxide particles. *RSC Adv.* 4, 22716–22732.

3. Ata, M. S., Poon, R., Syed, A. M., Milne, J., and Zhitomirsky, I. (2018). New developments in non-covalent surface modification, dispersion and electrophoretic deposition of carbon nanotubes. *Carbon* 130, 584–598.

4. Attias, R., Sharon, D., Borenstein, A., Malka, D., Hana, O., Luski, S., et al. (2017). Asymmetric supercapacitors using chemically prepared mno2 as positive electrode materials. *J. Electrochem. Soc.* 164, A2231– A2237.

5. Brisse, A.-L., Stevens, P., Toussaint, G., Crosnier, O., and Brousse, T. (2018). Ni(OH)$_2$ and nio based composites: battery type electrode materials for hybrid supercapacitor devices. *Materials* 11:1178. doi: 10.3390/ma11071178

6. Cesano, F., Cravanzola, S., Brunella, V., Damin, A., and Scarano, D. (2019). From polymer to magnetic porous carbon spheres: combined microscopy, spectroscopy, and porosity studies. *Front. Mater.* 6:84. doi: 10.3389/fmats.2019.00084

7. Chai, H., Chen, X., Jia, D., Bao, S., and Zhou, W. (2012). Flower-like nio structures: controlled hydrothermal synthesis and electrochemical characteristic. *Mater. Res. Bull.* 47, 3947–3951.

8. Chen, J., Mosquera-Giraldo, L. I., Ormes, J. D., Higgins, J. D., and Taylor, L. S. (2015). Bile salts as crystallization inhibitors of supersaturated solutions of poorly water-soluble compounds. *Cryst. Growth Des.* 15, 2593– 2597.

9. Chen, M., Liang, X., Wang, F., Xie, D., Pan, G., and Xia, X. (2019). Self-supported vo2 arrays decorated with n-doped carbon as an advanced cathode for lithium-ion storage. *J. Mater. Chem. A* 7, 6644–6650.

10. Chen, R., Puri, I. K., and Zhitomirsky, I. (2018). High areal capacitance of feooh-carbon nanotube negative electrodes for asymmetric supercapacitors. *Ceram. Intern.* 44, 18007–18015.

11. Chen, S., and Zhitomirsky, I. (2013). Influence of dopants and carbon nanotubes on polypyrrole electropolymerization and capacitive behavior. *Mater. Lett.* 98, 67–70.

12. Cheong, M., and Zhitomirsky, I. (2009). Electrophoretic deposition of manganese oxide films. *Surf. Eng.* 25, 346–352.

13. Dong, M., Wang, Z., Wang, J., Guo, H., Li, X., and Yan, G. (2019). Controlled

synthesis of nixcoys4/rgo composites for constructing high-performance asymmetric supercapacitor. *Front. Mater.* 6:176. doi: 10.3389/fmats.2019.000174

14. Dubal, D., Dhawale, D., Salunkhe, R., Pawar, S., Fulari, V., and Lokhande, C. (2009). A novel chemical synthesis of interlocked cubes of hausmannite mn3o4 thin films for supercapacitor application. *J. Alloys Compounds* 484, 218–221.

15. Gao, Z., Yang, W., Yan, Y., Wang, J., Ma, J., Zhang, X., et al. (2013). Synthesis and exfoliation of layered α-co (oh) 2 nanosheets and their electrochemical performance for supercapacitors. *Eur. J. Inorgan. Chem.* 2013, 4832– 4838.

16. Hu, M., Ji, X., Lei, L., and Lu, X. (2013). Structural and electrochemical stability of coal layered double hydroxide in alkali solutions. *Electrochim. Acta* 105, 261–274.

17. Jin, W.-H., Cao, G.-T., and Sun, J.-Y. (2008). Hybrid supercapacitor based on mno2 and columned feooh using li2so4 electrolyte solution. *J. Power Sourc.* 175, 686–691.

18. Krehula, S., Musiæ, S., Skoko, Z., and Popoviæ, S. (2006). The influence of zn-dopant on the precipitation of α-feooh in highly alkaline media. *J. Alloys Compounds* 420, 260–268.

19. Lakshmi, V., Ranjusha, R., Vineeth, S., Nair, S. V., and Balakrishnan, A. (2014). Supercapacitors based on microporous β-ni (oh) 2 nanorods. *Coll. Surf. A Physicochem. Eng. Aspects* 457, 462–468.

20. Li, H., Liu, S., Huang, C., Zhou, Z., Li, Y., and Fang, D. (2011). Characterization and supercapacitor application of coin-like β-nickel hydroxide nanoplates. *Electrochim. Acta* 58, 89–94.

21. Liu, X., Huang, J., Wei, X., Yuan, C., Liu, T., Cao, D., et al. (2013). Preparation and electrochemical performances of nanostructured coxni1- x (oh) 2 composites for supercapacitors. *J. Power Sourc.* 240, 338–343.

22. Ma, L., Liu, R., Liu, L., Wang, F., Niu, H., and Huang, Y. (2016). Facile synthesis of ni (oh) 2/graphene/bacterial cellulose paper for large areal mass, mechanically tough and flexible supercapacitor electrodes. *J. Power Sour.* 335, 76–83.

23. Nasibi, M., Golozar, M. A., and Rashed, G. (2012). Nano iron oxide (fe2o3)/carbon black electrodes for electrochemical capacitors. *Mater. Lett.* 85, 40–43.

24. Noorbakhsh, A., Salimi, A., and Sharifi, E. (2008). Fabrication of glucose biosensor based on encapsulation of glucose-oxidase on sol-gel composite at the surface of glassy carbon electrode modified with carbon nanotubes and celestine blue. *Electroanalysis* 20, 1788–1797.

25. Raj, C. J., Kim, B. C., Cho, W.-J., Park, S., Jeong, H. T., Yoo, K., et al. (2015). Rapid hydrothermal synthesis of cobalt oxyhydroxide nanorods for

supercapacitor applications. *J. Electroanaly. Chem.* 747, 130–135.

26. Sangeetha, N., and Sriman Narayanan, S. (2014). Hydrogen peroxide sensor based on carbon nanotubes-poly (celestine blue) nanohybrid modified electrode. *Adv. Mater. Res.* 938, 263–268.

27. Shi, C., and Zhitomirsky, I. (2010). Electrodeposition and capacitive behavior of films for electrodes of electrochemical supercapacitors. *Nanoscale Res. Lett.* 5:518. doi: 10.1007/s11671-009-9519-z

28. Shi, C., and Zhitomirsky, I. (2011). Electrodeposition of composite polypyrrole–carbon nanotube films. *Surf. Eng.* 27, 655–661.

29. Shou, Q., Cheng, J., Zhang, L., Nelson, B. J., and Zhang, X. (2012). Synthesis and characterization of a nanocomposite of goethite nanorods and reduced graphene oxide for electrochemical capacitors. *J. Solid State Chem.* 185, 191–197.

30. Silva, R., Poon, R., Milne, J., Syed, A., and Zhitomirsky, I. (2018). New developments in liquid-liquid extraction, surface modification and agglomerate-free processing of inorganic particles. *Adv. Coll. Interf. Sci.* 261, 15–27. doi: 10.1016/j.cis.2018.09.005

31. Su, Y., and Zhitomirsky, I. (2014). Hybrid mno2/carbon nanotube-vn/carbon nanotube supercapacitors. *J. Power Sourc.* 267, 235–242.

32. Tallman, D., Vang, C., Wallace, G., and Bierwagen, G. (2002). Direct electrodeposition of polypyrrole on aluminum and aluminum alloy by electron transfer mediation. *J. Electrochem. Soc.* 149, C173– C179.

33. Varaganti, S., and Ramakrishna, G. (2010). Dynamics of interfacial charge transfer emission in small molecule sensitized tio2 nanoparticles: is it localized or delocalized? *J. Phys. Chem. C* 114, 13917–13925.

34. Verma, S., Ghosh, A., Das, A., and Ghosh, H. N. (2011). Exciton-coupled charge-transfer dynamics in a porphyrin j-aggregate/tio2 complex. *Chem. A Eur. J.* 17, 3458–3464. doi: 10.1002/chem.201002537

35. Wallar, C., Poon, R., and Zhitomirsky, I. (2017). High areal capacitance of v2o3–carbon nanotube electrodes. *J. Electrochem. Soc.* 164, A3620– A3627.

36. Wang, G.-L., Xu, J.-J., and Chen, H.-Y. (2009). Dopamine sensitized nanoporous tio2 film on electrodes: photoelectrochemical sensing of nadh under visible irradiation. *Biosens. Bioelectron.* 24, 2494–2498. doi: 10.1016/j.bios.2008.12.031

37. Wang, J., Song, Y., Li, Z., Liu, Q., Zhou, J., Jing, X., et al. (2010). In situ ni/al layered double hydroxide and its electrochemical capacitance performance. *Energy Fuels* 24, 6463–6467.

38. Wang, Y., Deen, I., and Zhitomirsky, I. (2011). Electrophoretic deposition of polyacrylic acid and composite films containing nanotubes and oxide particles. *J. Coll. Interf. Sci.* 362, 367–374. doi: 10.1016/j.jcis.2011.07.007

39. Wang, Y., Yang, W., Zhang, S., Evans, D. G., and Duan, X. (2005). Synthesis and electrochemical characterization of co–al layered double hydroxides. *J. Electrochem. Soc.* 152, A2130–A2137.

40. Wang, Y.-G., Cheng, L., and Xia, Y.-Y. (2006a). Electrochemical profile of nano-particle coal double hydroxide/active carbon supercapacitor using koh electrolyte solution. *J. Power Sour.* 153, 191–196.

41. Wang, Y.-G., Yu, L., and Xia, Y.-Y. (2006b). Electrochemical capacitance performance of hybrid supercapacitors based on ni (oh) 2/carbon nanotube composites and activated carbon. *J. Electrochem. Soc.* 153, A743– A748.

42. Xi, Y., Wei, G., Li, J., Liu, X., Pang, M., Yang, Y., et al. (2017). Facile synthesis of mno2-ni(oh)2 3d ridge-like porous electrode materials by seed-induce method for high-performance asymmetric supercapacitor. *Electrochim. Acta* 233, 26–35.

43. Xia, X., Tu, J., Mai, Y., Wang, X., Gu, C., and Zhao, X. (2011). Self-supported hydrothermal synthesized hollow co3o4 nanowire arrays with high supercapacitor capacitance. *J. Mater. Chem.* 21, 9319–9325. doi: 10.34133/2019/8013285

44. Xu, P., Miao, C., Cheng, K., Ye, K., Yin, J., Cao, D., et al. (2016). Preparation of binder-free porous ultrathin ni (oh) 2 nanoleafs using zno as pore forming agent displaying both high mass loading and excellent electrochemical energy storage performance. *Electrochim. Acta* 216, 499–509.

45. Zhai, T., Sun, S., Liu, X., Liang, C., Wang, G., and Xia, H. (2018). Achieving insertion-like capacity at ultrahigh rate via tunable surface pseudocapacitance. *Adv. Mater.* 30:1706640.

46. Zhang, D., Shao, Y., Kong, X., Jiang, M., Lei, D., and Lei, X. (2016). Facile fabrication of large-area hybrid ni-co hydroxide/cu (oh) 2/copper foam composites. *Electrochim. Acta* 218, 294–302.

47. Zhang, G.-Q., Zhao, Y.-Q., Tao, F., and Li, H.-L. (2006). Electrochemical characteristics and impedance spectroscopy studies of nano-cobalt silicate hydroxide for supercapacitor. *J. Power Sour.* 161, 723–729.

48. Zhang, Z., Chi, K., Xiao, F., and Wang, S. (2015). Advanced solid-state asymmetric supercapacitors based on 3d graphene/mno 2 and graphene/polypyrrole hybrid architectures. *J. Mater. Chem. A* 3, 12828– 12835.

49. Zhang, Y., Liu, Y., Guo, Y., Yeow, Y. X., Duan, H., Li, H., et al. (2015). In situ preparation of flower-like α-ni (oh) 2 and nio from nickel formate with excellent capacitive properties as electrode materials for supercapacitors. *Mater. Chem. Phys.* 151, 160–166.

50. Zhou, F., Liu, Q., Gu, J., Zhang, W., and Zhang, D. (2015). Microwave-assisted anchoring of flowerlike co (oh) 2 nanosheets on activated carbon to prepare hybrid electrodes for high-rate electrochemical capacitors. *Electrochim.*

Acta 170, 328–336.

Chapter 8 Zn-doped FeOOH-polypyrrole electrodes for supercapacitors

W Liang* [=], Ryan Poon* [=] and I. Zhitomirsky* [α]

*Department of Materials Science and Engineering, McMaster University,

Hamilton, Ontario, L8S 4L7, Canada

[α]Corresponding Author: zhitom@mcmaster.ca; 905-525-9140 ext. 23914

Author's Contributions:

Development of new scalable synthesis of procedure for Zn-doped FeOOH electrode

Synthesis of negative electrodes

Electrochemical testing of FeOOH-based electrodes and devices

Manuscript preparation

=The authors contributed equally to this work

8.1 Abstract

The problem of poor cyclic stability of FeOOH anodes for supercapacitors was addressed by Zn-doping. Zn-doped FeOOH materials exhibited significant improvement in capacitance retention during cycling. Further improvement in capacitance retention and capacitive properties at low absolute values of negative potentials was achieved in composites containing Zn-doped FeOOH and polypyrrole-coated carbon nanotubes. Another important finding was a simple procedure for the fabrication of MnO_2 cathodes, which avoided particle agglomeration during the drying stage and facilitated enhanced mixing of MnO_2 and conductive carbon nanotube additives. Enhanced capacitive properties of cathodes and anodes at high active mass loadings allowed good capacitive behavior of the asymmetric devices, which showed promising charge-storage properties for practical applications.

8.2 Introduction

FeOOH is a promising material for anodes of aqueous supercapacitors[1, 2]. Of particular

interest are asymmetric supercapacitor cells with enlarged voltage windows, which contain

FeOOH anodes and MnO_2 cathodes in mild A_2SO_4 (A=Li, Na, K) electrolytes[1, 3]. The

charging mechanisms of FeOOH and MnO2 are described by the following reactions:

$$Fe(III)OOH + A^+ + e^- \leftrightarrow AFe(II)OOH \ (1)$$

$$AMn(III)O_2 \leftrightarrow Mn(IV)O_2 + A^+ + e^- \ (2)$$
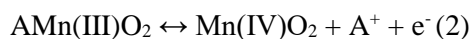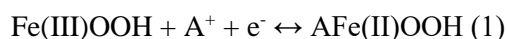
The interest in FeOOH anodes is attributed to relatively high specific capacitance of FeOOH,

which is comparable with specific capacitance of MnO_2 materials for cathodes. The ability to

match the capacitance of FeOOH anodes with high capacitance of MnO_2 cathodes is important

for the development of cells with high total capacitance. However, from the previous

investigations it appears that FeOOH based electrodes showed relatively high resistance and

poor cyclic stability[4]. The poor capacitance retention of FeOOH is attributed to relatively

high solubility of Fe(II) species formed during electrode cycling in A_2SO_4 electrolyte

solutions[5]. Another difficulty is related to the deviation of the shape of cyclic voltammograms

(CV) of FeOOH from the ideal box shape, especially at low negative potentials[4]. In contrast,

MnO_2 electrodes showed nearly ideal box shape CV even at high electrode mass[6]. This

introduces problems for the fabrication of asymmetric devices. Previous investigations[7]

highlighted the need in the development of efficient FeOOH electrodes with enhanced

performance at high active mass loadings in order to achieve high areal capacitance and

low relative mass of current collector and other passive components.

The goal of this investigation was the development of advanced anodes with enhanced cyclic stability and improved charge-discharge behavior for application in the asymmetric devices. The testing results presented below indicated that Zn doping of FeOOH resulted in enhanced cyclic stability. Further improvement in cyclic stability and charge-discharge behavior of the anodes as well as asymmetric devices was achieved by the fabrication of composites of Zn-doped FeOOH and polypyrrole coated multiwalled carbon nanotubes (MWCNT). Moreover, we report a new procedure for the fabrication of composite MnO_2-MWCNT cathodes, which offers benefits of simplicity and low cost for the mass scale production of the composites with reduced particle agglomeration and enhanced mixing of the individual components. The procedure facilitated the fabrication of electrodes and devices with high active mass loadings, which showed good electrochemical performance.

8.3 Experimental Procedure

Synthesis of FeOOH and Zn-doped FeOOH was based on the method, described in ref[8]. Pure FeOOH, 8%Zn-FeOOH and 12%Zn-FeOOH were mixed with MWCNT (Bayer) to form composites FC, 8ZFC and 12ZFC, respectively. Polypyrrole coated MWCNT were prepared by the method, described in ref[9] and mixed with 12ZFC to form 12ZFCPC composite, containing 50% 12ZFC. The composite slurries in ethanol

were impregnated in Ni foam current collectors. The composites contained 30%

MWCNT and 3 % polyvinyl butyral (PVB) binder.

For the synthesis of MnO_2-MWCNT composite, 0.5 mL of 40% $NaMnO_4$ solution

was added to a mixture of 1.5 mL water and 5 mL of ethanol. In this procedure,

ethanol was used as a reducing agent. The by-product of this reaction contained Na

ions. However, the washing procedure was avoided, because Na ions were involved in

charging of the active material in the Na_2SO_4 solutions. In this procedure we also

avoided drying of MnO_2, which usually results in agglomeration and generates

problems with re-dispersion in the device processing medium and mixing with

MWCNT. Therefore, MWCNT were added directly to the obtained MnO_2 suspension

in a mass ratio of MWCNT:MnO_2=1:4. PVB solution in ethanol was added to the

suspension. The mass of the PVB was 3% of the total mass of MWCNT and MnO_2.

The suspension was impregnated into the Ni foam current collector to form MnO_2-

MWCNT (MC) cathodes. The mass loadings of cathodes and anodes was 40 mg cm^{-2}.

The electrodes and devices were tested in 0.5 M Na_2SO_4 electrolyte solutions using

equipment described in ref.[9]. The individual electrodes were tested in a three-

electrode system and device was tested in a two-electrode system.

8.4 Results and Discussion

Figure 8.1(A-D) shows cyclic voltammetry (CV) data at different scan rates for FC,

8ZFC, 12ZFC, 12ZFCPC in the potential range -0.8-0.0 V. The CVs for FC, 8ZFC,

12ZFC show good capacitive behavior at potentials below -0.2 V, as indicated by high

currents and large CV areas. However, reduced currents were recorded at lower absolute

values of the negative potentials. In contrast, the 12ZFCPC electrodes showed

enhanced performance at potentials -0.2 - 0.0 V (Figure 5.1D) and -0.2 - +0.1

V(Supplementary materials, Figure 8.5). It will be shown below that improved charge

storage properties of 12ZFCPC offer benefits for the fabrication of asymmetric devices.
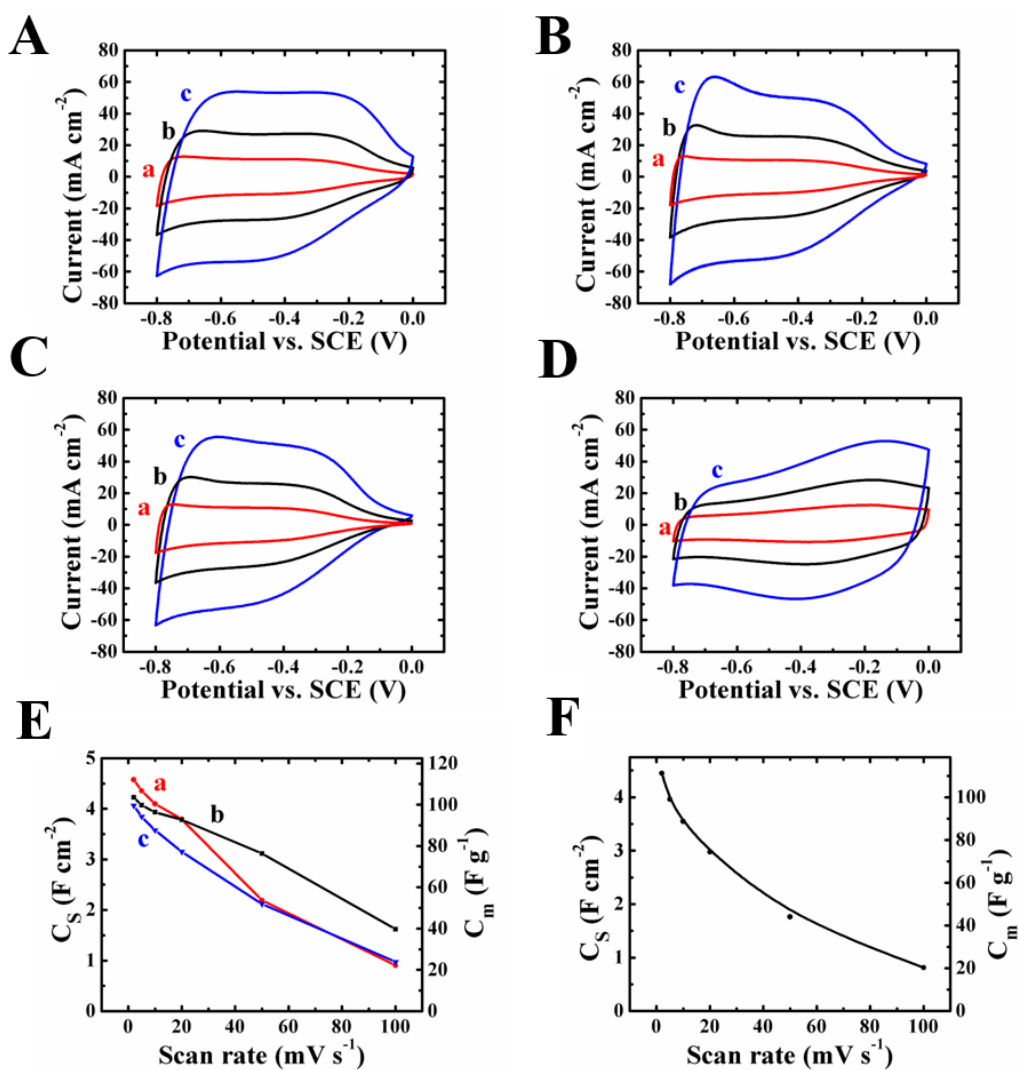
Figure 8.1 (A–D) CVs at scan rates of (a) 2, (b) 5 and (c) 10 mV s-1 and (E,F) CS and Cm versus scan rate for (A, E(a)) FC, (B, E(b)) 8ZFC, (C, E(c)) 12ZFC, (D,F) 12ZFCPC.

Figure 8.1(E,F) shows capacitances of the composites versus scan rate. The FC, 8ZFC, 12ZFC and

12ZFCPC electrodes showed capacitances of 4.5, 4.2, 4.0 and 4.4 F cm^{-2}, respectively, at a scan rate

of 2 mV s^{-1}. The capacitance, normalized by the FeOOH mass was 112.1, 111.7 and 111.7 F g^{-1} for

FC, 8ZFC and 12ZFC, respectively. The capacitance decreased with increasing scan rate due to

electrolyte diffusion limitations in pores of the electrode materials. The electrodes showed relatively

low impedance and relaxation type dispersion of complex AC capacitance, derived from the

impedance data (Figure 8.6, Figure 8.7).

FC, 8ZFC, 12ZFC electrodes exhibited maxima in the capacitance retention (Figure

8.2A). The capacitance increase at the beginning of the cycling can result from the

changes in the electrode microstructure. We suggested that partial dissolution of the

Fe(II) species can result in increased porosity and improved electrolyte access to the

bulk of the active materials.
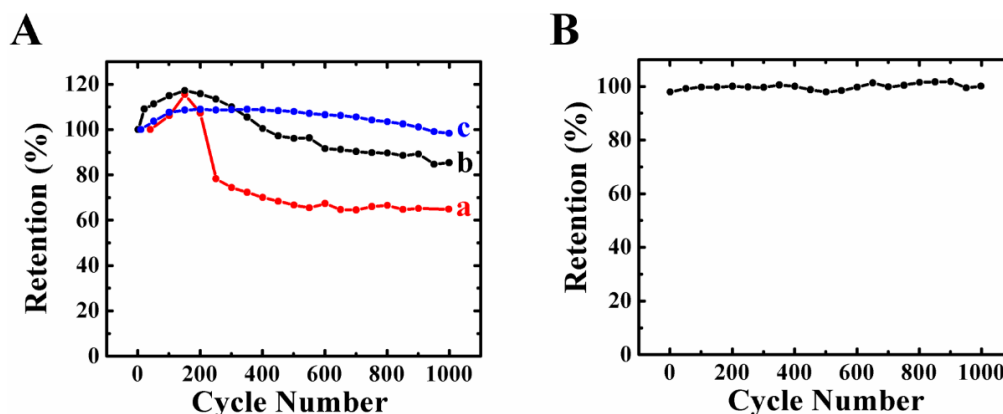
Figure 8.2 Capacitance retention versus cycle number for (A)(a) FC (b) 8ZFC (c) 12ZFC (B) 12ZFCPC.

However, FC showed significant reduction of the capacitance after first 150 cycles and

capacitance retention of 64% was obtained after 1000 cycles. In order to reduce

electrode degradation during cycling, we modified FeOOH with Zn. 8ZFC and 12ZFC

showed capacitance retention of 85 and 98%, respectively after 1000 cycles. It is known

that Zn compounds promote iron hydroxide precipitation [10]. Therefore, more

electrochemically negative Zn species prevent release of the Fe(II) ions from the

electrodes during cycling. 12ZFCPC showed 98% cyclic stability and reduced

capacitance variations during 1000 cycles (Figure 8.2B).

MC electrodes, prepared by a modified method showed (Figure 8.3) nearly box-shape

CVs in the potential range of 0.0 - +0.9V and relatively high capacitance of 5.3 F cm^{-2}

at 2 mV s^{-1}, which was achieved at low electrode impedance (Figure 8.8).
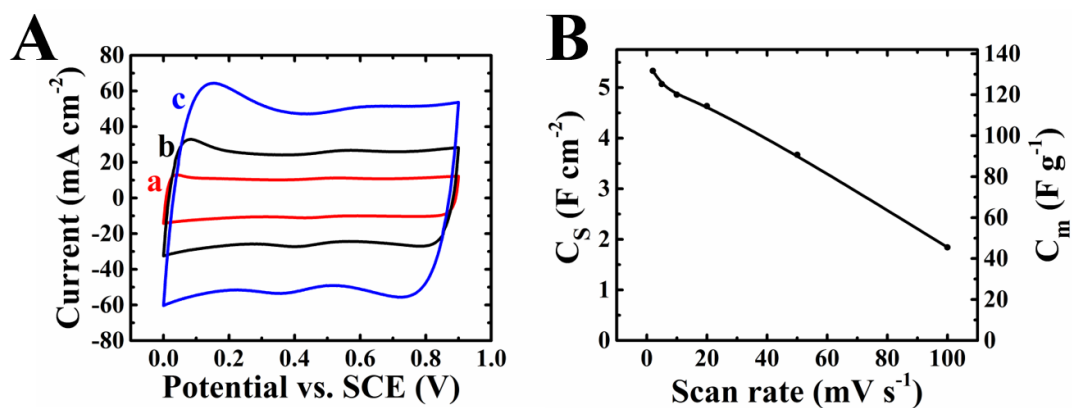
Figure 8.3 (A) CVs at scan rates of (a)2, (b) 5 and (c) 10 mV s^{-1}, and (B) C_S and Cm versus scan rate for MC.

Therefore, the procedure, developed in this investigation is promising for the practical

application. It offers benefits of simplicity, reduced agglomeration and improved

mixing of MnO_2 and MWCNT.

12ZFC and 12ZFCPC were combined with MC for the fabrication of the asymmetric devices. The capacitance of the asymmetric devices is given by formula $1/C=1/C_C +1/C_A$, where C_C and C_A are the capacitances of cathode and anode, respectively. The relatively poor capacitive properties of 12ZFC at low absolute values of the negative potential resulted in the poor capacitive properties of the 12ZFCMC device at voltages below 0.2 V, as indicated by the low CV areas in this range (Figure 8.4). However, nearly box-shape CVs were obtained for the 12ZFCPC-MC devices, which showed higher capacitance and low impedance (Figure 8.9). The galvanostatic charge-discharge curves were of nearly triangular shape (Figure 8.10). The highest capacitance of 2.2 F cm^{-2} was obtained at 2 mV s^{-1}. The 12ZFCPC-MC devices were capable of powering a blue LED display (Figure 8.4D, inset).
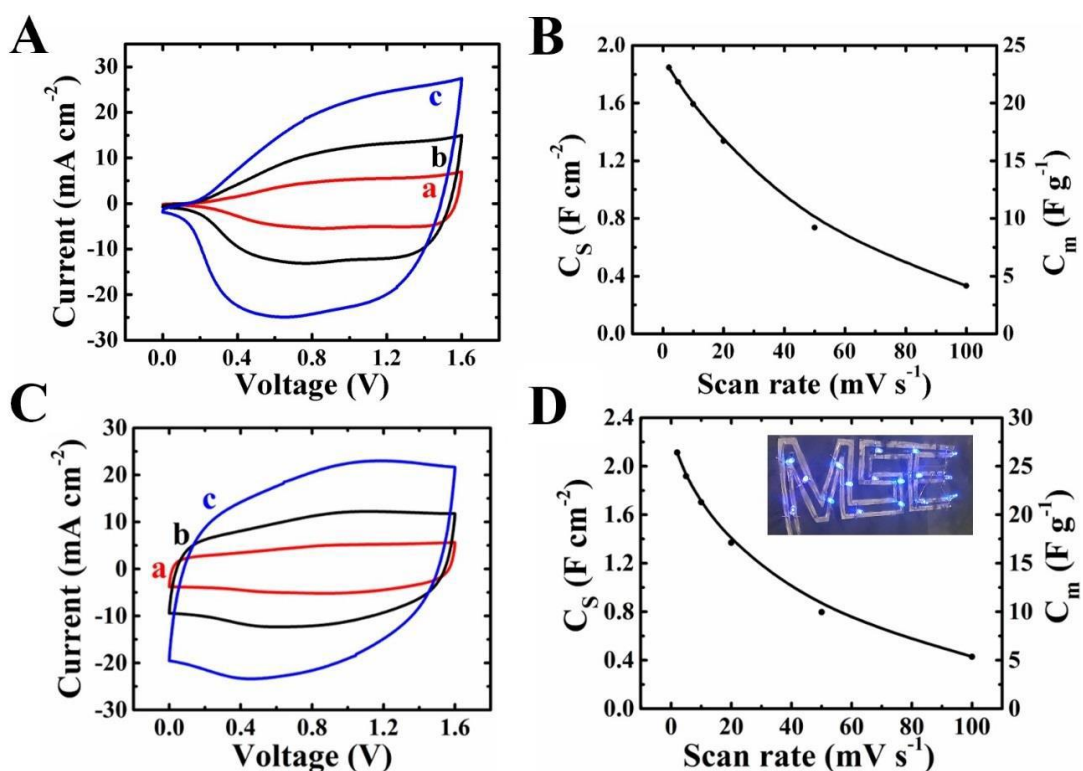
Figure 8.4 Testing data for (A,B) 12ZFC-MC and (C,D) 12ZFCPC-MC cells: (A,C) CVs at scan rates of (a)2, (b) 5 and (c) 10 mV s^{-1}, and (B,D) CS and Cm, inset shows LEDs powered by a supercapacitor module.

8.5 Conclusions

The problem of poor cyclic stability of FeOOH anodes was addressed by Zn-doping.

Testing results showed that 8ZFC, 12ZFC exhibit significant improvement in

capacitance retention during cycling. Further improvement in capacitance retention

and capacitive properties at low absolute values of negative potentials was achieved in

12ZFCPC composites. Another important finding was a simple procedure for the

fabrication of MC anodes, which avoided particle agglomeration during the drying

stage and facilitated enhanced mixing of the individual components. Enhanced

capacitive properties of cathodes and anodes allowed good capacitive behavior of the

12ZFCPC – MC devices, which showed promising capacitive properties for practical

applications.

8.6 Acknowledgements

8.7 Supplementary Materials
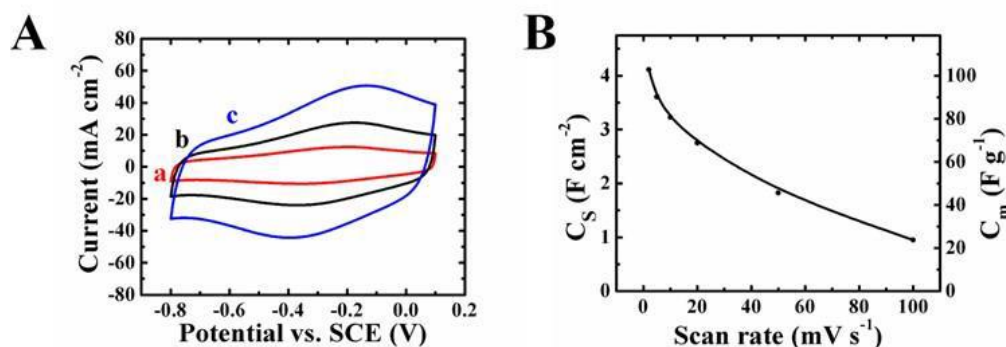
Figure 8.5 (A) CVs at scan rates of (a) 2, (b) 5 and (c) 10 mV s−1 and (B) CS and Cm versus scan rate for 12ZFCPC.
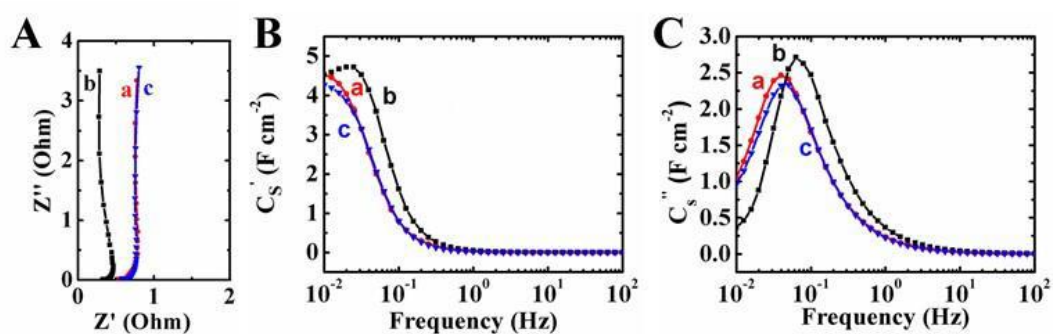
Figure 8.6 (A) Nyquist plot of complex impedance, and frequency dependences of (B) Cs' and (C) Cs" for (a) FC, (b) 8ZFC, (c) 12ZFC.
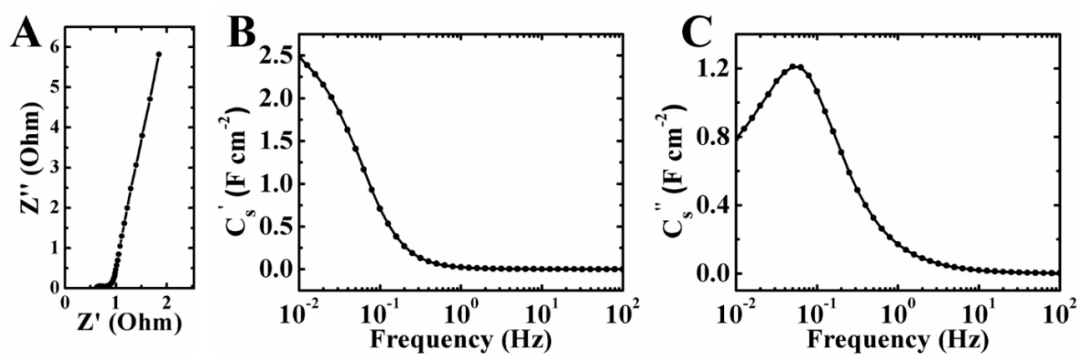
Figure 8.7 (A) Nyquist plot of complex impedance, and frequency dependence of (B) Cs' and (C) Cs" for 12ZFCPC.
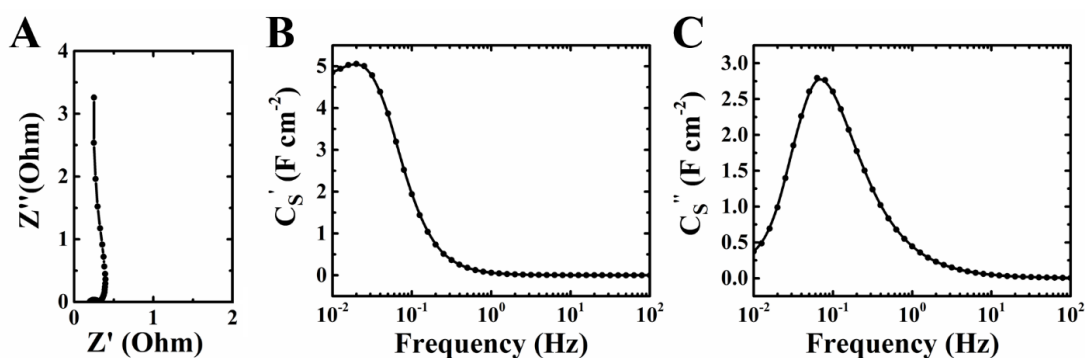
Figure 8.8 (A) Nyquist plot of complex impedance, and frequency dependence of complex capacitance (B) Cs' and (C) Cs" for MC.
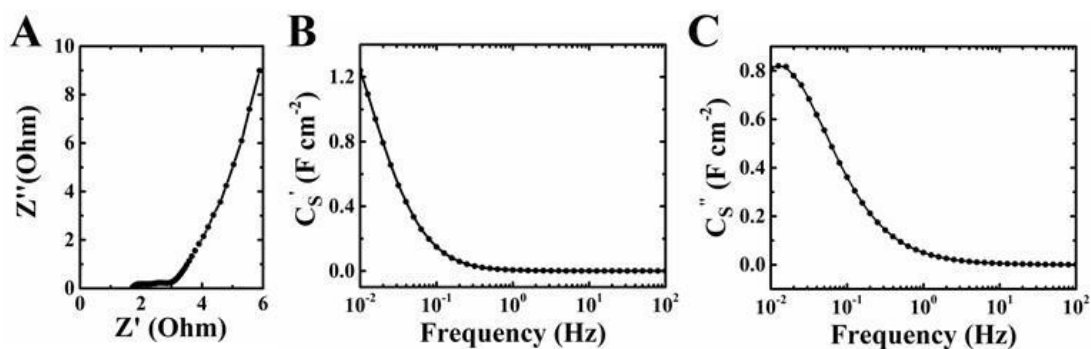
Figure 8.9 Nyquist plot of complex impedance, and frequency dependence of complex capacitance (B) Cs' and (C) Cs" for asymmetric 12ZFCPC-MC device.
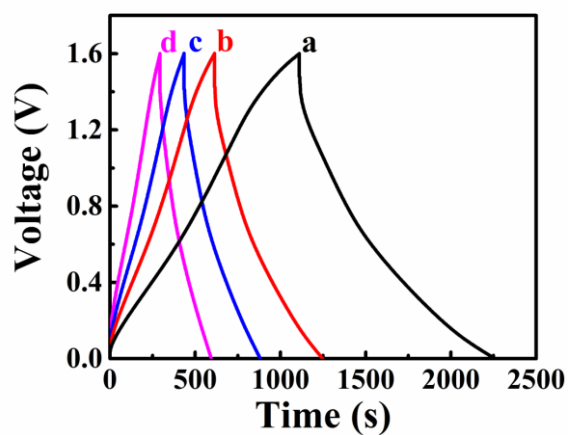
Figure 8.10 Galvanostatic charge-discharge for asymmetric 12ZFCPC-MC device at current densities of (a) 3, (b) 5, (c) 7 and (d) 10 mA cm^{-2}.

8.8 References

[1] Y.C. Chen, Y.G. Lin, Y.K. Hsu, S.C. Yen, K.H. Chen, L.C.J.S. Chen, Novel iron oxyhydroxide lepidocrocite nanosheet as ultrahigh power density anode material for asymmetric supercapacitors, *Small* 10 (2014) 3803-3810.

[2] X. Gong, S. Li, P.S. Lee, A fiber asymmetric supercapacitor based on FeOOH/PPy on carbon fibers as an anode electrode with high volumetric energy density for wearable applications, *Nanoscale* 9 (2017) 10794-10801.

[3] R. Barik, B.K. Jena, A. Dash, M. Mohapatra, In situ synthesis of flowery-shaped α-FeOOH/Fe2O3 nanoparticles and their phase dependent supercapacitive behaviour, *RSC Advances* 4 (2014) 18827-18834.

[4] Q. Shou, J. Cheng, L. Zhang, B.J. Nelson, X. Zhang, Synthesis and characterization of a nanocomposite of goethite nanorods and reduced graphene oxide for electrochemical capacitors, *Journal of Solid State Chemistry* 185 (2012) 191-197.

[5] K.K. Lee, R.W.Y. Ng, K.K. She, W.S. Chin, C.H. Sow, Vertically aligned iron (III) oxyhydroxide/oxide nanosheets grown on iron substrates for electrochemical charge storage, *Materials Letters* 118 (2014) 150-153.

[6] Y. Su, I. Zhitomirsky, Hybrid MnO2/carbon nanotube-VN/carbon nanotube supercapacitors, *Journal of Power Sources* 267 (2014) 235-242.

[7] R. Chen, I.K. Puri, I. Zhitomirsky, High areal capacitance of FeOOH-carbon nanotube negative electrodes for asymmetric supercapacitors, *Ceramics International* 44 (2018) 18007-18015.

[8] S. Krehula, S. Musić, Ž. Skoko, S. Popović, The influence of Zn-dopant on the precipitation of α-FeOOH in highly alkaline media, *Journal of Alloys and Compounds* 420 (2006) 260-268.

[9] Y. Su, I. Zhitomirsky, Asymmetric electrochemical supercapacitor, based on polypyrrole coated carbon nanotube electrodes, *Applied Energy* 153 (2015) 48-55.

[10] M.R.C. Ismael, J.M.R. Carvalho, Iron recovery from sulphate leach liquors in zinc hydrometallurgy, *Minerals Engineering* 16 (2003) 31-39.

Chapter 9 Mn$_3$O$_4$ and (ZnFe)OOH composites for supercapacitors with high active mass

R. Poon*=, W. Liang*= and I. Zhitomirsky*$^{\alpha}$

*Department of Materials Science and Engineering, McMaster University,

Hamilton, Ontario, L8S 4L7, Canada

αCorresponding Author: zhitom@mcmaster.ca; 905-525-9140 ext. 23914

Author's Contributions:

Synthesis and fabrication of (ZnFe)OOH – polypyrrole coated CNT composites

Electrochemical testing of (ZnFe)OOH – polypyrrole coated CNT electrode and devices

Literature review

Manuscript preparation

=The authors contributed equally to this work

9.1 Abstract

A new colloidal method has been developed for the fabrication of Mn_3O_4-carbon

nanotube (CNT) composites for positive electrodes of supercapacitors and areal

capacitance of 5.04 F cm^{-2} has been achieved. In this method, chemical precipitation

of Mn_3O_4 was performed in the presence of carbon nanotubes, dispersed using a

tolonium chloride dye. An electrostatic heterocoagulation mechanism has been

developed, which allowed for enhanced mixing of Mn_3O_4 and CNT, and resulted in

enhanced electrochemical performance at high active mass of 36 mg cm^{-2}. Testing

results revealed changes in microstructure and oxidation state of Mn during cycling,

which allowed for enhanced capacitance. In order to utilize the high capacitance of

the positive Mn_3O_4-CNT electrodes in supercapacitor devices, advanced negative

electrodes have been developed. (ZnFe)OOH – polypyrrole coated CNT electrodes

with enhanced areal capacitance in a negative potential window have been fabricated.

Asymmetric devices showed promising performance in a voltage window of 1.6 V.

9.2 Introduction

Mn_3O_4 is a promising ceramic cathode materials for supercapacitors due to its high capacitance and low cost[1,2]. However, the specific capacitance of Mn_3O_4 decreased significantly with increasing electrode mass due to poor electrolyte access to the active material and low electronic conductivity. It is challenging to achieve good electrode performance at practically important active mass above 10 mg cm^{-2}. Therefore, research efforts were focused on the synthesis of nanoparticles with high surface area and design of advanced composites.

It is important to note that Mn_3O_4 is a member of a large group of advanced materials with a spinel crystalline structure. Therefore, the advantage of Mn_3O_4, compared to other pseudocapacitive ceramic materials, is the ability to form solid solutions with various spinel compounds. The rich chemistry of spinel offers possibilities[3] for the modification of composition, conductivity and capacitive properties of Mn_3O_4.

Many investigations focused on pure Mn_3O_4 films[4-8] and reported capacitances at low active mass loadings in the range of 0.16 -1.2 mg cm^{-2}. High specific capacitances of 5687 and 5978 F g^{-1} were reported at mass loadings of 0.16 and 0.64 mg cm^{-2}, respectively. Good electrochemical performance at higher mass loadings in the range of 2-9.5 mg cm^{-2} was achieved in composites, containing various conductive additives, such as graphite[9], carbon black[10], acetylene black[11-13] and other materials[14]. High gravimetric capacitance of 222.4 F g^{-1} was achieved at a mass loading of 9.5 mg cm^{-2}

and resulted[13] in areal capacitance of 2.11 F cm^{-2}. Mn_3O_4 was combined with capacitive

carbon materials such as graphene[15,16] and activated carbon[17] for the fabrication of

composites. Of particular interest are Mn_3O_4-graphene oxide composites, which

showed capacitances of 538 F g^{-1} (2.69 F cm^{-2})[18] and 258.6 F g^{-1} (2.33 F cm^{-2})[19] at mass

loadings of 5 and 9 mg cm^{-2}, respectively. Recent studies showed that good capacitive

behavior can be achieved at higher mass loadings using advanced colloidal techniques[20].

Mn_3O_4-carbon nanotube electrodes showed areal capacitances of 2.820 and 4.221 F cm^{-2}

at active mass loadings of 28.4 and 33 mg cm^{-2}.

Mn_3O_4 cathodes were combined with various anodes, such as graphene[22], activated

carbon[23], lithium titanate[24] and polypyrrole[25] for the fabrication of asymmetric

devices with large voltage windows. However, the progress in the development of

Mn_3O_4 cathodes introduces problems related to the use of various anodes, which have

lower capacitances. Therefore, there is a need in the development of advanced

ceramic anodes, which match capacitive properties of the Mn_3O_4 cathodes.

The goal of this investigation was the development of advanced Mn_3O_4 electrodes and

asymmetric supercapacitor devices. The approach was based on the synthesis of Mn_3O_4

nanoparticles and electrostatic heterocoagulation with dispersed carbon nanotubes. The

results presented below indicated that this approach allowed enhanced mixing of the

individual components and enhanced capacitive behavior was achieved at mass loading

of 36 mg cm^{-2}. Good material utilization resulted in high areal capacitance of 5.04 F

cm^{-2} and good rate capability, which were achieved at low electrode resistance. In order to match high capacitance of Mn_3O_4 cathodes, we developed advanced negative electrodes, containing (Fe,Zn)OOH and polypyrrole coated carbon nanotubes (PNT). The use of composites allowed for improved capacitive behavior and enhanced cyclic stability. The asymmetric device showed promising capacitive properties.

9.3 Experimental Procedure

Tolonium chloride (TL), $Mn(NO_3)_2.4H_2O$, $FeCl_3 \cdot 6H_2O$, $ZnCl_2$, NaOH, Na_2SO_4, polyvinyl butyral(PVB) (Aldrich), carbon nanotubes (CNT, multiwalled, Bayer), and Ni foams (Vale) were used.

For the synthesis of Mn_3O_4-CNT composite, 1 g L^{-1} CNT and 0.5 g L^{-1} of TL were added to 100 mL DI water and ultrasonicated. $Mn(NO_3)_2$. was added to the CNT suspension, and the pH of the suspension was adjusted to pH = 10 by NaOH to synthesize Mn_3O_4. The mass ratio of CNT: Mn_3O_4 in the suspension was 1:4. The composite was filtrated, washed and dried at 60°C. The obtained material was mixed with PVB (3 wt%) to produce a slurry in ethanol and impregnated into the Ni foam.

The synthesis of pure FeOOH and (Fe,Zn)OOH ([Zn]/[Zn]+[Fe]= 0.1) was based on the method, described in the literature[26]. CNT were added to (Fe,Zn)OOH suspensions at pH = 7 in order to obtain (Fe,Zn)OOH-CNT suspensions.

The procedure for the formation of polypyrrole coated CNT (PNT) was described in a

previous investigation[27]. The suspensions of (Fe,Zn)OOH-CNT and PNT were mixed,

ultrasonicated, filtrated and dried at 60 °C. The mass ratio of (Fe,Zn)OOH-CNT:PNT

was 1:1. The obtained composite materials were mixed with PVB (2.5 wt%) in

ethanol and the slurries were impregnated into the Ni foam current collectors. The

mass loading of all the electrodes was 36 mg cm^{-2}.

XPS analysis was performed using Quantera II Scanning instrument (Physical

Electronics Inc.). JEOL JSM-7000F microscope was used for SEM investigations.

XRD studies were performed using a Bruker D8 diffractometer. Cyclic voltammetry

(CV) and impedance spectroscopy (EIS) were performed using equipment, described

in refs.[28,29]

9.4 Results and Discussion

The formation of Mn_3O_4 was confirmed by XRD studies (Figure 9.1), which showed

peaks, corresponding to JCPDS file 024-0734.
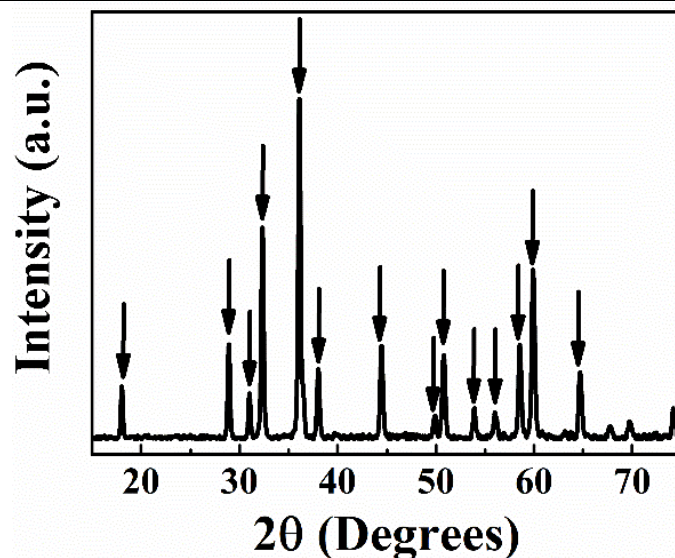
Figure 9.1 XRD pattern of as-precipitated powder, arrows show peaks, corresponding to JCPDS file 024-0734.

Figure 9.2A shows CVs for the Mn$_3$O$_4$-CNT electrode. The nearly box shapes of the CVs indicated good capacitive behavior. The areal capacitance (C$_S$) of 5.04 F cm^{-2} was obtained at a sweep rate of 2 mV s^{-1}. The capacitance decreased with sweep rate (Figure 9.2B) to the value of 1.78 F cm^{-2} at 100 mV s^{-1}. The C$_S$ of obtained Mn$_3$O$_4$-CNT electrode was higher, compared to the literature data for various Mn$_3$O$_4$ composites, described in the Introduction section.
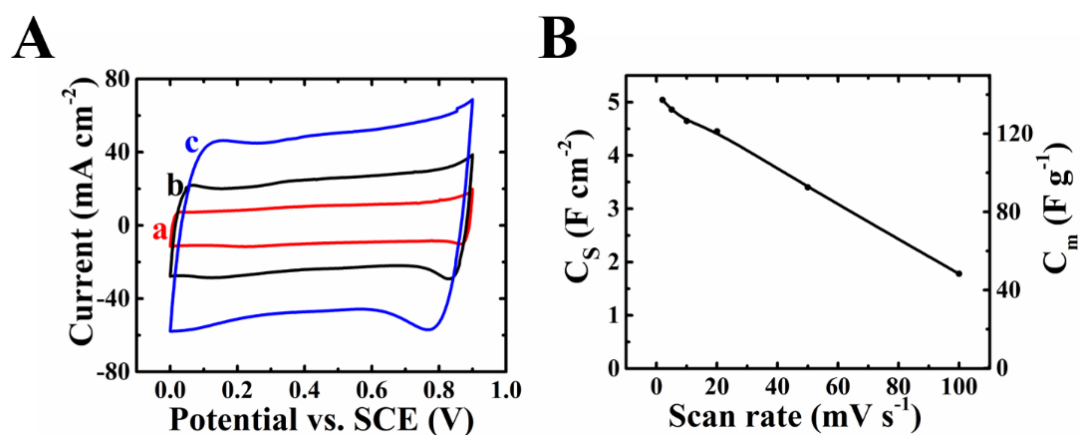
Figure 9.2 (A) CVs at scan rates of (a) 2, (b) 5 and (c) 10 mV s^{-1} and (B) C$_S$ and Cm for Mn$_3$O$_4$-CNT electrode.

The enhanced capacitance resulted from improved mixing of Mn_3O_4 and CNT. It was found that cationic TL adsorbed on CNT and provided good dispersion of CNT in water. The adsorption mechanism involved π-π interactions of the polyaromatic TL with CNT. The adsorbed cationic TL molecules imparted a positive charge to CNT and provided electrostatic dispersion of CNT. The TL adsorption on CNT resulted in good colloidal stability of 1 g L^{-1} CNT suspensions, containing 0.5 - 1 g L^{-1} TL. Literature data indicates that the isoelectric point of Mn_3O_4 is in the range of 3.7-5.730. Therefore, the Mn_3O_4 particles formed at pH = 10 were negatively charged. It is suggested that electrostatic attraction of the negatively charged Mn_3O_4 and well-dispersed positively charged CNT facilitated their enhanced mixing.

The low impedance of the Mn_3O_4-CNT composites provided additional evidence of good dispersion of CNT and enhanced mixing of Mn_3O_4 and CNT. Figure 9.3A shows a Nyquist plot of the impedance spectroscopy data. The low real part of the complex impedance indicated a low resistance, whereas the low imaginary part resulted from high capacitance. The components of complex capacitance derived from the impedance data (Figure 9.3B,C) showed a frequency dispersion of the relaxation type. The relaxation frequency, corresponding to the maximum of the imaginary part of the complex capacitance was about 0.08 Hz.
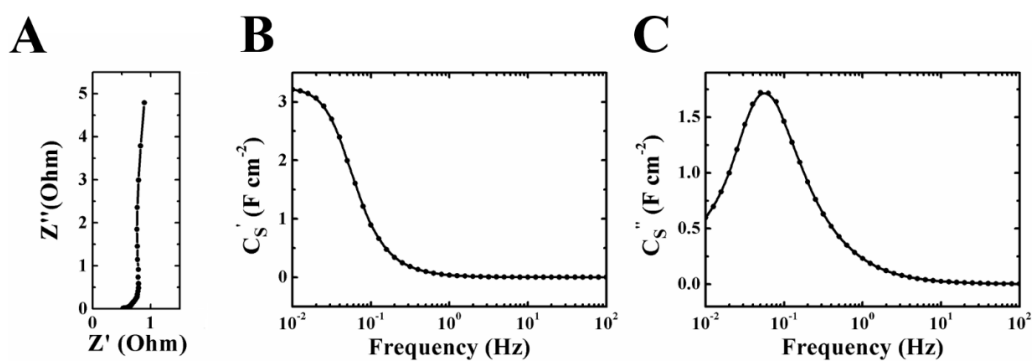
Figure 9.3 (A) Nyquist plot of complex impedance, and frequency dependence of complex capacitances (B) C_S' and (C) C_S'' for Mn_3O_4-CNT electrode.

SEM studies showed that as-prepared electrodes contained nanoparticles of Mn_3O_4

(Figure 9.4A) with a typical size of 30-50 nm. Cycling resulted in significant changes

of the electrode microstructure. The SEM image of the electrode after cycling showed

a porous microstructure, containing flakes of a manganese oxide (Figure 9.4B). Such

microstructure is beneficial for the electrolyte access to the active material. XPS

studies of the electrodes before and after cycling showed changes in the oxidation

state of Mn. It was found that cycling resulted in the reduction of the Mn^{2+} content

and increasing content of Mn^{3+} and Mn^{4+} (Figure 9.4C,D) in the electrode material.
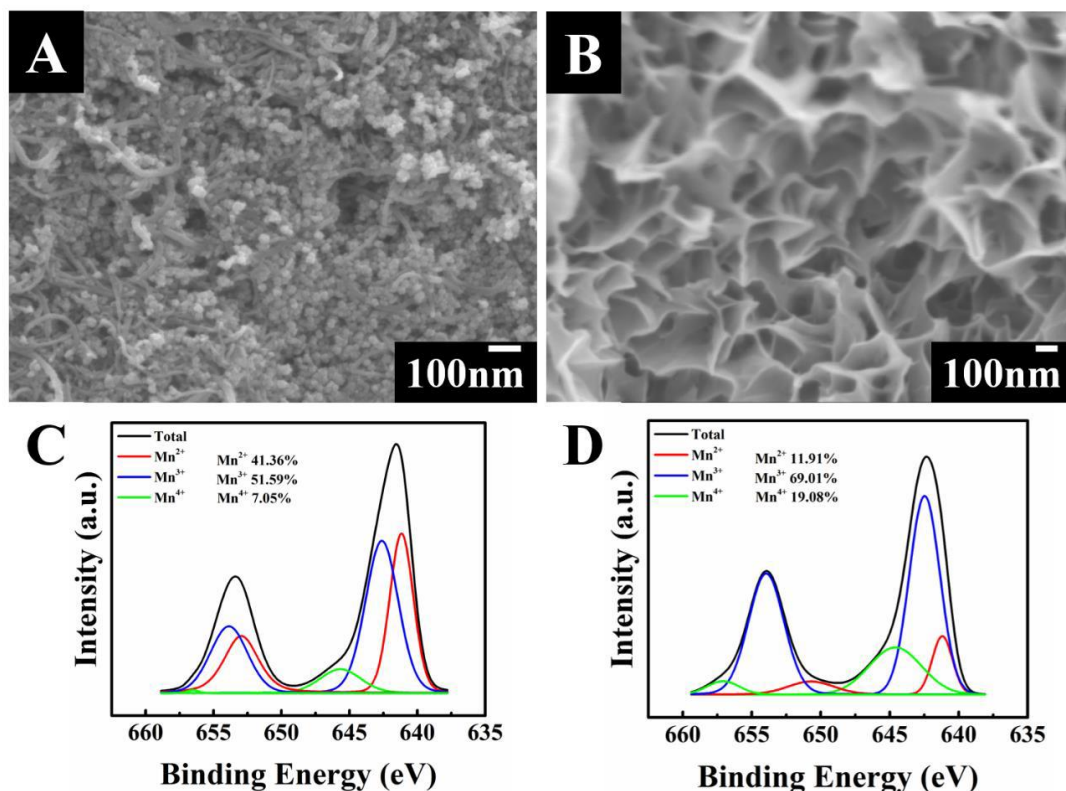
Figure 9.4 (A,B) SEM images and (C,D) XPS spectra for Mn_3O_4-CNT electrode: (A,C) as prepared and (B,D) after testing.

Cycling of the Mn_3O_4-CNT electrodes (Figure 9.5) showed initial increase in capacitance during the first 200 cycles and then capacitance reduction. The capacitance was relatively stable between 400th and 1000th cycles. The initial capacitance increase resulted from the increased porosity (Figure 9.4B), which facilitated electrolyte access to the active material.

The high capacitance of Mn_3O_4-CNT positive electrodes, obtained in this investigation, can be utilized for the fabrication of asymmetric supercapacitor devices. The development of asymmetric devices requires comparable capacitances of individual

electrodes in partially overlapping potential ranges[31,32].
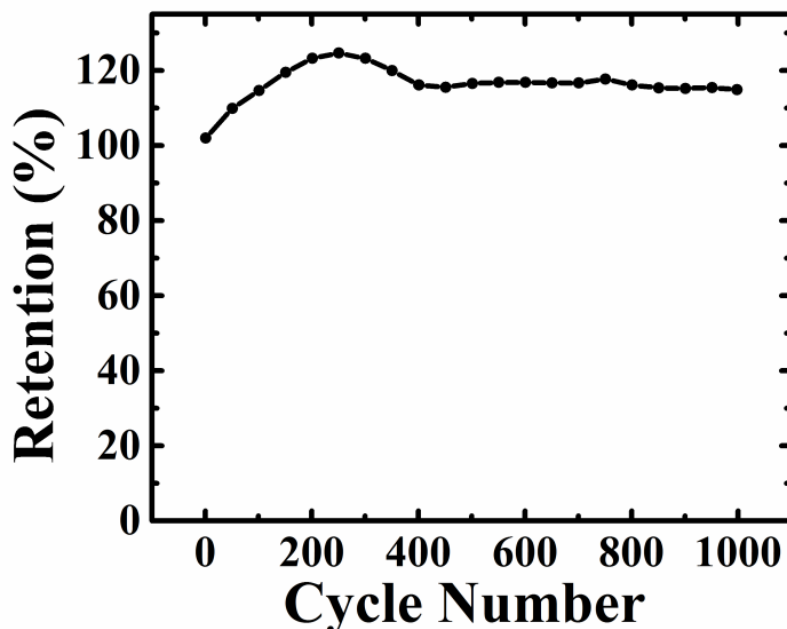
Figure 9.5 Capacitance retention of Mn_3O_4-MWCNT electrode during cycling.

FeOOH-CNT electrodes were tested in the potential range of -0.8 - +0.1 V in 0.5M

Na_2SO_4 electrolyte. Figure 9.6A shows CV for the FeOOH-CNT electrodes at

different scan rates. The CVs deviated significantly from the ideal box shape. The low

currents in the range of -0.2 - +0.1 V indicated poor capacitive properties in this

potential range. The integral areal capacitance (Figure 9.6D(a)) in the voltage window

of -0.8 - +0.1 V was 3.0 F cm^{-2} at a scan rate of 2 mV s^{-1}. The capacitance retention at

100 mV s^{-1} was found to be 31%. The capacitance of the FeOOH-CNT electrodes was

significantly lower, compared to that of Mn_3O_4-MWCNT electrodes. The FeOOH-

CNT electrodes showed poor cyclic stability.

The capacitance calculated from the CV for the 1000th cycle was 60% of the

capacitance calculated from the CV for the 1st cycle (Figure 9.7a). (Fe,Zn)OOH-CNT

showed improved capacitive performance, as indicated by the larger CV areas at the

same scan rates (Figure 9.6B). However, the currents remained low in the potential

range of -0.2 - +0.1 V. The capacitance decreased (Figure 9.6D(b)) from 3.6 F cm^{-2} to

1.4 F cm^{-2} with increasing sweep rate from 2 to 100 mV s^{-1}.
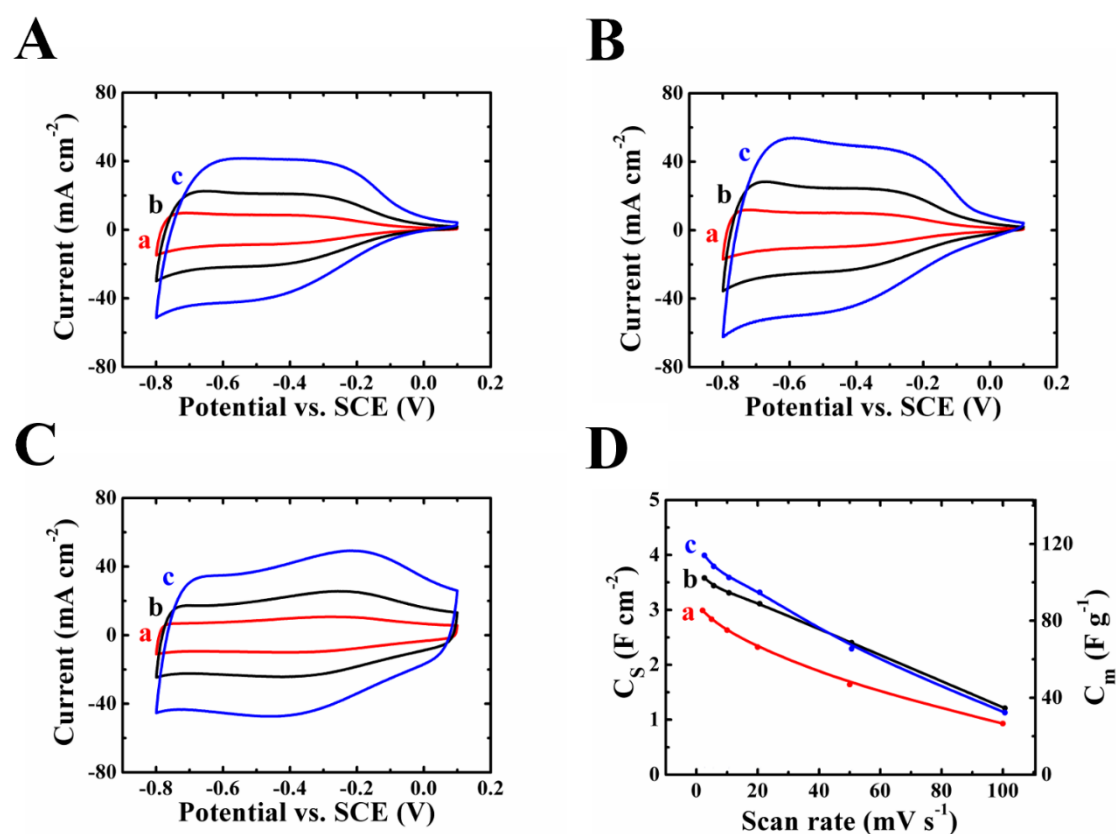
Figure 9.6 (A,B,C) CVs at scan rates of (a) 2, (b) 5 and (c) 10 mV s^{-1} and (D) C_S and
Cm for (A,D(a)) FeOOH-CNT, (B,D(b)) (Fe,Zn)OOH-CNT and (C,D(c))
(Fe,Zn)OOH-CNT-PNT electrodes.

(Fe,Zn)OOH-CNT showed enhanced cyclic stability, compared to FeOOH-CNT. The

capacitance retention was 80% after 1000 cycles (Figure 9.7b). The enhanced cyclic

stability is related to reduced dissolution of the capacitive Fe component of the solid

solution. It is suggested that more electrochemically negative Zn species prevent

release of Fe^{2+} ions from the electrodes and promote the precipitation of iron

hydroxide[33].
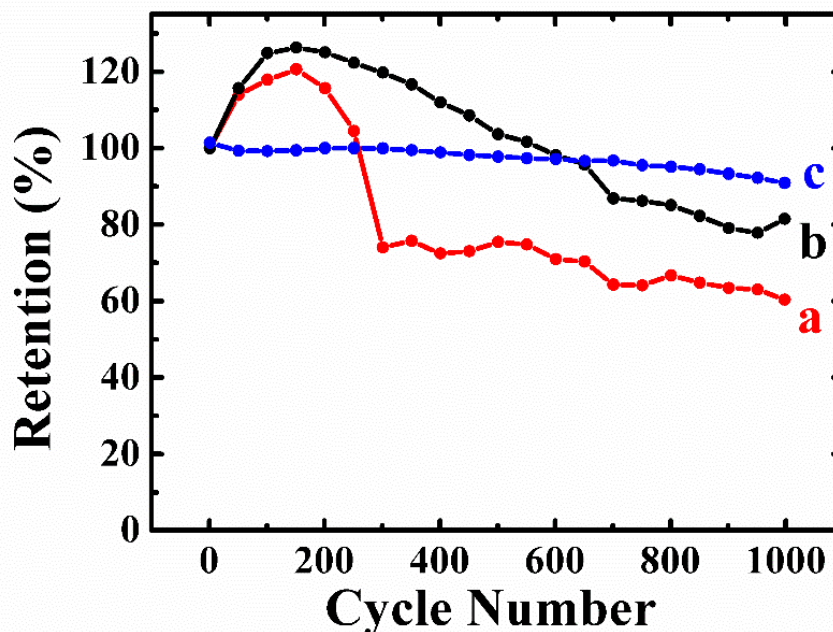
Figure 9.7 Capacitance retention during cycling for (a) FeOOH-CNT (b) (Fe,Zn)OOH-CNT (c) (Fe,Zn)OOH-CNT-PNT electrode.

Further improvement of the capacitive performance of the negative electrodes was

achieved using (Fe,Zn)OOH-CNT-PNT composites. The CV data for such composites

(Figure 9.6C) showed significant increase in currents in the potential range of -0.2 -

+0.1 V. The capacitance (Figure 9.6D(c)) of 4 F cm^{-2} was obtained.at a sweep rate of

2 mV s^{-1}. The capacitance retention was 91% after 1000 cycles (Figure 9.7c). The

improved capacitive behavior of (Fe,Zn)OOH-CNT-PNT compared with

(Fe,Zn)OOH-CNT was confirmed by impedance spectroscopy analysis, which was

performed at different electrode potentials.
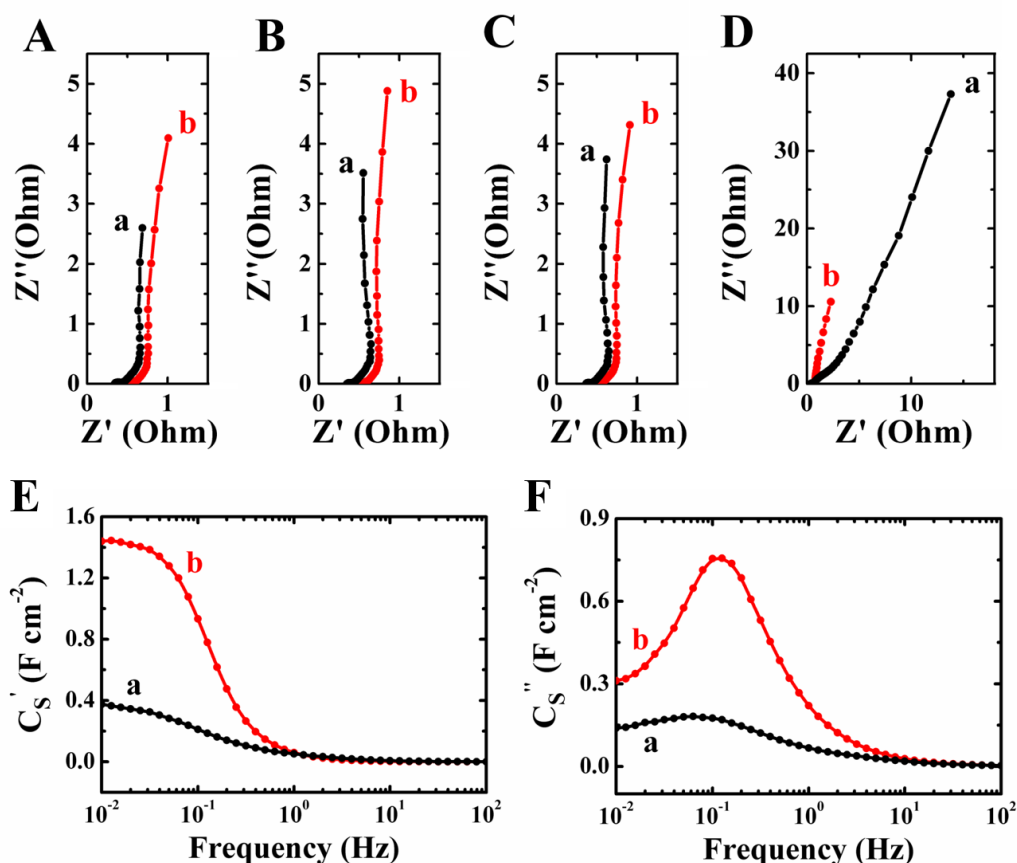
Figure 9.8 (A-D) Nyquist plot of complex impedances at (A)-0.8, (B)-0.5, (C)-0.3 V, and (D)+0.1 V vs. SCE for (a) (Fe,Zn)OOH-CNT (b) (Fe,Zn)OOH-CNT-PNT electrodes; (E,F) frequency dependence of complex capacitances (E) Cs' and (F) Cs" for (a) (Fe,Zn)OOH-CNT (b) (Fe,Zn)OOH-CNT-PNT electrode at fixed potential of +0.1 V vs. SCE.

Figure 9.8(A-C) shows Nyquist plot of impedance data at electrode potentials of -0.8, -0.5, and -0.3 V. The Nyquist plots show relatively low impedances for (Fe,Zn)OOH-CNT-PNT and (Fe,Zn)OOH-CNT electrodes. (Fe,Zn)OOH-CNT electrodes showed slightly lower impedance at potentials -0.8, -0.5 and -0.3 V. In contrast, (Fe,Zn)OOH-CNT showed (Figure 9.8D) significantly higher impedance at +0.1 V. The high real component of complex impedance of (Fe,Zn)OOH-CNT indicated high resistance, whereas high imaginary part resulted from low capacitance. The (Fe,Zn)OOH-CNT-

PNT electrode showed significantly lower impedance, indicating low resistance and

higher capacitance (Figure 9.8D). The real and imaginary components of capacitance

were calculated from the impedance data and presented in Figure 9.8(E,F).

(Fe,Zn)OOH-CNT-PNT electrodes showed significantly higher capacitances C_S' at low

frequencies, compared to (Fe,Zn)OOH-CNT (Figure 9.8E). Both electrodes showed a

relaxation type frequency dispersion of capacitance. The C_S'' maximum for

(Fe,Zn)OOH-CNT-PNT was observed at a higher frequency and indicated better rate

performance (Figure 9.8F).
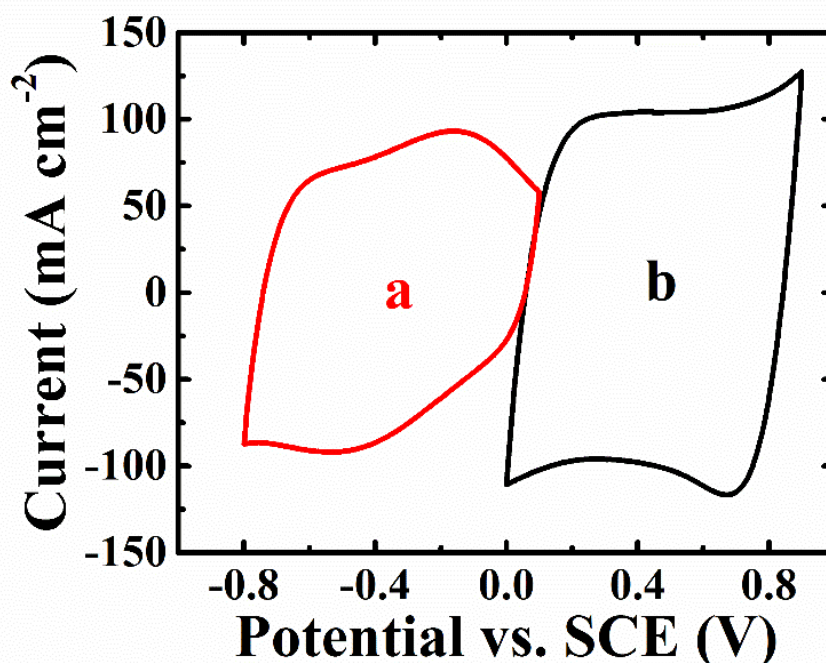
Figure 9.9 CVs at a scan rate of 20 mVs^{-1} for (a) (Fe,Zn)OOH-CNT-PNT electrode and
(b) Mn$_3$O$_4$-CNT electrode.

Figure 9.9 shows CVs for (Fe,Zn)OOH-CNT-PNT electrode in a negative potential

range and for Mn$_3$O$_4$-CNT electrode in a positive potential range in 0.5 M Na$_2$SO$_4$

electrolyte at a sweep rate of 20 mV s^{-1}. The CVs have comparable areas in partially

overlapped voltage windows. The electrodes were used for the fabrication of an

asymmetric capacitor device, which was tested in a voltage window of 1.6V. Figure

9.10 indicates that nearly box shape CVs were obtained at different sweep rates. The

device showed a capacitance of 1.87 F cm^{-2} at 2 mV s^{-1}. The capacitance retention at

100 mV s^{-1} was 24%. The analysis of the cyclic stability showed that capacitance

retention after 1000 cycles was 84% (Figure 9.11). Two devices connected in series

were used for powering of 20 mA LED bulbs (Figure 9.11inset).
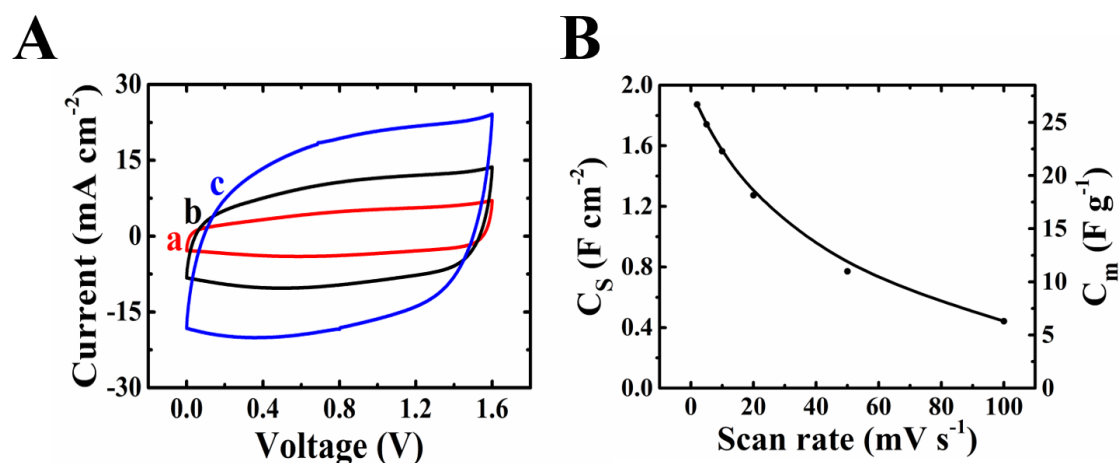
Figure 9.10 (A) CVs at scan rate of (a) 2, (b) 5 and (c) 10 mV s^{-1} and (B) C_S and Cm
for device, fabricated using Mn$_3$O$_4$-CNT and (Fe,Zn)OOH-CNT-PNT as positive and
negative electrodes, respectively.
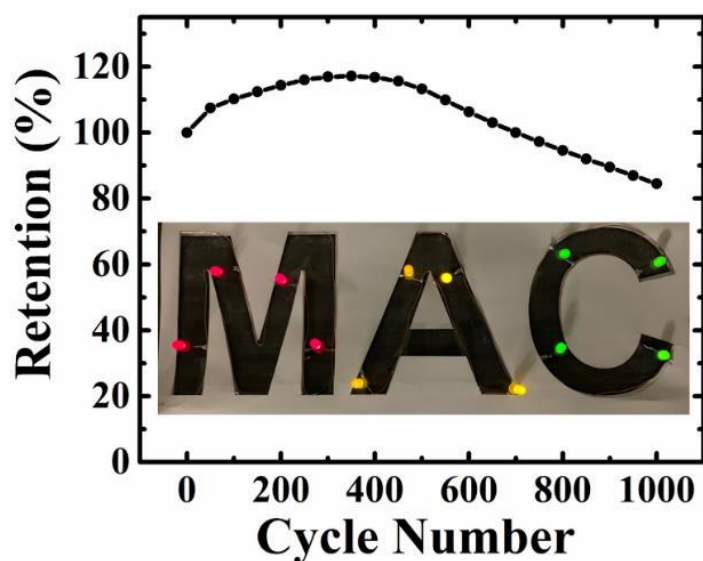
Figure 9.11 Capacitance retention during cycling of the device fabricated using Mn_3O_4-CNT and (Fe,Zn)OOH-CNT-PNT as positive and negative electrodes, respectively and (inset) LED bulbs powered by two devices connected in series.

9.5 Conclusions

Composite Mn_3O_4-CNT material has been prepared by chemical precipitation of

Mn_3O_4 and electrostatic heterocoagulation. The areal capacitance of Mn_3O_4-CNT

electrodes was higher than the capacitances of Mn_3O_4 composites, reported in the

literature. Good capacitive behavior has been achieved at high active mass loading of

36 mg cm^{-2} due to enhanced mixing of Mn_3O_4 and CNT, which resulted from several

factors, such as good dispersion of CNT using cationic TL, synthesis of

nanostructured Mn_3O_4 particles in the presence of well dispersed CNT and

electrostatic heterocoagulation of Mn_3O_4 and CNT. Cycling of the electrodes resulted

in changes in microstructure and oxidation state of Mn. The problem of low

capacitance of negative electrodes has been addressed by the development of

(ZnFe)OOH-CNT electrodes. These studies revealed beneficial effect of Zn and

polypyrrole on charge-discharge behavior and impedance at different electrode

potentials, enhanced capacitance and cyclic stability of the electrodes. Asymmetric

devices have been fabricated and tested, which showed promising performance in a

voltage window of 1.6 V.

9.6 Acknowledgements

9.7 Supplementary Information

Table 9.1 Mass loadings and specific capacitances of pure Mn_3O_4 and composite Mn_3O_4 based electrodes.

Mass Loading (mg cm^{-2})	Capacitance (F g^{-1})	Electrolytes	Ref.
1.66	471	1M Na_2SO_4	[34]
28.4	93	0.5M Na_2SO_4	[35]
5	53	1M Na_2SO_4	[36]
0.57	193	1M Na_2SO_4	[37]
2	274	1M Na_2SO_4	[38]
0.26	670	1M Na_2SO_4	[39]
0.5	193	0.5M Na_2SO_4	[40]
33	127	0.5M Na_2SO_4	[41]
2	286	1M Na_2SO_4	[42]
2	451	1M Na_2SO_4	[43]
2.8	193	Saturated Na_2SO_4	[44]
1.25	457	1M Na_2SO_4	[45]

1.6	435	1M Na$_2$SO$_4$	[46]
2	160	1M Na$_2$SO$_4$	[47]
0.65	1080	1M Na$_2$SO$_4$	[48]
3-5	131	1M Na$_2$SO$_4$	[49]
2-3	262	1M Na$_2$SO$_4$	[50]
1.2	239	1M Na$_2$SO$_4$	[51]
9	186	1M Na$_2$SO$_4$	[52]
9.5	222	1M Na$_2$SO$_4$	[53]
5	538	1M Na$_2$SO$_4$	[54]
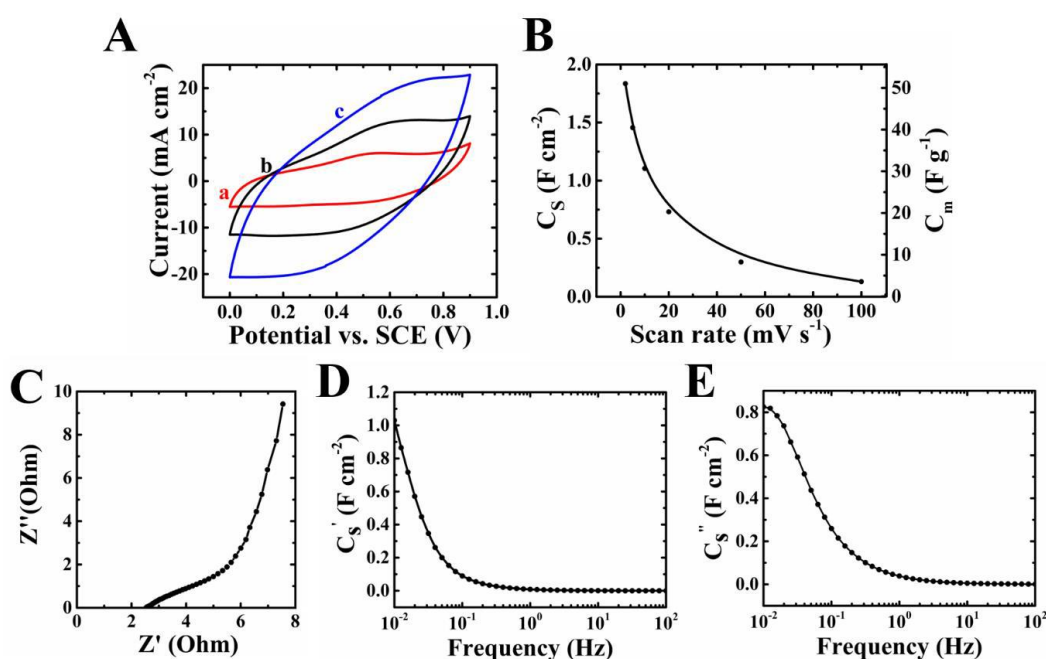
Figure 9.12 (A) CVs at scan rates of (a) 2, (b) 5 and (c) 10 mVs^{-1} and (B) Cs and Cm (C) Nyquist plot of complex impedance, and (D,E) frequency dependence of complex capacitances (D) Cs' and (E) Cs" for Mn$_3$O$_4$ electrode

Table 9.2 Components of complex impedance for Zn-FeOOH electrode at a frequency of 10 mHz.

Potential(V)	Zre(Ω)	Zimg(Ω)
-0.8	0.7	2.6
-0.5	0.5	3.5
-0.3	0.6	3.7
+0.1	13.8	37.3

Table 9.3 Components of complex impedance for Zn-FeOOH-PNT electrode at a frequency of 10 mHz.

Potential(V)	$Z_{re}(\Omega)$	$Z_{img}(\Omega)$
-0.8	1.0	4.1
-0.5	0.8	4.9
-0.3	0.9	4.3
+0.1	2.3	10.6

Table 9.4 Power-energy characteristics at different current densities for devices, containing positive Mn_3O_4-CNT and negative (Fe,Zn)OOH-CNT-PNT electrodes with active mass of the individual electrodes of 36 mg cm^{-2}.

Current density (mA cm^{-2})	3	5	7	10
Power density (W kg^{-1})	26.4	46.3	66.4	96.3
Energy density (Wh kg^{-1})	7.5	8.1	8.6	8.7

9.8 References

1. W. Wei, X. Cui, W. Chen, and D. G. Ivey,'Manganese oxide-based materials as electrochemical supercapacitor electrodes' *Chem. Soc.Rev.*, 2011, **40**(3), 1697-1721.

2. S. Zhang and G. Z. Chen,'Manganese oxide based materials for supercapacitors' *Energy Mater.*, 2008, **3**(3), 186-200.

3. R. Dong, Q. Ye, L. Kuang, X. Lu, Y. Zhang, X. Zhang, G. Tan, Y. Wen, and F. Wang,'Enhanced Supercapacitor Performance of Mn3O4 Nanocrystals by Doping Transition-Metal Ions' *ACS Appl. Mater. Interfaces*, 2013, **5**(19), 9508-9516.

4. D. Dubal, D. Dhawale, R. Salunkhe, S. Pawar, V. Fulari, and C. Lokhande,'A novel chemical synthesis of interlocked cubes of hausmannite Mn3O4 thin films for supercapacitor application' *J.Alloys Compounds*, 2009, **484**(1-2), 218-221.

5. Y.F. Lee, K.H. Chang, C.C. Hu, and Y.H. Chu,'Designing tunable microstructures of Mn3O4 nanoparticles by using surfactant-assisted dispersion' *J. Power Sources*, 2012, **206**, 469-475.

6. Z. Qi, A. Younis, D. Chu, and S. Li,'A facile and template-free one-pot synthesis of Mn3O4 nanostructures as electrochemical supercapacitors' *Nano-micro Letters*, 2016, **8**(2), 165-173.

7. D. P. Shaik, P. Rosaiah, K. S. Ganesh, Y. Qiu, and O. Hussain,'Improved electrochemical performance of Mn3O4 thin film electrodes for supercapacitors' *Mater. Sci. Semiconductor Processing*, 2018, **84**, 83-90.

8. A. A. Yadav,'Influence of electrode mass-loading on the properties of spray deposited Mn3O4 thin films for electrochemical supercapacitors' *Thin Solid Films*, 2016, **608**, 88-96.

9. J. Cao, Y. Wang, Y. Zhou, D. Jia, J.-H. Ouyang, and L. Guo,'Performances of high voltage electrochemical capacitor using ball-milled graphite/Mn3O4 composite electrodes' *J. Electroanal. Chem.*, 2012, **682**, 23-28.

10. S. Li, L.-L. Yu, R.-B. Li, J. Fan, and J.-T. Zhao,'Template-free and room-temperature synthesis of 3D sponge-like mesoporous Mn3O4 with high capacitive performance' *Energy Storage Mater.*, 2018, **11**, 176-183.

11. Y. Qiao, Q. Sun, J. Xi, H. Cui, Y. Tang, and X. Wang,'A modified solvothermal synthesis of porous Mn3O4 for supercapacitor with excellent rate capability and long cycle life' *Journal Alloys Compounds*, 2016, **660**, 416-422.

12. Y. Qiao, Q. Sun, O. Sha, X. Zhang, Y. Tang, T. Shen, L. Kong, and W. Gao,'Synthesis of Mn3O4 nano-materials via CTAB/SDS vesicle templating for high performance supercapacitors' *Mater. Lett.*, 2018, **210**, 128-132.

13. D. Yan, Y. Li, Y. Liu, R. Zhuo, Z. Wu, B. Geng, J. Wang, P. Ren, P. Yan, and Z. Geng,'Hydrothermal synthesis and electrochemical properties of hexagonal

hydrohausmannite plates as supercapacitor electrode material' *Mater. Lett.*, 2014, **117**, 62-65.

14. Z. Gao, H. Wang, Z. Cao, T. Zhou, C. An, and Y. Zhao,'Silver Nanowires@ Mn3O4 Core–Shell Nanocables as Advanced Electrode Materials for Aqueous Asymmetric Supercapacitors' *Energy Technol.*, 2017, **5**(12), 2275-2282.

15. L. Liu, L. Su, J. Lang, B. Hu, S. Xu, and X. Yan,'Controllable synthesis of Mn3O4 nanodots@nitrogen-doped graphene and its application for high energy density supercapacitors' *J. Mater. Chem. A*, 2017, **5**(11), 5523-5531.

16. K. Subramani, D. Jeyakumar, and M. Sathish,'Manganese hexacyanoferrate derived Mn3O4 nanocubes–reduced graphene oxide nanocomposites and their charge storage characteristics in supercapacitors' *Phys.Chem. Chem. Phys.*, 2014, **16**(10), 4952-4961.

17. X. Xiao, Y. Wang, G. Chen, L. Wang, and Y. Wang,' Mn3O4/activated carbon composites with enhanced electrochemical performances for electrochemical capacitors' *J. Alloys Compounds*, 2017, **703**, 163-173.

18. J. Yao, S. Yao, F. Gao, L. Duan, M. Niu, and J. Liu,'Reduced graphene oxide/Mn3O4 nanohybrid for high-rate pseduocapacitive electrodes' *J. Colloid Interface Sci.*, 2018, **511**, 434-439.

19. J. Xu, X. Fan, Q. Xia, Z. Shao, B. Pei, Z. Yang, Z. Chen, and W. Zhang,'A highly atom-efficient strategy to synthesize reduced graphene oxide-Mn3O4 nanoparticles composites for supercapacitors' *J. Alloys Compounds*, 2016, **685**, 949-956.

20. M. S. Ata, J. Milne, and I. Zhitomirsky,'Fabrication of Mn3O4–carbon nanotube composites with high areal capacitance using cationic and anionic dispersants' *J. Colloid Interface Sci.*, 2018, **512**, 758-766.

21. J. Milne and I. Zhitomirsky,'Application of octanohydroxamic acid for liquid-liquid extraction of manganese oxides and fabrication of supercapacitor electrodes' *J. Colloid Interface Sci.*, 2018, **515**, 50-57.

22. Y. Zhou, L. Guo, W. Shi, X. Zou, B. Xiang, and S. Xing,'Rapid Production of Mn3O4/rGO as an Efficient Electrode Material for Supercapacitor by Flame Plasma' *Materials*, 2018, **11**(6), 881.

23. Y. Xiao, Y. Cao, Y. Gong, A. Zhang, J. Zhao, S. Fang, D. Jia, and F. Li,'Electrolyte and composition effects on the performances of asymmetric supercapacitors constructed with Mn3O4 nanoparticles–graphene nanocomposites' *J.Power Sources*, 2014, **246**, 926-933.

24. C. Liu, H. Song, C. Zhang, Y. Liu, C. Zhang, X. Nan, and G. Cao,'Coherent Mn3O4-carbon nanocomposites with enhanced energy-storage capacitance' *Nano Research*, 2015, **8**(10), 3372- 3383.

25. N. S. Arul, J. I. Han, and P. C. Chen,'Solid State Supercapacitor Based on Manganese Oxide@Reduced Graphene Oxide and Polypyrrole Electrodes' *ChemElectroChem*, 2018, **5**(19), 2747-2757.

26. S. Krehula, S. Musić, Ž. Skoko, and S. Popović,'The influence of Zn-dopant on the precipitation of α-FeOOH in highly alkaline media' *J Alloys Compounds*, 2006, **420**(1), 260-268.

27. Y. Zhu, K. Shi, and I. Zhitomirsky,'Anionic dopant–dispersants for synthesis of polypyrrole coated carbon nanotubes and fabrication of supercapacitor electrodes with high active mass loading' *J. Mater. Chem. A*, 2014, **2**(35), 14666-14673.

28. C. Shi and I. Zhitomirsky,'Electrodeposition and Capacitive Behavior of Films for Electrodes of Electrochemical Supercapacitors' *Nanoscale Res. Lett.*, 2010, **5**(3), 518.

29. Y. Su and I. Zhitomirsky,'Hybrid MnO2/carbon nanotube-VN/carbon nanotube supercapacitors' *J. Power Sources*, 2014, **267**, 235-242.

30. M. Kosmulski,'Isoelectric points and points of zero charge of metal (hydr)oxides: 50 years after Parks' review' *Adv. Colloid and Interface Sci.*, 2016, **238**, 1-61.

31. R. Attias, D. Sharon, A. Borenstein, D. Malka, O. Hana, S. Luski, and D. Aurbach,'Asymmetric supercapacitors using chemically prepared MnO2 as positive electrode materials' *J. Electrochem. Soc.*, 2017, **164**(9), A2231-A2237.

32. Z. Zhang, K. Chi, F. Xiao, and S. Wang,'Advanced solid-state asymmetric supercapacitors based on 3D graphene/MnO2 and graphene/polypyrrole hybrid architectures' *J. Mater. Chem. A*, 2015, **3**(24), 12828-12835.

33. M. R. C. Ismael and J. M. R. Carvalho,'Iron recovery from sulphate leach liquors in zinc hydrometallurgy' *Minerals Eng.*, 2003, **16**(1), 31-39.

34. R. Aswathy, M. Ulaganathan and P. Ragupathy, Journal of Alloys and Compounds 2018, vol. 767, pp. 141-150.

35. M.S. Ata, J. Milne and I. Zhitomirsky, Journal of Colloid and Interface Science 2018, vol. 512, pp. 758-766.

36. J. Cao, Y. Wang, Y. Zhou, D. Jia, J.-H. Ouyang and L. Guo, Journal of Electroanalytical Chemistry 2012, vol. 682, pp. 23-28.

37. D. Dubal, D. Dhawale, R. Salunkhe, S. Pawar, V. Fulari and C. Lokhande, Journal of Alloys and Compounds 2009, vol. 484, pp. 218-221.

38. S. Li, L.-L. Yu, R.-B. Li, J. Fan and J.-T. Zhao, Energy Storage Materials 2018, vol. 11, pp. 176-183.

39. Q. Liao, S. Li, H. Cui and C. Wang, Journal of Materials Chemistry A 2016, vol. 4, pp. 8830-8836.

40. C.-L. Liu, K.-H. Chang, C.-C. Hu and W.-C. Wen, Journal of Power Sources 2012, vol. 217, pp. 184-192.

41. J. Milne and I. Zhitomirsky, Journal of Colloid and Interface Science 2018, vol. 515, pp. 50-57.

42. Y. Qiao, Q. Sun, J. Xi, H. Cui, Y. Tang and X. Wang, Journal of alloys and compounds 2016, vol. 660, pp. 416-422.

43. Y. Qiao, Q. Sun, O. Sha, X. Zhang, Y. Tang, T. Shen, L. Kong and W. Gao, Materials Letters 2018, vol. 210, pp. 128-132.

44. Q. Jiangying, G. Feng, Z. Quan, W. Zhiyu, H. Han, L. Beibei, W. Wubo, W. Xuzhen and Q. Jieshan, Nanoscale 2013, vol. 5, pp. 2999-3005.

45. H.U. Shah, F. Wang, M.S. Javed, N. Shaheen, M. Saleem and Y. Li, Ceramics International 2018, vol. 44, pp. 3580-3584.

46. D.P.M.D. Shaik, R. Pitcheri, Y. Qiu and O.M. Hussain, Ceramics International 2019, vol. 45, pp. 2226-2233.

47. X. She, X. Zhang, J. Liu, L. Li, X. Yu, Z. Huang and S. Shang, Materials research bulletin 2015, vol. 70, pp. 945-950.

48. Y. Song, R. Zhao, K. Zhang, J. Ding, X. Lv, M. Chen and J. Xie, Electrochimica Acta 2017, vol. 230, pp. 350-357.

49. K. Subramani, D. Jeyakumar and M. Sathish, Physical Chemistry Chemical Physics 2014, vol. 16, pp. 4952-4961.

50. L. Wang, L. Chen, Y. Li, H. Ji and G. Yang, Powder technology 2013, vol. 235, pp. 76-81.

51. Y. Xiao, Y. Cao, Y. Gong, A. Zhang, J. Zhao, S. Fang, D. Jia and F. Li, Journal of Power Sources 2014, vol. 246, pp. 926-933.

52. J. Xu, X. Fan, Q. Xia, Z. Shao, B. Pei, Z. Yang, Z. Chen and W. Zhang, Journal of Alloys and Compounds 2016, vol. 685, pp. 949-956.

53. D. Yan, Y. Li, Y. Liu, R. Zhuo, Z. Wu, B. Geng, J. Wang, P. Ren, P. Yan and Z. Geng, Materials Letters 2014, vol. 117, pp. 62-65.

54. J. Yao, S. Yao, F. Gao, L. Duan, M. Niu and J. Liu, Journal of Colloid and Interface Science 2018, vol. 511, pp. 434-439.

Chapter 10 MXene-polypyrrole electrodes for asymmetric supercapacitors

Wenyu Liang*[α] and Igor Zhitomirsky*

*Department of Materials Science and Engineering, McMaster University,

Hamilton, Ontario, L8S 4L7, Canada

αCorresponding Author: liangw26@mcmaster.ca

10.1 Abstract

Despite the tremendous progress in the development and applications of flexible high-performance MXene-polypyrrole (PPy) composites for supercapacitor (SC) technology, current research in this area is limited to symmetric devices with low active mass loading (AML) and operating in limited voltage windows of 0.5-1 V in acidic electrolytes. Here, we propose an asymmetric SC device operating in a neutral 0.5 M Na_2SO_4 electrolyte in a voltage window of 1.7 V. We report high capacitance of 1.37 F cm^{-2} from the cyclic voltammetry (CV) data and 1.18 F cm^{-2} from the galvanostatic charge-discharge (GCD) data. A useful strategy is provided for the fabrication of MXene-PPy composites, which allows their application in negative electrodes and facilitates remarkable capacitive performance at AML of 40 mg cm^{-2}. We optimize composition and performance of the negative electrodes and report high capacitance of 2.11 F cm^{-2} from CV data and 2.49 F cm^{-2} from GCD data, which is achieved at low electrode resistance. One of the key factors for the enhanced negative electrode performance is the use a conceptually new strategy for in-situ PPy polymerization on the MXene surface, which is based on the application of an efficient catecholate-type dispersant for electrostatic dispersion of MXene. The adsorbed dispersant acts as an anionic dopant for PPy, promoting PPy polymerization on the MXene surface. PPy coated multiwalled carbon nanotubes (MCNT) are formed by in-situ polymerization of PPy on dispersed MCNT for charge storage in positive electrodes of the SC devices.

The positive electrodes were designed to match capacitive properties of the negative electrodes in a complementary potential window.

Keywords: MXene, supercapacitor, polypyrrole, carbon nanotube, dopant, polymerization

10.2 Introduction

MXenes, after their discovery[1] in 2011, have attracted significant attention[2-4] in the field of electrical energy storage. In a general chemical formula $M_{n+1}X_nT_x$ (n=1-3) of MXenes, M represents Ti, Sc and V, X is C or N, and Tx stands for surface atoms or groups such as oxygen (-O), hydroxyl (-OH), or fluorine (-F)[1]. Among numerous MXene types, $Ti_3C_2T_x$ is the most studied material for electrochemical applications due to its high surface area[5], good conductivity[6], and improved chemical stability[7]. It has been proven by many researchers that $Ti_3C_2T_x$ is a promising candidate material for the development of high-performance supercapacitor electrodes[7-11]. Supercapacitors (SCs) meet the high demand for energy storage due to their superior performance features, such as fast charge-discharge rate, long cyclic life, and high power density[12]. The key factor to enhance the SC performance is the use of advanced electrode materials[13-15].

$Ti_3C_2T_x$ is a relatively new SC electrode material and great attention has been paid to explore its benefits[16]. Many investigations reported advanced fabrication methods and high capacitance of MXene films[17-19]. Of particular interest is the development of MXene based composites. Advanced composites have been developed by combining MXenes with polymers[19, 20], carbon nanotubes[21, 22], graphene[23], metal oxides[24, 25] and hydroxides[26]. However, the reported high gravimetric and volumetric capacitances were acquired at relatively low active mass loadings (AML).

It was suggested that high AML and high mass ratio between AML and inactive electrode parts are required for industrial applications[12]. The performance of MXene based electrodes was analyzed in different electrolytes[27].

Efforts to increase capacitance of MXene based electrodes have resulted in the development of MXene-polypyrrole composites[28-30]. This approach facilitated the fabrication of flexible electrodes and devices[29, 31]. Polypyrrole (PPy) is a conductive electrochemically active polymer, which exhibits pseudocapacitive properties. It was shown that improved electron transport and charge-discharge rates can be achieved in MXene-PPy composites[32] due to synergistic effect of the MXene and PPy individual layers.   Oxidant free polymerization of PPy was performed in spaces between MXene layers[28]. Especially interesting is the possibility to form aligned PPy layers[28], which provide enhanced conductivity. The chemical characteristics of MXene and PPy offer interesting effects at their interface, which allowed formation of PPy layers on the MXene surface and enhanced capacitive and cyclic performance of PPy[28]. The interlayer spacing of $Ti_3C_2T_x$ can also be expanded by the intercalation of homogeneous PPy nanoparticles, thus providing more pathways for electrolyte diffusion[33]. $Ti_3C_2T_x$ -PPy electrodes were tested in H_2SO_4[28, 32], KOH[30], and Na_2SO_4[33] electrolytes. Previous investigations focused on the fabrication of thin film electrodes with relatively low AML, which was typically below 3 mg cm^{-2}. In many previous investigations MXene-PPy composite electrodes were developed and tested in a relatively narrow

154

positive potential range[29, 34, 35]. Symmetric devices were obtained for operation in a voltage window of 0.5 V[36] or 1 V [37] in H_2SO_4 electrolyte and 0.5 V[36] or 0.6 V [31] in H_2SO_4/PVA electrolyte.

Despite the recent advances in the fabrication of MXene-PPy composites, there is a need in their further development for design of SC electrodes with high areal capacitance. The major problem in the development of such electrodes is the reduction of specific capacitance with increasing AML. Neutral electrolytes offer numerous benefits for the development of asymmetric SC with enlarged voltage windows, because such electrolytes are environmentally friendly, stable, cheap, non-corrosive and allow for the use of diverse current collectors[38]. It is widely accepted that the development of asymmetric SCs, containing individual electrodes operating in different potential windows, offers a possibility of increasing device voltage window and enhancing specific power and energy of the devices. It is also well known that the selection of anionic dopants is critically important for the fabrication of pure PPy electrodes. Significant increase in capacitance and reduction in resistance of PPy electrodes can be achieved by the use of advanced dopants[39, 40]. However, little attention has been paid in the literature to the selection of dopants for the fabrication of MXene-PPy electrodes.

The goal of this investigation was the fabrication of an asymmetric device, containing MXene-PPy negative electrodes and PPy-multiwalled carbon nanotube (MCNT)

positive electrodes operating in a neutral Na_2SO_4 electrolyte. The in-situ polymerization

method developed in this investigation facilitated the fabrication of MXene-PPy

electrodes with high areal capacitance of 2.11 F cm^{-2}, which is much higher than that

for other MXene-PPy electrodes reported in the literature. Enhanced capacitive

behavior and low resistance at AML of 40 mg cm^{-2} were linked to the beneficial effects

of pyrocatechol violet dopant for PPy polymerization, which adsorbed on MXene,

facilitated MXene dispersion, and promoted PPy polymerization on the MXene surface.

The results presented in this paper demonstrate that MXene-PPy negative electrodes

and PPy-MWCNT positive electrodes exhibited comparable capacitances in

complementary and overlapping potential ranges in a neutral Na_2SO_4 electrolyte.

Following this work objective, we have fabricated and tested an asymmetric SC,

containing MXene-PPy negative electrodes and PPy-MWCNT positive electrodes for

operation in a voltage window of 1.7 V.

10.3 Experimental procedure

$Ti_3C_2T_x$ (BET surface area 5.03 m^2 g^{-1}, Laizhou Kai Kai Ceramic Materials Co.),

pyrrole (Py), Na_2SO_4, poly(vinyl butyral-co-vinyl alcohol-co-vinyl acetate) (PVB,

M_w=50,000-80,000) (Millipore Sigma), pyrocatechol violet (PCV), ammonium

persulfate (APS), multiwalled carbon nanotubes (MCNT, Bayer) and commercial Ni

foam current collectors[41] (surface area 2.01 m^{2}g^{-1}, 95% porosity, Vale) were used in

this research.

$Ti_3C_2T_x$-PPy composites were synthesized by polymerization of pyrrole monomer in presence of $Ti_3C_2T_x$ in solution. Stable aqueous suspensions of $Ti_3C_2T_x$ particles were prepared using PCV as a dispersant. Ultrasonic agitation of the suspension was performed during 1 h for achieving good dispersion. Then Py was injected to the suspension and polymerization was performed by adding APS as an oxidant. The mass ratios between $Ti_3C_2T_x$ and Py were 9:1, 8:2 and 7:3, and corresponding materials were denoted as $Ti_3C_2T_x$-PPy-10, $Ti_3C_2T_x$-PPy-20 and $Ti_3C_2T_x$-PPy-30, respectively. Polymerization was performed in ice bath at 4 °C during 5 h under magnetic stirring. Followed by vacuum filtration and drying in oven for 12 h, the obtained powders were mixed with PVB binder solution and impregnated into Ni foam current collectors. The calendering procedure was used to reduce thickness of the current collectors to 25% of original thickness[41]. The total mass of impregnated material was 40 mg, the mass ratio of PVB binder to the total mass of $Ti_3C_2T_x$ and PPy was 3/100 and the electrode area was 1 cm^2.

The synthesis of PPy-MCNT composite materials was described in the previous work[40]. In a typical procedure, 2 g L^{-1} MCNT suspension, containing PCV as a dispersant was sonicated for 1 h to form a homogeneous suspension, then kept in ice bath with Py added at 4 °C. The molar ratio between pyrrole and PCV was 10:1. Polymerization was performed by addition of APS with mass ratio of 1:1 to Py. The

precipitate was filtrated and dried in oven for 12 h, then mixed with PVB binder solution and impregnated into Ni foam current collector. The total mass of impregnated material was 40 mg, the mass ratio of PVB binder to the total mass of PPy and MCNT was 3/100 and the electrode area was 1 cm^2.

Asymmetric devices were prepared using $Ti_3C_2T_x$-PPy negative electrodes and PPy-MCNT positive electrodes. The electrodes were separated by a porous polymer membrane. The electrolyte was 0.5 M Na_2SO_4 solution. The electrode area and AML of each electrode were 1 cm^2 and 40 mg cm^{-2}, respectively.

Morphology study was carried out by electron scanning microscopy (SEM) JEOL JSM-7000F. Potentiostat Princeton 2273 was used for electrochemical impedance spectroscopy (EIS) and cyclic voltammetry (CV). Galvanostatic charge discharge (GCD) was conducted by Biologic AMP 300 potentiostat. 0.5 M Na_2SO_4 solution was used as the electrolyte for electrochemical testing of electrodes and devices. In the three-electrode testing system for single electrodes, the counter electrode was a high surface area Pt gauze and the reference one was a saturated calomel electrode (SCE).). Geometrical area normalized capacitances C_S and mass normalized capacitances C_m were calculated from CV or GCD data, and complex capacitances C_S' and C_S'' were obtained from EIS data at AC signal of 5 mV as it was described in a previous publication[12].

10.4 Results and Discussion

At the beginning of this section, we describe important features and benefits of our approach to the fabrication of $Ti_3C_2T_x$-PPy electrodes with enhanced performance in the negative potential range in Na_2SO_4 electrolyte, which was a key factor for the fabrication of asymmetric devices with significantly enlarged voltage window and higher capacitance, compared to symmetric devices. Our approach was based on the use of PCV dye as a multifunctional agent for the fabrication of advanced $Ti_3C_2T_x$-PPy electrodes. As pointed out above, little attention has been paid in the previous investigations of $Ti_3C_2T_x$-PPy electrodes to the selection of dopants for PPy polymerization. However, dopants exert significant influence on the polymerization process and properties of PPy. Anionic dopants compensate positive charge of PPy generated during chemical or electrochemical polymerization processes. It is known that the conductivity of PPy can be increased by two orders of magnitude using different surfactants as anionic dopants[41]. Significantly higher conductivities can also be achieved using organic dyes as anionic dopants instead of anionic surfactants[41]. The conductivity of PPy is critical for achieving high capacitance of $Ti_3C_2T_x$-PPy electrodes. Many previous investigations focused on the development of $Ti_3C_2T_x$-PPy electrodes for operation in the positive potential range in H_2SO_4 electrolyte[42, 43]. It is known that SC electrodes usually show lower capacitance in neutral electrolytes, such as Na_2SO_4, compared to H_2SO_4 due to higher conductivity of the H_2SO_4

electrolytes[44, 45]. Moreover, it is challenging to achieve high capacitance of PPy in a negative potential range due to the local pH increase at the surface of the negative electrodes. It is in this regard that the conductivity of PPy decreases drastically in the presence of alkali[41]. However, it will be shown below that using PCV dye as a dopant we achieved significantly lower resistance of the $Ti_3C_2T_x$-PPy electrodes in the Na_2SO_4 electrolyte and negative potential range, compared to the literature on $Ti_3C_2T_x$-PPy electrodes operating in a positive potential range in H_2SO_4 electrolyte. It is also important to note that low resistance was achieved at significantly higher AML. The low resistance was one of the important factors for achieving high C_S of the electrodes. Another important factor was PPy polymerization on the $Ti_3C_2T_x$ surface.

Previous investigations highlighted the benefits of PPy polymerization on the $Ti_3C_2T_x$ surface. Our approach is conceptually different from the previous investigations. The good dispersion of $Ti_3C_2T_x$ particles and prevention of their agglomeration are critically important for the in-situ PPy deposition on the particles during PPy polymerization. The $Ti_3C_2T_x$ particles used in this investigation showed poor suspension stability and rapidly precipitated. We found that good colloidal stability of $Ti_3C_2T_x$ particles can be achieved using PCV as a dispersant. Figure 10.1A compares $Ti_3C_2T_x$ suspensions prepared with and without dispersant and presents evidence of efficient $Ti_3C_2T_x$ dispersion. The suspensions stabilized with PCV were stable for more than one month. We linked exceptional dispersion properties of PCV to important features of the

160

chemical structure of this molecule (Figure 10.1B). Three major factors govern

efficiency of the dispersant molecules: their adsorption on the particle surface, size and

electric charge. Adsorbed dispersant facilitates particle dispersion, whereas non-

adsorbed charged dispersant promotes particle coagulation. The chemical structure of

PCV includes a catechol group, which imparts strong adsorption properties to this

molecule. The interest in catecholate dispersants[46] resulted from the investigations

of mussel protein adhesion to different inorganic surfaces in sea water, which is based

on superstrong catecholate-type bonding. Previous investigations showed that various

catecholate dispersants adsorbed on TiO_2 surfaces[46-49]. Therefore, similar bidentate

bonding mechanisms (Figure 10.1C) can be suggested for PCV bonding to Ti atoms on

the $Ti_3C_2T_x$ surface. The bonding mechanism involved condensation of surface OH

groups bonded to Ti atoms at the $Ti_3C_2T_x$ surface and phenolic OH groups of PCV.

The electric charge of the anionic PCV molecules facilitated electrostatic repulsion and

dispersion of the $Ti_3C_2T_x$ particles. The adsorbed negatively charged PCV molecules

acted as anionic dopants, which promoted PPy polymerization on dispersed $Ti_3C_2T_x$

particles and compensated a positive charge of growing PPy chains. The electrostatic

attraction of the negatively charged PCV and growing positively charged PPy chains

promoted PPy deposition on the $Ti_3C_2T_x$ particles. Our previous experimental results

on the fabrication of PPy coated MCNT can be invoked in support of the suggested

coating mechanism[40, 50]. In the previous investigations[40, 50], polyaromatic

anionic dispersants adsorbed on carbon nanotubes by π-π interactions, acted as

dispersants for MCNT and facilitated the formation of uniform PPy coatings on

individual well-dispersed MCNT by in-situ polymerization.
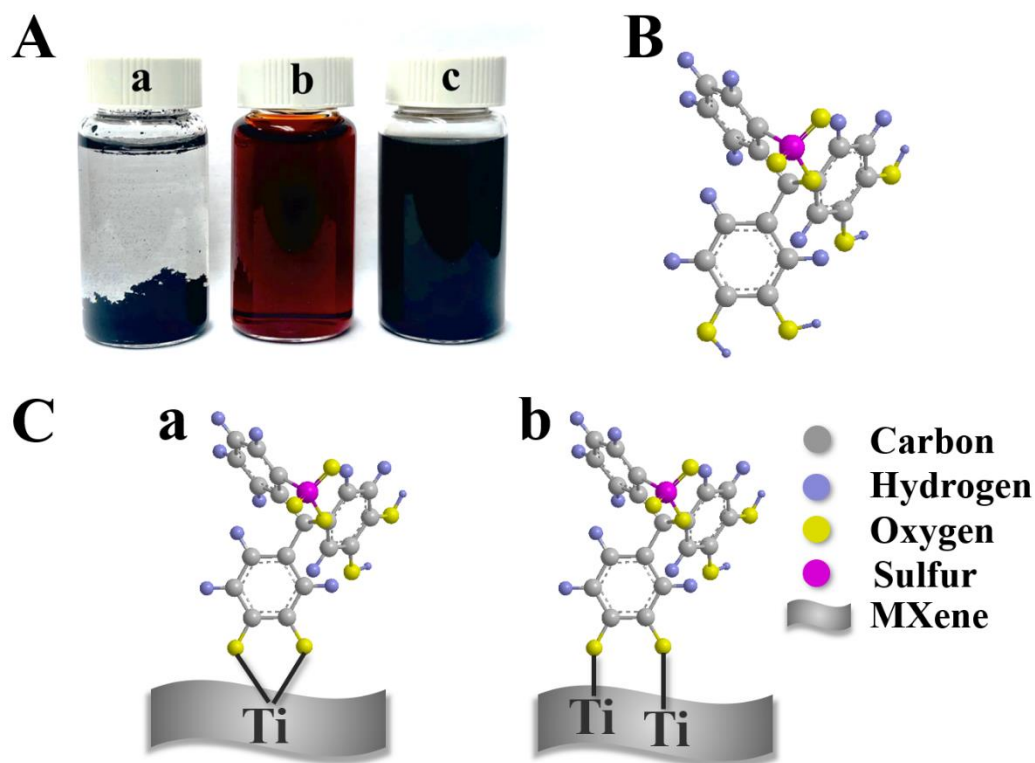
Figure 10.1. (A) (a) As-prepared 1 g L^{-1} $Ti_3C_2T_x$ (b) as-prepared 1 g L^{-1} PCV, and (c) 1 g L^{-1} $Ti_3C_2T_x$ and 1 g L^{-1} PCV in water, (B) chemical structure of PCV and (C) adsorption mechanisms of PCV on $Ti_3C_2T_x$ surface by (a) chelating and (b) bridging.

Figure 10.2 shows SEM images of coated and uncoated $Ti_3C_2T_x$ particles. PPy was

formed only on the $Ti_3C_2T_x$ surface and formation of separate PPy particles was avoided.

In contrast, the SEM images of $Ti_3C_2T_x$-PPy (Figure 10.9) prepared without PCV

showed separate agglomerates of PPy particles. The electrochemical performance was

studied by cyclic voltammetry in a potential window between -1.2 and -0.2 V. As it

is shown in Figure 10.3A, the CV shapes for the electrodes are close to ideal rectangular

shapes.
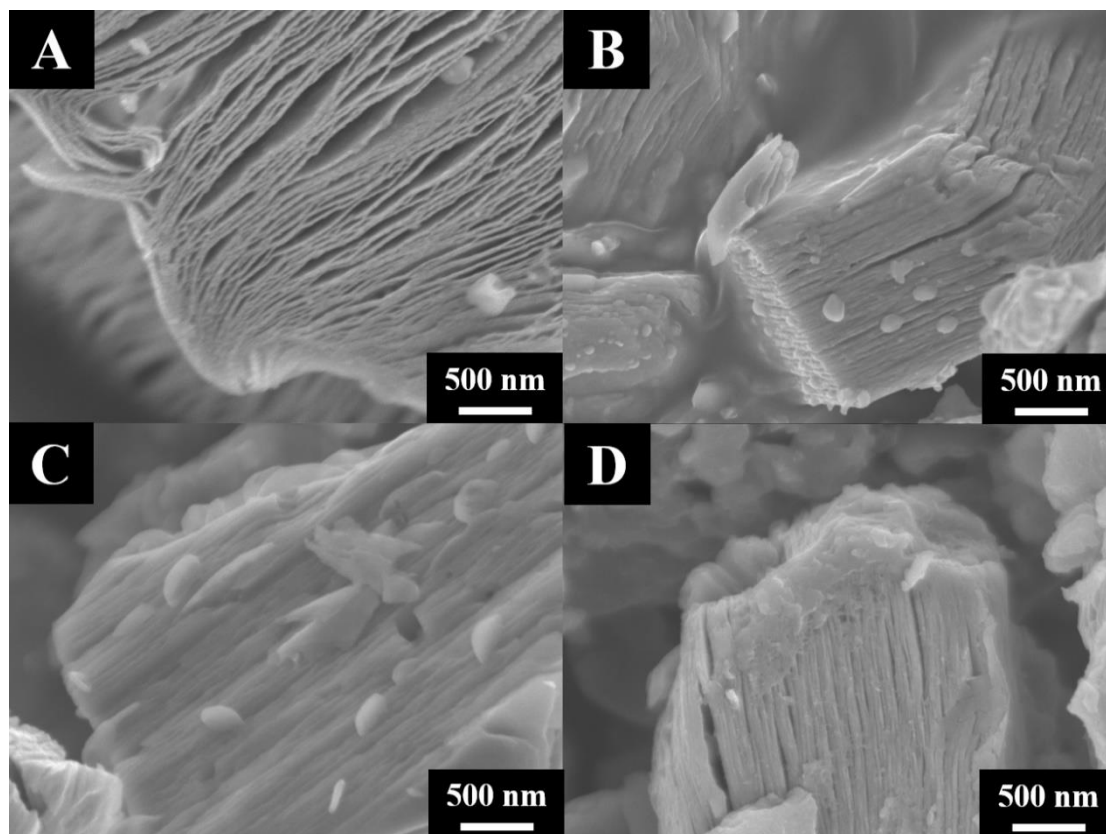
Figure 10.2. SEM images for (A) as-received pure $Ti_3C_2T_x$ (B) $Ti_3C_2T_x$-PPy-10 (C) $Ti_3C_2T_x$-PPy-20 and (D) $Ti_3C_2T_x$-PPy-30.

The CV area was highest for $Ti_3C_2T_x$-PPy-20 electrode with calculated capacitance of

2.11 F cm^{-2} (52.75 F g^{-1}), followed by $Ti_3C_2T_x$-PPy-10 electrode (2.03 F cm^{-2}, 50.75 F

g^{-1}), $Ti_3C_2T_x$-PPy-30 electrode (1.62 F cm^{-2}, 40.50 F g^{-1}), and $Ti_3C_2T_x$ electrode (1.53

F cm^{-2}, 38.25 F g^{-1}) at 2 mV s^{-1} sweep rate. It can be suggested that higher capacitance

of $Ti_3C_2T_x$-PPy composites compared with pure $Ti_3C_2T_x$ is due to the beneficial effect

of deposited conductive PPy. The capacitance retention at high scan rates is another

performance parameter which has an important influence on practical applications. At

100 mV s^{-1} sweep rate of potential, the capacitance retentions were 26.80%, 31.03%,

32.75% and 29.01% for Ti$_3$C$_2$T$_x$, Ti$_3$C$_2$T$_x$ -PPy-10, Ti$_3$C$_2$T$_x$-PPy-20 and Ti$_3$C$_2$T$_x$-PPy-

30, respectively.
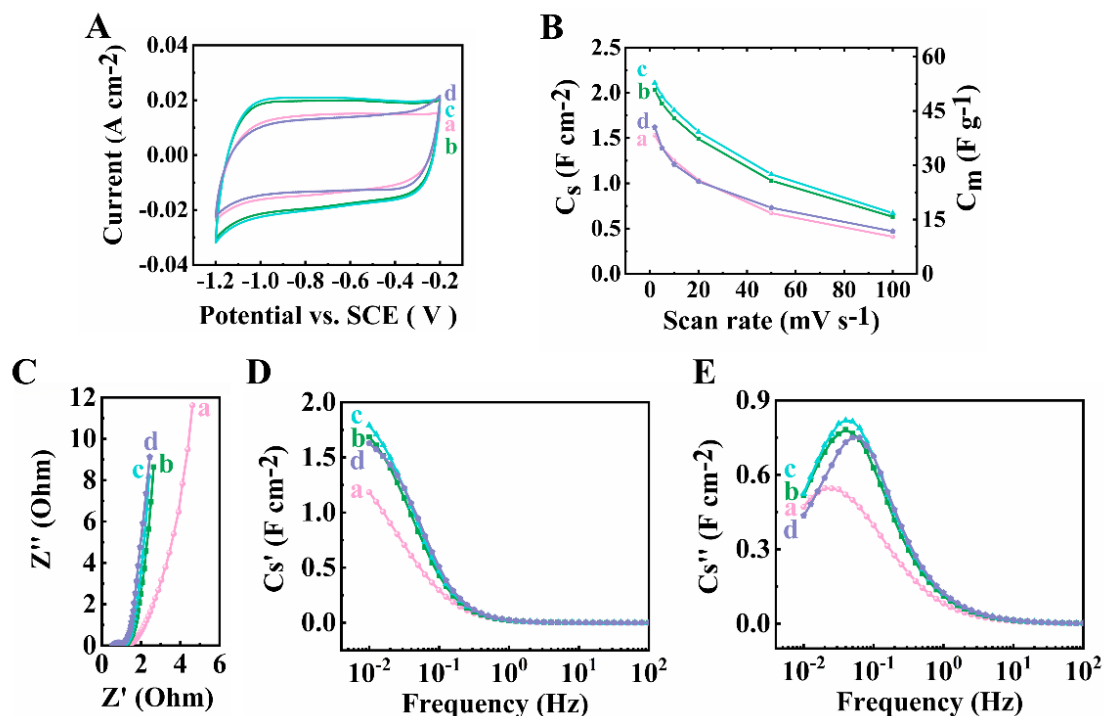
Fig. 10.3. (A) CVs at scan rate of 10 mV s^{-1} and (B) C$_S$ and C$_m$ versus scan rate, calculated from the CV data, (C) Nyquist plot of complex impedance, (D,E) frequency dependences of components of complex capacitance (D) Cs' and (E) Cs", calculated from the EIS data for (a) Ti$_3$C$_2$T$_x$ (b) Ti$_3$C$_2$T$_x$-PPy-10 (c) Ti$_3$C$_2$T$_x$-PPy-20 (d) Ti$_3$C$_2$T$_x$-PPy-30.

The CVs for electrodes prepared without PCV deviated from the ideal rectangular shape

and showed lower capacitances (Figures 10.10 and 10.11). The comparison with C$_S$

data for other electrodes reported in the literature (Table 10.1) indicates that the

approach developed in this investigation allowed for significantly higher C$_S$.

Table 10.1 Areal capacitances of Ti3C2Tx-PPy composite electrodes

Mass	Composition	Potential		Areal	Reference

loading (mg)	Ti$_3$C$_2$T$_x$:PPy	range (V)	Electrolyte	capacitance (F cm^{-2})	
2.8-3	7:3	0~0.6V vs Ag/AgCl	3M KOH	~1.83	[11]
3	8:1	-0.9~-0.3V vs Ag/AgCl	1M Na$_2$SO$_4$	0.55	[51]
~0.4	5:9	0~0.5V vs Ag/AgCl	0.5M H$_2$SO$_4$	0.203	[52]
0.93	2:1	-0.2~+0.35V vs Ag/AgCl	1M H$_2$SO$_4$	0.39	[53]
40	8:2	-1.2~-0.2V vs SCE	0.5M Na$_2$SO$_4$	2.11	This work

The electrochemical impedance spectroscopy data was presented in Figure 10.3C-E. The comparison of results for pure Ti$_3$C$_2$T$_x$ and Ti$_3$C$_2$T$_x$-PPy composites confirmed that the resistance R corresponding to real component of impedance Z', decreased with addition of PPy, which proved the beneficial effect of adsorbed conductive polymer in facilitating charge transfer in the bulk of the electrode. The electrode resistance was significantly lower, compared to literature data[11, 42, 53-55] despite the significantly higher AML, the use of Na$_2$SO$_4$ electrolyte, and testing in the negative potential range. The real component of capacitance C$_S$' calculated from the EIS data decreased with

increasing frequency. The highest C_S' value was obtained at lowest frequency of 10 mHz for $Ti_3C_2T_x$-PPy-20 electrode with Cs'=1.79 F cm^{-2}, followed by $Ti_3C_2T_x$-PPy-10 electrode (1.69 F cm^{-2}), $Ti_3C_2T_x$-PPy-30 electrode (1.63 F cm^{-2}), and $Ti_3C_2T_x$ electrode (1.18 F cm^{-2}). The lower capacitance of $Ti_3C_2T_x$-PPy-30 compared to $Ti_3C_2T_x$-PPy-20 resulted from blocking of $Ti_3C_2T_x$ open porosity by the deposited PPy.   The relaxation type dispersion was found for the dependence of complex capacitance vs. frequency. The C_s'' reached the maximum then decreased with increasing frequency. The relaxation frequencies obtained from EIS data were 25, 40, 42 and 54 mHz for $Ti_3C_2T_x$, $Ti_3C_2T_x$ -PPy-10, $Ti_3C_2T_x$-PPy-20 and $Ti_3C_2T_x$-PPy-30 respectively. It can be concluded that the $Ti_3C_2T_x$-PPy composites are more suitable for supercapacitor applications at higher frequencies, compared to pure $Ti_3C_2T_x$. The comparison of the capacitances obtained from impedance data for $Ti_3C_2T_x$-PPy-20 electrodes prepared using PCV and without PCV (Figure 10.12) showed higher capacitances of the electrodes prepared using PCV in agreement with the CV data.

Fig. 10.4 (A-D) exhibits galvanostatic charge-discharge profiles at different current densities of 5-20 mA cm^{-2}. The nearly-triangular shape of the curves indicates good electrochemical reversibility of electrodes. In contrast, the GCD curves for electrodes prepared without PCV deviated significantly from the ideal triangular shapes (Figure 10.13). The capacitance obtained from GCD data was shown in Fig. 10.4E. $Ti_3C_2T_x$-PPy-20 electrode showed high capacitance of 2.49 F cm^{-2} at low current density of 5

mA cm^{-2}, dropping to 2.30 F cm^{-2} at highest current density of 20 mA cm^{-2} with

capacitance retention of 92.37%. Ti$_3$C$_2$T$_x$-PPy-10 electrode with lower capacitance of

2.36 F cm^{-2} at 5 mA cm^{-2} showed slightly lower retention of 91.10%. The comparison

with retentions of other two electrodes, such as 74.71% for Ti$_3$C$_2$T$_x$ and 86.78% for

Ti$_3$C$_2$T$_x$-PPy-30, indicated that 20% PPy content allows for best performance. The

capacitances of electrodes remained nearly unchanged after 1000 cycles at a CV scan

rate of 50 mV s^{-1} (Figure 10.4F). Obtained data showed beneficial effect of PCV, which

acted as a dopant for PPy polymerization and dispersant for Ti$_3$C$_2$T$_x$. PCV promoted

PPy polymerization on the Ti$_3$C$_2$T$_x$ surface. The reduced resistance and increased

capacitance can result from improved contact of Ti$_3$C$_2$T$_x$ and conductive PPy polymer.

However, improved behavior can also be attributed to other factors. There is currently

increasing interest in application of catecholate molecules as charge transfer mediators

at the interface of different materials for various electrochemical, photoelectrochemical

and electrochemical sensor applications[49-54].   It is well documented in the literature

that anionic catecholate molecules act not only as dopants for PPy polymerization, but

also as charge transfer mediators between PPy and substrates[49-51]. This mechanism

can potentially improve performance of the Ti$_3$C$_2$T$_x$-PPy electrodes, prepared using

PCV.   The capacitive behavior of MXene can result from a double layer capacitance

and a redox capacitance. The relatively small surface area of as-received MXene

indicates that the contribution of the double layer capacitance is low and capacitive

properties are mainly related to pseudocapacitive behavior, which involved redox

reactions of surface groups or reduction of Ti ions[55].

The relatively high capacitance of the $Ti_3C_2T_x$-PPy-20 electrodes in the negative

potential range in 0.5 M Na_2SO_4 electrolyte facilitated the fabrication of an asymmetric

device with enlarged voltage window. PPy coated MCNTs were prepared according to

previous work[40]. However, in contrast to the previous work, the electrodes were

tested in a different potential window, which was from $-$ 0.3 to $+$ 0.5 V. The testing

results are shown in Figure 10.5. The high capacitance of 3.22 F cm^{-2} at 2 mV s^{-1} was

achieved (Figure 10.5 A,B) at high active mass loading of 40 mg cm^{-2} and maintained

0.48 F cm^{-2} at a sweep rate of 100 mV s^{-1}. The electrodes exhibited relatively low

resistance (Figure 10.5C). The relaxation-type dispersion of complex capacitance C^*

with real capacitance ($C^{'}$) of 1.99 F cm^{-2} at 10 mHz and relaxation frequency of 36 mHz

was recorded (Figure 10.5D).   The almost linear shape of GCD curves in Figure 5E

confirmed the pseudocapacitive behavior. The capacitance decreased from 3.38 F cm^{-2}

to 3.05 F cm^{-2} with increasing current density (Figure 10.5D). The positive PPy-MCNT

and negative $Ti_3C_2T_x$-PPy-20 electrodes showed comparable capacitances in the

complementary and overlapping voltage windows (Figure 10.6). Such electrodes were

utilized for the fabrication of an asymmetric device operating in the voltage window of

1.7 V. The total capacitance of a device $C_T=C_1C_2/(C_1+C_2)$ depends on the capacitances

of the individual electrodes C_1 and C_2. A low capacitance of one electrode results in a

low total capacitance. Therefore, it is important to match the areal capacitances of

individual electrodes. Mass balance of the electrodes is another important factor for the

device design. A low gravimetric capacitance of one electrode generates a need in a

larger electrode mass, which is detrimental for the development of efficient light-mass

devices. The electrodes, developed in this investigation showed comparable gravimetric

capacitances, which facilitated mass and capacitance balance.
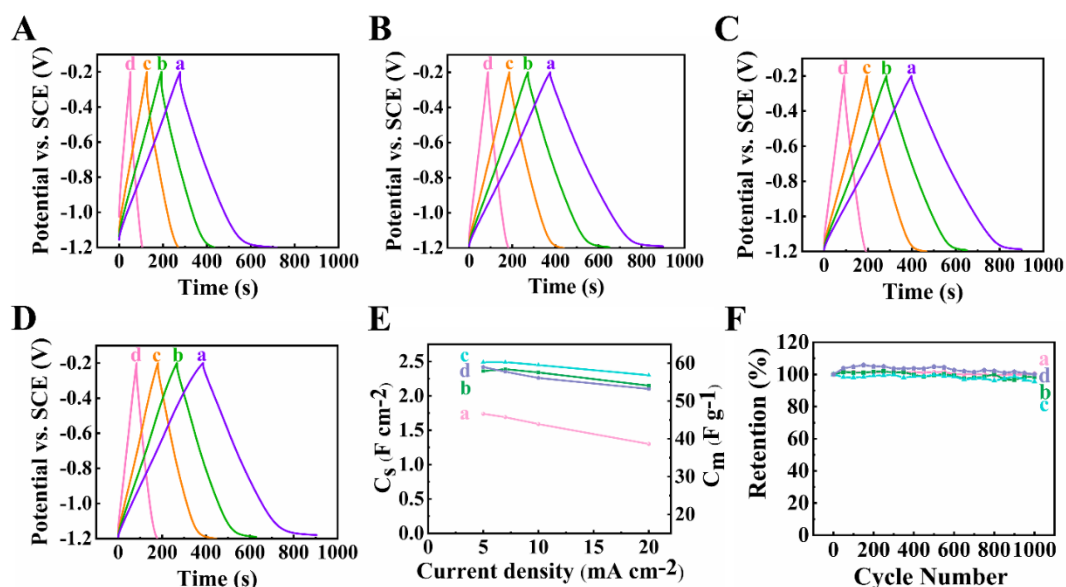
Figure 10.4. Galvanostatic charge-discharge curves at current densities of (a)5, (b)7 (c)10 and (d)20 mA cm^{-2} for (A) Ti$_3$C$_2$T$_x$ (B) Ti$_3$C$_2$T$_x$-PPy-10 (C) Ti$_3$C$_2$T$_x$-PPy-20 (D) Ti$_3$C$_2$T$_x$-PPy-30 and (E) Cs and Cm versus current density, calculated from GCD data, (F) Capacitance retention of (a) Ti$_3$C$_2$T$_x$ (b) Ti$_3$C$_2$T$_x$-PPy-10 (c) Ti$_3$C$_2$T$_x$-PPy-20 (d) Ti$_3$C$_2$T$_x$-PPy-30.
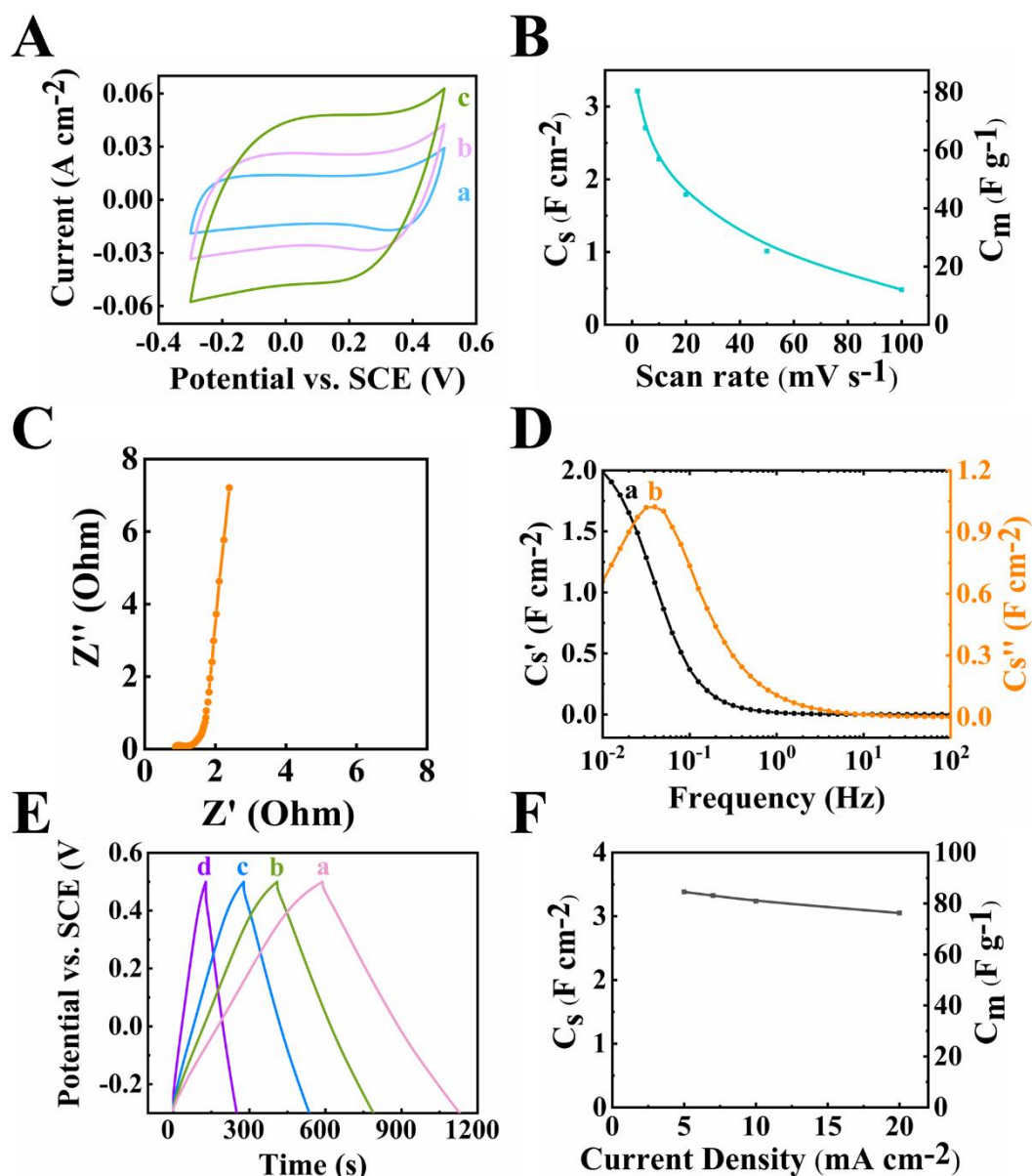
Fig. 10.5. (A) CVs at scan rates of (a)5, (b)10 and (c)20 mV s^{-1} (B) C_S and C_m versus scan rate (C) Nyquist plot of complex impedance, (D) frequency dependences of components of complex capacitance C_S' and C_S", calculated from the EIS data (E) Galvanostatic charge-discharge curves at current densities of (a)5 (b)7, (c)10 and (d)20mA cm^{-2} (F) Cs and Cm versus current density, calculated from GCD for positive PPy-MCNT electrode.
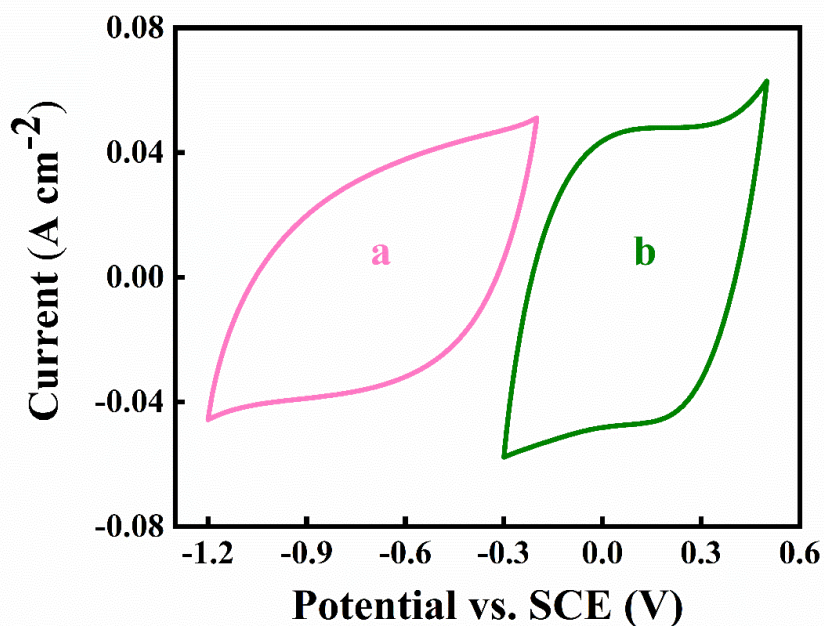
Figure 10.6. CVs at scan rate of 20 mV s^{-1} for (a) MXene-PPy-20 negative electrode and (b) PPy-MCNT positive electrode.

Figure 10.7A shows CV for the asymmetric SC device in a voltage window of 1.7 V.

The total capacitance of the device from CV data was 1.37 F cm^{-2} at 2 mV s^{-1} (Figure

10.7B). The capacitance decreased with increasing sweep rate due to low diffusion rate

of the electrolyte ions. The total resistance of the device (Figure 10.7C) included

contributions of the individual electrodes and the separator. The higher resistance of the

device, compared to individual electrodes resulted in the shift of the relaxation to lower

frequencies (Figure 10.7 D, E). GCD data in the voltage window of 1.7 V is presented

in Figure 8. The discharge curves showed an ohmic drop at the beginning of the

discharge process. Taking into account the nearly triangular GCD curves for the

Ti$_3$C$_2$T$_x$-PPy electrodes optimized at a MXene content of 80% (Ti$_3$C$_2$T$_x$-PPy-20) and

for the PPy-MCNT electrodes, the observed ohmic drop can be mainly attributed to the

171

electrolyte resistance in pores of the electrode separator.   The capacitances, obtained

from the galvanostatic discharge data (Figure 10.8A) were plotted versus current

density in Figure 10.8B.
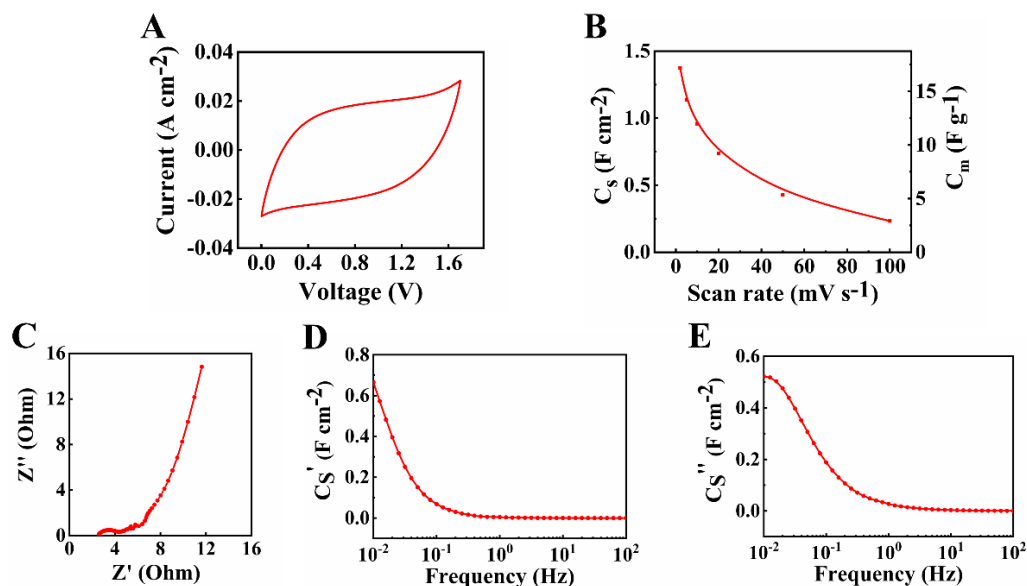
Figure 10.7. (A)CV at a scan rate of 20 mV s^{-1} (B)C$_S$ and C$_m$ versus scan rate, (C)Nyquist plot of complex impedance, (D,E) frequency dependences of components of complex capacitance (D)C$_S$' and (E)C$_S$", calculated from the EIS data for the asymmetric supercapacitor cell.
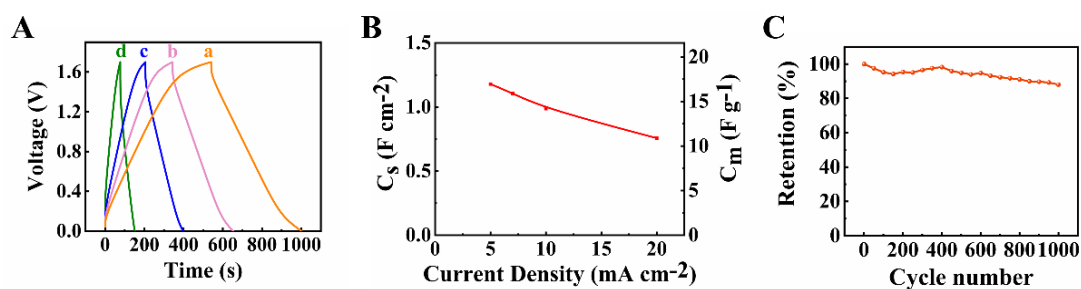
Fig. 10.8. (A)Galvanostatic charge-discharge curves at current densities of (a) 5, (b) 7, (c) 10, (d) 20 mA cm^{-2} and (B)C$_S$ and C$_m$ versus current density, calculated from GCD data (C) capacitance versus cycle number for asymmetric supercapacitor cell.

The C$_S$ obtained at 5 mA cm^{-2} from GCD data was 1.18 F cm^{-2} (Fig. 10.8A), it decreased

to the level of 0.76 F cm^{-2} at 20 mA cm^{-2}. CV cycling at a sweep rate of 50 mV s^{-1}

resulted in capacitance retention of 88.0%.

The results presented in this paper demonstrate that relatively high capacitance at low resistance can be achieved for $Ti_3C_2T_x$-PPy-20 electrodes in Na_2SO_4 electrolytes in a negative potential range, which allows fabrication of an asymmetric device with enlarged voltage window. Previous investigations showed the need in the fabrication of supercapacitor electrodes with high active mass[56]. It should be noted that the increase in active mass loading usually results in reduction of specific capacitance[12]. Investigations showed that the C_m can be decreased by 1-2 order of magnitude with increasing active mass[12]. Moreover, it was found that C_S can also be decreased with increasing active mass[57]. These studies highlighted the need in the development of advanced materials, additives, material and electrode design in order to achieve good electrode performance at commercially important high active mass loadings. The approach developed in this investigation allowed for good electrode performance at high active mass, which facilitated the development of electrodes with high capacitance. Preliminary cycling experiments showed good cyclic stability of $Ti_3C_2T_x$-PPy electrodes. However, in order to meet requirements for practical applications, good cyclic stability must be achieved for at least 500,000 cycles. Therefore, further experiments are necessary for the analysis of cyclic stability of individual electrodes, optimization of the voltage window and cyclic stability of the device.

10.5 Conclusions

Integrating PPy-MCNT positive electrodes and MXene-PPy negative electrodes is a promising strategy for the fabrication of asymmetric devices with enlarged voltage window and operating in a neutral Na_2SO_4 electrolyte. The device showed C_S of 1.37 F cm^{-2} from the CV data and 1.18 F cm^{-2} from the GCD data in a voltage window of 1.7 V. Compared to the literature data on symmetric devices operating in acidic electrolytes, the asymmetric device developed in this work offers benefits of larger voltage window, higher capacitance and ability to use a neutral non-corrosive electrolyte. The key factor for the development of asymmetric SC was the ability of achieving high capacitance of MXene-PPy electrodes in the negative potential range. The electrodes showed C_S of 2.11 F cm^{-2} from CV data and 2.49 F cm^{-2} from GCD data, which is significantly higher than literature data for MXene-PPy electrodes. Moreover, high capacitance was achieved at high active mass loading and significantly lower electrode resistance. Enhanced performance resulted from advantages of the fabrication method developed in this investigation, which is based on in-situ synthesis of PPy using catecholate-type PCV as a dispersant for MXene and anionic dopant for PPy polymerization. The adsorbed PCV dispersant facilitated deposition of conductive PCV on the MXene surface and allowed for enhanced charge transfer. PPy-MCNT positive electrodes matched capacitive properties of PPy-MCNT negative electrodes in a complimentary potential window.

10.6 Acknowledgments

10.7 Supplementary materials
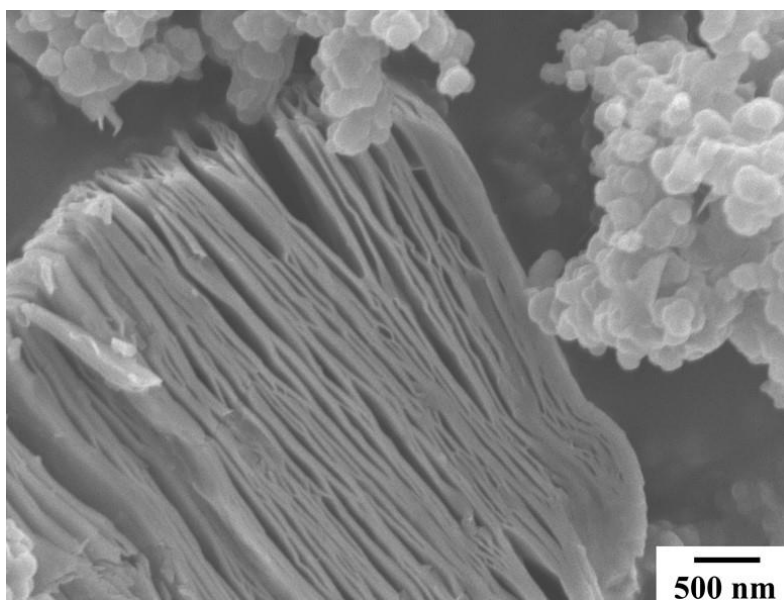
Figure 10.9. SEM image of $Ti_3C_2T_x$-PPy-20, prepared without PCV.
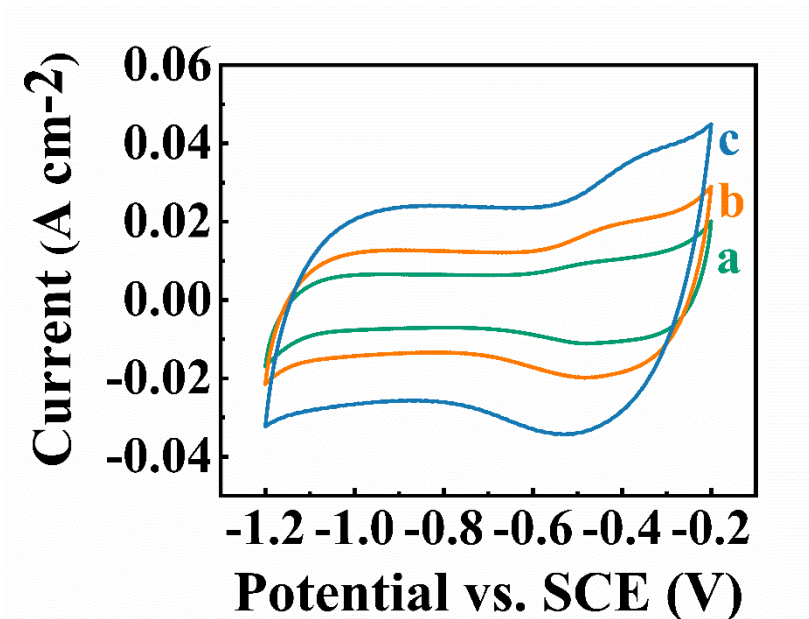
Figure 10.10. CVs at scan rates of (a) 5, (b) 10 and (c) 20 mV s^{-1} for Ti$_3$C$_2$T$_x$-PPy-20 electrodes, prepared without PCV
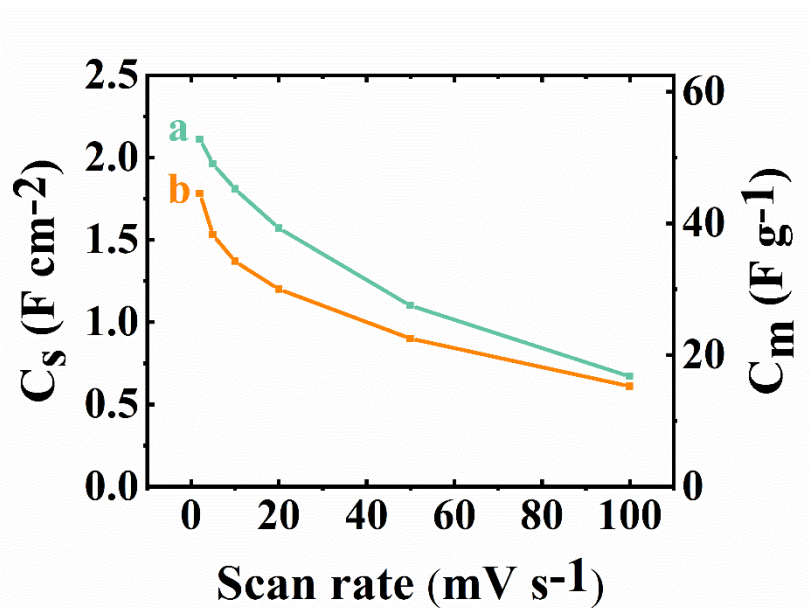
Figure 10.11. Comparison of capacitances at different scan rates for Ti$_3$C$_2$T$_x$-PPy-20 electrodes, prepared (a) with and (b) without PCV
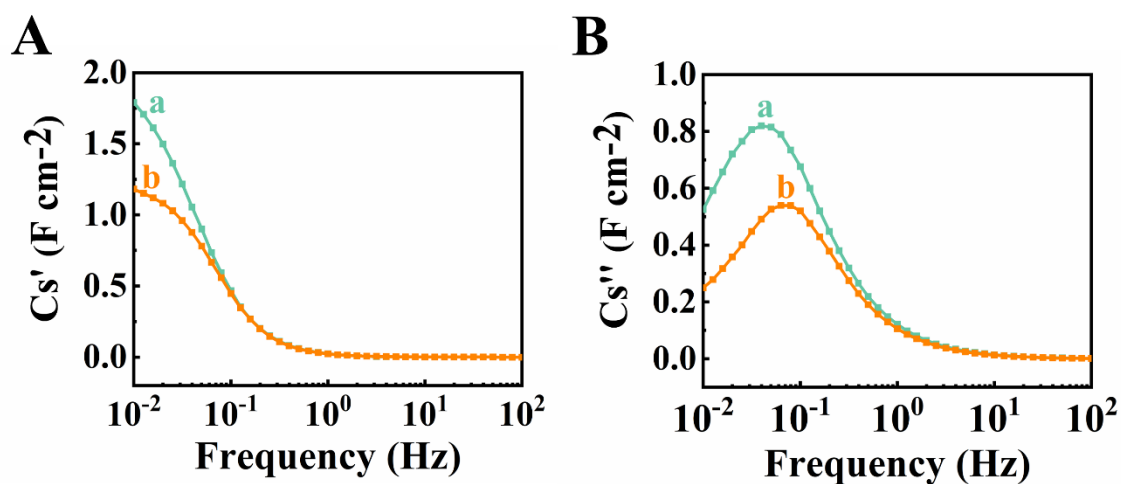
Figure 10.12. Comparison of capacitances obtained from impedance data for $Ti_3C_2T_x$-PPy-20 electrodes, prepared (a) with and (b) without PCV
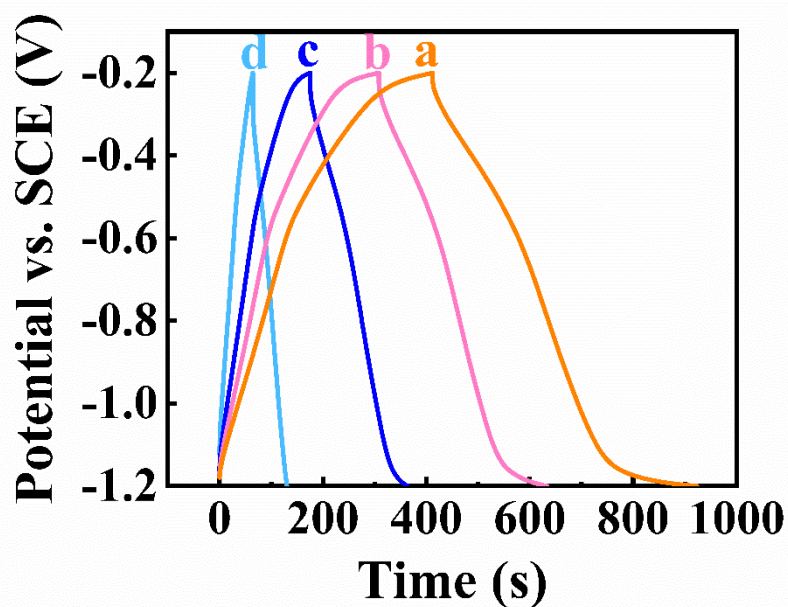
Figure 10.13. Galvanostatic charge-discharge curves at current densities of (a)5 (b)7, (c)10 and (d)20 mA cm^{-2}

177

10.8 References

[1]   M. Naguib *et al.*, Two-dimensional nanocrystals produced by exfoliation of Ti3AlC2, *Advanced materials,* vol. 23, no. 37, pp. 4248-4253, 2011

[2]   J. Xu *et al.*, Low-Temperature pseudocapacitive energy storage in Ti3C2Tx MXene, *Energy Storage Materials,* vol. 33, pp. 382-389, 2020

[3]   Y. Liu, J. Yu, D. Guo, Z. Li, and Y. Su, Ti3C2Tx MXene/graphene nanocomposites: Synthesis and application in electrochemical energy storage, *Journal of Alloys and Compounds,* vol. 815, p. 152403, 2020

[4]   H. Shao, Z. Lin, K. Xu, P.-L. Taberna, and P. Simon, Electrochemical study of pseudocapacitive behavior of Ti3C2Tx MXene material in aqueous electrolytes, *Energy Storage Materials,* vol. 18, pp. 456-461, 2019

[5]   Y. Wang *et al.*, Significantly enhanced ultrathin NiCo-based MOF nanosheet electrodes hybrided with Ti3C2Tx MXene for high performance asymmetric supercapacitor, *Engineered Science,* vol. 9, no. 7, pp. 50-59, 2020

[6]   H. Huang *et al.*, Extraordinary areal and volumetric performance of flexible solid-state micro-supercapacitors based on highly conductive freestanding Ti3C2Tx Films, *Advanced Electronic Materials,* vol. 4, no. 8, p. 1800179, 2018

[7]   M. Ghidiu, M.R. Lukatskaya, M.-Q. Zhao, Y. Gogotsi, and M.W. Barsoum, Conductive two-dimensional titanium carbide 'clay'with high volumetric capacitance, *Nature,* vol. 516, no. 7529, pp. 78-81, 2014

[8]   B. Anasori, M.R. Lukatskaya, and Y. Gogotsi, 2D metal carbides and nitrides (MXenes) for energy storage, *Nature Reviews Materials,* vol. 2, no. 2, pp. 1-17, 2017

[9]   Z. Wang *et al.*, Unraveling and Regulating Self-Discharge Behavior of Ti3C2T x MXene-Based Supercapacitors, *ACS nano,* vol. 14, no. 4, pp. 4916-4924, 2020

[10]   M. Torkamanzadeh, L. Wang, Y. Zhang, Ö. Budak, P. Srimuk, and V. Presser, MXene/Activated-Carbon Hybrid Capacitive Deionization for Permselective Ion Removal at Low and High Salinity, *ACS Applied Materials & Interfaces,* vol. 12, no. 23, pp. 26013-26025, 2020/06/10 2020

[11]   C.-F. Du, Q. Liang, Y. Zheng, Y. Luo, H. Mao, and Q. Yan, Porous MXene Frameworks Support Pyrite Nanodots toward High-Rate Pseudocapacitive Li/Na-Ion Storage, *ACS Applied Materials & Interfaces,* vol. 10, no. 40, pp. 33779-33784, 2018/10/10 2018

[12]   R. Chen, M. Yu, R.P. Sahu, I.K. Puri, and I. Zhitomirsky, The Development of Pseudocapacitor Electrodes and Devices with High Active Mass Loading, *Advanced Energy Materials,* vol. 10, no. 20, p. 1903848, 2020

[13]   J.A. Argüello, A. Cerpa, and R. Moreno, Reinforcing effect of graphene
        nanoplatelets in the electrochemical behaviour of manganese oxide-based
        supercapacitors produced by EPD, *Ceramics International,* vol. 45, no. 11, pp.
        14316-14321, 2019

[14]   J.A. Arguello, J.M. Rojo, and R. Moreno, Electrophoretic deposition of
        manganese oxide and graphene nanoplatelets on graphite paper for the
        manufacture of supercapacitor electrodes, *Electrochimica Acta,* vol. 294, pp.
        102-109, 2019

[15]   M. Nawwar, R. Poon, R. Chen, R.P. Sahu, I.K. Puri, and I. Zhitomirsky, High
        areal capacitance of Fe3O4-decorated carbon nanotubes for supercapacitor
        electrodes, *Carbon Energy,* vol. 1, no. 1, pp. 124-133, 2019

[16]   X. Zhang, Z. Zhang, and Z. Zhou, MXene-based materials for electrochemical
        energy storage, *Journal of energy chemistry,* vol. 27, no. 1, pp. 73-85, 2018

[17]   T. Zhang, J. Xiao, L. Li, J. Zhao, and H. Gao, A high-performance
        supercapacitor electrode based on freestanding N-doped Ti3C2Tx film,
        Ceramics International, vol. 46, no. 13, pp. 21482-21488, 2020

[18]   Z. Fan *et al.*, A Compact MXene Film with Folded Structure for Advanced
        Supercapacitor Electrode Material, *ACS Applied Energy Materials,* vol. 3, no.
        2, pp. 1811-1820, 2020/02/24 2020

[19]   Z. Ling *et al.*, Flexible and conductive MXene films and nanocomposites with
        high capacitance, *Proceedings of the National Academy of Sciences,* vol. 111,
        no. 47, pp. 16676-16681, 2014

[20]   M. Boota *et al.*, Interaction of polar and nonpolar polyfluorenes with layers of
        two-dimensional titanium carbide (MXene): intercalation and
        pseudocapacitance, *Chemistry of Materials,* vol. 29, no. 7, pp. 2731-2738,
        2017

[21]   M.Q. Zhao *et al.*, Flexible MXene/carbon nanotube composite paper with high
        volumetric capacitance, *Advanced materials,* vol. 27, no. 2, pp. 339-345, 2015

[22]   Y. Dall'Agnese, P. Rozier, P.-L. Taberna, Y. Gogotsi, and P. Simon,
        Capacitance of two-dimensional titanium carbide (MXene) and MXene/carbon
        nanotube composites in organic electrolytes, *Journal of Power Sources,* vol.
        306, pp. 510-515, 2016

[23]   J. Yan *et al.*, Flexible MXene/graphene films for ultrafast supercapacitors with
        outstanding volumetric capacitance, *Advanced Functional Materials,* vol. 27,
        no. 30, p. 1701264, 2017

[24]   F. Wang, M. Cao, Y. Qin, J. Zhu, L. Wang, and Y. Tang, ZnO nanoparticle-
        decorated two-dimensional titanium carbide with enhanced supercapacitive
        performance, *RSC advances,* vol. 6, no. 92, pp. 88934-88942, 2016

[25]   Y. Tian, C. Yang, W. Que, X. Liu, X. Yin, and L.B. Kong, Flexible and free-
        standing 2D titanium carbide film decorated with manganese oxide

nanoparticles as a high volumetric capacity electrode for supercapacitor, *Journal of Power Sources,* vol. 359, pp. 332-339, 2017

[26]   Y. Wang *et al.*, Three-dimensional porous MXene/layered double hydroxide composite for high performance supercapacitors, *Journal of Power Sources,* vol. 327, pp. 221-228, 2016

[27]   X. Zang *et al.*, Enhancing capacitance performance of Ti 3 C 2 T x MXene as electrode materials of supercapacitor: from controlled preparation to composite structure construction, *Nano-Micro Letters,* vol. 12, no. 1, pp. 1-24, 2020

[28]   M. Boota, B. Anasori, C. Voigt, M.Q. Zhao, M.W. Barsoum, and Y. Gogotsi, Pseudocapacitive electrodes produced by oxidant-free polymerization of pyrrole between the layers of 2D titanium carbide (MXene), *Advanced Materials,* vol. 28, no. 7, pp. 1517-1522, 2016

[29]   M. Zhu *et al.*, Highly flexible, freestanding supercapacitor electrode with enhanced performance obtained by hybridizing polypyrrole chains with MXene, *Advanced Energy Materials,* vol. 6, no. 21, p. 1600969, 2016

[30]   T.A. Le, N.Q. Tran, Y. Hong, and H. Lee, Intertwined titanium carbide MXene within a 3 D Tangled polypyrrole nanowires matrix for enhanced supercapacitor performances, *Chemistry–A European Journal,* vol. 25, no. 4, pp. 1037-1043, 2019

[31]   J. Yan *et al.*, Polypyrrole–MXene coated textile-based flexible energy storage device, *RSC advances,* vol. 8, no. 69, pp. 39742-39748, 2018

[32]   J. Cao, Y. Han, X. Zheng, and Q. Wang, Preparation and electrochemical performance of modified Ti3C2Tx/polypyrrole composites, *Journal of Applied Polymer Science,* vol. 136, no. 4, p. 47003, 2019

[33]   W. Wu *et al.*, Enhanced electrochemical performances of organ-like Ti3C2 MXenes/polypyrrole composites as supercapacitors electrode materials, *Ceramics International,* vol. 45, no. 6, pp. 7328-7337, 2019

[34]   X. Jian *et al.*, Three-dimensional carambola-like MXene/polypyrrole composite produced by one-step co-electrodeposition method for electrochemical energy storage, *Electrochimica Acta,* vol. 318, pp. 820-827, 2019

[35]   L. Yang, F. Lin, F. Zabihi, S. Yang, and M. Zhu, High specific capacitance cotton fiber electrode enhanced with PPy and MXene by in situ hybrid polymerization, *International Journal of Biological Macromolecules,* vol. 181, pp. 1063-1071, 2021

[36]   C. Zhang, S. Xu, D. Cai, J. Cao, L. Wang, and W. Han, Planar supercapacitor with high areal capacitance based on Ti3C2/polypyrrole composite film, *Electrochimica Acta,* vol. 330, p. 135277, 2020

[37]   D. Wei, W. Wu, J. Zhu, C. Wang, C. Zhao, and L. Wang, A facile strategy of
        polypyrrole nanospheres grown on Ti3C2-MXene nanosheets as advanced
        supercapacitor electrodes, *Journal of Electroanalytical Chemistry,* vol. 877, p.
        114538, 2020

[38]   K. Fic, G. Lota, M. Meller, and E. Frackowiak, Novel insight into neutral
        medium as electrolyte for high-voltage supercapacitors, *Energy &
        Environmental Science,* vol. 5, no. 2, pp. 5842-5850, 2012

[39]   Y. Zhu, K. Shi, and I. Zhitomirsky, Anionic dopant–dispersants for synthesis
        of polypyrrole coated carbon nanotubes and fabrication of supercapacitor
        electrodes with high active mass loading, *Journal of Materials Chemistry A,*
        vol. 2, no. 35, pp. 14666-14673, 2014

[40]   Y. Zhu, K. Shi, and I. Zhitomirsky, Polypyrrole coated carbon nanotubes for
        supercapacitor devices with enhanced electrochemical performance, *Journal
        of Power Sources,* vol. 268, pp. 233-239, 2014

[41]   Q. Yang, V. Ettel, J. Babjak, D. Charles, and M. Mosoiu, Pasted Ni (OH) 2
        electrodes using Ni powders for high-drain-rate, Ni-based batteries, *Journal of
        the Electrochemical Society,* vol. 150, no. 4, p. A543, 2003

[42]   J. Stejskal *et al.*, Polypyrrole salts and bases: superior conductivity of
        nanotubes and their stability towards the loss of conductivity by
        deprotonation, *RSC advances,* vol. 6, no. 91, pp. 88382-88391, 2016

[43]   M.Z. Iqbal, S. Zakar, and S.S. Haider, Role of aqueous electrolytes on the
        performance of electrochemical energy storage device, *Journal of
        Electroanalytical Chemistry,* vol. 858, p. 113793, 2020

[44]   L. Caixia *et al.*, CTAB-assisted microemulsion synthesis of unique 3D
        network nanostructured polypyrrole presenting significantly diverse
        capacitance performances in different electrolytes, *Journal of Materials
        Science: Materials in Electronics,* vol. 29, no. 20, pp. 17552-62, 10/ 2018

[45]   M. Ata, Y. Liu, and I. Zhitomirsky, A review of new methods of surface
        chemical modification, dispersion and electrophoretic deposition of metal
        oxide particles, *Rsc Advances,* vol. 4, no. 43, pp. 22716-22732, 2014

[46]   K. Wu, Y. Wang, and I. Zhitomirsky, Electrophoretic deposition of TiO2 and
        composite TiO2–MnO2 films using benzoic acid and phenolic molecules as
        charging additives, *Journal of colloid and interface science,* vol. 352, no. 2,
        pp. 371-378, 2010

[47]   A. Clifford, X. Pang, and I. Zhitomirsky, Biomimetically modified chitosan
        for electrophoretic deposition of composites, *Colloids and Surfaces A:
        Physicochemical and Engineering Aspects,* vol. 544, pp. 28-34, 2018

[48]   R.M.E. Silva, R. Poon, J. Milne, A. Syed, and I. Zhitomirsky, New
        developments in liquid-liquid extraction, surface modification and

agglomerate-free processing of inorganic particles, *Advances in Colloid and Interface Science,* vol. 261, pp. 15-27, 2018/11/01/ 2018

[49]   D. Tallman, C. Vang, G. Wallace, and G. Bierwagen, Direct electrodeposition of polypyrrole on aluminum and aluminum alloy by electron transfer mediation, *Journal of the Electrochemical Society,* vol. 149, no. 3, p. C173, 2002

[50]   C. Shi and I. Zhitomirsky, Electrodeposition of composite polypyrrole–carbon nanotube films, *Surface engineering,* vol. 27, no. 9, pp. 655-661, 2011

[51]   S. Chen and I. Zhitomirsky, Influence of dopants and carbon nanotubes on polypyrrole electropolymerization and capacitive behavior, *Materials Letters,* vol. 98, pp. 67-70, 2013

[52]   S. Sakib, F. Bakhshandeh, S. Saha, L. Soleymani, and I. Zhitomirsky, Surface Functionalization of Metal Oxide Semiconductors with Catechol Ligands for Enhancing Their Photoactivity, *Solar RRL,* vol. 5, no. 10, p. 2100512, 2021

[53]   G.-L. Wang, J.-J. Xu, and H.-Y. Chen, Dopamine sensitized nanoporous TiO2 film on electrodes: photoelectrochemical sensing of NADH under visible irradiation, *Biosensors and Bioelectronics,* vol. 24, no. 8, pp. 2494-2498, 2009

[54]   M. Nawwar, R.P. Sahu, I.K. Puri, and I. Zhitomirsky, Pseudocapacitive behavior of ferrimagnetic NiFe2O4-carbon nanotube electrodes prepared with a multifunctional dispersing agent, *Open Ceramics,* p. 100127, 2021

[55]   Y. Gogotsi and B. Anasori, The rise of MXenes, *ACS Nano,* vol. 13, pp. 8491-8494, 2019

[56]   Y. Gogotsi and P. Simon, True performance metrics in electrochemical energy storage, *Science,* vol. 334, no. 6058, pp. 917-918, 2011

[57]   R. Chen, R. Poon, R.P. Sahu, I.K. Puri, and I. Zhitomirsky, MnO2-carbon nanotube electrodes for supercapacitors with high active mass loadings, *Journal of The Electrochemical Society,* vol. 164, no. 7, pp. A1673-A1678, 2017

Chapter 11 Capacitive properties of magnetic CuFe₂O₄ nanoparticles for electrical energy storage

Wenyu Liang, Lory Wenjuan Yang, Sadman Sakib and Igor Zhitomirsky

Department of Materials Science and Engineering, McMaster University, Hamilton,

ON, L8S 4L7, Canada

Author's Contributions:

Synthesis and fabrication of CuFe₂O₄ and composite electrode

Electrochemical testing of CuFe₂O₄-MCNT electrodes

Characterization of CuFe₂O₄-CNT composite with XRD, SEM and TEM

Literature review

Manuscript preparation

11.1 Abstract

This paper reports pseudocapacitive properties of magnetic $CuFe_2O_4$ nanoparticles in a negative potential range. High capacitance of 2.76 F cm^{-2} is achieved at a low electrode resistance in a relatively large potential window of 0.8 V. The cyclic voltammograms and galvanostatic charge-discharge data show nearly ideal pseudocapacitive behavior. Good electrochemical performance is achieved at a high active mass loading due to the use of chelating murexide molecules as co-dispersants for $CuFe_2O_4$ nanoparticles and conductive carbon nanotube additives. The adsorption of murexide on different materials is linked to structural features of murexide, which allows for different interaction and adsorption mechanisms. The ability to achieve good capacitive behavior in a negative potential range in the environmentally friendly Na_2SO_4 electrolyte makes $CuFe_2O_4$ electrodes promising for the development of asymmetric devices with enlarged voltage window. The combination of advanced magnetic and pseudocapacitive properties in a negative potential range in a single material provides a platform for the investigation of influence of pseudocapacitive/magnetic properties on magnetic/pseudocapacitive behavior.

11.2 Introduction

The ability to combine advanced electrical and magnetic properties in a single material holds great potential for the development of novel devices based on the control of electrical/magnetic properties in magnetic/electric fields. Various materials, combining ferroelectric and magnetic properties[1], also called multiferroics[2], have been developed. Materials of different types such as perovskites, boracites, hexagonal manganates, materials of the $BaMeF_4$ (Me=Mn,Fe,Co,Ni) and hexagonal $BaTiO_3$ families have been investigated[1]. Interesting physical phenomena were observed in such materials, such as linear and non-linear magnetoelectric effects, anomalies of dielectric/magnetic properties near magnetic/ferroelectric phase transition temperatures, polarization reversal in a magnetic field and magnetization reversal in an electric field[1]. However, it is challenging to achieve a combination of ferroelectric and ferri- or ferromagnetic properties in a single crystalline phase at room temperature[1]. High electrical resistivity is important to achieving ferroelectric polarization in an electric field. Many multiferroic materials exhibit relatively low resistivity and investigation of their ferroelectric polarization presents difficulties. High dielectric constant is usually observed in soft ferroelectrics at low voltages, the increase in applied voltage results in significant reduction of the dielectric constant. Various multiferroic materials, such as $BiFeO_3$ exhibit antiferromagnetic properties at room temperature, other materials show weak ferri- or ferromagnetism at low temperatures[1]. Oxide materials offer benefits of

185

higher resistivity, however room temperature ferroelectricity has not been observed in advanced magnetic oxides, such as spinels, garnets and hexagonal ferrites.

Recently significant interest has been generated in magnetically ordered pseudocapacitors (MOPC)[3], which combine advanced magnetic and electrical charge storage properties. Pseudocapacitive properties of such materials are related to redox reactions of metal ions. The capacitance of pseudocapacitive materials is many orders of magnitude larger than that of the ferroelectric materials[4]. Many pseudocapacitive materials exhibit nearly rectangular cyclic voltammograms, indicating their ideal capacitive behavior[5]. In contrast to ferroelectric materials, low resistance is beneficial for charging of supercapacitor materials. The reduction of particle size of ferroelectric materials to the nanometric scale usually results in a drastic reduction of spontaneous polarization and dielectric constant. In contrast, significant increase in pseudocapacitive properties is achieved in nanostructured MOPC materials[5].

Ferrimagnetic spinels[6] and hexagonal ferrites[7] showed promising electrical charge storage properties, which are based on redox reactions. Interesting phenomena were observed in MOPC materials, such as enhancement of charge storage properties in magnetic fields[8]. Spinel materials showed good capacitive properties in various aqueous electrolytes[9]. High areal capacitance was reported for Fe_3O_4 spinel electrodes[10] in Na_2SO_4 electrolyte. $CoFe_2O_4$ was found to be another promising MOPC material, which showed high capacitance in KOH and NaOH electrolytes[11].

$NiFe_2O_4$ showed good capacitive performance in KOH electrolyte[12].

$CuFe_2O_4$ is a promising MOPC material, which exhibits ferrimagnetic properties. The saturation magnetization of this material is influenced by cation distribution in tetrahedral (T) and octahedral (O) cites of the spinel structure $[(1-x)Cu^{2+}(x)Fe^{3+}]^T[(x)Cu^{2+}(2-x)Fe^{3+}]^OO_4$. It is expected that the reduction of Cu^{2+} and Fe^{3+} ions in the negative potential range can result in pseudocapacitive charge storage properties. The electrochemical reduction of Cu^{2+} and Fe^{3+} ions can result in changes of their magnetic moments and influence superexchange interactions of the ions distributed in (T) and (O) positions of the crystal structure. This can potentially result in decrease or increase in total magnetization, which depends on the magnetization of the individual sublattices. Therefore, the investigation of capacitive properties of $CuFe_2O_4$ can potentially result in interesting phenomena, related to the influence of pseudocapacitive/magnetic properties on magnetic/pseudocapacitive behavior.

The goal of this investigation was the fabrication and testing of pseudocapacitive properties of $CuFe_2O_4$. We investigated magnetic and capacitive properties of $CuFe_2O_4$ nanoparticles and demonstrated that high areal capacitance can be achieved in a negative potential range in a neutral Na_2SO_4 electrolyte. The electrode showed nearly ideal pseudocapacitive behavior. High areal capacitance in a relatively large potential window was achieved at a low impedance, which is critical for practical applications. The ability to achieve high areal capacitance in the Na_2SO_4 electrolyte in a negative

potential range is promising for the fabrication of asymmetric devices with enlarged

voltage window and enhanced power-energy characteristics. Good capacitive behavior

was achieved by the development of an advanced colloidal strategy for the electrode

fabrication. The problem of strong agglomeration of ferrimagnetic $CuFe_2O_4$

nanoparticles was addressed using an advanced dispersant, which allows for strong

tridentate chelating bonding to the metal atoms on the particle surface. We

demonstrated that the colloidal strategy developed in this investigation was a key factor

for achieving superior capacitive behavior of $CuFe_2O_4$ nanoparticles with a record-high

areal capacitance for this material. Moreover, the $CuFe_2O_4$ electrodes prepared using

this strategy are on a par with the most promising negative electrodes for asymmetric

supercapacitors.

11.3 Experimental procedures

$CuFe_2O_4$ nanopowder (particle size <100 nm),   murexide, Na_2SO_4, polyvinyl butyral-

co-vinyl alcohol-co-vinyl acetate (PVBAA, Mw=65 kDa) were purchased from

Millipore Sigma. Multiwalled carbon nanotubes (MCNT, diameter 13nm, length 1-2μm)

were supplied by Bayer Corp.

Suspensions containing $CuFe_2O_4$, conductive MCNT additives and murexide as a co-

dispersing agent were prepared under probe sonication during 5 min. The mass of

murexide was 15% of the total mass of $CuFe_2O_4$ and MCNT. The mass of MCNT in

the $CuFe_2O_4$-MCNT composites CFO-0, CFO-10, CFO-20 and CFO-30 was 0, 10 20

and 30 wt.%, respectively. The electrodes were fabricated by impregnating Ni foam (95%

porosity, Vale) current collectors, with ethanol slurries, containing $CuFe_2O_4$, MCNT

and PVBAA as the binder. The binder content was 3% of the total mass of $CuFe_2O_4$ and

MCNT. The thickness, mass loading and area of electrodes were 0.38 mm, 40 mg cm^{-2}

and 1×1 cm^2, respectively.

The structures and morphologies of the composites were characterized by scanning

electron microscopy (SEM, JEOL JSM-7000F), transmission electron microscopy

(TEM, Talos 200X) and X-ray diffraction analysis   (Bruker Smart 6000 X-ray

diffractometer, CuKα radiation). The composites were also studied by Fourier

transform infrared microscopy (FTIR, HYPERION 3000). The magnetic measurements

were performed using a Quantum Design Magnetic Properties Measurement System

(MPMS). Electrochemical impedance spectroscopy (EIS) and cyclic voltammetry (CV)

investigations were conducted using a potentiostat (AMETEK 2273). Galvanostatic

charge discharge (GCD) was performed by Biologic AMP 300. The electrochemical

analysis was performed in a three-electrode setting, with a large surface area Pt gauze

and a saturated calomel electrode (SCE) as the counter and reference electrodes,

respectively. The electrodes were analyzed in a potential range between -0.8 and 0 V in

0.5 M Na_2SO_4 aqueous electrolyte. The areal (C_s) and gravimetric(C_m) specific

capacitances were calculated from CV, EIS and GCD data as it was described in the

previous investigations[5,13].

Following the goal of this investigation, we analyzed capacitive properties by cyclic

voltammetry, impedance spectroscopy and galvanostatic charge-discharge methods and

demonstrated good cyclic stability of the $CuFe_2O_4$ electrodes.

11.4 Results and discussion

$CuFe_2O_4$ is a ferrimagnetic material. The magnetization versus magnetic field

dependence at a temperature of 5K (Figure 11.1A) showed magnetic hysteresis.

However, the hysteresis was not observed at 293K (Figure 11.1B). Magnetic

measurements indicated superparamagnetic behavior of $CuFe_2O_4$ at room temperature.

Such behavior resulted from the small size of the $CuFe_2O_4$ particles.
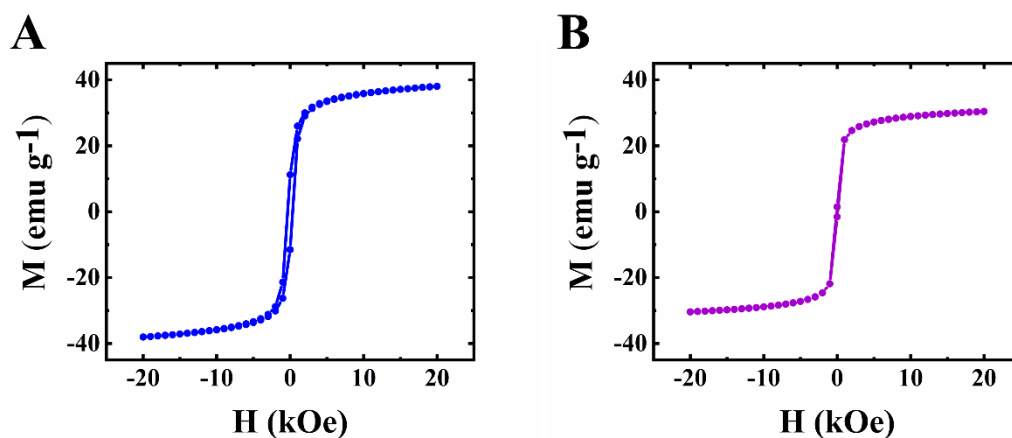

Figure 11.1. Magnetization (M) versus magnetic field (H) for $CuFe_2O_4$ at (A)5 K and (B) 293 K.

Figure 11.2(A,B) shows TEM images of the particles used in this investigation. The

size of the particles was below 100 nm. Such particles were used for the fabrication of

supercapacitor electrodes by a colloidal technique using MCNT as conductive additives.

It will be shown below that dispersion and efficient mixing of $CuFe_2O_4$ and MCNT had

a tremendous impact on pseudocapacitive properties of the $CuFe_2O_4$ based electrodes.

It is known that nanoparticles are prone to agglomeration due to their high surface

energy and Van der Waals attraction forces. Moreover, magnetic interactions of the

$CuFe_2O_4$ particles also promote their aggregation. Therefore, it is challenging to

achieve good dispersion of $CuFe_2O_4$ nanoparticles. Another challenge is good

dispersion of MCNT. Co-dispersion of $CuFe_2O_4$ particles and MCNT is critical for their

efficient mixing and fabricating composite electrodes with high conductivity. In such

composites, well dispersed MCNT must provide a conductive path to the $CuFe_2O_4$

particles and facilitate electrochemical redox reactions. As-received MCNT formed

agglomerates with a typical size of ~500 μm. The SEM images of such agglomerated

MCNT were presented in a previous investigation[14].

The choice of dispersants plays a crucial role in nanotechnology of composites. It is

important to find a dispersant, suitable for dispersion of both $CuFe_2O_4$ particles and

MCNT. The dispersant must be strongly adsorbed on $CuFe_2O_4$ particles and MCNT,

because non-adsorbed dispersant can promote agglomeration. The anchoring groups of

dispersants play a vital role in their adsorption on inorganic particles. Recent studies[15]

showed that monodentate bonding provides relatively weak adsorption and new types

of dispersants were developed with bidentate chelating or bridging bonding. Such
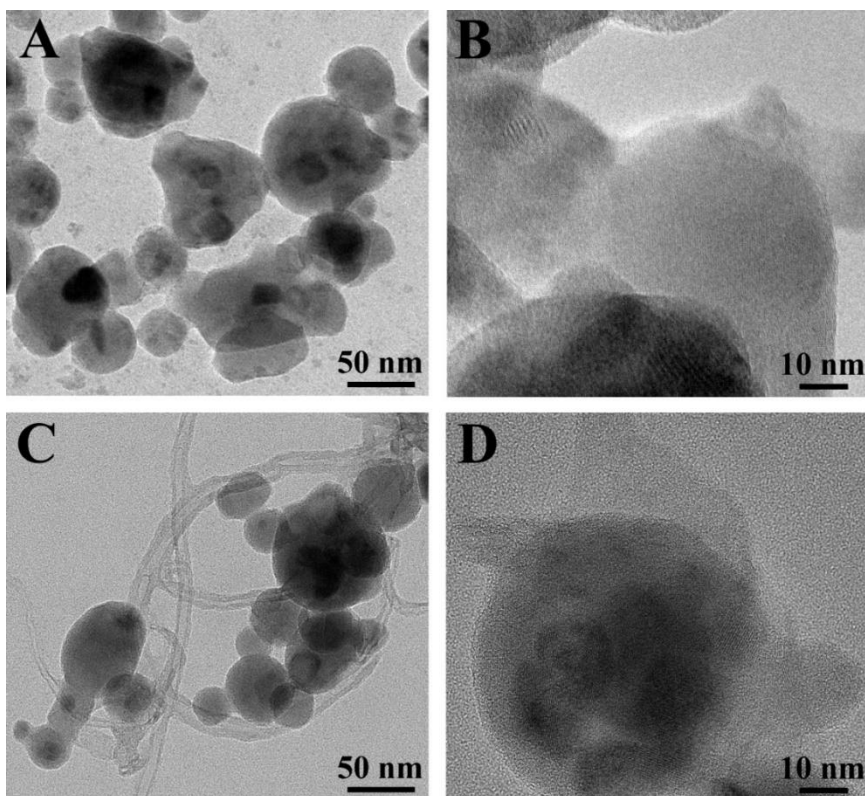
Figure 11.2. TEM images for (A,B)$CuFe_2O_4$ and (C,D)CFO-20.

dispersants showed superior adsorption and facilitated the development of advanced

nanocomposites and film deposition technologies[15]. These studies highlighted the

advantages of charged dispersants, containing chelating anchoring groups, which

facilitated dispersant adsorption by creating complexes with metal atoms on the particle

surface[15-16]. Moreover, it was found that redox-active dispersants, containing

chelating groups can facilitate charge transfer between oxide particles and conductive

additives or current collector and increase pseudocapacitance[17].

In this investigation we examined properties of murexide molecules for co-dispersion

of $CuFe_2O_4$ particles and MCNT. It is known that murexide exhibits redox-active

properties[18] in a negative potential range and forms complexes with Cu, Fe, Ni, Zn,

Co and other metals[19]. The complex formation involved a tridentate bonding[20]. It was suggested that similar complexes (Figure 11.3) can be formed with Cu and Fe atoms on the surface of $CuFe_2O_4$ particles. It was found that the adsorbed negatively charged murexide molecules allowed for improved suspension stability of $CuFe_2O_4$ particles. Moreover, good suspension stability of MCNT was achieved in the presence of murexide. It is suggested that murexide adsorption on MCNT involved hydrophobic interactions of the side walls of MCNT with barbiturate-like rings[20] of the murexide molecules. The electrostatic co-dispersion of the $CuFe_2O_4$ particles and MCNT facilitated their improved mixing.
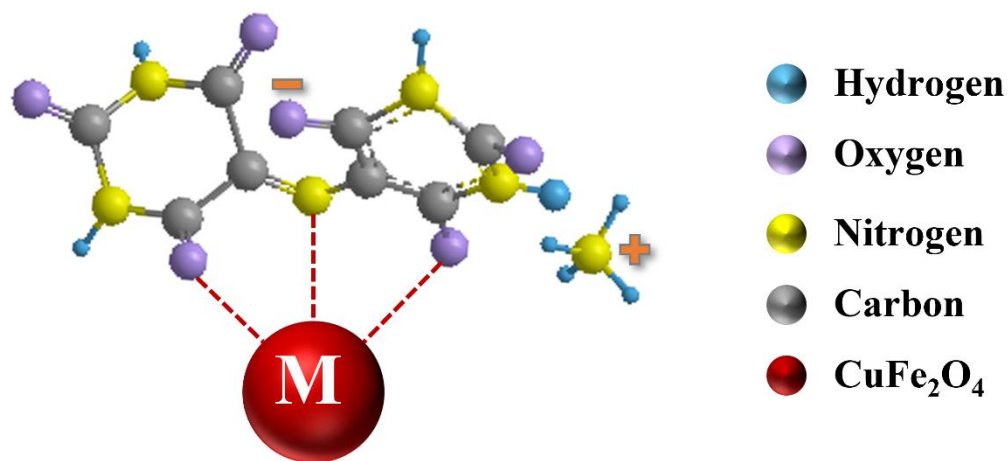
Figure 11.3. Adsorption of murexide on $CuFe_2O_4$ particles, involving chelation of surface atoms (M=Cu or Fe).

Small murexide molecules efficiently separated individual MWCN by breaking original large agglomerates and improved contact of $CuFe_2O_4$ particles and MCNT was achieved (Figure 11.2C,D). SEM image of $CuFe_2O_4$ electrodes showed non-

agglomerated nanoparticles (Figure 11.4A). The composite electrodes showed MCNT

dispersed between $CuFe_2O_4$ particles (Figure 11.4B-D). Good dispersion of MCNT was

a key factor for enhanced contact of $CuFe_2O_4$ particles with conductive MCNT network

and enhanced electrode performance. Figure 11.5 shows XRD patterns of as-received

$CuFe_2O_4$ and CFO-0, CFO-10, CFO-20 and CFO-30 composite electrodes. The XRD

data confirmed that composites contained $CuFe_2O_4$ and MCNT.
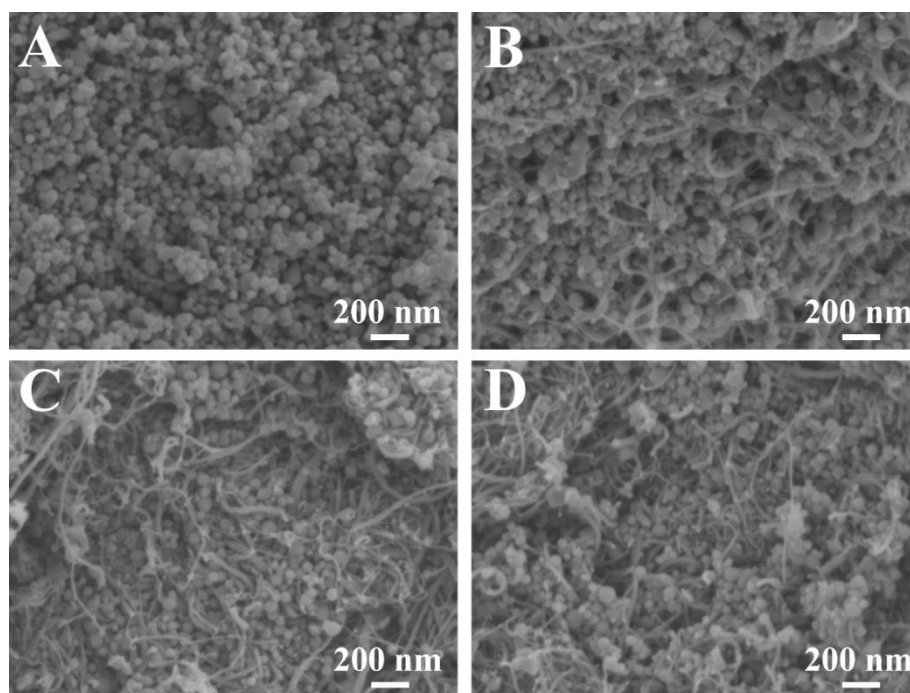
Figure 11.4. SEM images of (A) CFO-0, (B) CFO-10, (C) CFO-20 and (D) CFO-30 electrodes.

CV studies of the CFO-0 electrodes showed very low currents, which indicated poor

pseudocapacitive properties (Figure 11.6A). The addition of MCNT and efficient co-

dispersion of $CuFe_2O_4$ and MCNT resulted in good capacitive behavior of CFO-10,

CFO-20 and CFO-30 electrodes (Figure 11.6 B-D). CFO-10, CFO-20 and CFO-30

electrodes showed nearly rectangular shape CVs. Figure 11.6E shows capacitance

versus scan rate dependencies.
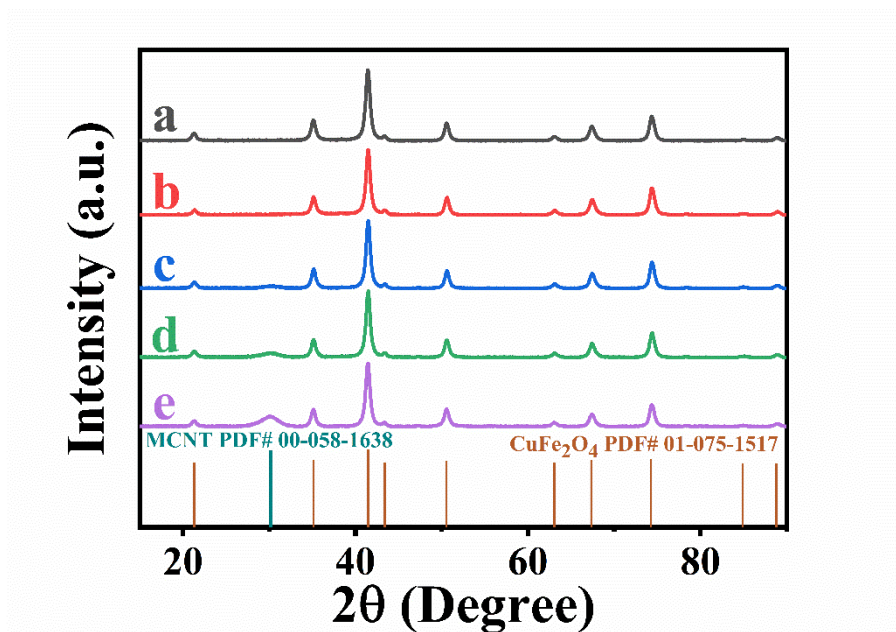
Figure 11.5. XRD data for (a) as-received $CuFe_2O_4$ and electrodes: (b) CFO-0, (c) CFO-10, (d) CFO-20 and (e) CFO-30.

CFO-0, CFO-10, CFO-20 and CFO-30 electrodes showed capacitances of 0.04, 2.75,

2.76 and 2.48 F cm^{-2} at a scan rate of 2 mV s^{-1} and capacitance retention of 25, 17.8,

25.7 and 19.8% at a scan rate of 100 mV s^{-1}. CV data indicated that CFO-20 electrodes

exhibited the best pseudocapacitive performance.
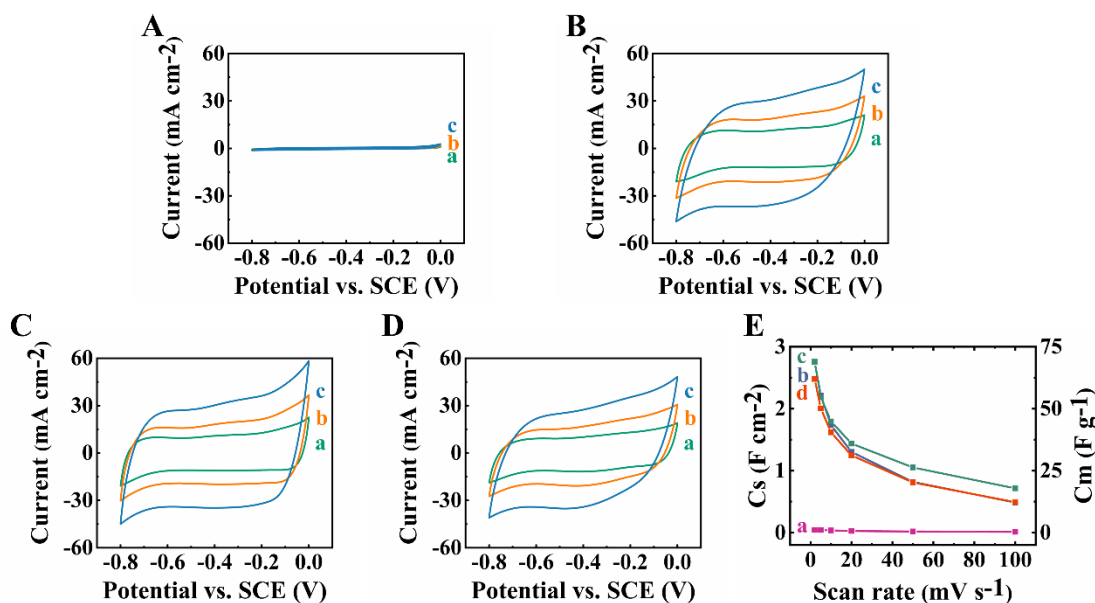
Figure 11.6. (A-D) CVs at scan rates of (a) 5, (b)10 and (c) 20 mV s^{-1} for (A) CFO-0, (B) CFO-10, (C) CFO-20 and (D) CFO-30 electrodes, (E) capacitance versus scan rate for (a) CFO-0, (b) CFO-10, (c) CFO-20 and (d) CFO-30 electrodes.

Impedance spectroscopy data showed high imaginary part of impedance for CFO-0, which was due to low capacitance (Fig.11.7A). The high real part of the complex impedance indicated high electrical resistance. The addition of MCNT resulted in significant decrease in the imaginary part of the impedance and increase in the slope of the Nyquist plot, which indicated improved capacitive behavior (Fig.11.7B). Moreover, significant reduction of the real part of impedance showed reduced electrode resistance. The CFO-20 electrodes showed lower resistance, compared to other electrodes.
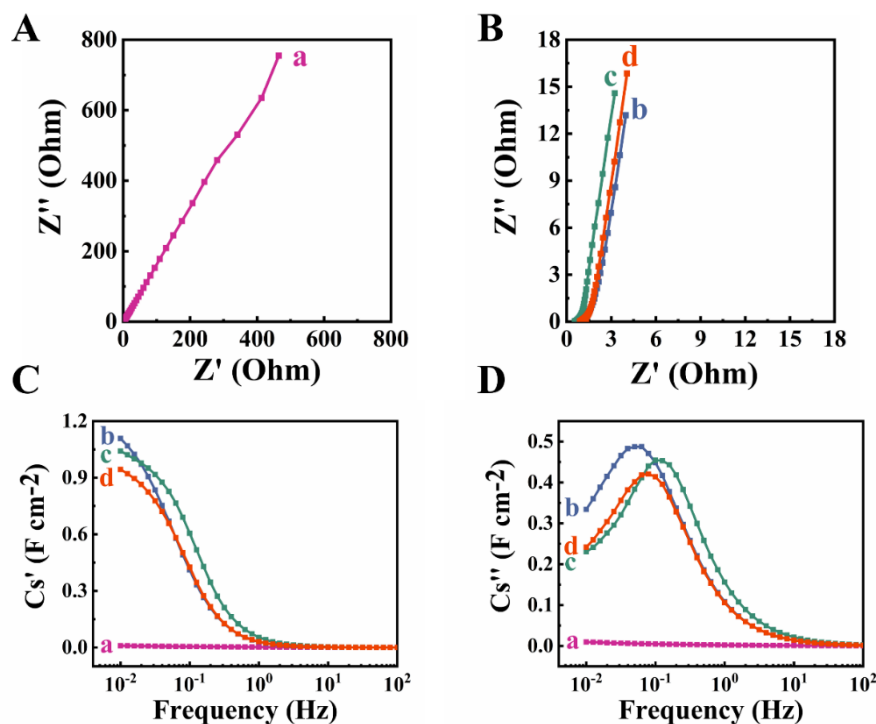
Figure 11.7 (A,B) Nyquist plots of impedance, (C) real and (D) imaginary part of complex capacitance derived from the impedance data versus frequency for (a) CFO-0, (b) CFO-10, (c) CFO-20 and (d) CFO-30 electrodes.

The CFO-0, CFO-10, CFO-20 and CFO-30 electrodes showed capacitances (C_S') of

0.01, 1.11, 1.04, 0.94 F cm^{-2}, respectively, at a frequency of 10 mHz (Figure 11.7).

The CFO-20 electrode showed the highest C_S' at frequencies above 30 mHz. The

CFO-10, CFO-20 and CFO-30 electrodes showed a relaxation type frequency

dispersion of C_S'. The relaxation frequencies for CFO-10, CFO-20 and CFO-30

electrodes, corresponding to C_S'' maxima, were found to be 0.05, 0.11 and 0.94 Hz,

respectively (Figure 11.7D). The highest C_S' at frequencies above 30 mHz and highest

relaxation frequency of the CFO-20 electrode indicated its improved performance at

high charge-discharge rates in agreement with CV data at different scan rates for the

same electrode. It should be noted that capacitance obtained from the CV data in a wide potential range (-0.8-0 V) was influenced by a scan rate, whereas the real part of capacitance derived from the impedance data using a low amplitude AC voltage (5 mV) depended on frequency.

Capacitive behavior of the electrodes has also been analyzed using galvanostatic charge-discharge data at different current densities (Figure 11.8). The increase in the MCNT content resulted in improved shape of the charge-discharge curves, which were nearly triangular (Figure 11.8 A-C) for CFO-20 and CFO-30.

The capacitances, obtained at 3 mA cm^{-2} were 2.03, 1.76 and 1.62 F cm^{-2} for CFO-10, CFO-20 and CFO-30 electrodes, respectively. Figure 11.9 shows cyclic stability data for the CFO-20 electrodes.
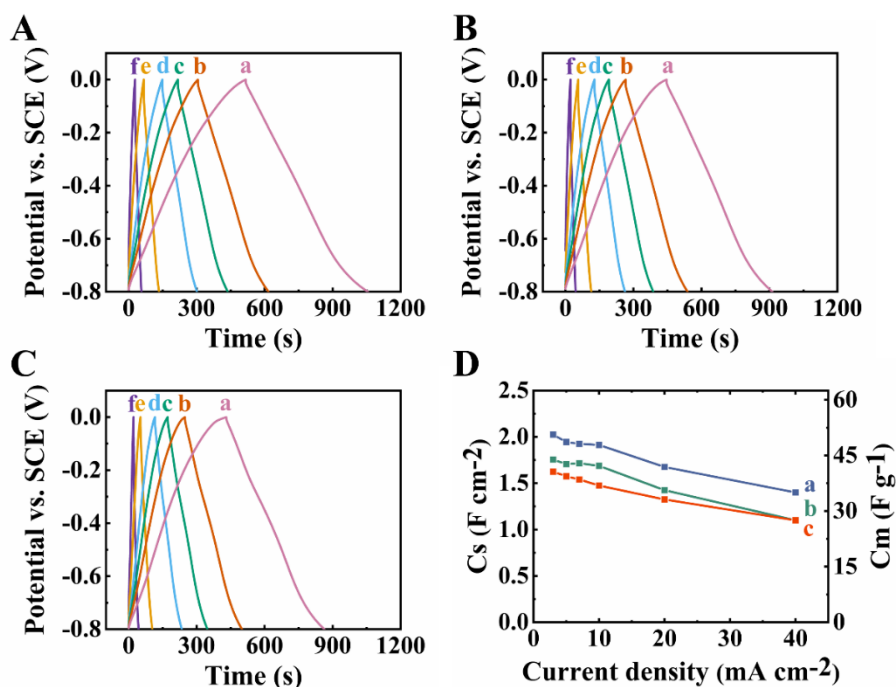
Figure 11.8. (A-C) galvanostatic charge discharge data at current densities of (a) 3, (b) 5, (c) 7, (d) 10, (e) 20 and (f) 40 mA cm^{-2} for (A) CFO-10, (B) CFO-20 and (C) CFO-30 electrodes, (D) capacitance versus current density for (a) CFO-10, (b) CFO-20 and (c) CFO-30 electrodes.
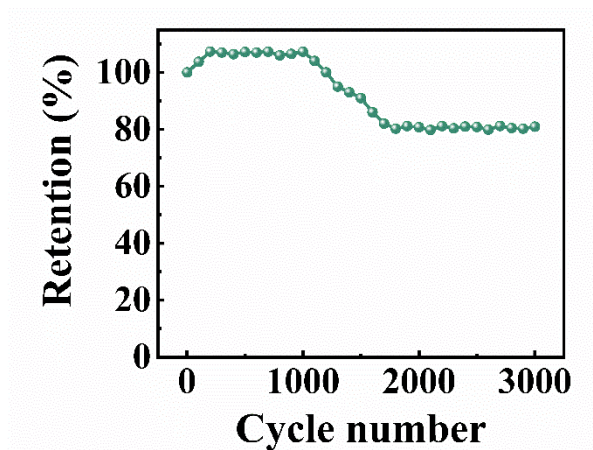
Figure 11.9. Capacitance retention for CFO-20 electrodes.

The increase in capacitance during the first 200 cycles can be attributed to morphology changes during cycling[21]. The capacitance decreased after about 1000 cycles, the capacitance retention after 3000 cycles was 81%.

Table 11.1 compares experimental results of this work with literature data of other

investigations. Capacitive properties of $CuFe_2O_4$ were mainly investigated in a positive

potential range[22]. The charging mechanism in the positive potential range[22b]

involved decomposition of $CuFe_2O_4$ to form individual oxides CuO and Fe_2O_3. It is not

clear if a reverse reaction at room temperature can result in synthesis of $CuFe_2O_4$. CV

data showed well-defined redox peaks indicating a battery-type behavior[22-23] in a

relatively narrow potential window. The galvanostatic charge-discharge curves

deviated significantly[22a-d] from the ideal triangular shape of capacitor materials.

$CuFe_2O_4$ electrodes were tested in KOH[22a-c, 22e] and H_2SO_4[22d]electrolytes.

$CuFe_2O_4$ based electrodes showed high resistance which is detrimental for the

development of electrodes and devices with high power density[22a, 22c, 22d].

Table 11.1. Properties of $CuFe_2O_4$ electrodes

| Mass loading	Capacitance or capacity	Scan rate or current density	Potential range	Electrolyte	Cyclic stability	Cycle number	Reference
§	*1940 F g^{-1} 1164 C g^{-1}	1 A g^{-1}	0-0.6V vs.Ag/AgCl	6M KOH	98%	10000	[22a]
§	*334 F g^{-1}	0.6 A g^{-1}	-0.1- +0.5V vs.SCE	1M KOH	88%	600	[22b]
§	*189.2 F g^{-1}	0.5 A g^{-1}	-0.1- +0.6V vs Ag/AgCl	2M KOH	84%	1000	[22c]
3 mg cm^{-2}	*437.3 F g^{-1}	0.004 V s^{-1}	0.15–0.75 V vs. SCE	0.5M H_2SO_4	88.6%	2000	[22d]
40 mg cm^{-2}	2.76 F cm^{-2}	2 mV s^{-1}	-0.8-0V vs. SCE	0.5 M Na_2SO_4	81%	3000	This work

§ - not presented in the reference

* battery-type behavior

In contrast to previous investigations, which reported a battery-type behavior in the positive potential range, in our investigation we observed a pseudocapacitive behavior in a negative potential range. Good capacitive behavior was achieved at a high active mass of 40 mg cm^{-2}. Recent studies[5, 24] highlighted the need in the development of efficient electrodes with active mass loading above 10-20 mg cm^{-2}, which is required for practical applications. Investigations revealed[5] significant influence of active material mass loading on the mass normalized capacitance, which reduced by 2-3 orders of magnitude with increasing active mass from several μg cm^{-2} to the level of 10-20 mg cm^{-2}. High active mass loading is important for reducing the contribution of inactive components to the total mass of the electrodes and devices. However, it is challenging to achieve good material performance at high active mass. The approach developed in this investigation allowed for high areal capacitance in Na_2SO_4 electrolyte, which is important for the development of asymmetric capacitors with large voltage windows. Despite the use of electrodes with high active mass, the electrode resistance was significantly lower, than resistances of $CuFe_2O_4$ electrodes, reported in the previous investigations[22a, 22c, 22d]. The ability to achieve high capacitance at a low resistance in a relatively large voltage window is promising for the development of devices with enhanced power-energy characteristics. The comparison with literature data[5] indicated that the areal capacitance of the $CuFe_2O_4$ based electrodes is on par with best negative electrodes for operation in an environmentally friendly Na_2SO_4 electrolyte.

Areal capacitance is an important parameter for matching of negative and positive electrodes and optimization of device performance. The pseudocapacitive properties of $CuFe_2O_4$ observed in this investigation coupled with advanced magnetic properties of this material make it a promising MOPC material. It is suggested that the pseudocapacitive properties of $CuFe_2O_4$ in the negative potential range are related to reduction of Cu^{2+} and Fe^{3+} ions. The reduction process can result in changes in material magnetization. Therefore, the results of this work provide a platform for the investigation of phenomena related to relationship between magnetic and pseudocapacitive properties of MOPC materials.

11.5 Conclusions

This investigation revealed pseudocapacitive properties of $CuFe_2O_4$. High areal capacitance of 2.76 F cm^{-2} was achieved at a low resistance in a relatively large negative potential window, which makes $CuFe_2O_4$ a promising negative electrode for the development of asymmetric supercapacitors operating in environmentally friendly Na_2SO_4 electrolyte. The approach developed in this investigation allowed good material performance at high active mass loading, which is important for practical applications. It was based on the use of murexide as a chelating co-dispersant for $CuFe_2O_4$ and MCNT. The murexide adsorption on $CuFe_2O_4$ and MCNT involved different mechanisms, which were linked to features of the murexide structure. $CuFe_2O_4$

nanoparticles combined magnetic ordering and advanced pseudocapacitive properties, which make $CuFe_2O_4$ a promising MOPC material. The combination of advanced magnetic and capacitive properties in $CuFe_2O_4$ in the negative potential range provides a platform for the investigation of new phenomena, related to the influence of pseudocapacitive/magnetic properties on magnetic/pseudocapacitive behavior.

11.6 Acknowledgments

11.7 References

[1]   Y. N. Venevtsev, V. V. Gagulin, I. D. Zhitomirsky, *Ferroelectrics* **1987**, 73,
        221.

[2]   H. Schmid, *Ferroelectrics* **1994**, 162, 317.

[3]   M. Nawwar, R. P. Sahu, I. K. Puri, I. Zhitomirsky, *Open Ceramics* **2021**,
        100127.

[4]   J. A. Argüello, A. Cerpa, R. Moreno, *Ceramics International* **2019**, 45, 14316.

[5]   R. Chen, M. Yu, R. P. Sahu, I. K. Puri, I. Zhitomirsky, *Advanced Energy
        Materials* **2020**, 10, 1903848.

[6]   a) S. M. Alshehri, J. Ahmed, A. N. Alhabarah, T. Ahamad, T. Ahmad,
        ChemElectroChem **2017**, 4, 2952; b) V. V. Deshmukh, H. P. Nagaswarupa, N.
        Raghavendra, *Ceramics International* **2021**, 47, 10268.

[7]   E. Rezaie, A. Rezanezhad, L. S. Ghadimi, A. Hajalilou, N. Arsalani, *Ceramics
        International* **2018**, 44, 20285.

[8]   a) A. Viswanathan, A. N. Shetty, *Electrochimica Acta* **2019**, 309, 187; b) S.
        Pal, S. Majumder, S. Dutta, S. Banerjee, B. Satpati, S. De, *Journal of Physics
        D: Applied Physics* **2018**, 51, 375501; c) M. Singh, A. Sahoo, K. Yadav, Y.
        Sharma, *ACS Applied Materials & Interfaces* **2020**, 12, 49530.

[9]   K. Malaie, M. R. Ganjali, *Journal of Energy Storage* **2020**, 102097.

[10]   M. Nawwar, R. Poon, R. Chen, R. P. Sahu, I. K. Puri, I. Zhitomirsky, *Carbon
        Energy* **2019**, 1, 124.

[11]   a) J. Acharya, B. G. S. Raj, T. H. Ko, M.-S. Khil, H.-Y. Kim, B.-S. Kim,
        international journal of hydrogen energy **2020**, 45, 3073; b) M. A.
        Almessiere, Y. A. Slimani, M. Hassan, M. A. Gondal, E. Cevik, A. Baykal,
        International Journal of Energy Research **2021**; c) G. Nabi, W. Raza, M. A.
        Kamran, T. Alharbi, M. Rafique, M. B. Tahir, S. Hussain, N. Khalid, N.
        Malik, R. S. Ahmed, *Journal of Energy Storage* **2020**, 29, 101452.

[12]   A. Thirumurugan, T. Kavinkumar, R. Udayabhaskar, K. Kiruthiga, M. J.
        Morel, R. Aepuru, N. Dineshbabu, K. Ravichandran, A. Akbari-Fakhrabadi,
        R. Mangalaraja, *Electrochimica Acta* **2021**, 139346.

[13]   a) K. Shi, I. Zhitomirsky, *ACS Applied Materials & Interfaces* **2013**, 5, 13161;
        b) K. Shi, I. Zhitomirsky, *Journal of Colloid and Interface Science* **2013**, 407,
        474.

[14]   C. Wallar, R. Poon, I. Zhitomirsky, *Journal of The Electrochemical Society*
        2017, 164, A3620.

[15]   M. Ata, Y. Liu, I. Zhitomirsky, *Rsc Advances* **2014**, 4, 22716.

[16]   a) R. M. E. Silva, R. Poon, J. Milne, A. Syed, I. Zhitomirsky, *Advances in Colloid and Interface Science* **2018**, 261, 15; b) K. Wu, Y. Wang, I. Zhitomirsky, *Journal of colloid and interface science* **2010**, 352, 371.

[17]   M. Nawwar, R. Poon, R. P. Sahu, I. K. Puri, I. Zhitomirsky, *Ceramics International* **2020**, 46, 18851.

[18]   H. S. Mohran, *American Journal of Applied Sciences* **2009**, 6, 964.

[19]   M. Masoud, T. Kassem, M. Shaker, A. Ali, *Journal of thermal analysis and calorimetry* **2006**, 84, 549.

[20]   R. L. Martin, A. H. White, A. C. Willis, *Journal of the Chemical Society, Dalton Transactions* **1977**, 1336.

[21]   K. Rorabeck, I. Zhitomirsky, *Colloids and Surfaces A: Physicochemical and Engineering Aspects* **2021**, 618, 126451.

[22]   a) S. B. Bandgar, M. M. Vadiyar, U. P. Suryawanshi, C. L. Jambhale, J.-H. Kim, S. S. Kolekar, *Materials Letters* **2020**, 279, 128514; b) M. Zhu, D. Meng, C. Wang, G. Diao, *ACS applied materials & interfaces* **2013**, 5, 6030; c) B. Saravanakumar, S. Ramachandran, G. Ravi, V. Ganesh, R. K. Guduru, R. Yuvakkumar, *Vacuum* **2019**, 168, 108798; d) Y. Guo, Y. Chen, X. Hu, Y. Yao, Z. Li, *Colloids and Surfaces A: Physicochemical and Engineering Aspects* **2021**, 631, 127676; e) W. Zhang, B. Quan, C. Lee, S.-K. Park, X. Li, E. Choi, G. Diao, Y. Piao, *ACS applied materials & interfaces* **2015**, 7, 2404.

[23]   S. Nilmoung, T. Sinprachim, I. Kotutha, P. Kidkhunthod, R. Yimnirun, S. Rujirawat, S. Maensiri, *Journal of Alloys and Compounds* **2016**, 688, 1131.

[24]   Y. Gogotsi, P. Simon, *Science* **2011**, 334, 917.

Chapter 12 Conclusions and Future works

Several advanced composite materials at very high mass loading were fabricated by conceptually new colloidal techniques. The asymmetric supercapacitor devices with enlarged voltage window were developed. The major achievements of this dissertation can be summarized as follows:

1. $Ti_3C_2T_x$-MCNT negative electrodes with high active mass loading at 35 mg cm^{-2} were fabricated and tested in a large voltage window of 0.8 V. The advanced colloidal fabrication technique allowed for a high areal capacitance of 1.93 F cm^{-2}. The very strong co-dispersants, cationic celestine blue and anionic catechol violet, promoted the dispersion and mixing between $Ti_3C_2T_x$ and MCNT. Besides, the content of selected PEMA and PVBAA as binder materials was optimized at 3%.

2. $Ti_3C_2T_x$-MCNT anodes with optimized MCNT ratio at a level of 10% were achieved. Enhanced capacitive performance was observed for electrodes at high active mass loading of 35 mg cm^{-2}, which can be attributed to the successful utilization of excellent catechol-type dispersant 3,4,5-trihydroxybenzamide (THB). The adsorption mechanisms involved bridging or chelating bonding of the catechol groups to the Ti atoms, and π-π interaction on MCNT.

3. Advanced negative electrodes of $Ti_3C_2T_x$- -CNT, Fe_3O_4-CNT and $Ti_3C_2T_x$-Fe_3O_4-CNT were achieved at 35 mg cm^{-2} mass loading. The comparison of the capacitive

behavior reveals a synergistic effect of each component. The capacitance as high as 5.52 F cm^{-2} was recorded in aqueous 0.5 M Na$_2$SO$_4$ electrolyte. Such electrode can be promising for application of asymmetric supercapacitor device.

4. Zn-Fe double hydroxide (Zn-Fe-DH)-multiwalled carbon nanotube (MWCNT) composites were developed. The multifunctional molecule celestine blue was applied as a charge transfer mediator as well as a dispersant, which facilitated the mixing and interfacial charge transfer between Zn-Fe-DH and MWCNT. Besides, a new asymmetrical device was fabricated, containing Zn-Fe-DH-MWCNT anode and PPy-MWCNT cathode in a partially overlapping potential window. A high areal capacitance of 2.2 F cm^{-2} was obtained in a large voltage window of 1.6 V.

5. The problem of poor cyclic stability of FeOOH electrodes was addressed by Zn-doping and the ratio of Zn was optimized at level of 12%. Capacitive performance was further enhanced by composites containing polypyrrole coated carbon nanotubes. The supercapacitor device of 12ZFCPC-MC showed promising performance and generated new direction for future SC applications.

6. (Zn-Fe)OOH-polypyrrole coated carbon nanotube (PNT) anode achieved high areal capacitance of 4 F cm^{-2} and good cyclic stability of 91% retention after 1000 cycles. Combined with advanced Mn$_3$O$_4$-CNT cathode, the device showed 1.87 F cm^{-2} high capacitance and excellent retention of 84% after 1000 cycles.

7. The advanced asymmetric device was fabricated based on MXene-PPy negative

electrode and PPy coated MCNT positive electrode. The remarkable capacitive

performance achieved at high active mass loading of 40 mg cm^{-2} can be attributed

to the conceptually new strategy of in-situ PPy polymerization on the MXene

surface, with the aid of efficient catecholate-type dispersant for electrostatic

dispersion of MXene.

8. The pseudocapacitive properties of magnetic material $CuFe_2O_4$ was investigated.

    Good electrochemical performance with nearly ideal cyclic voltammograms and

    galvanostatic charge-discharge data was recorded in a wide potential range of 0.8

    V. Besides, advanced chelating dispersant murexide was developed to enhance the

    interaction between $CuFe_2O_4$ and conducting additive MCNT. The successful

    combination of magnetic and pseudocapacitive material provides a platform for the

    future investigation on this field.

The results of this dissertation have addressed several problems related to synthesis of

composite materials and fabrication of supercapacitors. Further attention should be paid

to the influence of magnetic properties of SC electrodes and devices. Some spinel group

materials, such as $CuFe_2O_4$, $NiFe_2O_4$ and $Y_3Fe_5O_{12}$ can be promising candidates for

SCs. The influence of structure of materials on the electrochemical performance should

be noticed. New dispersants, colloidal techniques and further development should be

given to scalable production and practical application.